JOURNAL OF APPLIED PHYSICS

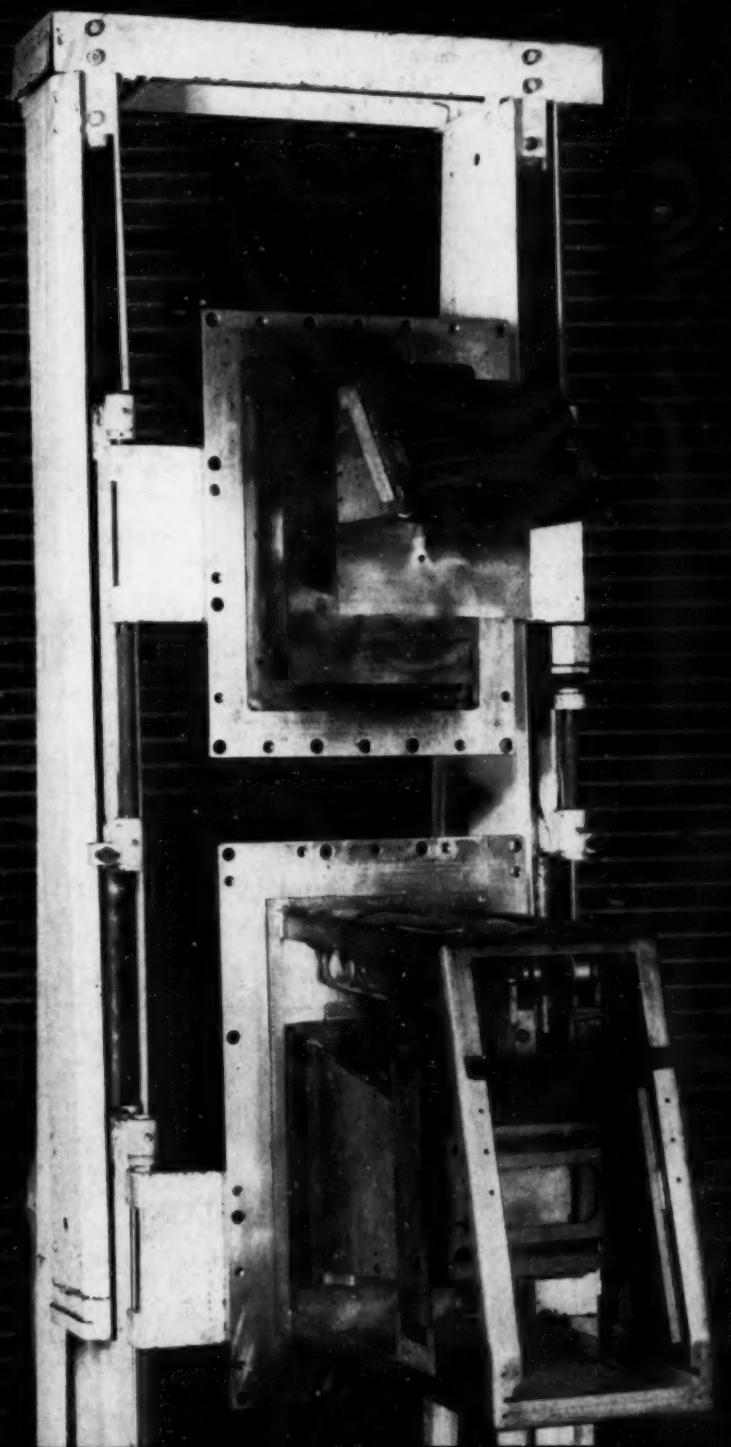

JOURNAL OF APPLIED PHYSICS

Vol. 24, No. 10 OCTOBER, 1953

In This Issue

		Page
Enriching Stable Isotopes Electromagnetically	C. P. Keim	1255
Trajectories in the Symmetrical Electron Lens	L. Jacob and J. R. Shah	1261
Recovery Currents in Germanium $p-n$ Junction Diodes	R. G. Shulman and M. E. McMahon	1267
Attenuation of Gamma Rays. I. Transmission Values for Finite Slabs of Lead, Iron, and the Compton Scatterer	Glenn H. Peebles	1272
Properties of Carbon Contacts	R. O. Grisdale	1288
Characteristics of an Elliptical Electromagnetic Resonant Cavity Operating in the TE_{111} Mode	T. P. Higgins and A. W. Straiton	1297
Ferry Reduction and the Activation Energy for Viscous Flow	I. L. Hopkins	1300
"Double" Camera for Electron Diffraction	Shigeto Yamaguchi	1305
Note on the Analysis of First-Order Glow Curves	Leonard I. Grossweiner	1308
Measurement of the Heat of Activation for Sodium Ion Diffusion in Glass	R. Kamel	1308
Heat Transfer at High-Power Densities	John S. Hickey, Jr.	1312
Preliminary Results on Photoelectric Yields of Pt and Ta and on Photoionization in O_2 and N_2 in the Vacuum Ultraviolet	N. Wainfan, W. C. Walker, and G. L. Weissler	1318
Electron Compounds of Transition Elements	H. J. Beattie, Jr.	1322
On the Propagation Constant in Gentle Circular Bends in Rectangular Wave Guides—Matrix Theory	A. T. de Hoop	1325
"Brillouin Flow" with Thermal Velocities	J. R. Pierce and L. R. Walker	1328
Erratum: Summation of Slowly Converging Series		1330
Letters to the Editor:		
Germanium Under Ultrasonic Stress. I: Anelastic Effects	G. S. Baker, L. M. Slifkin, and J. W. Marx	1331
Germanium Under Ultrasonic Stress. II: Dynamic Yield Point	G. S. Baker, L. M. Slifkin, and J. W. Marx	1331
Thermal Effects in Point Contact Rectifiers	H. L. Armstrong	1332
Electromotive Force Developed by a Creeping Zinc Crystal	Frances Dunkle Coffin and Sidney L. Simon	1333
Erratum: The Potential of Two Current Point Sources in a Homogeneous Conducting Prolate Spheroid	James R. Wait	1334
Time Effects in the Hysteresis Loop of Polycrystalline Barium Titanate	Malcolm McQuarrie	1334
Erratum: Instabilities in the Smooth-Anode Cylindrical Magnetron	Lawrence A. Harris	1335
Note on Shock Propagation in Brass	Jacob Savitt	1335
Molded Thermionic Cathodes	D. MacNair, R. T. Lynch, and N. B. Hannay	1335
On the Synthesis of Reactance 4-Poles	Herbert J. Carlin and R. La Rosa	1336
Shot Noise in Junction Transistors	H. C. Montgomery and M. A. Clark	1337
Note on the Cylindrical Antenna of Noncircular Cross Section	Y. T. Lo	1338
Force on a Shorted Ring in a uhf Field in a Coaxial Cavity	Surindra N. Kalra	1339
Bounds for Entropy	Nelson M. Blachman	1340
Forming Silicon Point Contact Transistors	Harold Jacobs, Frank A. Brand, and Wesley Matthei	1340
Announcement		1299
Index to Advertisers		xxvi

ELMER HUTCHISSON,
Editor

EARLE C. GREGG,
Assistant Editor

Board of Editors
RAY E. BOLZ
LYLE D. BORST
WALLACE J. ECKERT
ROBERT D. HEIDENREICH
LEONARD B. LOEB
W. JAMES LYONS
LOUIS A. PIPES
ROMAN SMOLUCHOWSKI
W. R. SMYTHE

Publication of the
American Institute of Physics

OFFICERS
GEORGE R. HARRISON,
Chairman
GEORGE B. PEGRAM,
Treasurer

GOVERNING BOARD
J. W. BUCHTA
KARL K. DARROW
G. J. DIENES
S. A. GOUDSMIT
GEORGE R. HARRISON
FREDERICK V. HUNT
DEANE B. JUDD
HUGH S. KNOWLES
C. C. LAURITSEN
WILLIAM F. MEGGERS
PHILIP M. MORSE
BRIAN O'BRIEN
GEORGE B. PEGRAM
I. I. RABI
DUANE ROLLER
FREDERICK SEITZ
WILLIAM SHOCKLEY
RICHARD M. SUTTON
J. H. VAN VLECK
MARK W. ZEMANSKY

Consultant on Printing
MELVIN LOOS

ADMINISTRATIVE STAFF
HENRY A. BARTON,
Director
WALLACE WATERFALL,
Executive Secretary
THEODORE VORBURGER,
Advertising Manager
RUTH F. BRYANS,
Publication Manager
EDITH I. NEFTEL
Circulation Manager
KATHRYN SETZE
Assistant Treasurer

The JOURNAL OF APPLIED PHYSICS, published monthly at Prince and Lemon Sts., Lancaster, Pa., is devoted to physics in its role as the science basic to other natural sciences and to the arts and industries. Previous to 1937 this publication was known as PHYSICS. The JOURNAL OF APPLIED PHYSICS publishes editorials and reviews, as well as technical papers of applied physics. Articles appearing in it are indexed regularly, according to their field, by Physics Abstracts, Chemical Abstracts, Engineering Index, Inc., Industrial Arts Index, etc.

Manuscripts should be submitted to Elmer Hutchisson, Editor, Case Institute of Technology, Cleveland 6, Ohio. Unless otherwise stated, submission of a manuscript is a representation that it has been neither copyrighted, published, nor submitted for publication elsewhere. The authors' institutions are requested to pay a **publication charge** of $8 per page which, if honored, entitles them to 100 reprints without further charge. Instructions will be sent with galley proofs.

Subscriptions, renewals, and orders for back numbers should be addressed to the American Institute of Physics, 57 East 55 Street, New York 22, New York.

Subscription Price	U.S. and Canada	Elsewhere
To members of the American Institute of Physics and Affiliated Societies	$10.00	$11.00
To all others	12.00	13.00

Back Number Prices

Yearly back number rate when complete year is available: $14.00. Single copies: $1.25 each.

Changes of address should be sent to the American Institute of Physics; **corrected proofs** should be sent to the Publication Manager, American Institute of Physics. **Advertising rates** supplied on request. Orders, advertising copy, and cuts should be sent to the American Institute of Physics.

Entered as second class matter January 22, 1937, at the Post Office at Lancaster, Pennsylvania, under the Act of March 3, 1879. Accepted for mailing at the special rate of postage provided for in paragraph (d-2), section 34.40, P. L. & R. of 1948, authorized May 2, 1932.

Journal
of
Applied Physics

Volume 24, Number 10 October, 1953

Enriching Stable Isotopes Electromagnetically

C. P. KEIM

Stable Isotope Research and Production Division, Oak Ridge National Laboratory, Oak Ridge, Tennessee*

The natural stable isotopes of forty-three elements, comprising 177 different nuclides, have been enriched; the goal is to enrich 257 isotopes of fifty-nine elements. The isotopic enrichments, the operation of the production mass spectrographs including a listing of best charge materials, a brief review of the chemical and analytical problems, a tabulation of the best compounds of the separated isotopes for mass spectrometer analyses, and a listing of some of the major uses of separated isotopes have been included in this survey of the electromagnetic isotope separation program.

INTRODUCTION

UNTIL 1946 the available enriched stable isotopes were limited to the isotopes of only a few elements. After large mass spectrographs were developed at Oak Ridge (the calutrons), enriched isotopes of forty-three elements (177 different isotopes) were produced during the first few years of using the calutrons for enriching natural isotopes. The electromagnetic separation of isotopes is outlined in Fig. 1.

The isotopes which have been separated in the

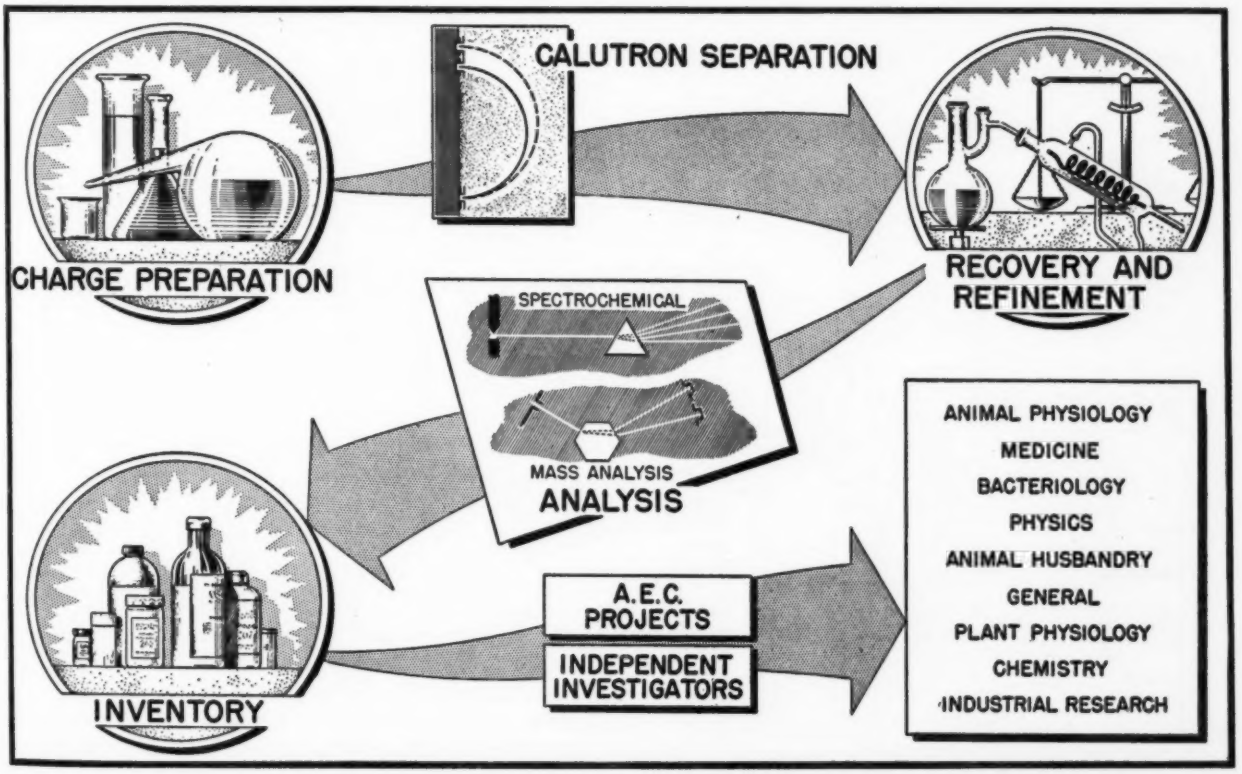

FIG. 1. The calutron isotope separation cycle showing the various operations performed.

* This report is based on work performed for the U. S. Atomic Energy Commission by Carbide and Carbon Chemicals Company, a division of Union Carbide and Carbon Corporation.

TABLE I. Isotopes processed and isotopic enrichments attained in the calutron.

Element	Isotope mass	Natural abundance percent	Enriched abundance percent
Lithium	6	7.52	99.40
	7	92.48	99.97
Boron	10	18.98	86.78
	11	81.02	*
Carbon	12	98.892	99.99
	13	1.108	7.52
Nitrogen	14	99.635	*
	15	0.365	
Oxygen	16	99.759	*
	17	0.0374	*
	18	0.2039	*
Magnesium	24	78.60	99.52
	25	10.11	92.33
	26	11.29	98.12
Silicon	28	92.27	99.4
	29	4.68	68.6
	30	3.05	64.0
Sulfur	32	95.06	98.45
	33	0.74	9.8
	34	4.18	20.65
	36	0.016	0.88
Chlorine	35	75.4	92.4
	37	24.6	65.6
Potassium	39	93.08	99.96
	40	0.0119	7.75
	41	6.91	99.21
Calcium	40	96.97	99.97
	42	0.64	82.52
	43	0.145	72.13
	44	2.06	97.99
	46	0.0033	10.16
	48	0.185	84.28
Titanium	46	7.95	84.26
	47	7.75	82.05
	48	73.45	99.23
	49	5.51	77.62
	50	5.34	84.69
Vanadium	50	0.24	22.93
	51	99.76	99.98
Chromium	50	4.31	88.3
	52	83.76	99.14
	53	9.55	92.1
	54	2.38	88.95
Iron	54	5.84	93.27
	56	91.68	99.84
	57	2.17	87.29
	58	0.31	86.0
Nickel	58	67.76	99.3
	60	26.16	97.7
	61	1.25	80.9
	62	3.66	94.7
	64	1.16	97.4
Copper	63	69.1	99.70
	65	30.9	98.16
Zinc	64	48.89	93.4
	66	27.82	93.79
	67	4.14	62.6
	68	18.54	95.47
	70	0.617	48.4
Gallium	69	60.2	98.42
	71	39.8	98.08
Germanium	70	20.55	88.1
	72	27.37	89.2
	73	7.61	68.9
	74	36.74	95.2
	76	7.67	79.3
Selenium	74	0.87	33.06
	76	9.02	88.51
	77	7.58	91.73
	78	23.52	96.55
Selenium	80	49.82	98.39
	82	9.19	89.87
Bromine	79	50.52	90.54
	81	49.48	96.81
Rubidium	85	72.15	95.97
	87	27.85	89.62
Strontium	84	0.56	63.68
	86	9.86	89.02
	87	7.02	73.1
	88	82.56	99.67
Zirconium	90	51.46	98.66
	91	11.23	86.89
	92	17.11	95.38
	94	17.40	97.92
	96	2.80	89.48
Molybdenum	92	15.86	95.5
	94	9.12	79.1
	95	15.70	91.27
	96	16.50	92.0
	97	9.45	89.63
	98	23.75	96.3
	100	9.62	93.0
Silver	107	51.35	96.10
	109	46.85	99.54
Cadmium	106	1.215	32.9
	108	0.875	24.8
	110	12.39	70.0
	111	12.75	64.5
	112	24.07	83.5
	113	12.26	54.1
	114	28.86	94.2
	116	7.58	71.2
Indium	113	4.23	65.4
	115	95.77	99.94
Tin	112	0.95	72.49
	114	0.65	50.03
	115	0.34	17.64
	116	14.24	92.64
	117	7.57	77.07
	118	24.01	94.91
	119	8.58	79.82
	120	32.97	98.21
	122	4.71	88.92
	124	5.98	95.04
Antimony	121	57.25	99.4
	123	42.75	96.7
Tellurium	120	0.089	22.3
	122	2.46	86.24
	123	0.87	60.91
	124	4.61	83.9
	125	6.99	87.9
	126	18.71	95.4
	128	31.79	96.47
	130	34.49	97.78
Barium	130	0.101	27.50
	132	0.097	12.01
	134	2.42	51.39
	135	6.59	67.32
	136	7.81	50.02
	137	11.32	38.98
	138	71.66	98.04
Lanthanum	138	0.089	0.597
	139	99.911	99.96
Cerium	136	0.193	29.97
	138	0.250	13.10
	140	88.48	99.65
	142	11.07	90.08
Neodymium	142	27.13	93.00
	143	12.20	83.93
	144	23.87	93.45

* No mass analysis performed.

TABLE I.—*Continued.*

Element	Isotope mass	Natural abundance percent	Enriched abundance percent
Neodymium	145	8.30	78.60
	146	17.18	95.60
	148	5.72	89.85
	150	5.60	94.76
Samarium	144	3.16	72.13
	147	15.07	81.63
	148	11.27	76.01
	149	13.84	73.01
	150	7.47	74.09
	152	26.63	93.92
	154	22.53	96.05
Hafnium	174	0.18	7.85
	176	5.15	48.46
	177	18.39	61.71
	178	27.08	80.91
	179	13.78	46.57
	180	35.44	93.96
Tungsten	180	0.135	9.0
	182	26.4	94.25
	183	14.4	86.21
	184	30.6	95.72
	186	28.4	97.94
Rhenium	185	37.07	85.38
	187	62.93	98.22
Mercury	196	0.146	8.44
	198	10.02	79.11
	199	16.84	73.09
	200	23.13	91.3
	201	13.22	71.9
	202	29.80	98.3
	204	6.85	89.17
Thallium	203	29.50	86.0
	205	70.50	98.7
Lead	204	1.48	27.0
	206	23.6	81.0
	207	22.6	66.8
	208	52.3	96.6

calutron in milligram to multigram quantities, and their isotopic enrichments, are summarized in Table I. Higher isotopic purities than those listed can be obtained for many of the isotopes if the importance of the product warrants it.

PRINCIPLE OF THE CALUTRON

The production calutron is similar to the laboratory mass spectrograph. In both instruments ions are produced, accelerated by an electric field, and separated according to isotopic masses in crossing a magnetic field. Ion source, trajectory, and collector are enclosed in a highly evacuated chamber. The calutron is a large output machine designed to collect usable quantities of separated isotopes, while the laboratory mass spectrograph is used almost entirely for the detection or analysis of extremely weak ion beams.

The element to be processed, or its compound, is introduced as a vapor into the ionization chamber of the calutron where the particles are dissociated, if complex, and ionized by a stream of electrons from an electrically heated tungsten or tantalum filament. Positively charged ions thus produced travel from the ionization chamber through a defining slit and through corresponding slits in the accelerating electrodes. The high velocity ions then travel across a magnetic field, such that $r=(2Vm/H^2e)^{\frac{1}{2}}$, where r is the radius of the ion path from source to collector, V is the accelerating voltage, H is the magnetic field, m is the mass and e the charge of the ion (ions carrying a single positive charge are usually most abundant).

At the end of half a circle ions of different masses attain their maximum separation. By placing collector pockets at this 180° position, spaced as calculated from the above equation, the different isotopes of a given element can be collected separately and simultaneously.

The nomograph (Fig. 2) may be used with the above equation if singly charged ions are being collected. In the calutron the radius of ion travel may be varied from a few inches up to forty-eight, the accelerating voltage from a few kilovolts up to forty, and the magnetic field up to over ten thousand oersteds.

SELECTION OF A SUITABLE CHARGE MATERIAL

In selecting a suitable calutron charge material several requirements must be met, including adequate vapor pressure at calutron operating temperatures, simplicity of molecular structure, stability of the compound, and absence of water of crystallization. If the element itself has a favorable vapor pressure it is generally used as charge material, since its use greatly reduces extraneous ions or side bands. Table II summarizes the charge materials most generally used.

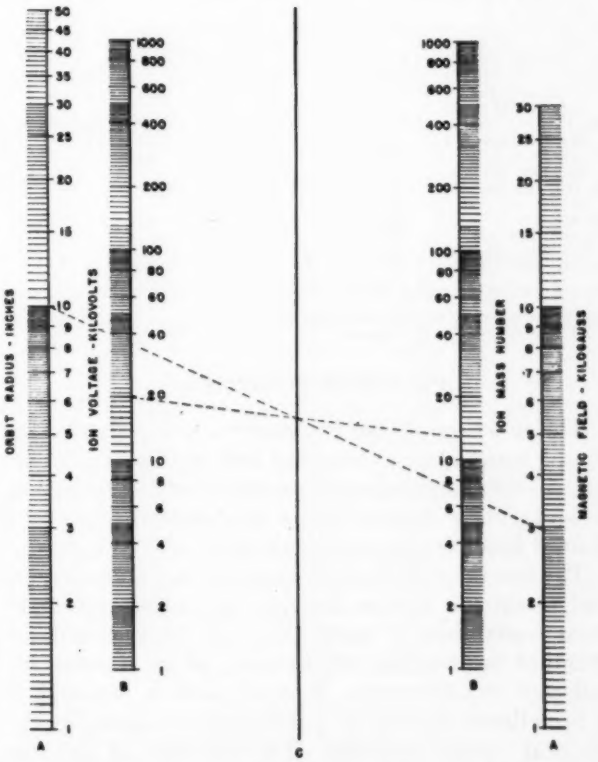

FIG. 2. A nomograph for a mass spectrograph of the calutron type.

TABLE II. Charge materials, operating temperatures, and types of collectors for stable isotope separations.

Isotopes	Charge material	Oven temp. °C	Collector material
Li-6, 7	LiBr-Li metal mixture	480–550	Copper[a]
Be-9, (10)[b]	$BeCl_2$	200–350	Graphite
B-10, 11	BCl_3		Copper
C-12, 13	CO_2		Copper
N-14, 15	N_2		Graphite with Mg to form nitride
O-16, 17, 18	O_2		Copper or graphite with fine Cu to form oxide
Mg-24, 25, 26	Mg	500–550	Copper
Si-28, 29, 30	$SiCl_4$		Copper
S-32, 33, 34, 36	CS_2		Copper with fine Cu to form sulfide
Cl-35, 37	BCl_3	250–415	Copper with Ba and Mg
K-39, 40, 41	K	175–225	Copper
Ca-40, 42, 43, 46, 48	Ca	550–650	Copper
Ti-46, 47, 48, 49, 50	$TiCl_4$		Graphite
V-50, 51	VF_3	225–800	Graphite
Cr-50, 52, 53, 54	$CrCl_3$	500–600	Graphite
Fe-54, 56, 57, 58	$FeCl_3$	480–590	Copper or graphite
Ni-58, 60, 61, 62	$NiCl_2$	550–625	Graphite
Cu-63, 65	CuCl	350–425	Graphite
Zn-64, 66, 67, 68, 70	Zn	400–550	Copper
Ga-69, 71	GaI_3	120–180	Graphite
Ge-70, 72, 73, 74, 76	$GeCl_4$		Graphite
Se-74, 76, 77, 78, 80, 82	SeO_2	150–250	Copper
Br-79, 81	$SrBr_2$	700–800	Copper containing Cd turnings
Rb-85, 87	RbI	550–650	Copper
Sr-84, 86, 88	Sr	535–625	Copper
Zr-90, 91, 92, 94, 96	$ZrCl_4$	200–350	Copper
Mo-92, 94, 95, 96 97, 98, 100	$MoCl_3$	75–100	Graphite
Ag-107, 109	AgCl	550–650	Copper
Cd-106, 108, 110, 111, 112, 113, 114, 116	Cd	275–325	Copper
In-113, 115	InI	250–300	Graphite
Sn-112, 114, 115, 116, 117, 118, 119, 120, 122, 124	$SnCl_4$		Graphite
Sb-121, 123	Sb_2O_3	350–450	Stainless steel
Te-120, 122, 123, 124, 125, 126, 128, 130	$TeCl_4$	150–200	Copper
Ba-130, 132, 134, 135, 136, 137, 138	Ba	725–800	Graphite
La-138, 139	$LaCl_3$	500–600	Graphite
Ce-136, 138, 140, 142	$CeCl_3$	525–625	Copper or graphite
Nd-142, 143, 144, 145, 146, 148, 150	$NdCl_3$	550–650	Graphite or copper
Sm-144, 147, 148, 149, 150, 152, 154	$SmCl_3$	600–700	Copper or graphite
Hf-174, 176, 177, 178, 179, 180	$HfCl_4$	110–170	Copper
W-180, 182, 183, 184, 186	WCl_6	150–250	Copper
Re-185, 187	Re_2O_7	190–250	Graphite
Hg-196, 198, 199, 200, 201, 202, 204	$HgCl_2$	50–110	Silver
Tl-203, 205	TlI	335–370	Copper

[a] All copper collectors are water-cooled.
[b] Pile-produced Be-10 separated from natural Be-9.

CALUTRON EQUIPMENT

The functions of the ion source are to vaporize the charge material at a controlled rate, to dissociate molecules of the charge material into their constituent atoms, to ionize these atoms, and to accelerate the ions in a defined beam across a magnetic field.

The functions of the receiver or collector are to receive and retain the various isotopes and to protect them from contamination until they can be removed for chemical purification. All isotopes of an element are collected simultaneously, if at all possible, although it is sometimes difficult to put collector pockets in the physical space available. The number of pockets varies from two to ten according to the number of isotopes in an element.

A water-cooled liner protects the evacuated chamber (tank) from overheating, and also condenses neutral volatile materials which would otherwise contaminate the collected material or be lost by passing through the pumping system.

The calutron tank, containing the liner, source, and collector is placed between the poles of a large electromagnet and is connected to high vacuum pumps having a pumping capacity of approximately 10^4 liters per second. The entire tank assembly is maintained at an operating pressure of less than 10^{-5} millimeter of mercury. Figure 3 is a diagram of the calutron assembly in which two separate ionization arcs are employed and Fig. 4 shows a pair of calutrons operating in a common magnetic field.

CALUTRON OPERATION

The calutron operation cycle is divided into three periods: start-up, innage, and cool-down.

Start-up is that time during which the tank pressure is reduced, the source is outgassed, the accelerating voltages are brought to the desired values, and the required oven temperature is reached.

Innage is the time during which ion beams are received at the isotope collectors. The beam strengths (usually in milliamperes) at the various pockets are first monitored on current meters, and compared with the relative natural abundance of the isotopes to make certain that the correct masses are being collected in the appropriate pockets. The calutron is then brought to full production by adjusting source and collector variables for optimum production. Control variables include charge temperature, arc voltage and current, accelerating voltage, accelerating electrode positions, and collector orientation.

The cool-down period begins with the turning off of the accelerating voltage and continues until the tank is brought to atmospheric pressure.

RECOVERY OF THE COLLECTED PRODUCT

The same collector pockets are usually used for a number of consecutive runs of an element without removal from the tank. Following a completed collection series the collector is removed, the individual pockets are wrapped to protect the contents from moisture and contaminants, and are sent to the chemical laboratory for product recovery.

CHEMICAL REFINEMENT

The isotope products of calutron separation are not immediately applicable to research. The collected isotopes usually carry with them numerous other elements, the identification of which reveals the chemical complexity of the calutron equipment.

Impurities in even the best obtainable charge materials sometimes reach the collectors in an excessive amount despite mass differences, because of peculiar

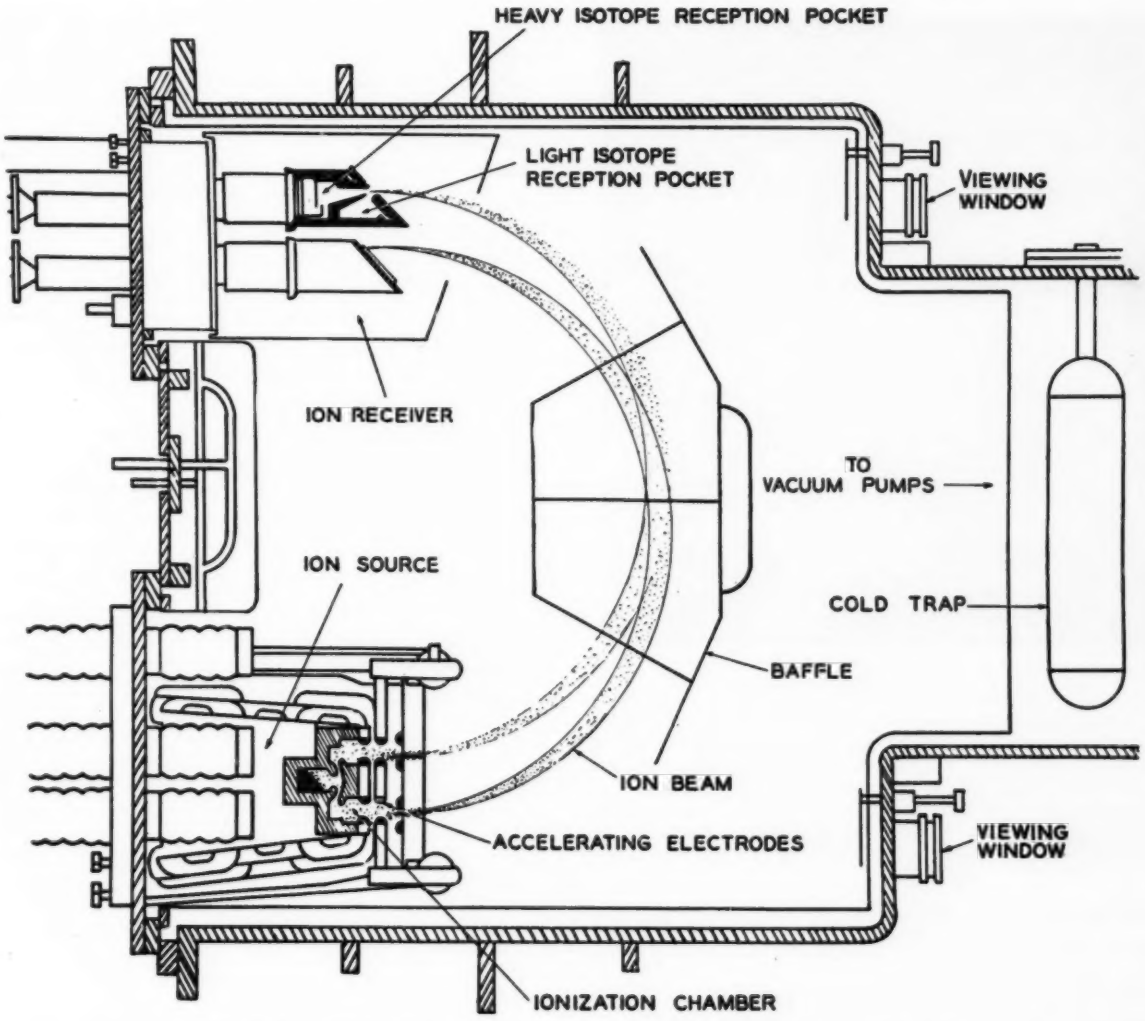

FIG. 3. A complete calutron assembly in which two ionization arcs are employed.

mass relationships, such as the collection of double charged strontium in calcium, of double charged hafnium in zirconium, and of sodium chloride in nickel.

Chemical refinement of isotopes is not the same as a chemical analysis by which the quantity of a given element is measured or estimated; it is much like the preparation of highly refined chemicals, but with severe limitations imposed by the necessity of making the operations quantitative and applicable to small amounts. In many cases chemical refinement is more like the quantitative recovery and purification of a rare element found as a minor constituent in a complex core.

CHEMICAL ANALYSIS

The goal of all operations in chemistry is to preserve the enrichment of isotopes attained in the calutron and to convert them to useful forms as free as practicable of all other elements. It has been necessary to confine product analyses to the simple and convenient method of spectrographic analysis. In this way the chemists have a guide to the effectiveness of their purification procedures, and the isotope users are supplied with helpful information regarding the absence or presence of particularly undesirable contaminants.

Any method for the spectrochemical analysis of isotopically enriched materials must meet the following conditions: the method should be sufficiently versatile to permit handling any isotope that would be separated in the calutron; analysis should utilize only a very small amount of material, yet give low limits of detection for the impurity sought; determinations should be rapid; sample preparation and handling should be a minimum.

PURITY STANDARDS

It has been found impracticable to set up rigid specifications or maximum limits of contamination in isotope products. Experience has been the chief guide by which the chemists have arrived at rather flexible standards of chemical purity. Factors which must be

FIG. 4. A pair of mass spectrograph (calutrons) operating in a common magnetic field. In the left bin, one ion source (below) and the isotope receiver (above) have the electrical connections and water lines in place ready for start-up. In the right bin, a calutron is in operation, the lower doors being closed since the source is at 35 kilovolts. On the servicing dolly at the extreme right, a source and collector stand by ready for use; the slots in the collector faceplate, for receiving the different isotopes of the element to be processed, are faintly visible.

considered are the difficulty and time necessary for repeated treatments, the amount of material which can be spared for repeated analyses, and the known effects of certain elements on nuclear reactions to which the isotopes will be applied.

PRODUCT FORMS

The first requirement for storage of an isotope is that the compound will not change weight when stored under ordinary conditions. This usually means that it will not absorb moisture, carbon dioxide, or oxygen from the air. The periodic table of the elements is used as a guide to the stable compounds which can be produced.

MASS SPECTROMETRY

Most users of stable isotopes need isotopic analyses. Furthermore, the isotopic analysis is a guide to the success of the calutron separation process and aids in the development of better separation methods.

Table III lists the compounds which have been found to be most suitable in the analytical mass spectrometer and those most readily prepared for isotopic analysis.

STABLE ISOTOPE DISTRIBUTION

One hundred seventy-seven isotopes of forty-three elements have been enriched; the goal is to enrich at least two hundred-fifty-seven isotopes of fifty-nine elements. The uses of many enriched isotopes require constant replenishment of the inventory.

In the seven years during which stable isotopes have been electromagnetically enriched (1946–1953), and made available for research, 1652 shipments have gone to the U. S. Atomic Energy Commission, university, and other laboratories. Twelve U. S. Atomic Energy Commission laboratories received 1026 shipments, 42 universities received 556 shipments, and 15 other laboratories received 70 shipments. Almost all of the isotope species which have been enriched have been requested for research purposes in both government and university laboratories.

Separated stable isotopes are being used in various ways in research, the following being typical: production of artificial radioactive isotopes of high specific activity from which the radioactive masses can be clearly established and the activities studied; beta- and gamma-decay investigations; neutron cross-section measurements and the location of resonances; determination of nuclear spins and magnetic moments; studies of hyperfine spectra and isotope shifts; isomerism and isobarism; nuclear energy levels; photoneutron and photoproton

TABLE III. Compounds used in mass spectrometer analysis.

Periodic group	Element	Compound used
I-A	Lithium	LiI
	Potassium	K-Alum
	Rubidium	RbI
I-B	Copper	CuI
	Silver	AgI
II-A	Calcium	CaI_2
	Strontium	SrI
	Barium	$BaCl_2$
II-B	Magnesium	$MgI_2 \cdot XNH_4I$
	Zinc	ZnI_2
	Cadmium	CdI_2
	Mercury	Hg metal
III-A	Lanthanum	$LaI_3 \cdot XNH_4I$
	Cerium	CeO_2
	Neodymium	$NdCl_3$
	Samarium	$SmI_3 \cdot XNH_4I$
II-B	Boron	BF_3
	Gallium	GaI_3
	Indium	InI_3
	Thallium	TlI_3
IV-A	Titanium	$TiBr_4$
	Zirconium	$ZrCl_4$
	Hafnium	$HfCl_4$
IV-B	Carbon	CO_2
	Silicon	SiF_4
	Germanium	GeI_4
	Tin	SnI_4
	Lead	PbI_2
V-A	Vanadium	$VOCl_3$
V-B	Antimony	Sb Metal
VI-A	Chromium	$CrCl_3$
	Molybdenum	MoO_2Cl_2
	Tungsten	$WOCl_4$
VII-A	Rhenium	Re_2O_7
VII-B	Chlorine	AgCl
	Bromine	AgBr
VIII	Iron	$FeCl_3$
	Nickel	$NiCl_2$

emission; super-conductivity effects; as stable isotope tracers and in isotope dilution analysis; the assignment of natural radioactivity to specific isotopes; as target materials in particle accelerators; and in other studies characteristic of the nuclei of specific isotopes. Over four hundred reports in the technical literature, and presented to scientific societies since enriched isotopes first became available, emphasize their importance as research materials.

The contributions of all members of The Stable Isotope Research and Production Division of Oak Ridge National Laboratory are gratefully acknowledged.

JOURNAL OF APPLIED PHYSICS VOLUME 24, NUMBER 10 OCTOBER, 1953

Contributed Original Research

Trajectories in the Symmetrical Electron Lens

L. JACOB* AND J. R. SHAH
University of Manchester, Manchester, England
(Received January 29, 1953)

The complete field plot obtained by "relaxation" was used to determine electron trajectories for parallel incidence at heights up to one-third the bore diameter, from a numerical integration of the trajectory equation using the method of differences. The accuracy attained in this method yields cardinal points to within one percent. It was found that the focal length f_n for a ray of height r_n was given by $f_n=f_0-br_n^2$, where b is a constant; also, because of the curvature of the principal planes, the distance d_n to the midplane follows a law $d_n=c-dr_n^2$ where c and d are constants. A consequence of this is that for the same variation in focal length, the greater the curvature of the principal plane the larger the spherical aberration of the lens.

The trajectory tracings indicate that spherical aberration is small at heights up to one-twelfth the bore diameter, but increases with height till at a value of one-third the bore, the percentage change in focal length has decreased by some 40 percent. Confirmation of focal properties was obtained using the lens in a single stage electron microscope and examining the pincushion distortion in the image of a gauze object.

Evaluation of the spherical aberration using the weak lens approximation of Scherzer leads to gross errors both in magnitude and variation, e.g., the aberration does not remain constant with voltage ratio. The experimental data with the electron microscope indicate little or no change in aberration with increase in the power of the lens; this does not agree with the results of the mathematical analysis of Ramberg.

1. INTRODUCTION

THE problem of determining the trajectories of electrons through known electric or magnetic fields has received considerable attention since it affords a means for elucidating the focusing qualities of the lens field; consequently the solution provides a measure of its main aberrations. The principal line of attack has usually centered round numerical step by step methods such as those of Maloff and Epstein;[1] Spangenberg and Field;[2] Goddard;[3] Motz and Klanfer;[4] Liebmann,[5] though trigonometrical ray tracing such as that used by Klemperer and Wright[6] and the graphical method of Jacob[7] have also been tried with some success.

A feature of the development of computing methods has been the increased accuracy which it has been possible to attain by the use of difference formulas, provided a really accurate plot of the field has been obtained. In the case of trajectories in the symmetrical lens with which this paper deals, such a plot using the relaxation technique has already been presented by the authors.[8] Here the entire field was mapped out; for the purpose of numerical calculation it was later extended in the space outside the outer electrodes to points at which the field became negligibly small, that is, up to distances of 21.5 a from the midplane, where "a" the mesh length was taken as the thickness of the middle electrode. Four trajectories at heights a, $2a$, $3a$, $4a$, above the axis were traced using the difference method of Motz and Klanfer[4] which they had applied to a weak two-cylinder lens system. The present unipotential lens was however a strong lens, and it was necessary to recalculate functions used in the interpolation formulae to the fourth significant figure. It was thus considered important to carry the calculations to at least five significant figures; this was done on an electrical computing machine. The time involved for

* Now at George Holt Physics Laboratories, University of Liverpool, Liverpool, England.

[1] I. G. Maloff and D. W. Epstein, *Electron Optics in Television* (McGraw-Hill Book Company, Inc., New York, 1938).

[2] K. Spangenberg and L. M. Field, Proc. Inst. Radio Engrs. **30**, 138 (1942).

[3] L. S. Goddard, Proc. Phys. Soc. (London) **56**, 372 (1944).

[4] H. Motz and L. Klanfer, Proc. Phys. Soc. (London) **58**, 30 (1946).

[5] G. Liebmann, Proc. Phys. Soc. (London) **62B**, 213 (1949); *Advances in Electronics* (Academic Press, Inc., New York, 1948), Vol. II, p. 101.

[6] O. Klemperer and W. D. Wright, Proc. Phys. Soc. (London) **51**, 296 (1939).

[7] L. Jacob, Phil. Mag. **26**, 570 (1938).

[8] J. R. Shah and L. Jacob, J. Appl. Phys. **22**, 1236 (1951).

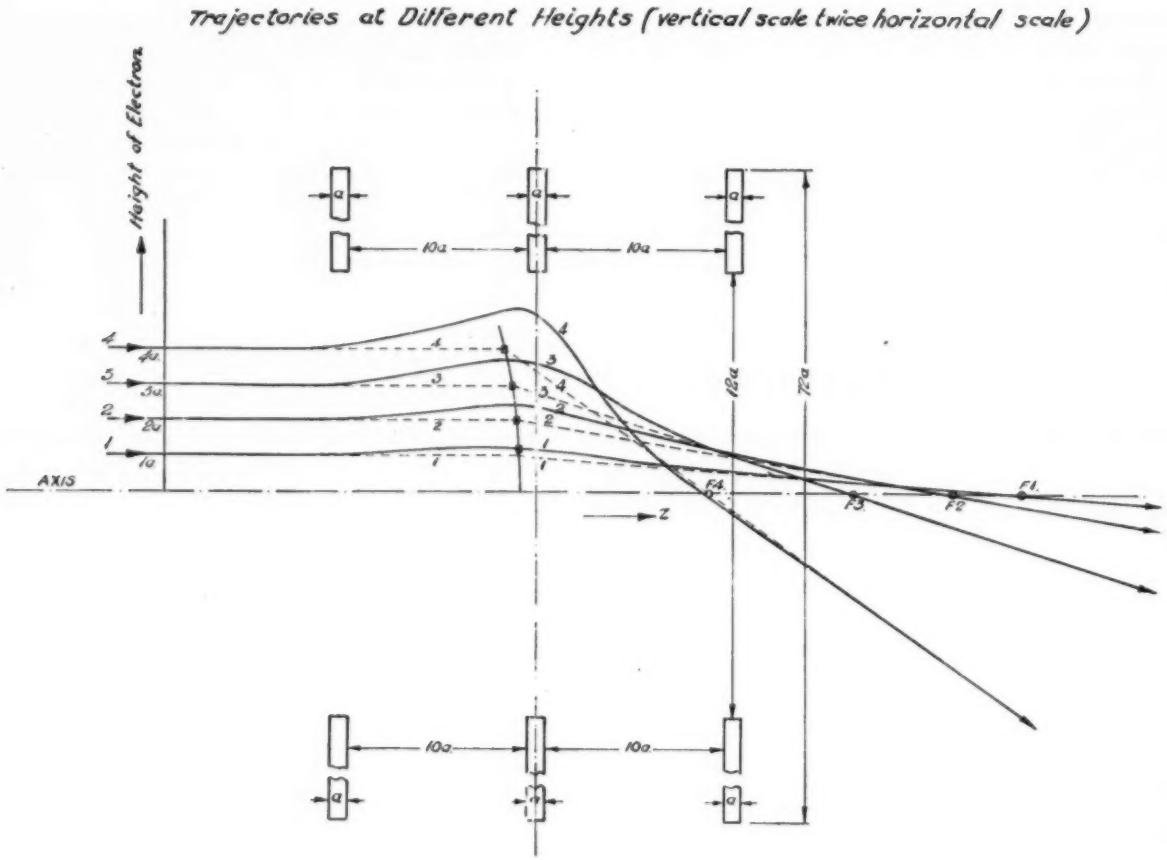

FIG. 1. Electron trajectories for parallel entry at various heights.

the respective trajectories was 15, 15, 25, 35 hours. The results yielded information on the extent of the spherical error. An examination and comparison with the weak lens approximation as well as with direct experiment using the lens in a single stage electron microscope was also made.

2. THE NUMERICAL METHOD

The stages of the method of computation will merely be sketched here; fuller details can be obtained from reference 4.

We begin with the well-known trajectory equation:

$$(d^2r/dz^2)+\frac{1+(dr/dz)^2}{2V}\frac{\partial V}{\partial z}\frac{dr}{dz}-\left[\frac{1+(dr/dz)^2}{2V}\right]\frac{\partial V}{\partial r}=0 \quad (1)$$

where $(\partial V/\partial z)$ and $(\partial V/\partial r)$ are the axial and radial gradients of potential, and 'r' the height of the trajectory above the axis at any axial point z. Now put $P=4(d^2r/dz^2)$, $p=2(dr/dz)$,

$$P=-\frac{\partial V}{\partial z}\left(\frac{1+p^2/4}{V}\right)p+\frac{2\partial V}{\partial r}\left(\frac{1+p^2/4}{V}\right). \quad (2)$$

The complete relaxation plot was next used to determine $(\partial V/\partial z)$ and $(\partial V/\partial r)$ from the following difference formulas involving differences up to the third order:

$$(\partial V/\partial z)=\Delta_z V-\tfrac{1}{6}\Delta_z{}^3V, \quad (3)$$

$$(\partial V/\partial r)=\Delta_r V-\tfrac{1}{6}\Delta_r{}^3V. \quad (4)$$

The electron was taken to enter the lens from the field free region in a direction parallel to the axis, and its height calculated at successive intervals of $(z/a)=1, 2, 3 \cdots$ where a=mesh length. To begin the calculation we assume r_1; r_2 to be the same as r_0 while p_0; p_1; p_2 were taken to be zero. It was now possible to calculate P_0; P_1; P_2 from (2). We then make use of the difference formula

$$p_{n+2}=p_n+P_{n+1}+\tfrac{1}{6}\Delta''_{n+1}+\cdots, \quad (5)$$

so that $p_3=p_1+P_2+\frac{1}{6}\Delta_2''$, where Δ'' represents second differences of P. Knowing the approximate value of p_3 from (5), P_3 was derived from (2) and hence Δ_2'' calculated. This was now inserted in

$$d_n''=\tfrac{1}{4}(P_n+\tfrac{1}{12}\Delta_n''+\cdots), \quad (6)$$

where d_n'' represents second differences of 'r'. Thus knowing the values of P_2 and Δ_2'' it was possible to calculate d_2''. By building up the difference column, we could then evaluate d_3' and r_3.

The value of p_1 was checked from

$$p_n = 2d_n' - \tfrac{1}{6}(2d_n'''), \tag{7}$$

that is

$$p_n = \{d_{(2n+1/2)}' + d_{(2n-1/2)}'\} - \tfrac{1}{6}\{d_{(2n+1/2)}''' + d_{(2n-1/2)}'''\},$$

where d'; d''', are first and third central differences of r, corrected where necessary. This enabled the value of p_3 to be accurately determined. To determine P_3 from (2), the values of V, $(\partial V/\partial z)$, $(\partial V/\partial r)$ must be accurately known at r_3; these were calculated by the Lagrange four point interpolation formula. When the radial height of the electron was less than the mesh length, the Gregory-Newton interpolation formula using third-order differences was applied. With the accurate values of V, $(\partial V/\partial z)$, $(\partial V/\partial r)$ at r_3, the use of (2) gives P_3 accurately. Similarly Δ_3''; d_3''; r_4, were derived from p_4 and P_4, while cross checks were made to see what corrections had to be applied to p_2. The whole process was repeated at each successive step. With this strong type of lens where the values of p_n obtained from (5) differed by more than five in the fourth decimal place from that given by (7) P_n and d_n'' were recalculated with the value of p_n from (7). This, while entailing a large amount of labor insured increased accuracy. In the vicinity of the midplane the values of Δ_n'' were somewhat large, and to maintain the earlier accuracy it was necessary to subdivide this region into a net of half the original mesh length $a/2$. To continue the calculation in this middle region, the values of r/a; p, P were interpolated at the midpoints of the last two steps in the net with mesh length "a"; on coming through this region the step interval was again made equal to "a" so that we had a continuous record of the trajectory through the lens field extending over a length $Z=43a$ from the point of entry into the lens.

We assume the electrons emerging in the region of this latter axial point enter a field-free space. That this is justified is indicated by the almost constant value of d_n', the first differences of the height, as the axial distance increases from this point; that is, the electrons are taken to follow a rectilinear path. We then derive the position of the principal planes in the usual way from the intersection of the initial and final directions. The tracings also allow us to determine the distances of the principal planes and focal point from the mid-plane, designated by d_n and q_n, respectively, for each radial height at entry.

3. THE TRAJECTORY TRACINGS

The paths of the selected electrons are shown in Fig. 1. The principal planes are symmetrical about the midplane and are curved though the curvature in this case is not large. Trajectories (1) and (2) cross the axis in field-free space, while (3) and (4) do so in the field. The variation of mid-focal length with radial height was found to conform with the relation $q_n=26.90-1.102r_n^2$ where 26.90 represents the paraxial mid-focal length. A plot of focal length f_n (measured from the principal plane) against r_n^2 revealed the law $f_n=27.79-1.049r_n^2$. If d_n represents the distance of the principal plane from the midplane for an electron of height r_n, then $q_n-d_n=f_n$. As f_n and q_n vary as r_n^2 we expect d_n to show a linear variation with r_n^2—in fact, the law found was $d_n=-0.890-0.053r_n^2$. Hence for the same variation in focal length, the greater the curvature of the principal plane the greater is dq_n and consequently the greater the spherical aberration of the lens.

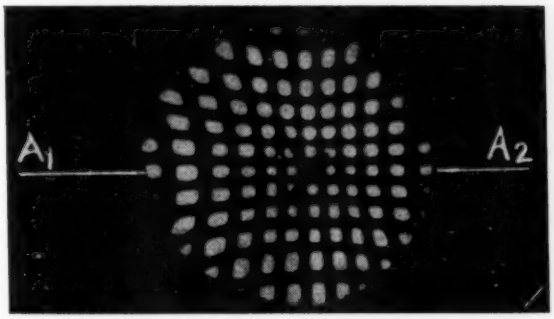

FIG. 2. Distortion arising from spherical aberration in image of mesh.

As far as such aberrations go, analysis of the results showing the relation between the percentage focal length (expressed in terms of its paraxial value) and radial height indicates no serious variations till the height exceeds one-twelfth the bore diameter. At a radial height of one third the bore diameter the focal length has decreased to some 40 percent of its paraxial value for this particular lens system.

4. THE LENS AS A MICROSCOPE ELEMENT

Independent confirmation of the variation of focal length with height was obtained by using the lens as an *einzel* element in a single-stage electron microscope in which the object was a mesh gauze (pitch 6 squares/mm) irradiated by an approximately parallel beam of electrons. If it is assumed as a first approximation that the major part of the pincushion distortion in such an image, Fig. 2, is caused by spherical aberration, then the law for the variation in focal length with height should correspond with that determined from the trajectory tracings.

In this experiment, the principal planes were assumed to be at the midplane of the lens, since the screen distance D to the center of the lens was some 500 times the distance between the principal plane and midplane. For a parallel beam, the magnification in the image for any incident height r_n is simply:

$$M_n \doteqdot \frac{D-f_n}{f_n}, \tag{8}$$

i.e.,

$$f_n \doteqdot D/(M_n+1). \tag{9}$$

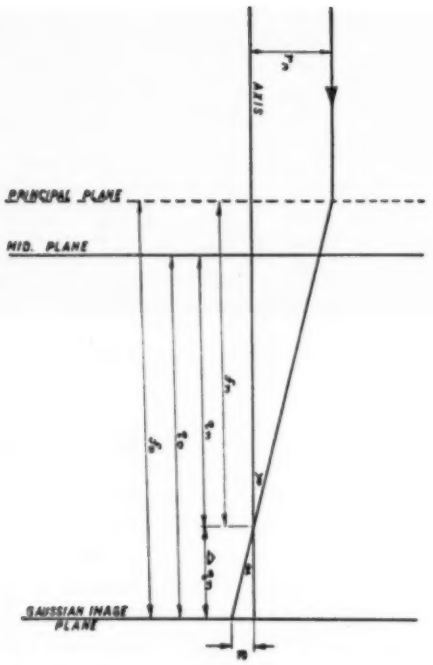

FIG. 3. Scheme defining aberration parameters.

The magnification at different radial distances from the true center of the mesh image (marked X) was measured using a traveling microscope. Detailed examination of the spacings in the photograph shows that beyond a distance of four mesh lengths from the center, the magnification is no longer regular. No further measurements were made beyond this point; this limit corresponds with an incident height of one-third the bore radius. When expressed in mm, the measurements gave the law $f_n=9.69\ (1-0.346r_n^2)$ while the traced paths led to $f_n=9.26\ (1-0.342r_n^2)$ which can be considered a satisfactory agreement. We conclude that for radial heights up to one-third the bore radius, distortion in the image is due primarily to the spherical aberration. At further distances from the axis the pattern is affected by the presence of other aberrations combined with the spherical.

5. COMPARISON OF DIFFERENT METHODS

To get some idea of the accuracy obtainable in the numerical method applied to the present trajectory tracings, it was necessary to perform an alternative calculation for the focal length using the thick lens formula:

$$\frac{1}{f}=\frac{1}{4\sqrt{V_0}}\int_{-\infty}^{\infty}\frac{V''}{\sqrt{V}}dz-\tfrac{1}{16}\sqrt{V_0}\int_{-\infty}^{\infty}\frac{V''}{\sqrt{V}}\int_{-\infty}^{z}\frac{1}{\sqrt{V_0}}\int_{-\infty}^{z}\frac{V''}{\sqrt{V}}dzdzdz$$

$$+\frac{1}{64\sqrt{V_0}}\int_{-\infty}^{\infty}\frac{V''}{\sqrt{V}}\int_{-\infty}^{z}\frac{1}{\sqrt{V_0}}\int_{-\infty}^{z}\frac{V''}{\sqrt{V}}\times\int_{-\infty}^{\infty}\frac{1}{\sqrt{V_0}}\int\frac{V''}{\sqrt{V}}dzdzdzdzdz. \quad (10)$$

The calculations of Plass[9] for the symmetrical lens had indicated rapid convergence of Eq. (10) after the first two terms; neglect of the third term introduced a percentage error of some 3–4 percent. Calculations were thus carried through for the present lens geometry using the method of differences applied to the relaxation field plot in order to evaluate Eq. (10).

A further independent check was sought by using the lens as an element in the electron microscope as discussed in the previous section. A comparison of results is shown in Table I where the focal length has been derived by the three separate methods. It thus appears that the numerical method employing the full relaxation field plot to compute the trajectories yields results accurate to within 1 percent. This leads to confidence in the derived equations established for the aberration parameters.

6. THE SPHERICAL ABERRATION

The accurate trajectory tracings furnished by the numerical method thus enable a precise value of the aberration constant for the lens system to be derived. This constant is as usual determined from the relation:

$$R=Cf_0\alpha^3, \quad (11)$$

where f_0 is the paraxial focal length; C is a dimensionless constant associated with the particular focal properties of the lens, while 'α' in the present tracings of rays parallel to the axis is the angle between the refracted ray and the axis. The scheme is shown in Fig. 3, where for small angles,

$$\Delta q_n=\frac{R}{\alpha}=Cf_0\alpha^2=Cf_0\left(\frac{r_n}{f_n}\right)^2. \quad (12)$$

As the law established from the tracings was

$$\Delta q_n=kr_n^2, \quad (13)$$

TABLE I. Focal length derivation by three independent methods to assess accuracy of trajectory tracings.

	Method	Focal length	Approx. % variation
1	Numerical (10) first-term	69.8	+50%
	Numerical (10) first two terms	48.0	+ 3%
	Numerical (10) first three terms	46.5	0
2	Experimental: elec. mic.	48.5	+ 4%
3	Numerical, trajectory tracings	46.03	− 1.0%

[9] G. N. Plass, J. Appl. Phys. 13, 49 (1942).

where $k=1.102$. Hence,

$$C=1.102f_n^2/f_0. \quad (14)$$

This yields a value of C for the paraxial case of 30.62. In the relation (13),

$$\Delta q_n/f_0=(k/f_0)r_n^2, \quad (15)$$

the factor (k/f_0) can be taken as a measure of the longitudinal spherical aberration of the system. It can be expressed in the equivalent form introduced by Scherzer[10] as the ratio between the aberration coefficient S_8 and the magnification M, referred back to the object plane

$$k/f_0=S_8/M, \quad (16)$$

This ratio is constant for any one lens field, though both S_8 and M vary with the height of the ray through it. If we substitute the values of f_0 (in mesh units) and k, we find

$$S_8/M=1.102/27.79=0.0396\alpha^{-2}=5.71.$$

A comparison of the aberration of this lens with that obtained by Ramberg[11] as well as by Plass[9] (for his minimum aberration lens) is shown in Table II for the *einzel* condition. The variation of the ratio S_8/M for constant refractive power is also included.

There is fair agreement between these results and the special care taken in design does not appear to give improved performance above some 20 percent.

An alternative assessment of the magnitude of the aberration can be obtained by calculating it directly from the formula given by Scherzer[10] which applies to a weak lens. For parallel incidence this takes the form

$$R=\frac{5r_n^3f_0}{64V_0^2}\int_{-\infty}^{\infty}V''^2dz+\text{terms in}\ \frac{1}{V_0^3}\ (\text{small}). \quad (17)$$

Since f_0, V_0 the potential of the outer electrodes wrt cathode, and V'' are known from the "relaxation" plots, we can calculate R/r_n^3 which gives a direct measure of the aberration in terms of S_8/M already established. The relation between these can be seen if we rewrite

$$\Delta q_n=f_0r_n^2\frac{S_8}{M}=Cf_0\left(\frac{r_n}{f_n}\right)^2. \quad (18)$$

Therefore,

$$S_8/M=C/f_n^2. \quad (19)$$

Now

$$R=Cf_0\alpha^3=Cf_0r_n^3/f_n^3.$$

Therefore,

$$R/r_n^3=Cf_0/f_n^3. \quad (20)$$

This gives for the weak lens

$$R/r_n^3=C/f_0^2=S_8/M. \quad (21)$$

[10] O. Scherzer, Z. Physik **101**, 593 (1936).
[11] E. G. Ramberg, J. Appl. Phys. **13**, 582 (1942).

TABLE II. Comparison of aberrations S_8/M for symmetrical electron lens.

Lens system	S_8/M (diam)² Einzel condition	S_8/M (diam)² same refractive power
(a) Ramberg	4.69	3.79
(b) Plass	5.75	4.10
(c) Shah and Jacob	5.71	5.71

The integral (17) when evaluated for the *einzel* condition gives the value 16.54 for S_8/M(diam)², which is roughly three times the value obtained from the trajectory tracings. If time (and labor) had been available it would have been possible to dispense with the weak lens formula and use the earlier numerical method for computing such sets of trajectories as are shown in Fig. 1 for the different lens strengths, in order to provide a relation between the aberration and the field strength. This, however, was not possible, so recourse was had to (17) for calculating the aberration to be expected under weak lens conditious for various values of the voltage ratio $(V_2-V_1)/V_1=n$. The value of V'' was known from earlier work for the *einzel* condition, so that the value of the integral in each case was simply n^2 times this value. This ultimately yields a value for the aberration

$$S_8/M=R/r_n^3=0.5914\times10^{-4}f_0n^2(mm^{-2}). \quad (22)$$

The values of S_8/M over a range in "n" from -1.25 to $+3.0$ are shown in Table III. The relation between S_8/M and $(V_2-V_1)/V_1$ shown in Fig. 4 is practically a straight line with a considerable slope. The data in Table III seem to suggest that the aberration for a voltage ratio of 2.5 is about seven times that for a ratio

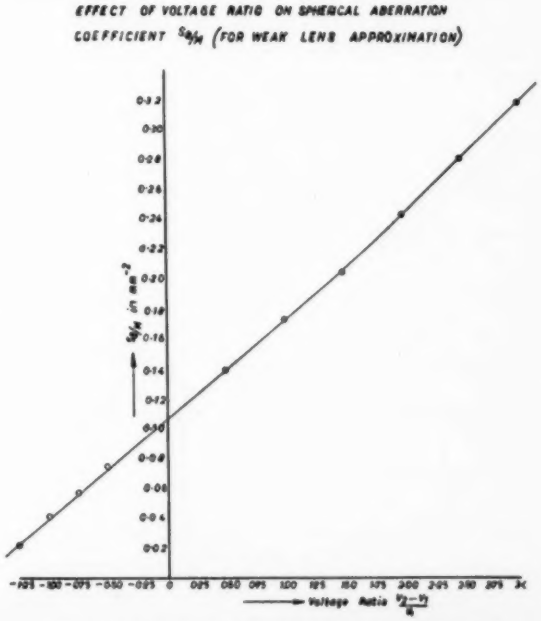
EFFECT OF VOLTAGE RATIO ON SPHERICAL ABERRATION
COEFFICIENT S_8/M (FOR WEAK LENS APPROXIMATION)
S_8/M mm^{-2}
Voltage Ratio $\frac{V_2-V_1}{V_1}$

FIG. 4. Variation of aberration with voltage ratio.

TABLE III. The aberration calculated from the weak lens formula for various voltage ratios.

$\left(\frac{V_2-V_1}{V_1}\right)=n$	n^2	$f_0(mm)$ weak lens (on scaled model)	$S_8/M=R/r_0^3$ (mm^{-2})
−1.25	1.576	24	0.02240
−1.00	1.000	69.8	0.04136
−0.75	0.563	174.1	0.05808
−0.50	0.250	503	0.07448
0.50	0.250	941	0.13940
1.00	1.000	293	0.17360
1.50	2.250	153.7	0.20520
2.0	4.000	102.7	0.24360
2.50	6.250	76.5	0.28140
3.00	9.00	59.8	0.31900

−1 for almost the same paraxial focal length. This is rather surprising; it means that if the weak lens formula for the aberration was valid, then the latter would increase with positive middle electrode for the same power of lens. The weak lens approximation does not then appear to yield a constant value for the aberration for all values of lens strength as might have been expected from Scherzer's work; this arises from the fact as shown earlier[8] that f_n^2 does not remain constant, but varies as $An+B$ where A and B are constants. We conclude that the weak lens formula is not a valid approximation in the present case, where, in spite of the known error of some 50 percent in f_0, strong lens conditions prevail.

Experimental evidence of the effect of refractive power on the distortion in the image, arising from spherical aberration, was sought using the lens as the first stage of an electron microscope. Here, it was found that over the range of voltage ratios recorded above, the value of S_8/M remained constant. This conclusion does not agree with that derived from Ramberg's calculations, where there was a definite increase of aberration with lens strength within the range of voltage ratios explored in the present paper.

Recovery Currents in Germanium $p-n$ Junction Diodes

R. G. SHULMAN* AND M. E. MCMAHON
Hughes Research and Development Laboratories, Culver City, California

(Received February 2, 1953)

When a germanium $p-n$ junction biased in the forward direction has a reverse voltage suddenly applied, a large transient current flows during the "recovery time." A proposed mechanism for this current involving diffusion of stored minority carriers to the barrier is compared with experimental results. Since the current is related to the diode forward direction characteristics these are examined. Finally a variable time delay utilizing the recovery current effect is discussed.

PREVIOUS investigators have reported that germanium point contact rectifiers exhibit transient behavior[1] when a reverse voltage pulse is suddenly applied. The high currents observed have been called "recovery currents." We have observed these effects in drawn $p-n$ junctions where they are the frequency limiting characteristic for many applications. Since our quantitative explanation of recovery currents depends, among other things, on the forward diode characteristics, these properties are considered first.

The measurements described below were made on four germanium junction diodes drawn from melts. Three of these diodes, 1*A*, 1*B*, and 1*C*, were cut from one crystal and the fourth, 2*B*, from another. Areas, lengths of the n and p regions, resistivities, and lifetimes are given in Table I.

TABLE I. Physical properties of junctions.

	Area A (cm²)	Length of n region l_n (cm)	Length of P region l_p (cm)	Resistivity of n region ρ_n (ohm-cm)	Resistivity of p region ρ_p (ohm-cm)	Hole lifetime in n region τ_p (μsec)
1*A*	3.4×10^{-3}	0.23	0.46	0.90	0.067	20
1*B*	4.7×10^{-3}	0.58	0.48	0.90	0.067	34
1*C*	2.3×10^{-3}	0.46	0.13	0.90	0.067	20
2*B*	3.2×10^{-3}	0.47	0.42	0.79	0.059	19

Experimental values of saturation current, I_0, in the reverse direction, were compared with the following equation which is derived from Shockley's[2] theory at T=300°K.

$$I_0=0.24\times10^{-6}A[N_p/(\tau_n)^{\frac{1}{2}}+P_n/(\tau_p)^{\frac{1}{2}}], \qquad (1)$$

where A is the junction area, P_n is the density of holes in the n region, N_p is the density of electrons in the p region, τ_n is the electron lifetime in the p region, and τ_p is the hole lifetime in the n-region.

Calculated and experimental values of I_0 agreed to within a factor of two.

FORWARD DC CHARACTERISTICS

All four dc forward characteristics which are shown in Fig. 1 have the same form. In the low voltage region, $V<0.2$ volt, the current follows the ideal rectifier law $I=I_0(e^{qV/kT}-1)$, where k is the Boltzmann constant, T is the absolute temperature, I_0 is the saturation current, q is the electronic charge, and V is the voltage across the diode. At higher voltages each diode acts like a resistance with a series voltage drop of the form $V=IR_m+V_0$. Extrapolating the curves back to zero current the intercept, V_0, is measured as 0.29 ± 0.02 volt for all four diodes. This can be explained by assuming, in this region, a constant voltage drop across the barrier which is equal in magnitude but opposite in sign to the height of the $p-n$ barrier at equilibrium. The height of the barrier can be calculated by following Shockley's treatment.[2] In the absence of an applied potential, the Fermi level must be the same on both sides of the $p-n$ junction. In order to prevent current flow by electrons diffusing into the p region and holes into the n region, a certain voltage drop V_0 must exist at equilibrium. Since the diffusion forces depend upon

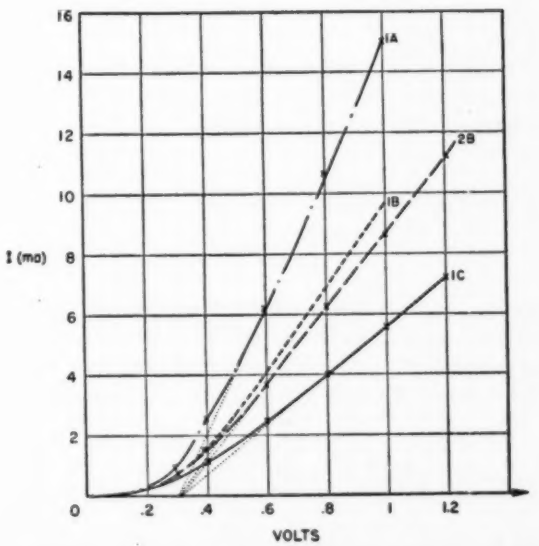

FIG. 1. Diodes direct current forward characteristics.

* Now with the Bell Telephone Laboratories, Murray Hill, New Jersey.

[1] S. E. Michaels and L. A. Meacham, Phys. Rev. **78**, 185 (1950).

[2] W. Shockley, Bell System Tech. J. **28**, 435 (1949).

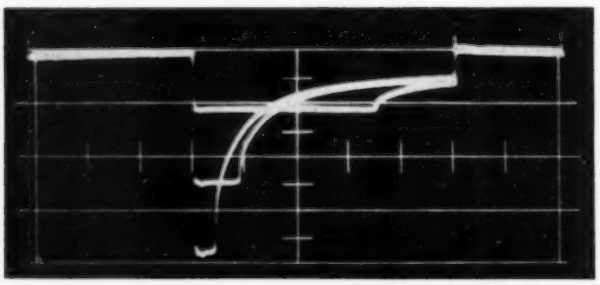

FIG. 2. Typical drawn diode recovery currents, two μsec per division, with reverse voltages of 10, 20, and 30 volts.

the density of carriers and since the barrier serves to counterbalance these forces, the barrier height is related to the carrier densities. This relation is given by

$$V_0=(kT/q)\ln(P_pN_n/n_i^2), \quad (2)$$

where N_n is the density of electrons in the n region, P_p is the density of holes in the p region, and n_i is the intrinsic density of carriers. This equation yields for V_0 values of 0.29 volt for diode $2B$ and 0.28 volt for diodes $1A$, $1B$, and $1C$, in good agreement with the measured intercepts.

The voltage across the diode bar has been considered above as two voltages in series. From the dimensions and resistivities of the two end regions, listed in Table I, the total series resistance can be calculated. These calculated values (R_n+R_p) are listed in Table II. The measured resistances R_m in the linear range are also listed. The values measured are smaller than those computed from resistivities and geometry. These lower resistances are due to conductivity modulation of the end regions by injected carriers. In the four diodes the conductivity of the p region was greater than that of the n region. Hence, the forward current will be carried primarily by holes flowing from the p to the n region, and only the conductivity of the n region will be appreciably modulated.

The density of holes in the n region as a function of distance x from the barrier for a voltage drop V across the barrier, if we assume linear recombination, is given by[2]

$$P(x)=P_n(e^{qV/kT}-1)e^{-(x-x_{Tn})/L_p}+P_n$$
$$=P(x_{Tn})e^{(x-x_{Tn})/L_p}+P_n, \quad (3)$$

where x_{Tn} is the n-region side of the barrier, L_p is the diffusion length of holes in the n region $=(D_{TP})^{\frac{1}{2}}$, and $P(x_{Tn})$ equals $P_n(e^{qV/kT}-1)$. We find that the resistance of the n region for this distribution of carriers is

$$R_{nc}=\frac{L_p}{\sigma_nA}\ln\left[1+\frac{bN_n(e^{l_n/L_p}-1)}{(1+b)P_n(e^{qV/kT}-1)+bN_n}\right], \quad (4)$$

where R_{nc} is the modulated resistance of n region, σ_n is the n-region conductivity, A is the cross-sectional area, l_n is the length of n region, and b is the ratio of electron to hole mobilities, and further where it has been assumed in the derivation that the equilibrium density of holes in the n region P_n is negligible compared to the equilibrium density of electrons N_n.

The maximum density of injected holes in the n region is at x_{Tn} the n side of the transition region and $P(x_{Tn})=P_n(e^{qV/kT}-1)$. When V approaches V_0, $P(x_{Tn})$ approaches P_p, which is the equilibrium density of holes in the p region. This can be seen by substituting Eq. (3) for V_0 into the above expression for $P(x_{Tn})$ and using the relation $P_nN_n=n_i^2$. At this operating point the current is limited not by the restraining potential of the barrier but by the series resistance of the end regions and, as we have seen, the device acts like a resistance. Therefore, to a first approximation P_p can be substituted for $P_n(e^{qV/kT}-1)$ in Eq. (4) in order to determine the modulated resistance of the n region. Since, in the diodes tested, the resistance of the p region should not be appreciably modulated by current, the unmodulated value R_p is added to the calculated value of R_{nc} and presented in Table II as $R_c=R_p+R_{nc}$. The agreement with the measured values R_m is seen to be fairly good considering the inhomogeneities in material resistivity and lifetime and the errors in measuring areas.

TABLE II. Calculated and observed values of diode resistances.

Diode	Derived unmodulated resistances R_n+R_p	Measured slope R_m	Calculated modulated resistance R_c	Resistance after voltage reversal R_0^+
$1A$	69	47	47	50
$1B$	118	72	91	86
$1C$	163	130	121	125
$2B$	122	81	97	81

DIODE RECOVERY

When a $p-n$ junction biased in the forward direction has a reverse voltage suddenly applied, a large transient current flows during the "recovery time." This current in a particular sample is a function of time, applied voltage, and forward bias. Figure 2 is a typical oscillogram of this current as observed with three different values of reverse voltage in the circuit shown in Fig. 3. The duration of these currents varies with the diode from millimicroseconds to tens of microseconds, while current peaks may be as high as several amperes. By examining oscillograms such as Fig. 2, we can quantitatively explain several aspects of this recovery current. Immediately after reversing the voltage the current is constant. During this interval the resistance of each diode has been measured and is listed as R_0^+ in Table II. It can be seen that this resistance essentially equals R_m, the measured resistance in the forward direction. Thus, during this time the rectifying junction is shorted and the current is limited by the resistance of the diode end regions and the external circuit. As the initial current

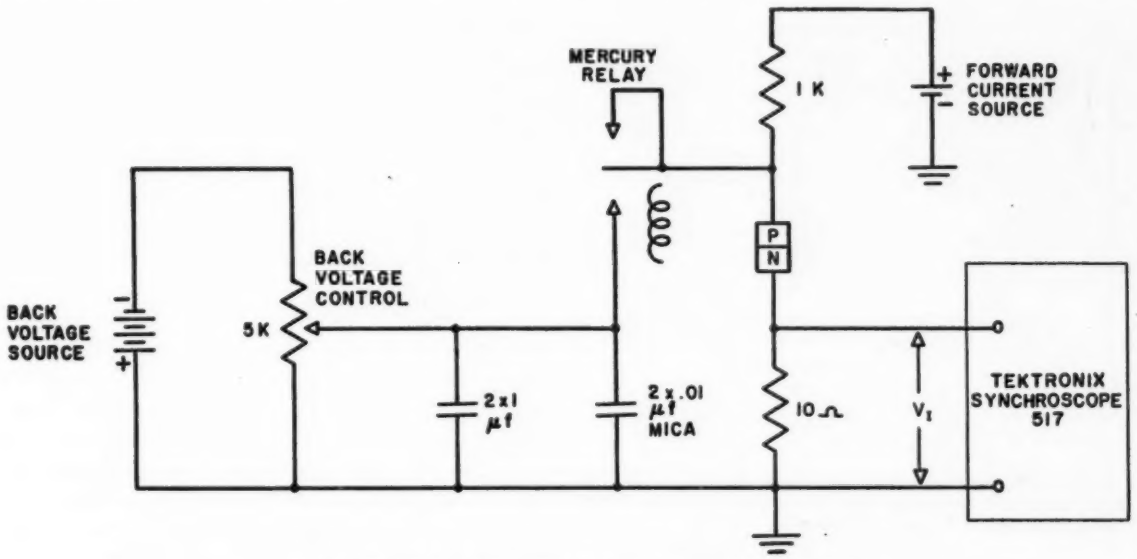

FIG. 3. Circuit for observation of back recovery characteristics.

increases, either due to lower series resistance or to higher applied voltages, the break point moves to shorter times as seen in Fig. 2.

In order to understand these observed currents, it must be recognized that carriers serve the double purpose of carrying current and of maintaining the space charge layer which regulates this current flow. Figure 4(a) shows the potential distribution at equilibrium and the space charge ρ. At equilibrium the electrostatic potential, supported by the space charge, balances the tendency of the holes and electrons to diffuse so that $I_n=I_p=0$. This space charge consists of positively ionized donors towards the n side of the transition region and negatively ionized acceptors towards the p side. The positive charge is due to the absence of electrons or majority carriers, and the negative charge to the absence of holes. To change this space charge region we need only have majority carriers flowing and this acts like a condenser. In Fig. 4(b) we see that for high forward currents, when the potential drop across the barrier almost equals the equilibrium barrier height, $V=V_0$, that the space charge approaches zero. This is caused by holes flowing into the p side of the barrier and electrons into the n side. In addition, holes have been injected into the n region and electrons into the p region. It is the concentration of these injected carriers, as represented by the quasi-Fermi levels which is responsible for current flow across the junction. Furthermore, this high density of stored carriers is the source of the recovery currents in junction diodes. The charge from the junction capacitance is negligible compared to the charge flowing during recovery due to the injected or stored carriers.

Therefore, as soon as the voltage is reversed, the majority carrier flow in each end region partially restores the barrier potential. After this, minority carriers stored on either side can flow back across the barrier, but the majority carriers are opposed by the field of the barrier. Since at first the diffusion of stored carriers to the barrier is very rapid, the current flow is only limited by the series resistance of the diode, which is still the resistance of the conductivity modulated state.

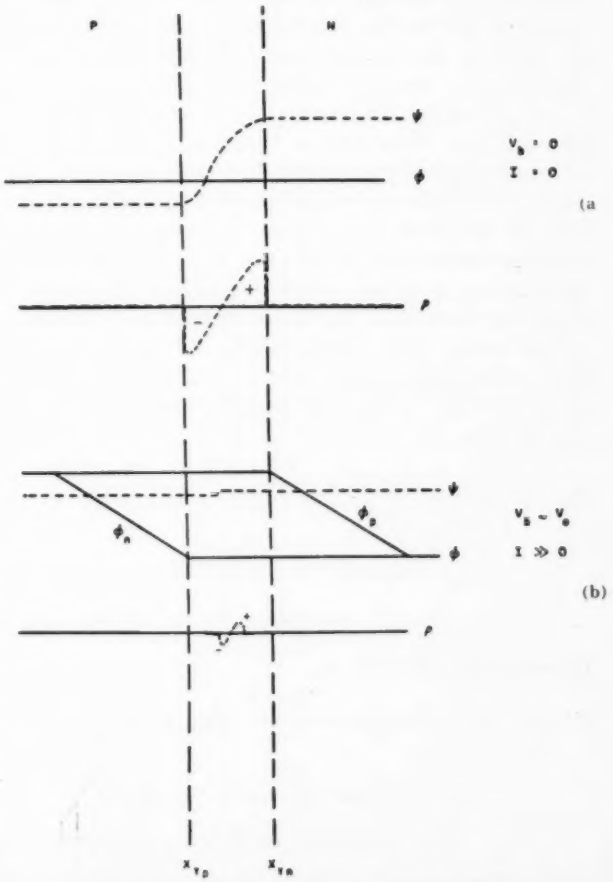

FIG. 4. Charge distribution at $p-n$ junction.

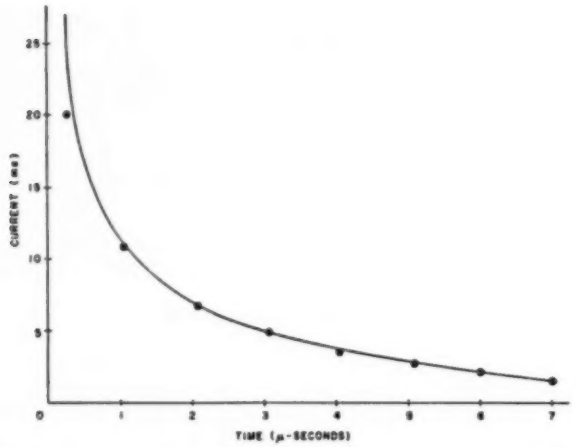

FIG. 5. Recovery current *vs* time for drawn junction diode 1*A*. Solid line calculated assuming that $P_n \exp(qV/kT)=1.3\times10^{16}$ holes/cm³ and that $\tau_p=20$ μsec as measured.

After a certain time the minority carriers are not arriving at the barrier as fast as the external potential can sweep current through the circuit. From this time on, the current is limited by the diffusion of carriers to the barrier and decreases rapidly.

In the following calculation of the time dependent current, it is assumed that $\sigma_p \gg \sigma_n$. Immediately after reversing the voltage, the concentration of holes on the n side of the barrier is reduced to practically zero by the field of the barrier sweeping these holes back to the p region. Recombination during recovery is neglected since these effects were observed within a fraction of a lifetime. Furthermore, because of the high concentration gradients established and the high conductivity of this region compared to the unmodulated ends of the diode, the current is assumed to flow by diffusion rather than by the sweeping field. With these assumptions a rather simple model can be examined. Given at time zero the concentration of carriers described in Eq. (3) as determined by the forward voltage. For $t>0$ the concentration at $x=x_{Tn}\equiv 0$ is maintained at zero. From Carslaw and Jaeger[3] the solution, assuming diffusion, is

$$P(x,t)=1/2(\pi Dt)^{\frac{1}{2}}\int_0^\infty \{P_0\exp(-x/L_p)+P_n\}\times\{\exp[-(x-x')^2/4Dt]-\exp[-(x+x')^2/4Dt]\}dx'. \quad (5)$$

Rearranging, we have

$$P(x,t)=P_n\,\mathrm{erf}x/2(Dt)^{\frac{1}{2}}+\frac{P_0-P_n}{2}\exp(Dt/L_p^2)\times\{e^{-x/L_p}\,\mathrm{erfc}[(Dt/L_p)^{\frac{1}{2}}-x/2(Dt)^{\frac{1}{2}}]-e^{x/L_p}\,\mathrm{erfc}[(Dt/L_p)^{\frac{1}{2}}+x/2(Dt)^{\frac{1}{2}}]\}. \quad (6)$$

[3] H. S. Carslaw and J. C. Jaeger, *Conduction of Heat in Solids* (Clarendon Press, Oxford, 1947).

The concentration gradient at $x=0$ is

$$\frac{\partial P}{\partial x}\Big]_{x=0}=\frac{P_0}{(\pi Dt)^{\frac{1}{2}}}-\frac{P_0-P_n}{L_p}\exp(Dt/L_p^2)\times\mathrm{erfc}[(Dt/L_p)^{\frac{1}{2}}]. \quad (7)$$

Substituting in the expression for the current, namely, $I_p=qDA\partial P/\partial x]_{x=0}$, neglecting P_n with respect to P_0, and using $L_p=(D\tau_p)^{\frac{1}{2}}$, we have

$$I_p=AP_0qD^{\frac{1}{2}}\tau_p^{-\frac{1}{2}}[\exp(t/\tau_p)\,\mathrm{erfc}(t/\tau_p)^{\frac{1}{2}}-1/(\pi t/\tau_p)^{\frac{1}{2}}]. \quad (8)$$

Equation (8) gives the current as a function of time for a given P_0 and τ_p when it is limited by diffusion to the barrier rather than by the external resistance. Experimentally this has been confirmed by increasing the reverse voltage and thereby decreasing the duration of the constant current. The results are shown for diode 1*A* in Fig. 5. It is assumed in this plot that the distribution of carriers has not been appreciably changed from the initial distribution by the finite flow of current during the first 4×10^{-7} sec. To show the dependence of the recovery current upon the lifetime of stored carriers, use was made of another drawn diode *D*-1-9 with a much shorter lifetime, $\tau_p=1$ μsec (measured by photoconductivity). Figure 6 shows the experimental points and the theoretical curve for this diode. In both cases it was necessary to assume a value of P_0 to fit the theoretical curves, and it can be seen that the values assumed are reasonable in view of the limiting values of P_p. Furthermore, at different forward biases the back currents can be normalized to the same theoretical curve by adjusting P_0.

The diffusion theory described above not only satisfies the observed decay currents but is also consistent with the time of onset of this decay or the "break-time." Before the break-point the density of carriers at the

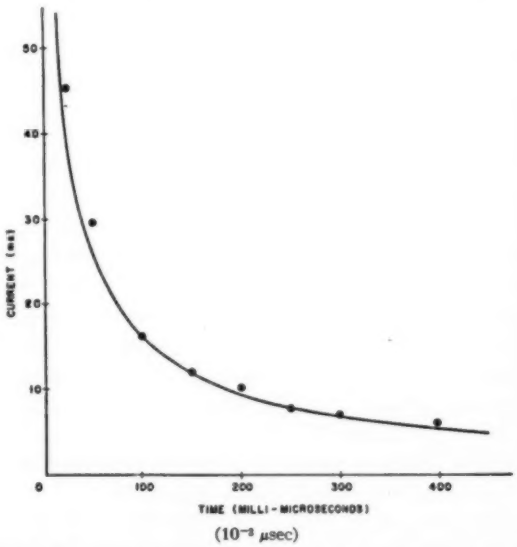

FIG. 6. Recovery current *vs* time for drawn junction diode *D*-1-9. Solid line calculated assuming that $P_n \exp(qV/kT)=7\times10^{15}$ holes/cm³ and that $\tau_p=0.9$ μsec as measured.

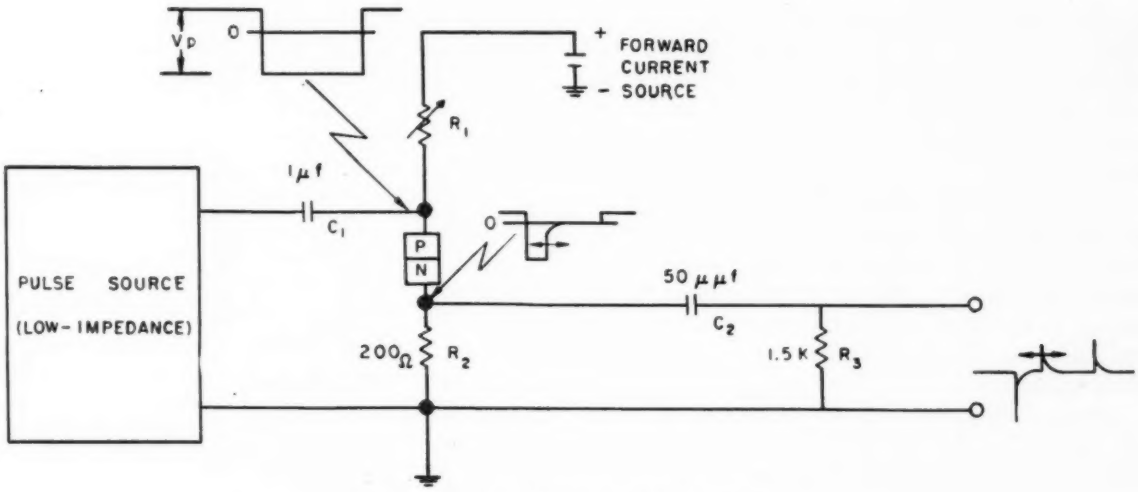

FIG. 7. Variable-width pulse and delay circuit.

junction will be greater than zero. Hence the rate of diffusion to the barrier will be smaller than it would be if the barrier density were zero. In this manner it takes a longer time for the stored carrier density away from the junction to decrease. Since the dissipation of this stored charge is slower, the time when its gradient will fall below any definite value is greater than it would be when the current flow is unimpeded. It seems reasonable, therefore, that the break-time at a given current will be greater than the time it would take for the current to decay to that value if the flow were free. This is seen to be the case in Fig. 2. Another reason for considering the diffusion mechanism to be of primary importance is a comparison of the total charge recovered with the total amount calculated as being stored. In all four diodes the charge recovered was only five to ten percent of the total charge stored. If the field were sweeping carriers back to the junction it

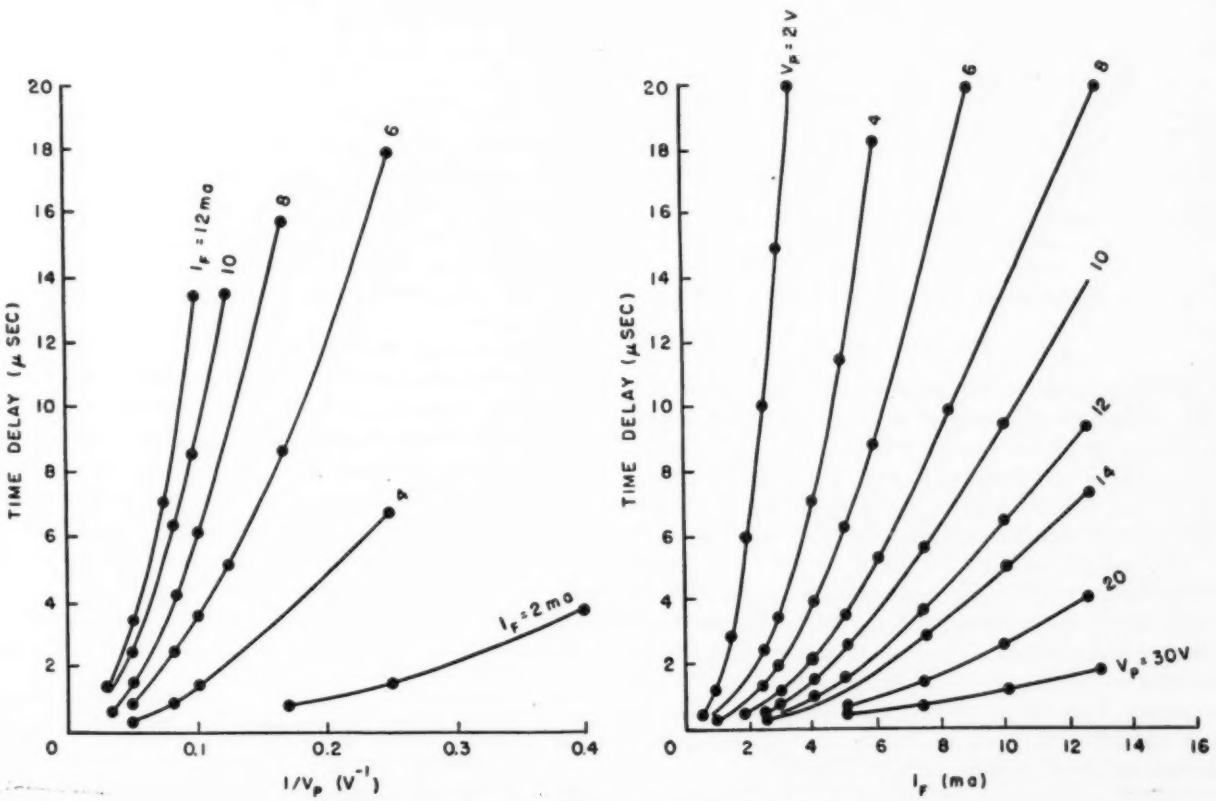

FIG. 8. Time delay as a function of applied voltage and current.

should pile them up in a shock wave effect since the carriers further away will be in a lower resistance and higher field region than those in close. It is hard to see how this field mechanism would allow the barrier resistance to increase before most of the carriers were depleted.

JUNCTION DELAY ELEMENT

The recovery characteristics of junction diodes can be used to produce a voltage or current pulse of continuously controllable width which varies from tenths to tens of microseconds. Figure 7 shows a simple circuit for the development of a variable-width voltage pulse which may be differentiated to yield a delayed pip. The voltage pulse width and pip delay vary approximately directly with the forward bias current and inversely with reverse voltage step amplitude, as indicated by Fig. 8 for a typical diode. The circuit illustrated is simple and can occupy a very small space. An inductor can be substituted for the $R_2-C_2-R_3$ combination, resulting in a still smaller volume. More complicated circuits may be required for other applications. Appropriate prebiases would allow the device to be used as an analog computing element for division. One limitation of the use of junction diodes as delay elements is the 1 percent per degree centigrade temperature sensitivity of delay. Other limitations are the requirement of a pulse source and of milliwatts of dc power for forward biasing. The variation of output voltage amplitude with delay may or may not be useful, according to the particular application.

We wish to thank T. E. Firle for assistance in making the measurements reported here.

JOURNAL OF APPLIED PHYSICS VOLUME 24, NUMBER 10 OCTOBER, 1953

Attenuation of Gamma Rays. I. Transmission Values for Finite Slabs of Lead, Iron, and the Compton Scatterer*

GLENN H. PEEBLES
The Rand Corporation, Santa Monica, California

(Received March 9, 1953)

An approximate integral recursion formula is developed which gives a relation between the probability that a photon will be transmitted through a slab of finite thickness with exactly $k+1$ collisions and the probability that it will be transmitted with exactly k collisions, where the latter probability is known for suitable ranges of slab thickness, of incident energy, and of incident angle. A similar formula also exists for the expected energy transmitted. The two recursion formulas have been used to calculate the transmissions with one, two, and three scatterings for photons incident on slabs of lead and of iron, and from these calculated transmissions the "build-up" factors have been estimated. The build-up factor for normally incident photons of 1 to 20 mc^2 are given for lead slabs and for iron slabs having a thickness of 0 to 20 mfp.

A second method, which considers the transmission through a thick slab as a succession of transmissions through thin slabs, is used to check the estimates of the build-up factor obtained by the first method. This second method provides additional information in the form of the distributions of the transmitted photons.

Finally, some transmission and reflection values for thin slabs of the Compton scatterer are presented along with some results for air which are obtained by the second (thin-slab) method.

1. INTRODUCTION

THE purpose of this paper is to present data which, it is hoped, those who work on practical problems in gamma-ray transmission will find of use. The conditions under which gamma-ray attenuation can be calculated are so idealized that the results cannot typically provide a shield designer with exact solutions to his problems. High accuracy, therefore, does not add greatly to the usefulness of data. A characteristic more likely to increase usefulness is extensiveness, since in the practical problem an unexpected use for uncommon data is often found. The calculations presented here were made to obtain fairly complete and varied data with a degree of accuracy which, though not high, is fairly well established.

The quantity which is considered in this paper to be of first importance is the "build-up" factor for a monoenergetic, monoangular beam of photons incident on a slab of finite thickness but infinite extent. The method, which is used to obtain this quantity, calculates successively the probability that a photon will be transmitted with zero, one, two, and three scatterings, estimates the probability that the photon will be transmitted with four, five, etc., scatterings, and then sums to find the total probability of transmission with any number of scatterings.[1] To check the results of these calculations

* This paper describes work done for the U. S. Air Force and U. S. Atomic Energy Commission.

[1] For similar attacks on the problem of gamma-ray transmission, see Cave, Corner, and Liston, Proc. Roy. Soc. (London) **A204**, 223 (1950); J. Corner and R. H. A. Liston, Proc. Roy. Soc. (London) **A204**, 323 (1950); Corner, Day, and Weir, Proc. Roy. Soc. (London) **A204**, 329 (1950); Hirschfelder, Magee, and Hull, Phys. Rev. **73**, 852 (1948); J. O. Hirschfelder and E. N. Adams, Phys. Rev. **73**, 868 (1948).

a second method, which considers the transmission through a thick slab as a succession of transmissions through thin slabs, is applied to an incident distribution which is discrete in energy, but continuous over angle.

Backscatter is neglected in both methods. This neglect is shown to be small by examining in detail the transmission through, and the reflection from, thin slabs of the pure Compton scatterer. The consequent set of results (build-up factors, probabilities of reflection, etc.) for the pure Compton scatterer are augmented by results obtained by applying the thin-slab method to air, a material which is almost a pure Compton scatterer.

2. TRANSMISSION OF PHOTONS OF 1 TO 20 mc^2 THROUGH SLABS OF LEAD AND OF IRON

The probability that a photon will be transmitted through a slab of finite thickness but infinite extent is the sum of the probabilities that it will be transmitted with no scatterings, one scattering, two scatterings, etc. If the slab is sufficiently thin, the first few scatterings are enough to determine the total transmission accurately. Thick slabs require the calculation of the transmission for an excessive number of scatterings, but, if errors of the order of 20 to 30 percent are acceptable, estimates of the total transmission through thicknesses of 20 mean free paths (mfp) are possible from relatively few scatterings, particularly in the case of the heavy materials, where the absorption from the photoelectric effect and pair production is large.

Theory

A method, which is very simple in concept, exists for calculating transmission by successive scatterings. The probability that a photon will pass through a slab with exactly k collisions can be considered as the product of four probabilities: (1) $e^{-\mu_0 s}$, the probability that the photon will travel a distance s without collision (see Fig. 1), where μ_0 is the total absorption coefficient at the incident energy; (2) $\mu_0 ds$, the probability that it will collide in ds at s; (3) $\nu d\sigma/\mu_0$, the probability that the photon will survive the collision and scatter into a new path, where ν is the electron density and $d\sigma$ is the differential Klein-Nishina scattering formula for one electron; and (4) N_{k-1}, the probability that the photon will pass on through the slab with exactly $k-1$ collisions.

Let us now consider N_{k-1}. It is the probability that a photon *originating in the interior of a slab* of thickness a (see Fig. 1) will escape through a specified face with exactly $k-1$ collisions. Except for the fact that the photon can scatter backwards into the forepart of the slab, it could be considered as the probability that a photon will pass through a slab of thickness $b(b \leqslant a)$ with exactly $k-1$ collisions. The probability of transmission with two scatterings is the first to require consideration of backscatter, since transmission with no collision or one collision does not allow the possibility of backscatter. It was found, however, that those photons which are transmitted with a backward scatter after the first collision make a significant contribution to the twice-scattered beam only for slabs so thin that the transmission is composed mainly of unscattered and once-scattered photons. For example, a slab 1-mfp thick may typically be expected to have 10 to 15 percent of the total transmission in twice-scattered photons, and of these twice-scattered photons, 10 to 15 percent have suffered a backward scattering. Similarly, a slab thick enough to make thrice-scattered photons important is too thick for backscatter to count heavily. It follows then that one can write, with a consequent error of only a few percent, for small values of k:

$$dN_k = e^{-\mu_0 s} \cdot \mu_0 ds \cdot \frac{\nu d\sigma}{\mu_0} \cdot N_{k-1},$$

where N_k is now defined as the probability that a photon will be transmitted with exactly k collisions.

By beginning with

$$N_0 = e^{-X/\gamma_0},$$

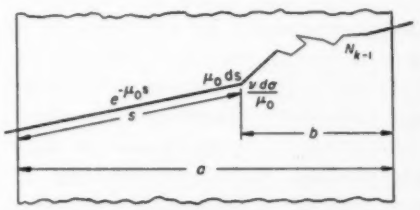

FIG. 1. The succession of probabilities governing the passage of a photon through a slab with exactly k collisions: $e^{-\mu_0 s}$ is the probability that the photon will travel a distance s without collision; $\mu_0 ds$ is the probability that the photon will collide in ds at s; $\nu d\sigma/\mu_0$ is the probability that the photon will survive the collision, where ν is the electron density and $d\sigma$ is the differential of the Klein-Nishina scattering formula; and N_{k-1} is the probability that the photon will pass on through the slab with $k-1$ collisions.

where X is the slab thickness in mean free paths (calculated at the incident energy) and γ_0 is the cosine of the angle between the normal to the slab and the incident path, it is possible to calculate successively $N_1, N_2, \cdots$. At each step N_{k-1} must be known for a sufficiently wide range of three parameters—slab thickness, incident energy, and incident angle—so that a considerable amount of work is entailed. But by the same token, a considerable amount of information is gained.

Similar arguments hold for E_k, the expected energy transmitted in the beam of exactly k scatterings. Since backscatter plays a role in the transmission of energy even smaller than it does in the transmission of photons, one can write, with error less than that for N_k,

$$dE_k = e^{-\mu_0 s} \cdot \mu_0 ds \cdot \frac{\nu d\sigma}{\mu_0} \cdot E_{k-1}.$$

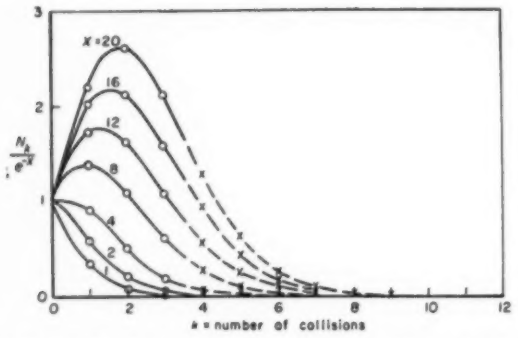

FIG. 2. Graphical representation of the calculated and estimated behavior of N_k/e^{-X} with respect to k for 5 mc² photons, normally incident on a lead slab. N_k is the probability that a photon will be transmitted with exactly k collisions. X is the thickness of the slab in mfp.

Estimation of the Build-Up Factors

When a cycle from $k-1$ to k has been completed, it is possible to put a lower bound on the probability of transmission by summing the individual calculated probabilities. For thin slabs this lower bound may be close to the sum of the infinite sequence, but for thick slabs the partial sum is far short of the limit sum. In these calculations three cycles were completed so that the first four terms of the infinite sequence are known. In the case of normal incidence, the most interesting case and the only case to be presented fully here,[2] the sum to four terms is a satisfactory approximation to the sum to infinity up to a thickness of about 4 mfp, but for the greatest thickness considered, 20 mfp, the partial sum may be as little as 50 percent of the full sum. For the large thicknesses, it is natural to try to improve on the approximation represented by the lower bound by estimating the values of the terms beyond the fourth. Consideration of the mechanism of transmission and the probable convergence behavior of the infinite series leads one to expect that some degree of success will attend the attempt.

Estimates of the total transmission are conveniently expressed in the form of the so-called build-up factor. The build-up factor is defined here as $\sum_{k=0}^{\infty} N_k/e^{-X}$, in the case of the number of photons transmitted, and as $\sum_{k=0}^{\infty} E_k/\alpha_0 e^{-X}$, in the case of the energy transmitted.

Figure 2 shows graphically the calculated and estimated values of N_k/e^{-X} for $\gamma_0=1$, $\alpha_0=5$. Calculated values of N_k/e^{-X} for a fixed value of X are connected by a solid line, estimated values by a dashed line. The estimated values are obtained by extending the line through the calculated points so as to approach zero asymptotically. The resultant values are reasonable enough and it is clear that unless the point at which N_k/e^{-X} becomes negligibly small is moved out to a large value of k, the value of $\sum_0^{\infty} N_k/e^{-X}$ is not excessively in error by the standards of these calculations. To increase the value of the build-up factor for $X=20$ by 20 percent, the point of negligibility must be moved from its present position at about $k=10$ to about $k=15$. This is, of course, possible, but it does not seem from the figure that the point could be moved much farther. Thus an accuracy of about 20 percent for the total transmission is indicated.

The position in this respect can be made stronger. Suppose a photon originates within an infinite homogeneous medium of the same material as the slab. Let r_k be the probability that this photon will reach and survive its kth collision and let ρ_k be the corresponding probability that the same photon—i.e., a photon of the same energy—incident on the slab of finite thickness will also reach and survive its kth collision. After surviving each collision, the photon in the slab has a probability of avoiding the next collision by escaping through one of the faces. The photon in the infinite medium is certain to make the next collision; hence $r_k > \rho_k$. The probability ρ_k, in turn, exceeds N_k, since a photon must survive its kth collision in order to be transmitted with exactly k collisions. So far all slab thicknesses,

$$r_k > \rho_k > N_k.$$

TABLE I. Values of r_k for lead, $\alpha_0=5$.[a]

k	r_k	k	r_k	k	r_k
1	7.03×10^{-1}	6	5.82×10^{-3}	11	1.94×10^{-6}
2	4.14×10^{-1}	7	1.38×10^{-3}	12	3.38×10^{-7}
3	1.89×10^{-1}	8	2.97×10^{-4}	13	5.75×10^{-8}
4	6.97×10^{-2}	9	5.80×10^{-5}	14	1.00×10^{-8}
5	2.16×10^{-2}	10	1.09×10^{-5}	15	1.67×10^{-9}

[a] r_k is the probability that a photon will survive its kth collision in an infinite homogeneous medium.

It will be recognized that r_k satisfies a recurrent integral formula much like the one for N_k, but with the important difference that the integral for r_k is readily expressed in one variable.[3] The recurrent calculation of r_k, therefore, is rapid. Values of r_k, in the instance of lead, $\alpha_0=5$, are given in Table I.

Since r_k bounds N_k above, one can establish an upper limit on the remainder $\sum_{k=4}^{\infty} N_k/e^{-X}$. This bound, however, is far too large to be of any use, at least for present purposes. To get a reasonable estimate of the remainder,

[2] Results for oblique incidence are given by Glenn H. Peebles, *Gamma-Ray Transmission through Finite Slabs*, The Rand Corporation, R240 (1952).

[3] The reasoning, which leads to the recursion formula for N_k, applies without essential change to r_k. Thus

$$dr_k = e^{-\mu_0 s}\cdot\mu_0 ds\cdot\frac{\nu d\sigma}{\mu_0}\cdot r_{k-1}.$$

But the variable s serves no useful purpose here, since the photon in the infinite homogeneous medium is certain to make its first collision. That is, $\int_0^{\infty} e^{-\mu_0 s}\mu_0 ds = 1$. Similarly the azimuthal angle ϕ implicit in the differential $d\sigma$ is also readily removed by integration, since ϕ appears only in the form of the differential $d\phi$. This leaves the angle of deflection θ as the only essential variable.

rigor will have to be set aside and a persuasive argument built around r_k.

When one examines the mechanism of transmission, it seems likely that the sequence $\{N_k\}$ and $\{\rho_k\}$ should exhibit similar behavior. To put it more exactly, one expects the ratio N_k/ρ_k to vary more slowly as a function of k than either N_k or ρ_k. For N_k/ρ_k is that fraction of the photons surviving after k collisions which succeed in passing on through the slab. This fraction depends on the distribution of the photons with respect to position, energy, and direction immediately after collision. As the photons become disorganized—lose all "memory" of their initial state—during a succession of collisions, the character of the distribution function

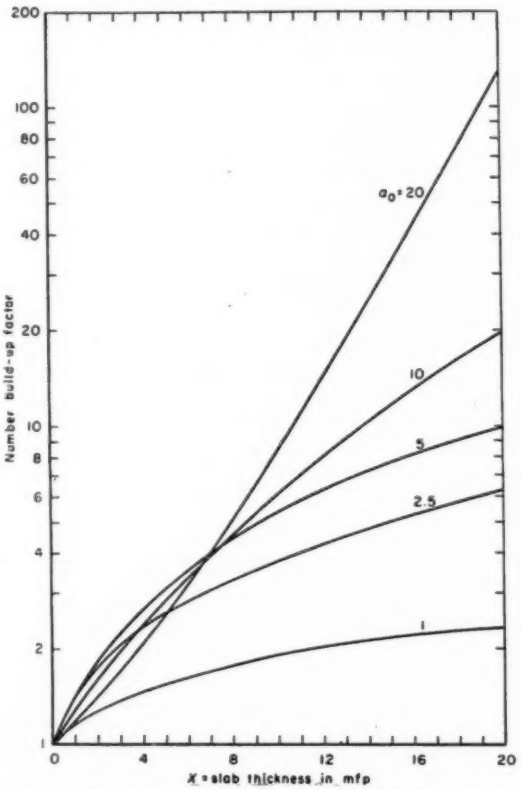

FIG. 3. Number build-up factors for photons normally incident on lead slabs.

should tend to stabilize. If so, then N_k/ρ_k should tend toward a constant value as k increases.

The behavior of N_k/ρ_k for the first values of k can be easily determined for thick slabs from the calculated values of N_k and r_k. For, when the slab is sufficiently thick, ρ_k is nearly identical to r_k, so that N_k/r_k can be used instead of N_k/ρ_k. In the case under consideration above (lead, $\alpha_0=5$, $\gamma_0=1$, $X=20$), one has

$$N_1/r_1=.657\times10^{-8},\quad N_2/r_2=1.29\times10^{-8},\quad N_3/r_3=2.31\times10^{-8}.$$

A reasonable extrapolation of this sequence gave the estimated values for $X=20$ shown in Fig. 2. Only by

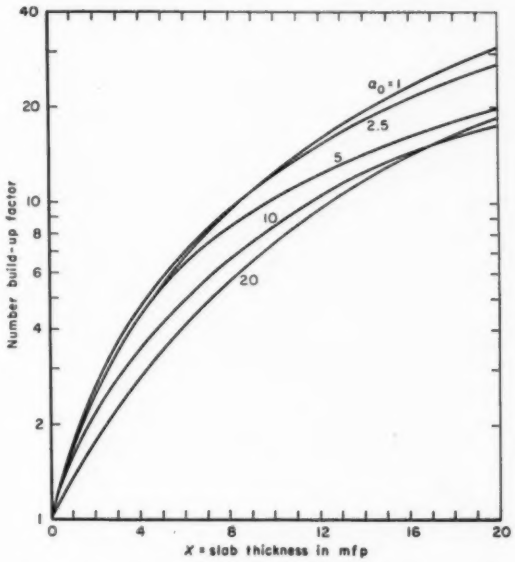

FIG. 4. Number build-up factors for photons normally incident on iron slabs.

assuming an extreme behavior for the sequence can the estimates of N_4/e^{-X}, N_5/e^{-X}, etc., be increased so as to affect the estimates of the build-up factor significantly in accordance with the standards of these calculations. For example, to increase the build-up factor by 20 percent by moving the point where N_k/e^{-X} becomes negligible from $k=10$ to $k=15$ requires that N_k/r_k be allowed to increase to a value of about 10^{-2} at $k=15$. The first few values of N_k/r_k do not indicate the existence of the necessary rate of growth, and since the first values should show the greatest variation, it seems likely that the estimate of a 20 percent error in the build-up factor will not turn out to be too small.

All build-up factors were obtained by extrapolation of the ratio N_k/r_k. Whether or not the extrapolation of N_k/r_k is an improvement over the one for N_k, the former extrapolation has the unforeseen advantage of a procedure which could be made similar in all cases. One set of data, when suitably prepared, was remarkably like another for the first values of k. Therefore, a reasonable way of extrapolation having been settled upon in a particular case, it was possible to parallel the process in all cases. Although such parallelism does not signify a better estimate of the build-up factor, all estimates are expected to have comparable accuracy. This is a rather important point because certain cases will be checked later by an entirely different calculation. A definite, consistent scheme of extrapolation gives some substance to the thought that the degree of accuracy found in the cases checked holds in all cases.

The number and energy build-up factors for photons of 20, 10, 5, 2.5, and 1 mc²,[4] normally incident[2] on plane

[4] For lower incident energies, see Appendix.

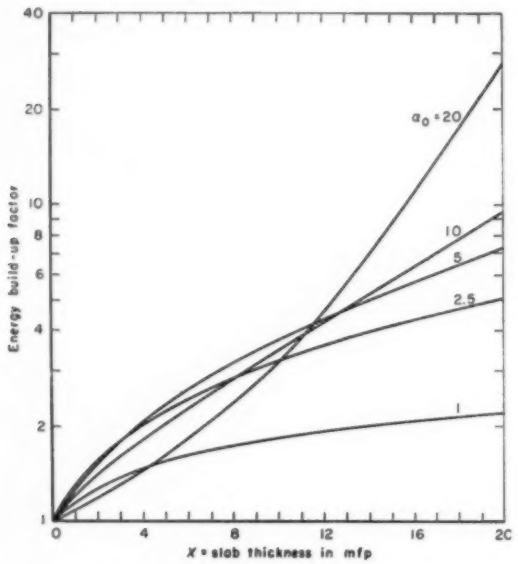

FIG. 5. Energy build-up factors for photons normally incident on lead slabs.

slabs of lead and of iron are given in Figs. 3–6.[5] The error in these build-up factors is, of course, zero when X is zero and is judged to be more or less proportional to X, reaching about 20 percent at $X=20$.

This estimate of the error is based on such considerations as outlined above. It is probably conservative, more so in some instances than in others. For example, in almost all cases, the build-up factors for lead can be expected to be more accurate than their counterparts for iron. The chief cause of the difference lies in the fact that the infinite series defining the build-up factor converges more rapidly for lead than for iron. This is particularly true for $\alpha_0=1$. Inherent limitations of the calculational procedure tend to make the transmission values for the second and third scatterings less accurate for the incident energy of 1 mc². In the case of lead, this is not too important since photoelectric absorption reduces the contributions of the higher order scatterings, but for iron the absorption is small near $\alpha=1$ (see Fig. 7) so that errors in the calculations for the second and third scatterings, if they exist, can have an appreciable effect on the build-up factors. The same remarks apply to a lesser degree when $\alpha_0=2.5$.

In addition to these known sources of likely error, there is, of course, the undetected inadvertent error which may enter at any point from the start of the calculations to the final placement of the results in table or on graph. Although many safeguards against error were used, it is estimated that errors of the order of 10 percent in N_k and E_k, with the help of coincidence, might have escaped detection. Errors of this magnitude could decrease the accuracy of the build-up factors below that stated.

However, supplementary calculations and consistency of results indicate that the accuracy is at least as good as stated. If so, then the build-up factors given in Figs. 3–6 should be satisfactory for the purposes for which they are intended, namely, quick and rough estimates of the transmission of gamma rays.

3. TRANSMISSION OF PHOTONS OF 10 mc² AND 20 mc² THROUGH A SUCCESSION OF THIN SLABS OF LEAD AND OF IRON

Lengthy, intricate calculations in the best of circumstances, tend to turn up with errors larger than are supposed possible. The reader without first-hand knowledge of the reliability of the procedures used to obtain the above results will no doubt welcome supporting calculations. A method which considers the transmission through thick slabs as a succession of transmissions through thin slabs seemed suitable for this purpose. Since this method and the one of the foregoing section are considerably different and therefore do not yield exactly the same information, it will be found that the preceding results have been extended as well as supported.

Description of Method

A matrix is constructed which transforms a frequency distribution incident on a thin slab into the distribution transmitted through the slab.[6] The incident and emergent distributions are functions respectively of the incident and emergent angles and energies and are represented by a grid of discrete values. In essence, the

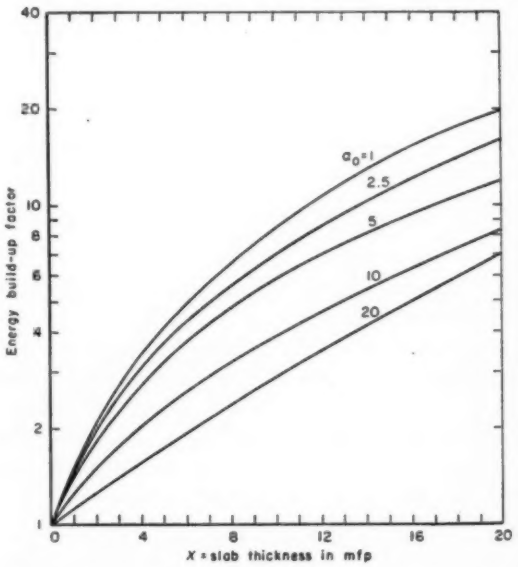

FIG. 6. Energy build-up factors for photons normally incident on iron slabs.

[5] The build-up factors of these figures can be compared with the build-up factors given in the last two references of footnote 1 and with the build-up factors obtained experimentally by W. R. Dixon, Phys. Rev., 85, 498 (1952). In making such comparisons it is necessary to allow for the differences in the total absorption coefficients used by each author.

[6] G. H. Peebles and M. S. Plesset, Phys. Rev. 81, 430 (1951).

transformation matrix is the sum of three matrices which, if applied individually to the incident distribution, yield the emergent distribution for the unscattered, once-scattered, and twice-scattered photons. The slab is taken thin enough to make the contribution of photons scattered three or more times negligible; all photons scattered backwards by any collision are ignored. The thick slab is supposedly divided into a number of thin elemental slabs, and the distribution incident on the thick slab is transformed by the matrix into the distribution emerging from the first elemental slab. This emergent distribution considered as incident on the second elemental slab, is transformed again, and so on, until the distribution emerging from the thick slab (i.e., the last elemental slab) is found.

To obtain data for comparison with those given in Sec. 2, the incident distribution on the thick slab is taken as the one corresponding to an isotropic point source from which is accepted radiation within a cone of half-angle $\cos^{-1} 0.8$; the axis of the cone is normal to the slab. The choice of distribution is motivated by several considerations which need not be discussed here.[7] The source energies are 20 mc^2 and 10 mc^2, and iron and lead are the slab materials. The thickness of the elemental slab is 1 mfp. The frequency distribution of the photons emerging from each elemental slab is obtained as a function of two variables: α', the energy, and γ', the cosine of the angle with the normal to the slab.

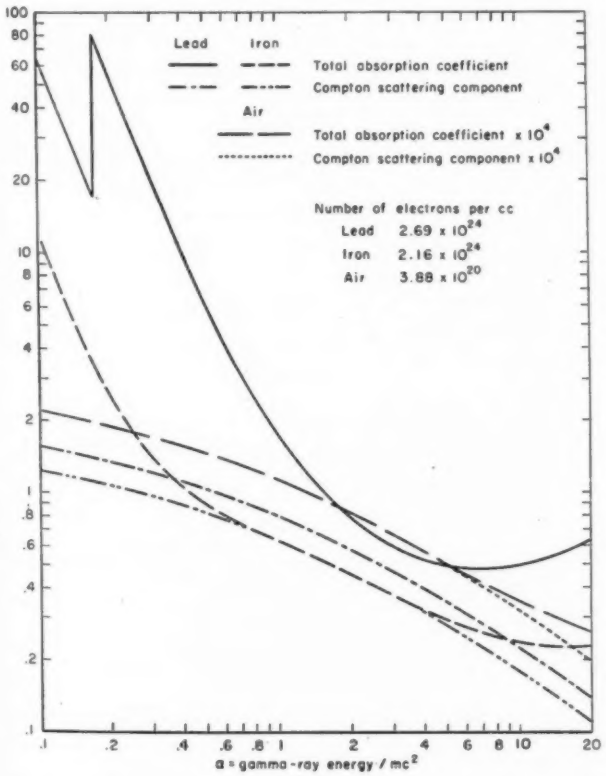

FIG. 7. The absorption coefficients for lead, iron, and air used in the calculations of this paper.

[7] See reference 6, p. 437.

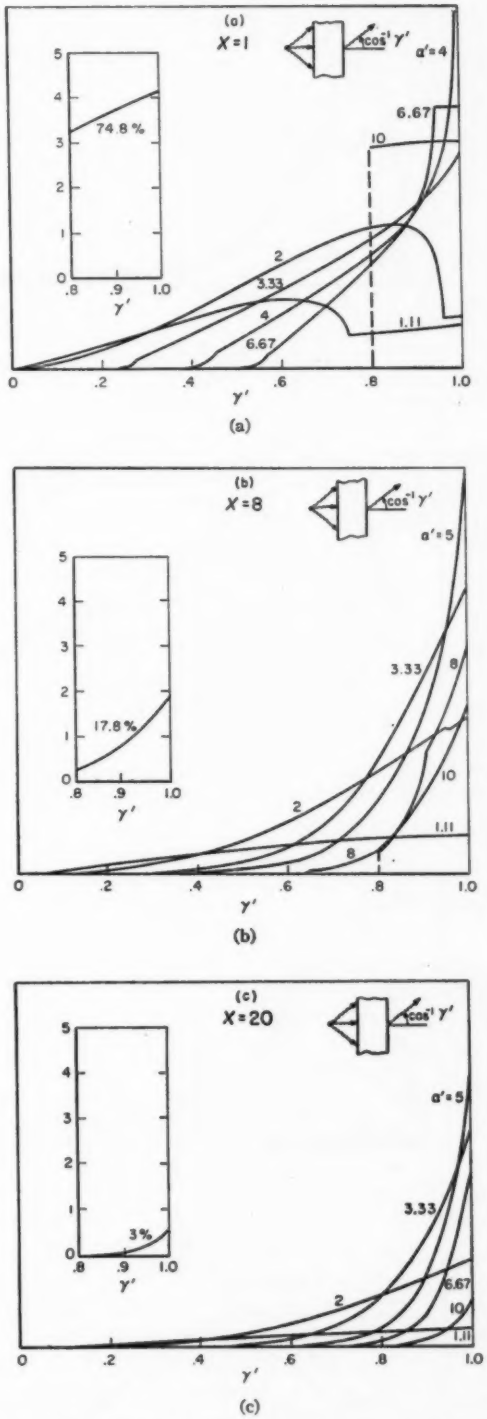

FIG. 8. Frequency distributions for photons of 10 mc^2 transmitted through lead slabs. Constant-energy sections from the distributions for scattered photons are shown. In the boxes on the left are the distributions over γ' of the unscattered photons. The percentage figures in the boxes indicate the proportion of the transmission in the unscattered photons.

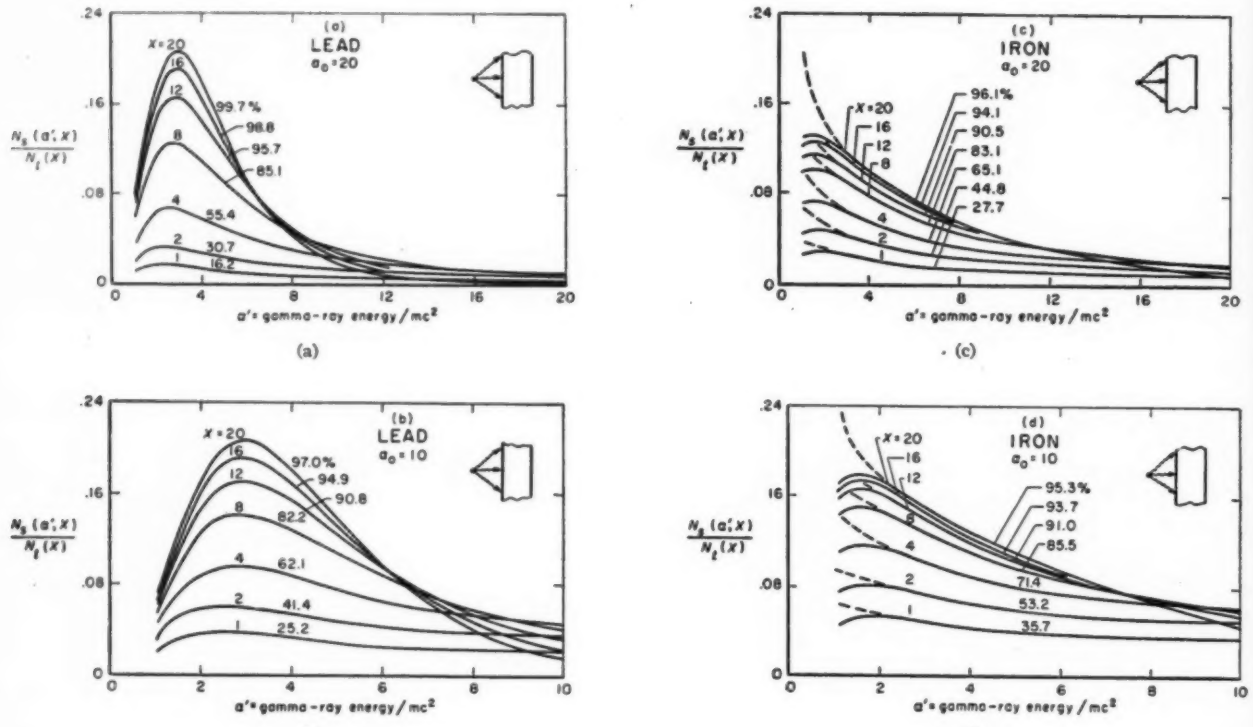

FIG. 9. Distributions of scattered photons for several slab thicknesses, each distribution normalized by dividing by the total of all transmitted photons. The percentage figure on each curve indicates the proportion of transmission in the scattered photons.

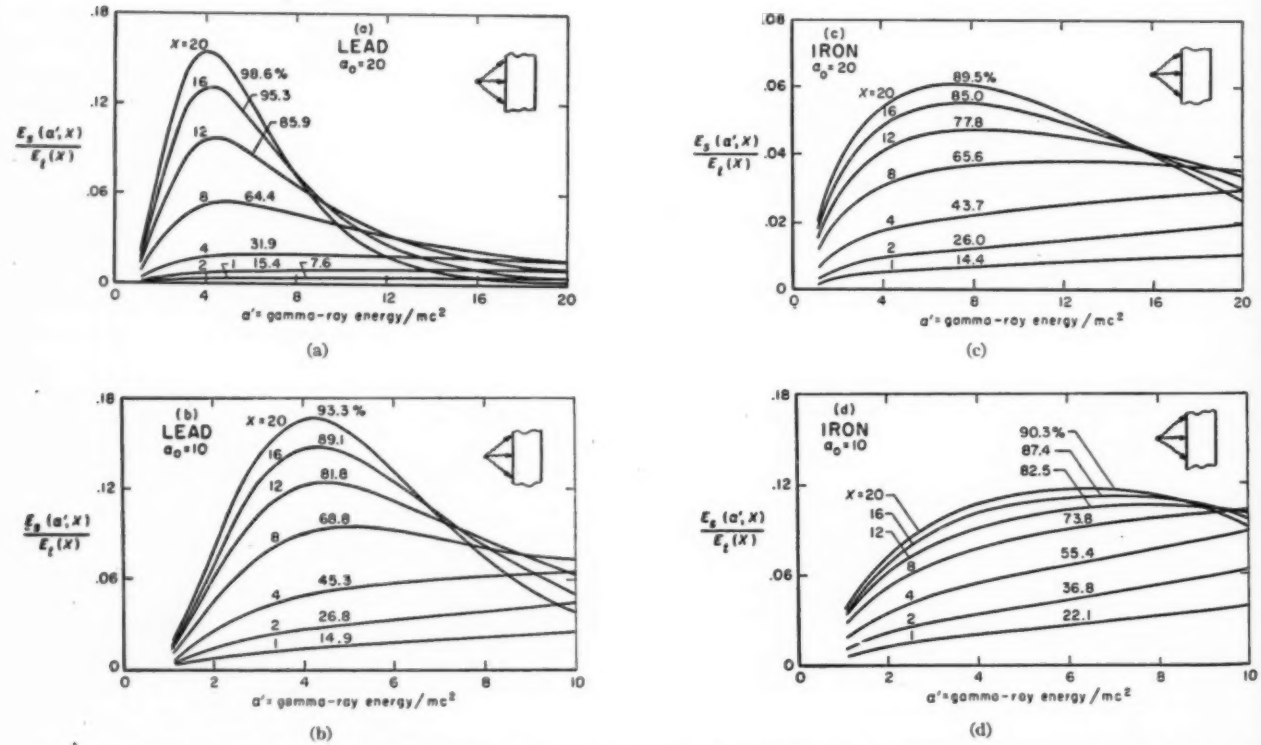

FIG. 10. Distributions of the energy in scattered photons for several slab thicknesses, each distribution normalized by dividing by the total energy in all transmitted photons. The percentage figure on each curve indicates the proportion of transmission in the scattered photons.

Discussion of Results

The distributions obtained are not very manageable and, in their unprocessed state, not very informative. However, representative distributions for three thicknesses are shown graphically in Fig. 8. The source energy is 10 mc^2 and the material of the slab is lead. The described incident distribution is a δ function in α and it is a constant ($\neq 0$) in γ on the interval $0.8 \leq \gamma \leq 1$, zero elsewhere. The unscattered transmitted photons, therefore, have a distribution which is a δ function in α' and which has a discontinuity at $\gamma' = 0.8$. These unscattered distributions are shown as functions of γ'. The percentage of the total transmission in unscattered transmission is given with each curve.

The distribution of scattered photons is represented by sections for fixed values of α'. The finite discontinuity in the incident distribution at $\gamma = 0.8$ shows its effect in a discontinuity in the section $\alpha' = \alpha_0 = 10$ at $\gamma' = 0.8$, where the distribution drops to zero, and in the discontinuities in the slope of the sections for values of α' less than 10. These discontinuities appear strongly in the small thicknesses, and they disappear in the large thicknesses because their origin is in the once-scattered photons. The scattering laws for photons are such that a photon cannot pass with one collision from one energy and direction to any other arbitrarily chosen energy and direction. The distribution at, say, $\alpha' = 8$, $\gamma' = 1$ draws all its once-scattered photons from the interval $0.8 \leq \gamma \leq 1$, but the value at, say, $\alpha' = 8$, $\gamma' = 0.6$ draws none from this interval. As γ' decreases from 1 to 0.6, there is a point at which photons would begin to be received from outside the interval $0.8 \leq \gamma \leq 1$, were there any photons there, and there is another point at which, for the first time, no photons can be received from the interval. At these points ($\gamma' = 0.913$ and $\gamma' = 0.647$) there are, understandably, discontinuities—in fact, discontinuities of infinite jump—in the slope of the sections. These discontinuities exist in every section above the lower limit of α' for one collision. Other discontinuities exist in the higher derivatives, but they are not discernible in the figures.

More informative than the distributions over α' and γ' are the marginal distributions over α'. Four quantities are of interest as functions of α': (1) the number of photons transmitted, (2) the energy transmitted, (3) the density of the photons at the rear face, and (4) the energy density at the rear face. In the case of the first two quantities, one can think of the transmission through the slab either from an isotropic point source from which gamma rays are accepted in a cone of half-angle $\cos^{-1} 0.8$ or from a plane of such sources; but in the case of the last two quantities, one must suppose only a plane of sources. The first two of the four quantities named are shown, respectively, in Figs. 9 and 10 for several thicknesses of lead and of iron with source energies of 20 mc^2 and 10 mc^2. Both quantities are treated alike. Since the unscattered photons all emerge with their incident energy, only the scattered photons give functions of α'. These functions are normalized for each thickness by dividing by the total obtained by summing over all energies and over the scattered and unscattered photons. The result for both quantities is a family of curves with parameter X. Figures 9 and 10 give the number of photons transmitted and the energy transmitted[8] in the form of the ratios $N_s(\alpha', X)/N_t(X)$ and $E_s(\alpha', X)/E_t(X)$, where the meaning of the new symbols introduced is clear from the

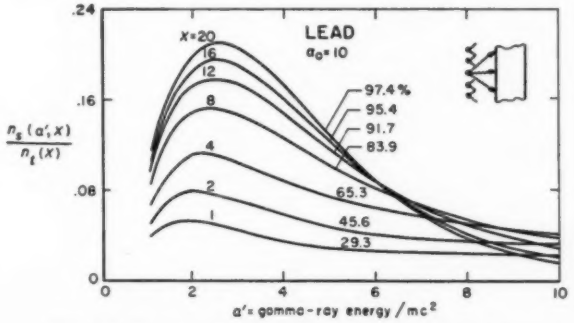

FIG. 11. Density distributions corresponding to the flux distributions of Fig. 9(b).

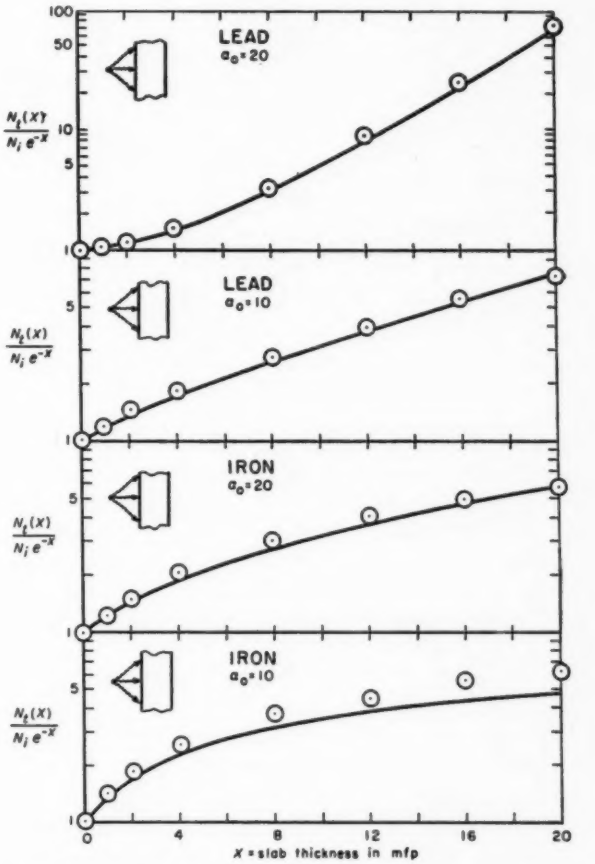

FIG. 12. The ratio of the number of photons transmitted to the number incident, normalized by the factor $1/e^{-X}$.

[8] Compare Fig. 10(a) with Fig. 5 given by Lewis V. Spencer and U. Fano, J. Research Natl. Bur. Standards **46**, 446 (1951).

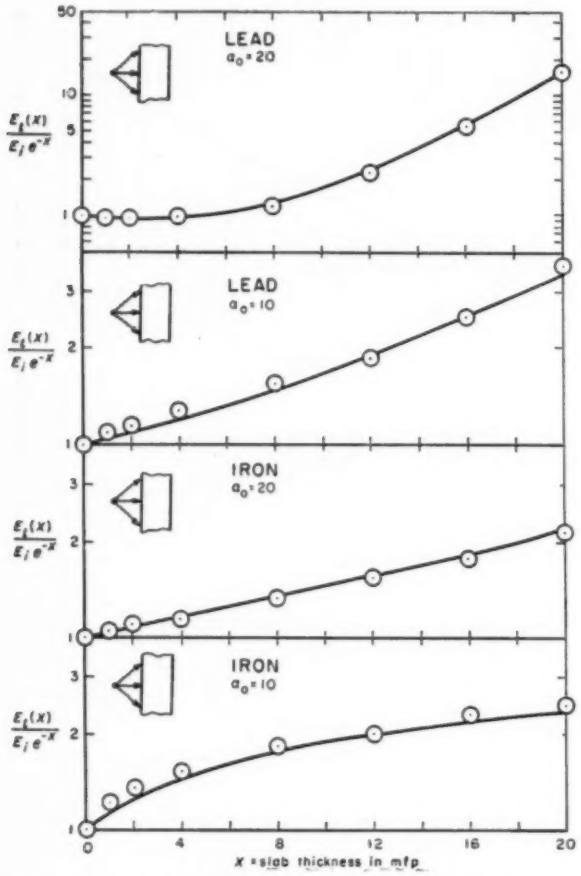

FIG. 13. The ratio of the energy in transmitted photons to the energy in incident photons, normalized by the factor $1/e^{-X}$.

choice and from the text. The percentage figure associated with each curve gives the proportion of the total contained in the scattered photons.

The other two quantities, i.e., the number density and the energy density at the exit face of the slab, if given a parallel treatment, yield a set of curves differing very little from those of Figs. 9 and 10. How small the difference is can be seen by comparing Fig. 9(b) with its counterpart, Fig. 11, which gives the density ratio $n_s(\alpha', X)/n_t(X)$ for lead, $\alpha_0=10$. Every curve of Figs. 9 and 10 is matched just as closely by a density curve as those in the example selected. The cause for the similarity between density and flux is, of course, the fact that the distribution of the transmitted photons heavily favors the normal direction, as Fig. 8 showed.

Most of the comment on Figs. 9 and 10 will be incidental to later discussion. However, it might be remarked here that the curves all terminate before reaching $\alpha'=0$, because it is not feasible to make calculations down into the neighborhood of zero energy by the thin-slab method. The totals used for normalizing are from the curves as shown, without benefit of any correction. The dashed curves diverging from the solid curves in Figs. 9(c) and 9(d) denote defects which will be discussed shortly.

The normalizing factors, or rather their reciprocals, $N_t(X)$, $E_t(X)$, have the greatest interest, since they may be considered as the main goal of the calculations. These factors are shown as functions of X in Figs. 12 and 13 and are themselves normalized by the factors $1/N_i e^{-X}$, in the case of number, and $1/E_i e^{-X}$, in the case of energy, where N_i is the number of photons incident on the first elemental slab, and E_i is the corresponding incident energy. Comments on these figures are confined here to the statement that the significance of the circled points will be made clear later.

Inherent Errors

Since the thin-slab method is used to provide something in the way of a check on the results obtained by summing the individual scatterings, it is well to leave as little question with regard to the accuracy of the thin-slab results as possible. The three weaknesses

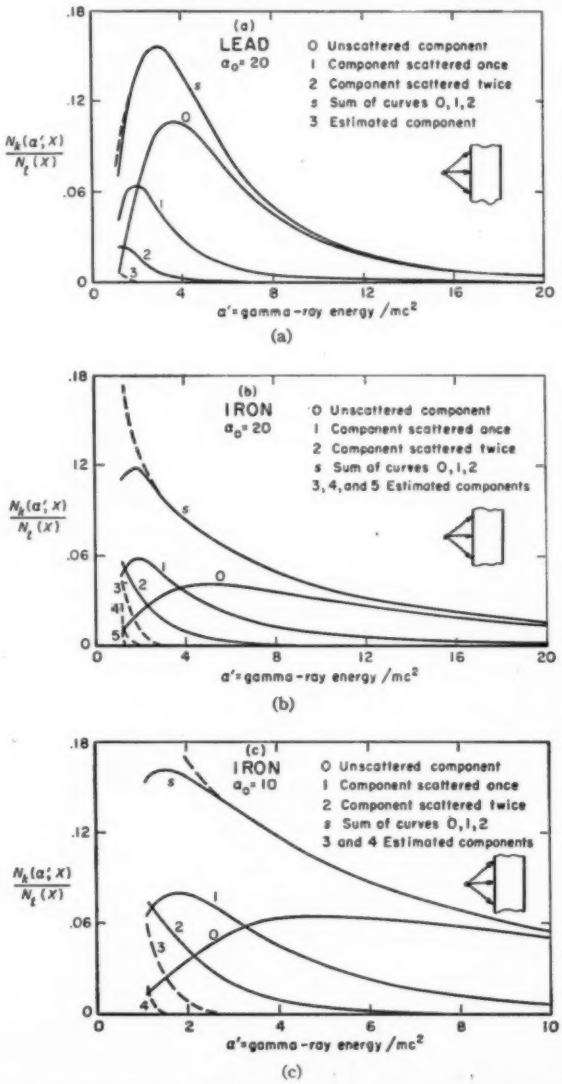

FIG. 14. Component distributions for the 11th elemental slab.

of the thin-slab method are: (1) neglect of three or more scatterings; (2) neglect of backward scattering, both within the elemental slab and from one elemental slab to another; and (3) the presence of ample opportunity for accumulated error in the twenty iterative operations between 1 and 20 mfp.

The error due to the neglect of everything beyond the twice-scattered transmission can be assessed by examining Fig. 14. This figure shows, as a function of the photon energy, the component frequency distributions for the photons scattered by the 11th slab. The distributions for the photons previously scattered, but unscattered by the 11th slab, are labeled with the numeral 0. The distributions of the photons scattered once and scattered twice by the 11th slab are respectively marked with the numerals 1 and 2, and estimates of the contributions of the third, fourth, etc., scatterings are marked with the numerals 3, 4, etc. The curves labeled with the letter s are the sums of the 0-, 1-, and 2-curves and are members ($X=11$) of the families of Fig. 9. The dashed curves diverging from the s curves are estimates of the transmission from all scatterings, i.e., the sum of the curves 0, 1, 2, 3, etc. Only the incident energy 20 mc^2 is considered for lead since the analysis for 10 mc^2 does not differ in any essential respect from the analysis for 20 mc^2.

In the case of lead, the divergence of the dashed curve from the s curve is small. Since the analysis of the transmission through the 11th elemental slab was found to be typical, a thickness of 1 mfp seems sufficiently thin for the elemental slab.

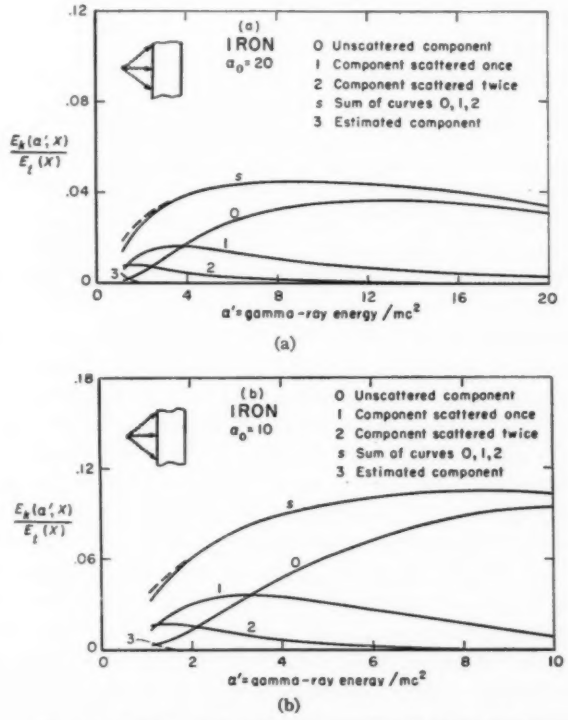

FIG. 15. Components of the energy distribution for the 11th elemental slab.

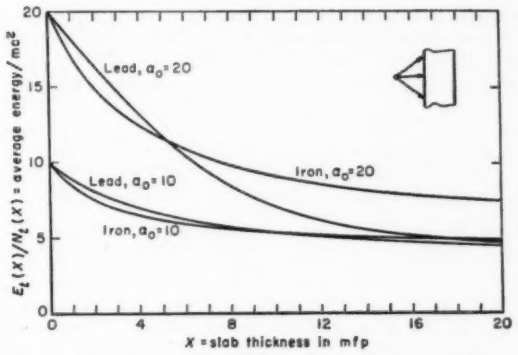

FIG. 16. Comparison of the average energy in the photons transmitted through slabs of lead and iron.

In the case of iron, the neglect of the third and higher scatterings is clearly not so trivial. Even so, the damage may not be too great. In the middle energy range the divergence of the partial sums (represented by the s curves) from the limiting sums (indicated roughly by the dashed curves) is undoubtedly large, but photoelectric absorption must bring both sums quickly to zero in the low energy range. The defection of the partial sum in the middle energy range, though large, cannot compound at an enormous rate because the middle range receives most of its photons from the high range, where, since three or more scatterings contribute negligibly, the distributions are accurate. It seems unlikely, therefore, that the total transmission of photons as calculated from the solid curves for iron can be deficient by more than 10 to 30 percent.

The error in the energy transmitted should be even smaller, not more than a few percent at most. Figure 15, which gives the component energy distributions for iron, $\alpha_0=20$, shows this clearly.

The defect noted earlier, and indicated in Figs. 9(c), and 9(d) by dashed curves, is the one just considered. Although the dashed curves are intended only to warn of the presence of error in the solid curves, they are certainly more nearly correct than the solid curves and may therefore be considered as partial estimates of the true distributions. Since transmission is calculated on the basis of the solid curves, the percentage of the total in scattered photons given for each thickness is low, but perhaps not so low as one might think. One cannot, for instance, use this known error to explain why Fig. 9 shows the percentage of scattered transmission to be greater for iron than for lead at 1 mfp, but to be less at 20 mfp. That iron should transmit a greater percentage of scattered photons through a slab of 1 mfp thickness is to be expected, since the total absorption coefficients (Fig. 7) show that a photon has a greater probability of surviving a collision in iron than in lead. But the failure of iron to maintain the larger percentage as X increases is not conveniently explained by the neglect of three or more scatterings in the low energies. For to bring the percentage for iron up to that for lead at 20 mfp would require an error in the

TABLE II. Probabilities of transmission and reflection with one and two scatterings for photons of 0.2–10 mc² normally incident on slabs of the pure Compton scatterer.[a]

α_0	X	N_0	N_f	N_b	N_{ff}	N_{bf}	N_{bb}	N_{fb}
10	0.5	0.6065	0.156	0.0169	0.0430	0.00305	0.0076	0.0070
	1.	0.3679	0.164	0.0173	0.0654	0.00182	0.0088	0.0073
	2.	0.1353	0.0947	0.0173	0.0525	0.000545	0.0090	0.0074
	4.	0.0183	0.0191	0.0173	0.0129	0.0000859	0.00908	0.00741
5	0.5	0.6065	0.167	0.0264	0.0407	0.0054	0.011	0.0093
	1.	0.3679	0.174	0.0292	0.0672	0.0034	0.015	0.012
	2.	0.1353	0.103	0.0294	0.0613	0.00085	0.016	0.012
	4.	0.0183	0.0210	0.0294	0.0167	0.00012	0.016	0.012
2.5	0.5	0.6065	0.169	0.0405	0.0385	0.0078	0.015	0.013
	1.	0.3679	0.180	0.0458	0.0659	0.0066	0.020	0.017
	2.	0.1353	0.110	0.0462	0.0616	0.0018	0.022	0.018
	4.	0.0183	0.0229	0.0462	0.0179	0.00022	0.022	0.018
1.0	0.5	0.6065	0.160	0.0606	0.0374	0.010	0.018	0.017
	1.	0.3679	0.172	0.0720	0.0645	0.012	0.028	0.024
	2.	0.1353	0.104	0.0744	0.0609	0.0052	0.032	0.027
	4.	0.0183	0.0215	0.0745	0.0181	0.00055	0.032	0.027
0.2	0.5	0.6065	0.133	0.0996	0.0278	0.013	0.021	0.023
	1.	0.3679	0.144	0.119	0.0531	0.020	0.033	0.036
	2.	0.1353	0.0886	0.128	0.0516	0.013	0.039	0.044
	4.	0.0183	0.0179	0.130	0.0153	0.0022	0.040	0.045

[a] N_0 = the probability of transmission without collision. In the cases of the other probabilities the subscripts "f" and "b," indicate respectively a forward scattering and a backward scattering. For example, N_{bf} is the probability that a photon will be transmitted with exactly two collisions, the first resulting in a backward scattering, the second, in a forward scattering.

scattered transmission of over 1000 percent for a source energy of 20 mc² and 59 percent for a source energy of 10 mc². Not only is the minimum increase in the case of 20 mc² impossibly large, but there is also no reason why the increase should need to be so much larger for 20 mc² than for 10 mc².

The true explanation lies in the fact that the absorption coefficient for lead falls to a pronounced minimum as α decreases from 10 or 20, whereas the coefficient for iron is almost at a minimum at 20. The length of 1 mfp for the first collision, therefore, is smaller than the average for subsequent collisions in the case of iron and larger than the average, or tending to be larger, in the case of lead. The comparison on the basis of mean free paths for the first collision amounts to considering thicknesses of lead and iron which are not fundamentally equivalent. For large thicknesses, the inequality offsets the greater probability of photon survival in iron to such an extent that lead has the greater percentage of transmission in scattered photons. Another manifestation of this phenomenon is seen in Fig. 16, which gives a plot of the average energy *versus* X for all cases. The fact that the average energy for iron crosses that for lead for both 10 mc² and 20 mc² is readily understood in the light of the preceding remarks. An explanation of the comparative behavior of the build-up factors for iron and for lead in the monoangular cases of 10 mc² and 20 mc² (Figs. 3 and 4) would also hinge on these same considerations.

The neglect of backscatter, which is usual in gamma-ray transmission, is more conveniently discussed in the section following. This leaves the cumulative error to be considered. The discontinuities exhibited in Fig. 8(a) by the distribution for a thickness of 1 mfp lead one to expect large error in the distribution for 2 mfp, particularly when it is known that the operation with the transformation matrix is equivalent to a numerical integration. Careful examination revealed that the discontinuities do produce errors in the calculated distributions. For the second elemental slab, the discrete values are in most cases too large, have a maximum error of about 3 percent and when integrated, yield a total transmission in excess of the correct value by at most 1 or 2 percent. For large thicknesses, the steep constant-energy sections, such as shown in Fig. 8(c), were found to give values on the small side. Since with increasing thickness the discontinuities tend to disappear and the steepness of the sections to increase, one has a schedule of errors which should not compound powerfully, and one would not expect the distributions shown in Figs. 8–10 to contain large accumulated errors except possibly in the case of iron, where the neglect of the third collision has been seen to have its effect.

Comparison of Results from the Two Methods

The two quantities $N_t(X)/N_i e^{-X}$ and $E_t(X)/E_i e^{-X}$ of Figs. 12 and 13 can be considered as build-up factors for the incident distribution of the thin-slab method. Both quantities can also be calculated from the build-up factors for the δ distributions, which, in the case of normal incidence are shown in Figs. 3–6. The circled points in Figs. 12 and 13, which were passed over earlier, are values calculated from the build-up factors for the δ distributions. One would expect, in the light of the preceding discussion of the accuracy of thin-slab results, that the agreement would be good except for the case of the number of photons transmitted through iron. For this case, Fig. 14 shows that the circled points in Fig. 12 should lie above the curve, higher when $\alpha_0=10$ than when $\alpha_0=20$. If Figs. 12 and 13 are examined carefully, it will be found that within a latitude consistent with the stated error, these expectations are realized. To be sure, the points for $X=16$ and $X=20$ for iron-number-20 mc² undoubtedly should be raised so as to stand in the same relation to their comparison curve as the points at $X=4, 8, 12$; and there are other evidences of error. If in some cases, notably iron-energy-10 mc², the deviation is larger than the 1 percent expected at $X=1$ or the 2 percent at $X=2$, the explanation almost certainly lies in the accumulation of error due to the succession of graphical and numerical steps required to pass from the transmission with zero, one, two, and three scatterings to the values of the circled points. But the deviations in the two sets of results do not indicate that there is any reason to increase the magnitude of error stated to hold for the build-up factors of Figs. 3–6. In fact, except for number-iron, a rule giving errors smaller by half would stand. It is true that these comparisons do not directly support the factors for $\alpha_0=5$, 2.5, and 1, but the same method of

extrapolation was used in all cases and, since the method is consistent and definite over all cases, the support is considered as extending with some force to the low energies.

4. TRANSMISSION IN THE ABSENCE OF ABSORPTION BY PAIR PRODUCTION AND PHOTOELECTRIC EFFECT

The Contribution of Backscattered Radiation to Transmission

It will be recalled that photons scattered out of the forward hemisphere were ignored both in the method of thin slabs and in the method of successive scatterings. Although this neglect is intuitively acceptable, data indicating the magnitude of the quantities neglected have some interest. Table II gives probabilities of transmission through, and reflection from, thin slabs of the pure Compton scatterer; transmissions and reflections for one and two collisions with all possible successions of forward and backward scatterings are tabulated for photons normally incident and of energies 10, 5, 2.5, 1, and 0.2 mc². The probability of transmission with a backward and a forward scattering, N_{bf}, in comparison with the probability of transmission with two forward scatterings, N_{ff}, is seen to dwindle in importance as the thickness of the slab increases. At a thickness of $\frac{1}{2}$ mfp N_{bf} is significant, running from slightly less than one-tenth of N_{ff} in the case of 10 mc² to about one-half in the case of 0.2 mc². At a thickness of four mean free paths, N_{bf} is very small except in the case of 0.2 mc², where it is about one-seventh of N_{ff}. The increased importance of N_{bf} for 0.2 mc² is of course due to the increased probability of large angles of deflection.

TABLE III. Expected energies of transmission and reflection with one and two scatterings for photons of 0.2–10 mc² normally incident on slabs of the pure Compton scatterer.[a]

α_0	X	E_0	E_f	E_b	E_{ff}	E_{bf}	E_{bb}	E_{fb}
10	0.5	6.065	0.896	0.0102	0.111	0.0014	0.0046	0.0042
	1.	3.679	0.969	0.0103	0.205	0.00083	0.0048	0.0043
	2.	1.353	0.605	0.0103	0.204	0.00026	0.0049	0.0044
	4.	0.1832	0.130	0.0103	0.0633	0.0000388	0.0049	0.0044
5	0.5	3.032	0.522	0.0153	0.0691	0.0023	0.0055	0.0043
	1.	1.839	0.568	0.0164	0.130	0.0015	0.0072	0.0065
	2.	0.6765	0.355	0.0164	0.135	0.00044	0.0075	0.0069
	4.	0.0916	0.0768	0.0164	0.0434	0.000049	0.0076	0.0069
2.5	0.5	1.516	0.306	0.0202	0.0435	0.0030	0.0060	0.0061
	1.	0.920	0.325	0.0227	0.0811	0.0026	0.0086	0.0081
	2.	0.338	0.198	0.0232	0.0835	0.00073	0.0099	0.0091
	4.	0.0458	0.0421	0.0232	0.0274	0.000082	0.0101	0.0092
1.0	0.5	0.6065	0.130	0.0236	0.0225	0.0030	0.0060	0.0062
	1.	0.3679	0.143	0.0277	0.0400	0.0035	0.0086	0.0089
	2.	0.1353	0.0885	0.0285	0.0403	0.0014	0.011	0.010
	4.	0.01832	0.0189	0.0285	0.0134	0.00014	0.011	0.010
0.2	0.5	0.1213	0.0247	0.0143	0.00541	0.0015	0.0034	0.0032
	1.	0.07358	0.0266	0.0183	0.00874	0.0025	0.0051	0.0048
	2.	0.02706	0.0164	0.0195	0.00834	0.0018	0.0063	0.0058
	4.	0.00366	0.00342	0.0196	0.00269	0.00027	0.0065	0.0058

[a] E_0 = the expected energy transmitted by unscattered photons. In the cases of the other expected energies the subscripts "f" and "b" indicate respectively a forward scattering and a backward scattering. For example, E_{bf} is the expected energy in the photons transmitted with exactly two collisions, the first resulting in a backward scattering, the second, in a forward scattering.

TABLE IV. Values of N_k/e^{-X} and $E_k/\alpha_0 e^{-X}$ ($k=1, 2$) for 10 mc² photons normally incident on slabs of lead, of iron, and of the Compton scatterer.[a]

Quantity	X	Compton Scatterer	Iron	Lead
N_1/e^{-X}	1	0.445	0.387	0.257
	8	1.44	1.52	1.40
	20	2.22	2.46	2.94
N_2/e^{-X}	1	0.178	0.129	0.053
	8	1.19	1.39	1.11
	20	2.53	3.30	4.36
$E_1/\alpha_0 e^{-X}$	1	0.262	0.218	0.141
	8	1.06	1.09	0.936
	20	1.75	1.89	2.11
$E_2/\alpha_0 e^{-X}$	1	0.0558	0.0396	0.0157
	8	0.660	0.737	0.482
	20	1.56	2.00	2.43

[a] N_k is the probability that a photon will be transmitted through a slab with exactly k collisions, E_k is the corresponding expected energy, and X is the thickness of the slab in mfp.

Backward scattering is even less important for energy transmission. This can be seen in Table III, the energy counterpart of Table II. Only for 0.2 mc² does E_{bf} attain much importance.

The importance of backward scattering to the transmission scattered k times is controlled by the relative magnitudes of k and X. If k is large, the probability of one or more backward scatterings is large. But, if X is large, the slab tends to allow transmission only to those photons which have wasted no collision in traveling backward. Hence, if X is fixed and k is allowed to increase sufficiently, nearly all the photons transmitted with k scatterings will have suffered a backward scattering. On the other hand, if k is fixed and X increases sufficiently, almost none of the transmitted photons will have suffered a backward scattering. The upshot is that one can say for a slab of any thickness that backward scattering is negligible to the k-tuply scattered transmission when k is sufficiently small, but all important when k is sufficiently large. Whether or not backward-scattered photons form a significant part of the total transmission depends on the value of k reached before the k-tuply scattered transmission becomes negligible. In the cases of lead and iron, the evidence is that backward scattering does not have the opportunity to become important. A slab thick enough to make twice- or thrice-scattered transmission count heavily was found to be too thick for the backward-scattered component to have significance. The rapid convergence of N_k and E_k to zero indicated that the same situation would be found to exist for transmission with a larger number of scatterings. It seems unlikely, therefore, that neglect of backward scattering can introduce large errors into the transmission results for lead and iron, or any of the heavier materials.

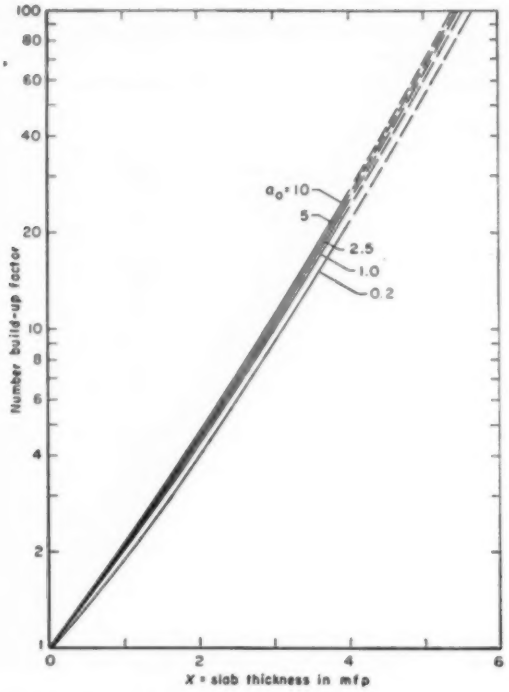

FIG. 17. Number build-up factors for photons normally incident on a thin slab of the pure Compton scatterer.

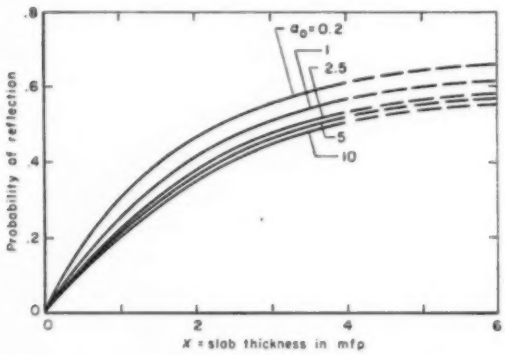

FIG. 18. Probabilities of reflection for photons normally incident on a thin slab of the pure Compton scatterer.

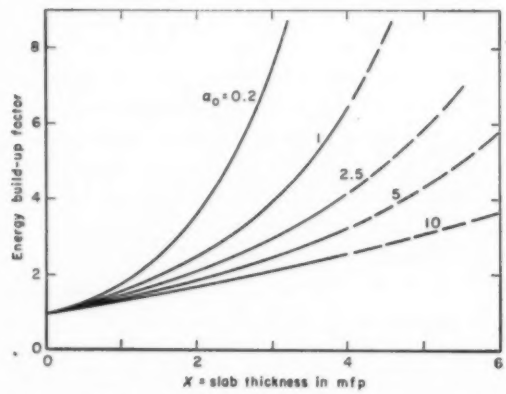

FIG. 19. Energy build-up factors for photons normally incident on a thin slab of the pure Compton scatterer.

Comparison of *k*th-Scattered Transmission for Lead, Iron, and the Compton Scatterer

Absorption by pair production and the photoelectric effect tends to reduce the probability of transmission. The reduction, however, does not necessarily appear in the transmission values for the first few scatterings. Table IV, which gives N_1/e^{-X}, N_2/e^{-X}, $E_1/\alpha_0 e^{-X}$, and $E_2/\alpha_0 e^{-X}$ for 10 mc² photons normally incident on slabs of lead, of iron, and of the Compton scatterer, shows that for $X=20$ the transmission values actually increase as the three materials are considered in the order: Compton scatterer, iron, lead. This seeming paradox will be resolved in Part II.

For the higher-ordered scatterings, pair production and the photoelectric effect do decrease the transmission by very significant amounts as can easily be shown.

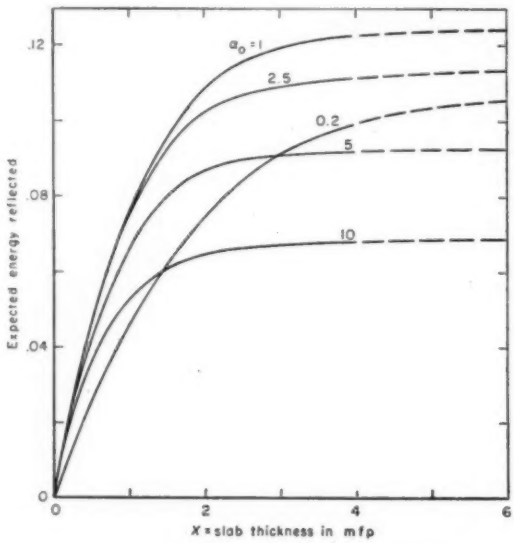

FIG. 20. Expected energies of reflection for photons normally incident on a thin slab of the pure Compton scatterer.

For example, in Table IV one finds values of N_k/e^{-X} for the Compton scatterer, $\alpha_0=10$, $X=8$, such that

$$N_0=0.000335, \quad N_1=0.000483, \quad N_2=0.000399.$$

The quantity N_k has reached its maximum value in the first collision. If, say, 20 terms are needed to reach an approximation to the sum of the series $\sum_0^\infty N_k$, a liberal estimate of the probability of transmission would not exceed 0.005. But no photons are lost through absorption, so that all must eventually escape. Therefore, the individual transmissions and reflections must sum to unity, and if the probability of transmission is 0.005, the probability of reflection is 0.995. The latter probability seems unreasonably large for a slab only 8 mfp thick. To get a reasonable value, the series $\sum_0^\infty N_k$ must converge so slowly that hundreds or thousands of terms are needed to approximate its sum. Photons on their way to being scattered hundreds or

thousands of times must come into the low-energy range where, in the cases of lead and iron, they are absorbed by the photoelectric effect. That the photoelectric effect is able to bring the count of terms required for lead and iron down to tens and not hundreds or thousands was proved in Sec. 2 by the rapid convergence of the quantity r_k, an example of which is given in Table I.

Estimates of Transmission and Reflection for Thin Slabs of the Compton Scatterer

It is clear that the method of successive scatterings must be considerably less successful for the Compton scatterer than for lead or iron. Nevertheless, for thin slabs, the results in Tables II and III can be used to obtain estimates of both transmission and reflection for normally incident photons. Estimation is aided, in the case of number, by the fact that the probabilities of transmission and reflection must sum to unity and, in the case of energy, by the fact that $\sum_0^\infty E_k$ is given a degree of rapidity of convergence (compared to $\sum_0^\infty N_k$) by the degradation of the energy with each collision. These estimates appear in Figs. 17 through 20. Figure 17 gives the number build-up factors; Fig. 18, the estimated probabilities of reflection; Fig. 19, the energy build-up factors; and Fig. 20, the expected reflected energies. The accuracy of the estimates is uncertain, but, in the case of number, the error is believed to be about 5 percent at $X=4$. In the case of energy, the error may be larger, particularly for the low incident energies, where the convergence is very slow.

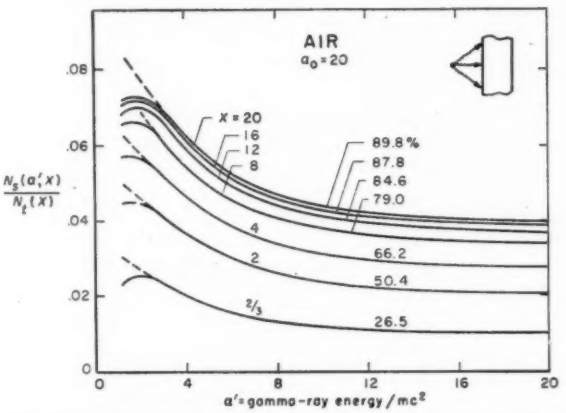

FIG. 21. Distributions of photons scattered by slabs of air, each distribution normalized by dividing by the total of all high-energy photons transmitted.

Thin-Slab Method Applied to Air

In the absence, or near absence, of photoelectric absorption in the low energies, backward scattering will become important to transmission. Therefore, the thin-slab method will not be entirely successful. It is not without profit, however, to apply this method to a light material for which absorption by pair production and photoelectric effect is small. Typical of the light materials, and of considerable interest, is air; Fig. 7 gives the total absorption coefficient assumed to hold for air.

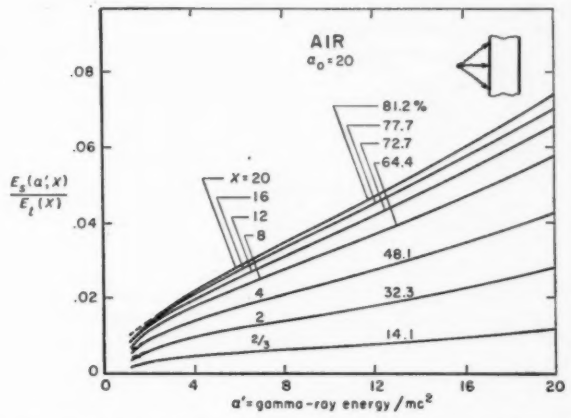

FIG. 22. Distributions of the energy in the photons scattered by slabs of air, each distribution normalized by dividing by the total energy in all transmitted photons.

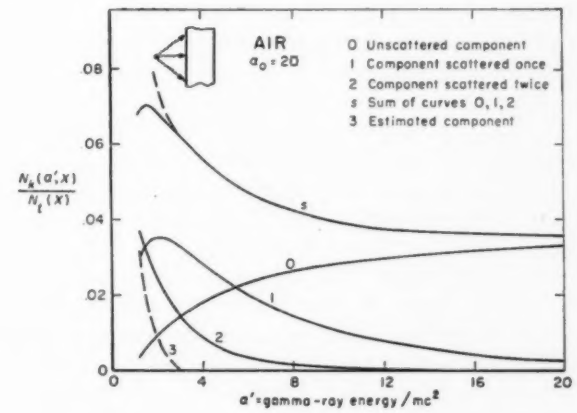

FIG. 23. Components of the distribution for the 16th elemental slab of air

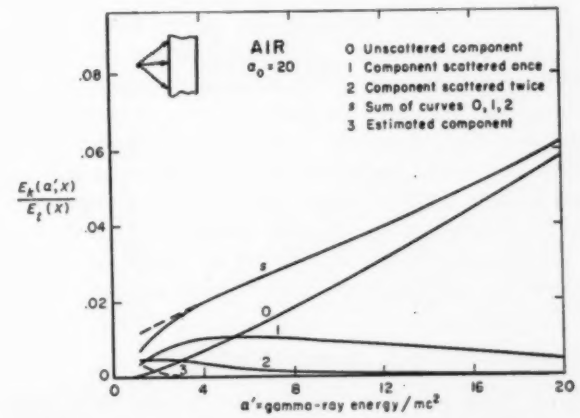

FIG. 24. Components of the energy distribution for the 16th elemental slab of air.

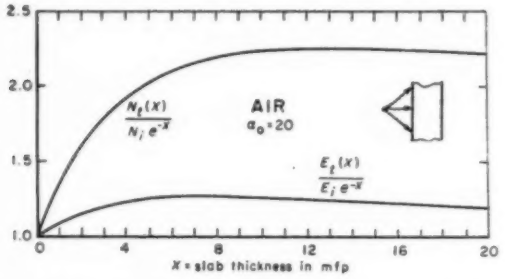

FIG. 25. The ratio of the number of photons transmitted to the number incident and the ratio of the energy transmitted to the energy incident, for slabs of air, both ratios normalized by the factor $1/e^{-X}$.

The treatment of air parallels that of lead and of iron. The same incident distribution is used and the same quantities are calculated. Only one incident energy, 20 mc², is considered, however, and the thickness of the elemental slab is $\frac{2}{3}$mfp. Figures 21 and 22 show, respectively, the ratios $N_s(\alpha', X)/N_t(X)$, and $E_s(\alpha', X)/E_t(X)$, where the normalizing factors $1/N_t(X)$ and $1/E_t(X)$ correspond, as in the cases of lead and iron, to the area under the terminated solid curves rather than the dashed curves. In the case of number, the differences between the two areas are very large, so that $N_t(X)$ far underestimates the true number of photons transmitted and the true density; but in the case of energy, the differences are presumably comparatively small, so that $E_t(X)$ only slightly underestimates the true energy transmitted. This is shown very clearly in Figs. 23 and 24, which give the components of the distribution for the 16th elemental slab. Figure 25 gives the quantities $N_t(X)/N_i e^{-X}$ and $E_t(X)/E_i e^{-X}$. It may seem pointless to develop $N_t(X)$ as though $N_t(X)$ were not known to be below its true value, but the thought is that the reader interested in estimating the true value may find it a service to have the undervalue of $N_t(X)$; in any event, the values given may be considered as being the true values when photons enfeebled by many collisions are disregarded.

The curves of Figs. 21 through 25 behave qualitatively as one would expect from the results for lead and iron. Trends that are apparent on considering first lead and then iron are continued to air. Backward scatter is undoubtedly more important than it was for lead or iron, but since the distribution over direction of the incident photons favors the normal, those photons which have been scattered backward at some time in their history tend to appear in the energy range below that considered in the thin-slab method. Little change in the curves of Figs. 21 through 24 would have been discernible had backward scatter been included in the calculations.

5. CONCLUSION

It is believed that the results, which have been presented, are at least as accurate as they are stated to be. The important basis for this belief is found largely in the support that the two sets of results, one set obtained by the method of successive scatterings and the other by the method of thin slabs, give to each other. The pattern of agreement and disagreement between corresponding values of $N_t/N_i e^{-X}$ (Fig. 12) and corresponding values of $E_t/E_i e^{-X}$ (Fig. 13), as calculated by the two methods, is almost precisely as expected from the study of the inherent errors of the thin-slab method. In fact, if errors larger than stated do exist, then it must be that a pair of corresponding values are either both too high or both too low. The thin-slab method can hardly give values too high, since the errors of this method tend to produce values which are too low. If the results from both systems of calculation are far too low, then (1) the errors in the thin-slab method are larger than the investigation of their magnitude demonstrated to be possible and (2) the convergence of the sequence $\{N_k\}$ is much slower than the convergence of the sequence $\{r_k\}$ indicates. Neither consequence is easy to accept, particularly in the case of lead, where the error due to neglecting backscatter and all scatterings beyond the second must be small and where the convergence of $\{N_k\}$ is surely rapid.

APPENDIX. TRANSMISSION OF PHOTONS OF ENERGIES LESS THAN 1 mc² THROUGH SLABS OF LEAD AND OF IRON

Results were presented in Sec. 2 for values of α_0 ranging between 1 and 20. Since α', the energy after collision, is related to α, the energy before collision, by the formula

$$\alpha' = \frac{\alpha}{1+\alpha(1-\cos\theta)},$$

where θ is the angle of deflection, one cannot calculate N_{k+1} at $\alpha_0=1$ without knowing N_k in the interval between $\frac{1}{3}$ mc² and 1 mc².[9] Consequently, the results

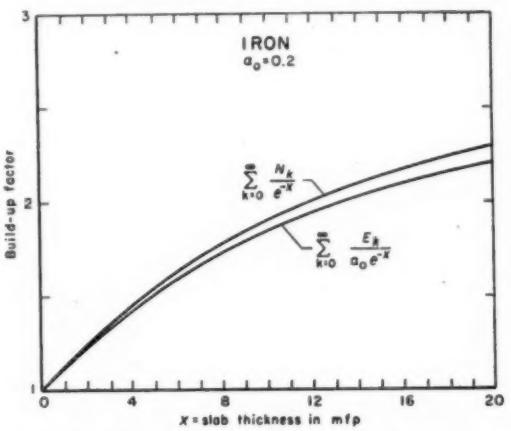

FIG. 26. Number and energy build-up factors for iron slabs, $\alpha_0=0.2$.

[9] Since a collision degrades a photon's energy, this statement may seem at first glance to be incorrect. However, if the formulation of the recurrence relation between N_k and N_{k+1} is recalled, it will be seen that in order to calculate N_{k+1} at 1 mc², it is necessary to know N_k below 1 mc² rather than above 1 mc².

given in Sec. 2 for $\alpha_0=20, 10, 5, 2.5, 1$ imply additional results at lower incident energies. These additional results were not discussed because they did not lie in the more or less arbitrarily selected range of interest between 1 and 20 mc² and because their irregularities tended to destroy the uniformity of the exposition. They do have some interest, however, so that it seems desirable to give them in an appendix by themselves, where the difficulties of their presentation can be minimized.

In the case of iron, no first-collision results were calculated below $\alpha_0=0.2$. This meant that second-collision results could be calculated to an energy no lower than $\frac{1}{3}$ mc² and third-collision results, no lower than 1 mc². Since only three scatterings and a lower energy limit of 1 mc² were contemplated, this retreat up the energy scale would have been acceptable. To calculate N_{k+1} at $\alpha_0=0.2$, however, it is only necessary to know N_k between the energies 1/5 mc² and 1/7 mc². Since the variation in the functions fundamental to the calculations is not large within this narrow range, the computation of the results for the second scattering from the first and for the third from the second could, and did, proceed in the case of $\alpha_0=0.2$ with the help of an apparently safe extrapolation. Although the second- and third-collision results at $\alpha_0=0.2$ may have questionable accuracy, the spread of inaccuracy to larger values of α_0 is slow. A large error in the values of N_2 at 0.2 mc² causes a comparatively small error in the values of N_3 at $\frac{1}{3}$ mc², provided that N_2 is correct at the latter energy. The reason is, of course, that the interval near α_0 is by far the most important in the calculation of transmission for an incident energy of α_0.

The build-up factors for iron slabs at $\alpha_0=0.2$ are shown in Fig. 26. The contributions to the build-up factors of N_2/e^{-X}, N_3/e^{-X}, $E_2/\alpha_0 e^{-X}$, and $E_3/\alpha_0 e^{-X}$ are so small, because of large absorption by the photoelectric effect, that errors in their values due to the extrapolation mentioned above should not significantly affect the build-up factors.

The treatment of lead in the low-energy range does not parallel that of iron because of two marked differences in the total absorption coefficients. Figure 7 shows that the absorption coefficient for lead has a much larger photoelectric component than that for iron and, in addition, has a discontinuity at 0.172 mc², where the energy reaches the limit of the K level. So large is the absorption by the photoelectric effect for low energies that one might expect the build-up factors for normal, or nearly normal, incidence to be merely the sum of N_0/e^{-X} and N_1/e^{-X}, the latter contributing very little even for large values of X. But the first-collision results in Table V for $\alpha_0=0.2$, 0.172+, 0.172− and 0.1 show that the discontinuity gives rise to values for N_1/e^{-X} very much larger than those for N_0/e^{-X}, and it is not instantly clear what to anticipate for the magnitudes of N_2/e^{-X}, N_3/e^{-X}, etc.

TABLE V. N_1/e^{-X} and $\Sigma_0^{\infty}N_k/e^{-X}$ for photons of low energy normally incident on lead slabs.[a]

α_0	X	N_1/e^{-X}	$\Sigma_0^{\infty}N_k/e^{-X}$
0.2	1	0.0087	1.01
	8	0.029	1.03
	20	0.041	1.04
0.172+	1	0.012	1.01
	2	0.030	1.03
	4	0.14	1.15
	8	2.5	3.7
	12	46.	53.
	16	840.	930.
	20	17000.	18000.
0.172−	1	0.027	1.03
	8	0.091	1.10
	20	0.13	1.14
0.1	1	0.0077	1.01
	8	0.027	1.03
	20	0.040	1.04

[a] N_k is the probability that a photon will be transmitted with exactly k collisions and X is the thickness of the slab in mfp.

Consider the case, $\alpha_0=0.172+$, $\gamma_0=1$, $X=20$. Until the first collision, the photons move in a thick slab; the unscattered beam and the distribution of the points of first collision through the slab correspond to a value of $X=20$. After the first collision the photons have a lower energy and the absorption coefficient is about one-fifth of its incident value. The probability that the photon will pass on through the slab after the first collision and the probabilities of its transmission with two or more scatterings are therefore governed more by a thickness of 4 mfp than by a thickness of 20 mfp. Because N_0 is associated with 20 mfp, N_0 is much smaller than N_1. Also N_2 can be expected to be smaller than N_1 since ordinarily N_2 is considerably less than N_1 for 4 mfp. In view of the large amount of photoelectric absorption associated with $\alpha_0=0.172+$, one would expect N_2 to be not more than 10 to 20 percent of N_1. A quick, rough calculation of N_2/e^{-X} at 20 mfp yielded the value 1350, which is less than 10 percent of N_1/e^{-X}. It is clear then, that the probability of transmission of low-energy photons normally incident on lead slabs is accurately obtained from the sum N_0+N_1, with a moderate upward correction as the incident energy approaches 0.172 mc² from above.

Table V contains, in addition to values of N_1/e^{-X}, the corresponding number build-up factors. The factors should be accurate, since estimation has little or no role. The values of the energy build-up factors are identical, within the error of the calculations, with the corresponding values of the number build-up factors.

The Properties of Carbon Contacts

R. O. GRISDALE
Bell Telephone Laboratories, Inc., Murray Hill, New Jersey
(Received March 16, 1953)

Microphone carbon has been produced by deposition of pyrolytic carbon films over the surfaces of small spherules of silica. The properties of contacts between these spherules are shown to be dependent on the structure and geometry of the carbon surface as determined by electron diffraction and microscopic studies. The graphite-like crystallites in pyrolytic carbon surfaces are more or less preferentially oriented with their basal planes parallel to the surface, and the contact properties depend systematically on the degree of orientation. This is explained in terms of the anisotropy in properties of these crystallites which are closely approximated by those of single crystal graphite which were determined. The contact resistance and its temperature coefficient and the "burning voltage" for carbon contacts are explicable on this basis. However, the microphonic sensitivity of carbon contacts is independent of the surface structure and depends only on the surface geometry.

INTRODUCTION

STUDY of the carbon microphone and of single contacts between carbon granules has led to the view that the carbon surfaces are submicroscopically rough so that when two surfaces are brought together by compressional forces, both the number of "roughnesses" in intimate contact and the contact area between any two of them vary through deformations which are primarily elastic.[1]

Although the microphonic sensitivity of a loose contact is independent only on the geometry of the contacting surfaces, the contact resistance and the dependence of contact temperature on applied voltage are determined also by the electrical and thermal conductivities of the material in the immediate vicinity of the contact.[2] The behavior of such a contact may also depend upon the hardness and elastic properties of the contact material; for if its elastic limit is exceeded, plastic flow arises with associated irreversible changes in area of contact. Only in this way are these mechanical properties important, however, since it has been established that a given force modulation leads to the same modulation in area and hence in resistance of a contact regardless of the elastic constants of the material, provided only that its elastic limit is not exceeded.

Although measurements of the properties of carbon have been applied to the interpretation of the characteristics of microphonic contacts, no satisfactory correlation has been obtained. In view of this fact, a study of the structure and properties of black carbon and their correlation with the microphonic behavior of carbon contacts was undertaken.

To produce the carbon granules in the commercial telephone transmitter, a specially selected and carefully crushed anthracite coal is roasted in hydrogen at an elevated temperature. The roasting process is essential to the production of a satisfactory microphonic material and it has long been suspected that this heat treatment forms over the granule surfaces a layer of pyrolytic carbon, or Glanzkohl, the properties of which have been the subject of repeated study.[3,4] An electron diffraction investigation made in the course of the present study has confirmed this view. Before this confirmation was available, however, another process capable of producing microphonic carbon equivalent in most respects to anthracite coal had been developed.[5,6] This process consists in the production of thin layers of carbon over the surfaces of specially prepared silica particles through the pyrolysis of a hydrocarbon vapor.

It is on similar films of pyrolytic carbon, ordinarily though not invariably deposited on rods or polished plates of fused silica, that the physical measurements described below were made. Since microphonic materials such as those described above were produced at the same time and their characteristics determined there were made available data for a determination of the correlation of the structure and physical properties of pyrolytic carbon with its microphonic behavior.

PREPARATION OF THE SPECIMENS

For determination of its physical properties, carbon was deposited over the surfaces of rods and flat polished plates of fused silica and, in some cases, of rods of other materials, and with each specimen thus produced a quantity of microphonic material was also prepared. The base for this microphonic material consisted of roughly spherical particles of intumesced silica[6] having apparent densities between 0.85 and 1.0 gram/cc and diameters between 0.17 and 0.25 mm. The appearance of the rods, plates, and semispherical silica specimens before and after deposition of carbon films on their surfaces is illustrated in Fig. 1.

[1] F. S. Goucher, J. Franklin Inst. **217**, 407 (1934).
[2] R. Holm, Z. tech. Phys. **3**, 290, 320, 349 (1922); Also *Electric Contacts* (Almquist and Wiksells, Stockholm, 1946).
[3] Else Koch-Holm, Wiss. Veroffen. Siemens-Konzern **6**, 188 (1927).
[4] C. A. Hartmann and H. Dosmann, Z. tech. Phys. **9**, 434 (1928).
[5] U. S. Patent 1,973,703 (September 18, 1934).
[6] U. S. Patent 2,151,083 (March 21, 1939).

The carbon was produced by pyrolysis in a specially constructed furnace[5] of methane purified by fractional condensation at −153°C. The specimens to be carbon coated were introduced into the rotating core of the furnace in air and, when temperature equilibrium was established, the furnace was flushed out with oxygen-free nitrogen. Thereafter, methane mixed with nitrogen was introduced at the center of the furnace core. The furnace temperature was held constant within ±2°C during pyrolysis, and tumbling of the specimens due to rotation of the furnace insured their uniform exposure to the furnace atmosphere. After deposition of a suitable thickness of carbon, the methane flow was stopped and the specimens were removed from the furnace, being allowed to cool quickly to room temperature in nitrogen. Immediately thereafter the microphonic material was sealed off in glass tubes in nitrogen. Experiment showed that the measured properties of the carbon were independent of the rate of cooling from the pyrolyzing temperature.

Specimens were prepared at furnace temperatures ranging from 950° to 1100°C and with volume concentrations of methane in the methane-nitrogen mixture admitted to the furnace ranging from 10 to 90 percent, previous experience having shown that the microphonic properties of pyrolytic carbon varied widely over this range of pyrolyzing conditions.[5] The rates at which carbon was deposited were determined by weighing silica rods and plates before and after deposition of the carbon, and it was found by trial that the weight of the silica itself was unchanged within the limits of experimental error during deposition.

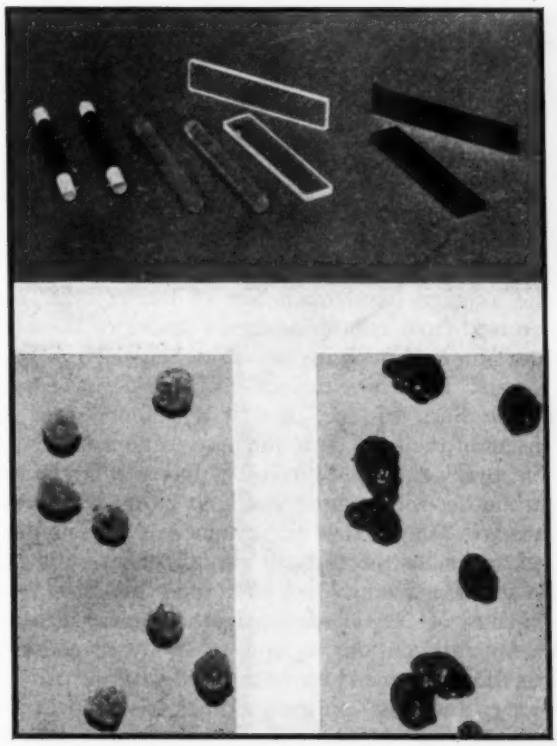

FIG. 1. Samples of fused silica before and after coating with pyrolytic carbon. The silica granules, shown magnified, have diameters of about 0.25 mm. The coated rods are shown with silver electrodes applied to their ends.

STRUCTURE OF THE CARBON FILMS

Electron diffraction diagrams obtained by reflection from carbon films deposited on polished silica plates[7] showed the crystal structure to be that of graphite modified in one principal respect. Whereas successive layers of atoms in graphite are so located that their projections on the basal plane gives an ordered atomic array, successive parallel layers of atoms in crystals of pyrolytic carbon are randomly displaced laterally with respect to each other so that the structure gives no evidence of regularities other than that of atomic location in the individual planes and the uniform separation between successive planes.

This electron diffraction evidence confirms the structure deduced from Debye-Scherrer x-ray patterns of black carbon.[8] It was found also, in confirmation of the results of x-ray analysis,[8–10] that the interatomic separation in the base plane was significantly less than in macrocrystal graphite and that the interplanar spacing along the *c* axis was appreciably greater. No extended study of this change in lattice constants was made but the values obtained were consistent with those previously observed,[8,9] the interatom spacing for a representative specimen being 1.398A and the interplanar spacing 3.59A. These values are to be compared with those for crystal graphite, 1.415A and 3.345A, respectively.[8] The magnitude of the change in the lattice constants of pyrolytic carbon relative to graphite has been found to increase as the average crystal or packet size decreases[8,9] and data obtained in the present study confirm this result.

These changes in lattice constants in mesomorphic carbon, together with the destruction of the regularity of atomic arrangement along the *c* axis probably appreciably increase the anisotropy in the properties of its crystals compared to single crystal graphite.[11]

The average thickness of the crystals along the *c* axis in the carbon films was found to be about 10A, indicating that they are composed, on the average, of about four atom layers. This average thickness appeared to be largely independent of the particular pyrolyzing conditions employed in producing the carbon. It is certain, however, that there is a distribution in thickness of the crystals, and it is probable that some consist of but single atom layers.

[7] A. H. White and L. H. Germer, J. Chem. Phys. **9**, 492 (1941).
[8] U. Hofmann and D. Wilm, Z. Elektrochem. **42**, 504 (1936).
[9] Blayden, Riley, and Taylor, J. Am. Chem. Soc. **62**, 180 (1940).
[10] H. L. Riley, J. Royal Coll. Sci. **10**, 10 (1940).
[11] K. S. Krishnan and N. Ganguli, Proc. Roy. Soc. (London) **177**, 168 (1941).

TABLE I.

Furnace temperature °C	Percent methane	Rate of deposit g/cm²/hr	Average crystal diameter, A
1000	10	1×10^{-5}	27.6
1000	30	2.7×10^{-5}	24.4
1000	60	1×10^{-4}	22.0
1000	90	2.1×10^{-4}	17.2

The average basal diameters of the crystals were determined from microphotometer traces of the (110) feature obtained by transmission of the electron beam at normal incidence through carbon films stripped from the silica surface,[7] and it was found that the extension of the crystals in the base plane is dependent on the pyrolyzing conditions. An increase in the rate of carbon deposition, brought about either by increase of furnace temperature or by increase in methane concentration in the furnace atmosphere, results in a decrease in the average diameter. Table I illustrates the dependence of crystal size on methane concentration.

Electron diffraction patterns taken by reflection as well as those obtained by transmission with the primary beam incident at 45° on the specimen have shown that the graphitic crystals in these specimens of carbon are preferentially oriented with their basal planes more or less parallel to the surface on which they are deposited.[7] The degree of orientation is dependent on the thickness of the carbon film, on the conditions under which it is prepared, and on the treatment to which it is subsequently subjected.

To assess the degree of this orientation, a series of diffraction patterns was selected and arranged in order of increasing orientation as judged primarily by the angular intensity distribution or the degree of "arcing" of the features.[7] By assigning arbitrary sequential numbers to these patterns a scale was obtained which was employed, by comparison, in determining the relative degrees of orientation in the various specimens of pyrolytic carbon.[12] The degree of orientation on this scale as it depends on the pyrolizing conditions, is given in Figs. 4 and 5.

These figures show that the extent of preferential crystal orientation in pyrolytic carbon depends systematically on the conditions under which the carbon is produced. An explanation for this has been found in the fact that the carbon films are built up by the accretion of minute molten droplets of complex hydrocarbons in which graphitic nuclei are arranged with their basal planes tangential to the droplet surface.[12] Variations in the hydrogen content of these droplets produce variations in their rigidities, and their rigidities determine the extent to which they can be smeared over a surface on which they are deposited. Fluid droplets can be readily smeared during deposition to yield carbon films with a high degree of preferred crystal orientation, but more viscous or rigid droplets cannot be smeared and hence yield carbon films in which the crystallites are randomly oriented.

A flat surface was ground and polished on a piece of anthracite coal and, after roasting to 1150° in hydrogen according to the standard practice for microphonic carbon, a diffraction pattern showed the surface to consist of crystals of mesomorphic carbon about 50A in diameter and 12A thick preferentially oriented with their base planes parallel to the surface. The larger diameter of these crystals relative to those in the specimens of Table I is consistent with their low rate of deposition from the very dilute hydrocarbon which comes from volatile organic matter in raw coal. Except for this difference in crystal size, the surface of the coal is the same as that of pyrolytic carbon from methane. It is this fact which makes measurement of the physical properties of mesomorphic carbon applicable to interpretation of the behavior of anthracite carbon in the commercial telephone transmitter.

PROPERTIES OF THE CARBON FILMS

Pyrolytic carbon, graphitic in structure, has physical properties which can be correlated in part at least with the size and properties of its constituent crystals and the way these crystals are arranged. While the lattice of these minute crystals differs in certain respects from that of the parent graphite it is probable that the metallic character of the layer planes is retained, that the anisotropy in properties of the crystal packets is greater than for graphite, and, hence, that conclusions as to the properties of pyrolytic carbon based on this anisotropy are valid to good approximation if the crystal packets are regarded as possessing the properties of macrocrystal graphite.

The properties of pyrolytic carbon have been determined in the course of the present study and they are listed in Table II, together with those of macrocrystal graphite which were also measured.[13] It was found that the specific resistance and the hardness are dependent on the degree of preferential orientation of the crystallites, but that other bulk properties are unaffected by change in the extent of preferred orientation.

While definite correlations are observed between structure and properties without considering the effects of crystal interfaces, the intercrystal boundaries in pyrolytic carbon modify its bulk properties for two reasons. In the first place, the interruption of lattice period at such boundaries is greatly accentuated by the anisotropy of the graphite crystals, and this interruption is of particular influence on thermal conductivity. Secondly, there is an actual chemical contamination at the interfaces due to the presence of peripheral hydrocarbon shells at the crystal edges.[13]

The correlation between the bulk properties of carbon

[12] R. O. Grisdale, J. Appl. Phys. 24, 1082 (1953).

[13] Grisdale, Pfister, and van Roosbroeck, Bell System Tech. J. 30, 271 (1951).

TABLE II.

Property	Unit	Polycrystal graphite	Graphite basal plane	Graphite c axis	Pyrolytic carbon
Density	grams/cc	2.26	—	—	2.07
Hardness	MOH's scale	0.5–1.0	>6.5	~0.5	9.8
Thermal coefficient of expansion	$(°C^{-1})\cdot 10^{-6}$	7.5	6.6	26.0	6.5–7.0
Specific resistance ρ	ohm-cm	8×10^{-4}	3.9×10^{-5}	$\sim1\times10^{-2}$	$1-1.8\times10^{-3}$
Temperature coefficient of Resistance	$°C^{-1}$	-1×10^{-3}	$+9\times10^{-3}$	$\sim-4\times10^{-2}$	-1.8×10^{-4}
Thermal conductivity K	watt/cm²/cm/°C	0.4	>4.0	~0.8	0.08
Temperature coefficient of thermal conductivity	$°C^{-1}$	−0.0011	~−0.005	—	−0.007
Wiedemann-Franz ratio $K\rho$	(watt ohm/°C)·10^4	3.2	1.6	~80.	1.1
Rate of oxidation	relative	—	17.	1.0	—

and its crystalline constitution is thus partially masked by the influence of intercrystal boundaries. However, the correlation between the properties of contacts between carbon surfaces and the crystallographic structure of the surfaces is relatively little influenced by these boundaries. For, as will be shown below, the contact properties are determined by those of a relatively small number of single crystals or oriented aggregates of crystals which project above the average surface of the bulk material.

THE PROPERTIES OF MICROPHONIC CARBON CONTACTS

Carbon is uniquely suited for use in the microphone because it combines three properties of great significance to stable, sensitive microphonic contacts. Its extreme hardness and high elastic modulus permit it to withstand very high local pressures without permanent deformation. Its specific resistance is sufficiently great that relatively high resistances can be obtained in volumes small enough to be suceptible to appreciable elastic deformation under the influence of the small forces operative in the microphone. And, finally, its oxides are gaseous and hence do not remain as solid surface contaminants which permanently alter the interfacial contact resistance.

The force between two carbon granules in the telephone transmitter averages only a few dynes, yet experiment and theory show the contact areas to be so small that only the hardest materials will support the stress without plastic deformation, and it is for this reason that the carbon must be extremely hard, as the above measurements show it to be. Several avenues of approach lead to values less than 1×10^{-5} cm for the diameter of gross contact between two carbon granules. Accepting this figure, and taking 2.5×10^{-7} cm as the average basal diameter of the crystals in the contact surface, about 1600 crystals would be involved if intimate contact extended over the entire gross area of contact. Actually the two surfaces are in intimate contact over but a small fraction of the apparent contact area and it is probable that the discrete crystals involved in intimate contact are at most a few hundred in number.

The Contact Resistance

The resistance of a contact is confined largely to a minute volume of material directly beneath the contact interface, and this "spreading resistance"[2] is, therefore, critically dependent on the specific resistance of the material in this region. In the case of contact between two specimens of carbon whose crystals are highly oriented, the current through the contact must flow largely along the c axis of the crystals as is shown schematically in Fig. 2B. On the other hand, at contact between two specimens of random crystal orientation, such as shown in Fig. 2A, the current is shared over approximately equal areas parallel and perpendicular to the c axis of the crystals. In view of the marked anisotropy of the crystals, the two contacts illustrated in Fig. 2 would be expected to have quite different properties, and this is in fact the case.

The resistance in a suitable measuring cell of an aggregate of carbon coated silica particles such as described earlier is the sum of two parts—first, the resistance of the intergranular contacts themselves, and,

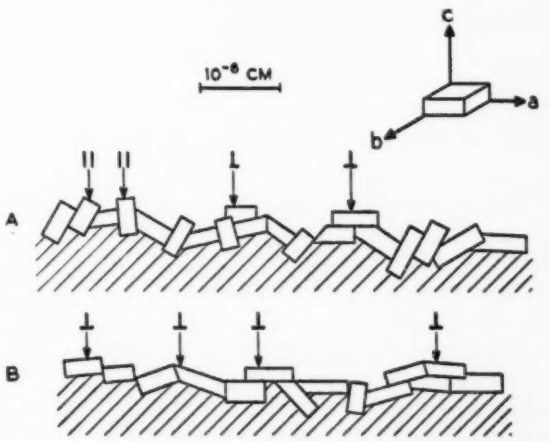

FIG. 2. Schematic diagrams showing the sizes and orientations of crystallites at the surface of a film of pyrolytic carbon. The arrows indicate points on the surface which would be concerned in microphonic contact, showing how, for different orientations, the spreading resistance will lie along the base plane (parallel) or along the c axis (perpendicular) of the anisotropic crystallites. A random orientation. B preferential orientation with base plane parallel to surface.

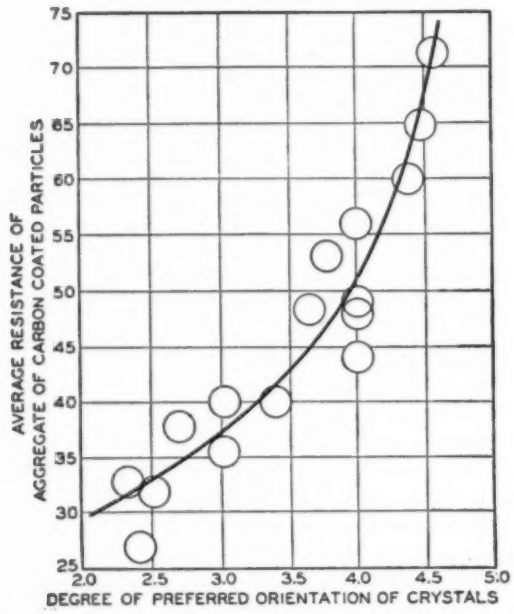

FIG. 3. The cell resistance of an aggregate of carbon coated particles as a function of the degree of preferred crystal orientation in the carbon surface.

second, the resistance of the spherical carbon shells acting in series with these contacts. It is only the first of these which can be modulated by compressional contact forces, and the series resistance is small relative to it if the carbon thickness exceeds 3×10^{-5} cm. For lesser thicknesses, the apparent modulation efficiency of the contact—its average resistance R divided into the change in its resistance ΔR when it is acoustically modulated—is less than its true value, and the resistance of the aggregate is greater than that originating at the contacts themselves. Most measurements in the present study were made on materials for which the series resistance was negligible compared to the true contact resistance, in other words, on materials with films of carbon at least 3×10^{-5} cm thick.

The measurements were made by filling a commercial telephone transmitter with the microphone carbon and, at a given average current and in a given sound field, determining its average resistance R and its alternating voltage output ΔE, whence $\Delta E/E=\Delta R/R$. The recorded values of R and $\Delta R/R$ are the averages of at least nine measurements, three being made on each of three fillings of carbon.

It has been known for some time that the resistance of an aggregate of microphonic carbon granules is dependent on the conditions under which the carbon is deposited.[5] The present study shows that this cell resistance R and hence that of the intergranular contacts, is dependent on the degree of preferential orientation of the graphitic crystals in the carbon surface. Thus, in Fig. 3, the values of R for a variety of carbons prepared by varying both the pyrolyzing temperature and the methane concentration are given as functions of the degree of preferential crystal orientation in carbon surfaces prepared at the same time. The contact resistance increases regularly with increase in the degree of orientation of the crystals, a behavior just the reverse of that for the specific resistance of the carbon film.[12] Figure 2 indicates that this is the expected behavior, however, for the specific resistance is measured with a current flowing parallel to the surface of the film while the current through the contact flows normal to its surface. With increasing orientation an increasing portion of the spreading resistance at the contact therefore lies along the high resistance c axis of the surface crystals, while a decreasing part of the current used to measure the specific resistance is carried along this axis.

For carbon films thicker than 3×10^{-5} cm the contact resistance is thus clearly dependent on the degree of orientation of the graphitic crystals in their surfaces. This is not true, however, for thinner films and it has been found that for these the measured resistance of the aggregate is a function of the film thickness. In such cases, therefore, it is the resistance of the spherical carbon shells acting in series with the contacts themselves which determines the resistance of the aggregate.

If s is the radius of a thin spherical conducting shell and if electrodes of radius b are applied at opposite poles of this shell, then the resistance between the electrodes is

$$R_p=\frac{2r}{\pi}\int_{b/s}^{\pi/2}\frac{d\varphi}{\sin\varphi}=\frac{r}{\pi}\ln\frac{1+\cos b/s}{1-\cos b/s}, \qquad (1)$$

where r is the resistance of a unit square of the film measured between opposite edges. In the case where $b\ll s$ this reduces to

$$R_p=\frac{2r}{\pi}\ln\frac{2s}{b}. \qquad (2)$$

Now if the disk-shaped electrodes be sufficiently small, as is true in the present instance, the resistance of the spherical shell between them does not depend on their relative location, because the two-dimensional spreading resistance near the electrodes is controlling. Thus, even though the contacts to a granule in an aggregate are not made at opposite poles, the value of R_p given above represents the series resistance R_s of the conducting shell between them, regardless of their relative location. The contact radius b almost certainly lies between 10^{-4} and 10^{-6} cm, and when the shell radius s is 10^{-2} cm, a lower limit to the value of R_s may thus be taken as $4r$.

In Figs. 4 and 5 the values of cell resistance R series resistance R_s and modulation efficiency $\Delta R/R$ are given as functions of the temperature and the methane concentration, respectively, employed in preparing various specimens of microphonic material; and in each figure the degree of preferred orientation of the surface crystals in specimens prepared at the same time is also given.[12] For temperatures greater than 975° or methane

concentrations exceeding 10 percent, the cell resistance R is dependent on the degree of preferred orientation as has already been shown in Fig. 3; but as the temperature or concentration is decreased below these limits, R increases rapidly. Under the conditions employed in preparing the specimens, these limits correspond to a thickness close to 3×10^{-5} cm, and the data suggest that above this thickness the degree of preferred crystal orientation determines the value of cell resistance while for lesser thicknesses the series resistance R_s is controlling.

The dependence of cell resistance and modulation efficiency on the value of series resistance is shown in Fig. 6. There it will be noted that R and $\Delta R/R$ are independent of R_s up to about 150 ohms, which corresponds to a film thickness of 3.2×10^{-5} cm. If R_c is the

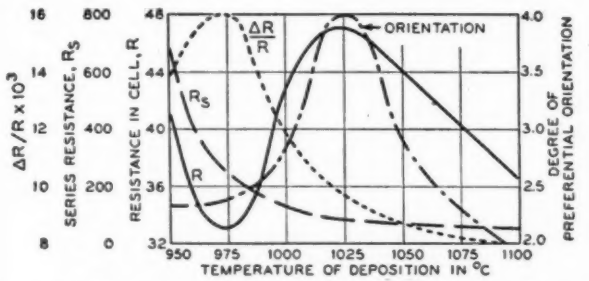

FIG. 4. The properties of pyrolytic microphone carbon as functions of pyrolyzing temperature at constant methane concentration. The degree of preferred crystal orientation is also shown.

true average contact resistance and ΔR_c is the change in it due to acoustic modulation, then

$$\Delta R/R=\Delta R_c/(R_c+R_s) \tag{3}$$

and

$$R=K(R_c+R_s), \tag{4}$$

where K is a constant determined by the dimensions of the measuring cell. Now for a given rate of carbon

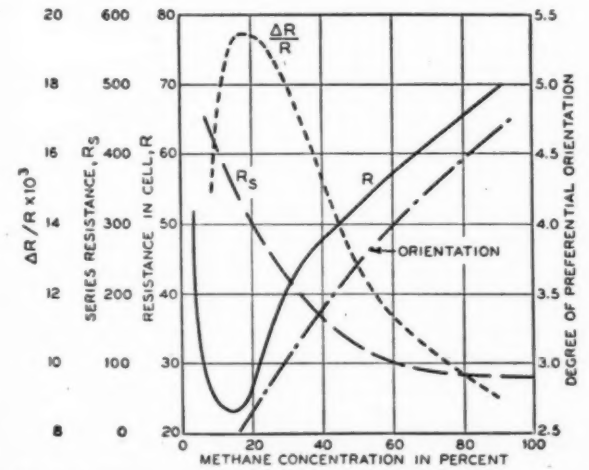

FIG. 5. The properties of pyrolytic microphone carbon as functions of methane concentration at constant temperature. The degree of preferred crystal orientation is also shown.

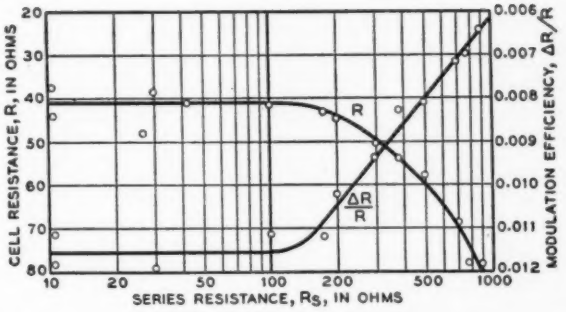

FIG. 6. The modulation efficiency $\Delta R/R$ and the cell resistance R for pyrolytic microphone carbon aggregates as functions of the resistance of the carbon shells R_s in series with the intergranular contacts.

deposition the intrinsic modulation efficiency of a single contact $\Delta R_c/R_c$ is independent of film thickness and hence of R_s, since, as is shown below, the basic modulation efficiency depends only on the geometrical nature of the surface. The true contact resistance depends on this surface geometry and, as shown above, on the extent of preferred crystal orientation in the surface. The data of Fig. 6 were obtained from specimens differing only in film thickness and hence R_c and $\Delta R_c/R_c$ are constants, and changes in the measured values of R and $\Delta R/R$ are due to change in R_s. By fitting the data of Fig. 6 to the expressions (3) and (4), values of R_c, the contact resistance, of 990 ohms and 813 ohms are obtained, respectively. The average value of 900 ohms for the contact resistance thus found is in good agreement with that measured directly on single contacts. However, this method of measurement provides a value for the effective contact resistance within an aggregate free from any assumption as to contact force.

The resistance of a contact between two smooth solid spheres when their common radius is large relative to that of the contact area b is

$$R=\rho/2b, \tag{5}$$

where ρ is the specific resistance of the material of which the spheres are composed. While the total area of intimate contact probably is made up of a number of smaller areas resulting from coincidence between discrete "roughnesses,"[14] it is permissible to lump these together for computation of the contact radius from the above expression. It is apparent from the relation between crystal orientation and contact resistance that it is the specific resistance along the c axis of the graphitic crystal which, in the limit, determines the contact resistance. Therefore, taking $\rho=0.01$ ohm-cm from Table II and accepting the above value of 900 ohms as the resistance of a single contact, the expression above gives the value 5.5×10^{-6} cm for the radius of the area of intimate contact.

[14] C. J. Christensen and G. L. Pearson, Bell System Tech. J. 15, 197 (1936).

Since the average basal diameter of the crystals in the contact interface is about 2.5×10^{-7} cm, this indicates that there about 1900 crystals in the area of intimate contact. Now preferential orientation of the crystals is never perfect and hence the effective value for the specific resistance of the carbon in the region of contact will be less than 0.01 ohm-cm characteristic of the c axis. In addition, as has been pointed out above, 900 ohms is probably a lower limit to the contact resistance, and its true value in the aggregate may be greater. In view of these facts it appears probable that the crystals involved in a single microphonic carbon contact are at most a few hundred in number, and other data, described below, support this view.

The Temperature Coefficient of Contact Resistance

The temperature coefficient of resistance α measured at constant force for single carbon contacts averages $-0.015°C^{-1}$ and reaches values as great as $-0.03°C^{-1}$.[1] The value of α varies from one contact to the next and from one variety of carbon to another; and it has also been found to vary significantly in a nonsystematic manner with change in contact force. This large value of α is incompatible with measurements of the coefficient for "hard carbon"[2] and with that for bulk pyrolytic carbon given in Table II. However, it has been shown in the foregoing that the spreading resistance at a carbon contact is determined largely by that measured with current flow along the c axis of the graphitic crystals, and the observed value of α for the contact is in good agreement with the value characteristic of this axis given in Table II. In view of local variations in the degree of preferred orientation of crystals in the contact area and from one type of carbon to another, the observed variability of α is thus to be expected. Furthermore, the fact that small changes in contact force significantly alter the value of α may be taken as evidence that a relatively small number of single crystals is involved in contact. For if there were a large number, the small increment in this number occasioned by small changes in force would, on statistical grounds, have little effect on the average value of α for the contact as a whole.

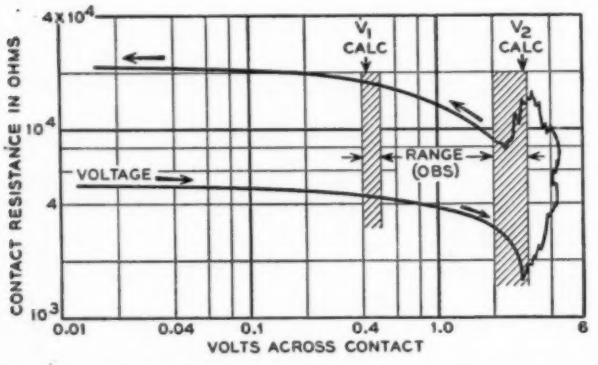

FIG. 7. A typical resistance-voltage characteristic for a single carbon contact showing the changes due to "burning" and the correspondence between observed and calculated values for the critical voltages.

When the force on a single carbon contact is held constant while the voltage across it is increased, the contact resistance decreases; and, if the contact drop is not more than about two volts, the change is reversible. This decrease in resistance is the result of Joule heating of the contact and the temperature rise T at the contact surface which causes the decrease is given in terms of contact voltage V by the expression[2]

$$8\int_0^T K\rho dT = V^2,$$

where K is the thermal conductivity of the contact material and ρ is its specific resistance. Disregarding the temperature coefficients of K and ρ, the temperature at the contact interface is

$$T = T_0 + V^2 8/K\rho,$$

where T_0 is the ambient temperature.

By use of this expression the value of α for a contact can be obtained from the voltage-resistance characteristic, and it has been found[1] that the values of α thus obtained agree with those measured directly when the contact temperature rise is set equal to $40V^2$. This fixes the effective value of the Wiedemann-Franz ratio for carbon $K\rho$ at 3.1×10^{-3} watt/ohm/°C, a value almost thirty times as great as that for bulk pyrolytic carbon. However, the value of $K\rho$ along the c axis of graphite is about 8×10^{-3} according to the data of Table II, while along the base plane of the crystal it is 1.6×10^{-4}. The value inferred from contact measurements thus lies between those characteristic of the two principal axes in graphite crystals, and it approaches that typical of the c axis. This may be taken as subsidiary evidence that the surfaces of roasted anthracite coal and pyrolytic carbon consist of graphite crystals preferentially oriented with their c axes normal to the surface.

The Burning Voltage

The change in resistance of a carbon contact with change in applied voltage is reversible only if a certain critical voltage V_2 is not exceeded, the value of V_2 lying, in general, between 2 and 3 volts. If the voltage exceeds this value, large and random fluctuations in contact resistance arise; and, on subsequent decrease of voltage, it is found that the contact resistance has permanently increased as much as fivefold from its initial value and that the temperature coefficient of resistance, measured by the slope of the resistance-voltage characteristic, is increased appreciably.[1] This phenomenon has been termed "burning" and, since it is not observed when the contact is thoroughly outgassed and sealed in vacuum, it has been presumed that it is due to oxidation of the contact material.

The resistance fluctuations occurring during "burning" give rise to a high level of contact noise, but this noise does not first set in at V_2. Rather, it is found that "burning noise" is first detectable at an appreciably lower critical voltage V_1 which ranges from about 0.4 to 0.5 volt. A typical characteristic for a contact, which illustrates the changes which occur during burning is given in Fig. 7.

In the course of the present study it has been found that at a temperature of 160°C in air the resistance of a film of pyrolytic carbon increases irreversibly. This increase is not detectable at lower temperatures and the time rate of change of resistance increases rapidly as the temperature is increased. Determination of the change in weight of the film has shown that the resistance increase is the result of oxidation which, therefore, is first detectable at 160°C.

By setting the contact temperature at this figure and employing the values of the Wiedemann-Franz ratio for pyrolytic carbon and graphite given in Table II, the contact voltages at which oxidation would first be appreciable have been computed and listed in Table III.

If burning is indeed due to actual oxidation of the contact surface, then, as is shown in this table, when the contact material is assumed to be homogeneous and to have the properties of bulk pyrolytic carbon, there is a single critical voltage which is lower than either of the two experimentally determined. On the other hand, if the contact interface is pictured as consisting of discrete graphitic crystals largely but not entirely oriented with their basal planes parallel to the surface, then two critical voltages are obtained.

As Table III shows, those crystals in the contact which are oriented with their basal planes perpendicular to the contact interface will reach a temperature sufficient to produce oxidation at 0.42 volt. The changes in contact geometry associated with this oxidation result in small fluctuations of resistance and evidence themselves as burning noise. The voltage at which this first occurs is in excellent agreement with the experimentally determined value for V_1, and the contact noise is at a low level since relatively few crystals are oriented with their basal planes perpendicular to the contact surface. As Table III shows, when the potential across the contact reaches about 3 volts, the entire contact area will undergo oxidation and the resistance fluctuations and noise at the contact will be large. The computed value of 2.94 volts for V_2 agrees well with the experimental value of this critical voltage, and "burning" may thus be identified as true oxidation. The correspondence between the experimental and calculated values of V_1 and V_2 is indicated in Fig. 7.

As has been described earlier, the degree of orientation of graphitic crystals in the surface of pyrolytic carbon is appreciably increased by oxidation. In view of this fact, the increases in contact resistance and in its temperature coefficient which occur when V_2 is exceeded and which are evident in Fig. 7 may be identified with increase in the degree of preferential crystal orientation. The magnitude of the Wiedemann-Franz ratio in the vicinity of the contact will also be increased by oxidation and hence the true difference between the values of α determined from resistance-voltage characteristics before and after burning will be larger than the calculated difference since at a given voltage increase in $K\rho$ corresponds to decrease in contact temperature.

TABLE III.

Contact material	T	T_0	$K\rho$	$V=(1.08\times10^{9}k\rho)^{\frac{1}{2}}$
Pyrolytic carbon	160°	25°	1.1×10^{-4}	0.35
Graphite basal plane	160°	25°	1.6×10^{-4}	0.42
Graphite c axis	160°	25°	8×10^{-4}	2.94

The Modulation Efficiency

While the electrical resistances of films of pyrolytic carbon and of contacts between carbon surfaces are thus related to the degree of preferred orientation of the surface crystals, this is not true of the modulation efficiencies of microphonic carbon contacts. This has already been indicated in Figs. 4 and 5 where the modulation efficiencies and the cell or contact resistances are given as functions of pyrolyzing temperature and methane concentration. Correlation of the cell resistance with the degree of orientation is apparent, but the modulation efficiencies of the specimens of microphonic material are clearly independent of the degree of orientation.

The modulation efficiency for contact between carbon films thicker than 3×10^{-5} cm decreases regularly with increase in either temperature or methane concentration in the pyrolyzing furnace, and hence with increase in the rate at which the carbon is deposited. To illustrate this, values of $\Delta R/R$ are given as functions of the rate of deposition in Fig. 8, the data there given representing measurements on a large number of specimens including all those prepared for the present study. Since change in the rate of deposition alters the average crystal size and distribution of crystal sizes this might be interpreted to indicate that the modulation efficiency is determined primarily by these factors. To make this evident, the average crystal sizes given in Table I have also been plotted in the figure.

The average crystal dimensions in pyrolytic carbon range from about 1×10^{-7} cm to about 5×10^{-7} cm and these dimensions are of the same order as the displacements which occur in the microphone. It is not improbable, therefore, that the roughness dealt with in microphonic carbon contacts may be individual graphitic crystals or oriented aggregates of but a few crystals.

Alteration in either average crystal size or in the distribution of sizes might be expected to produce corresponding changes in the geometrical nature of the

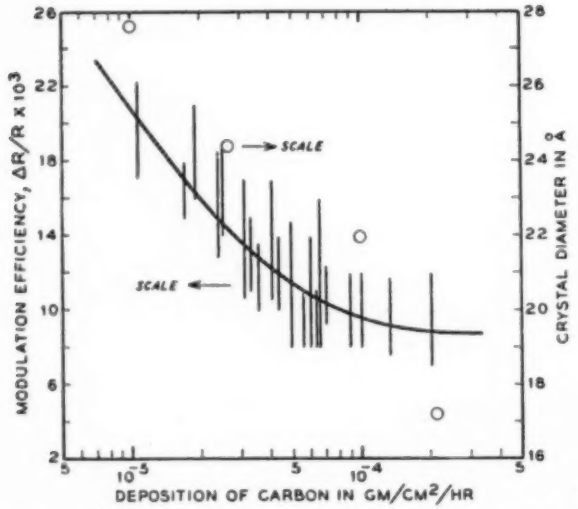

FIG. 8. The modulation efficiency of microphonic carbon contacts (lines) and the average size of the graphitic crystals (circles) as functions of the rate of carbon deposition.

carbon surface, such as change in the distribution in height of "roughnesses" above some arbitrary reference plane. The nature of this distribution in height has been inferred from measurements of force displacement characteristics of single contacts[15] which indicated that the average height of an individual "roughness" or projection is about 1×10^{-5} cm. The hills or projections are pictured as varying in height statistically in such a way that increments in displacement less than 1×10^{-7} cm will bring roughnesses in the two contact surfaces into coincidence, and such displacements are of the order of magnitude of those between individual contacting granules in the commercial transmitter. For, since the diaphragm displacement for normal speech is less than 1×10^{-5} cm and since experiment indicates at least ten contacts to be operating in series, the displacement of centers of adjacent contacting granules will be less than 1×10^{-6} cm.

Figure 9 is an electron micrograph obtained by transmission through a fragment of carbon film removed from the surface of a semispherical silica granule. Inspection of this micrograph, in which the scale is indicated, shows that it is readily possible to resolve roughnesses of about 1×10^{-6} cm. By analysis of this micrograph on a recording microdensitometer it has been found that the average size of the roughnesses is 8×10^{-6} cm, in excellent agreement with the value inferred from force-displacement characteristics of single carbon contacts. A corresponding analysis of "shadowgraphs" obtained from the same specimen of carbon yields the same value for the roughness index, a fact which promotes confidence in the results of either method.[12]

While the ultimate fine scale roughnesses important to microphonic action in carbon contacts may consist, as suggested above, of aggregates of but few crystallites, the geometry of pyrolytic carbon surfaces and the roughnesses apparent in electron micrographs are determined by the manner in which carbon is produced through pyrolysis of a gaseous hydrocarbon. The "droplet" mechanism for the formation of pyrolytic carbon referred to earlier provides an explanation for the geometry of carbon surfaces and studies of this geometry clearly indicate the correlation between roughness and microphonic sensitivity.[12]

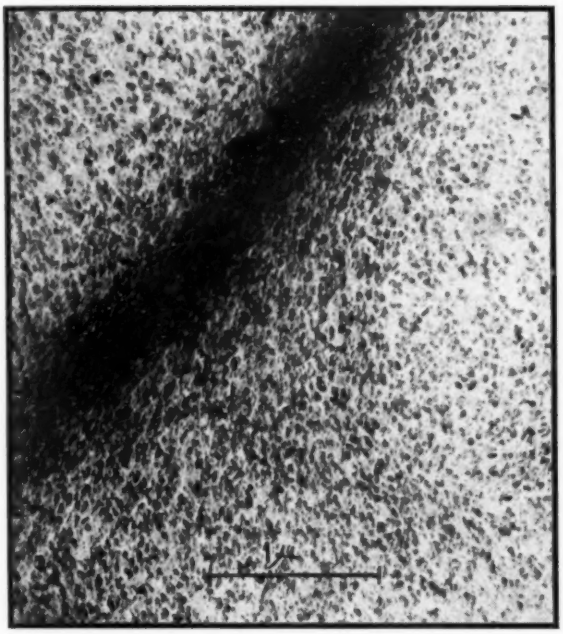

FIG. 9. Transmission electron micrograph of a pyrolytic carbon carbon film removed from a semispherical silica particle.

ACKNOWLEDGMENT

It is a pleasure to acknowledge the assistance of Mr. K. H. Storks, Mr. L. H. Germer, and Mr. A. H. White in the electron diffraction studies, and of Mr. A. C. Pfister in the physical measurements. Mr. F. S. Goucher, from his long experience in studies of the carbon microphone, furnished continual assistance in the interpretation of the data.

[15] F. S. Goucher, Bell Lab. Record (July, 1935).

Characteristics of an Elliptical Electromagnetic Resonant Cavity Operating in the TE_{111} Mode

T. P. Higgins and A. W. Straiton
The University of Texas, Austin, Texas

(Received March 23, 1953)

Equations and graphs are presented of the resonant wavelength and quality factor of elliptical resonant cavities operating in the TE_{111} mode. Both components of this mode are treated and distinctive characteristics of each are shown as a function of eccentricity of the cavity.

THE paper presents the results of numerical computations of the resonant frequency and quality factor of an elliptical cavity operating in the TE_{111} mode with small amounts of eccentricity.

The solutions for the cylindrical cavity resonator are expressed in terms of trigonometric and Bessel functions, but the solutions for elliptical cavity resonator must be expressed in terms of Mathieu functions.[1] Numerical tables of Mathieu functions are not feasible, and they cannot be integrated analytically. A large number of numerical calculations are required, therefore, to determine the results for a single set of dimensions.

The problem of elliptical waveguides has been treated by Chu,[2] whereas Kinzer and Wilson[3] have determined the resonant frequency for certain modes in the elliptical cavity and have derived an expression for the quality factor for one value of eccentricity for the TE_{011} mode.

The expressions for the electric and magnetic field components inside of the cavity can be derived directly from the equations for the components of the TE_{11} mode in an elliptical pipe as given by Stratton.[4] The cavity equations are as follows with sinusodial time variations assumed:

$$H_z=\frac{\mathrm{Br}^2c^2}{q^2}S_1(c,\cos\eta)J_1(c,\cosh\xi)\sin\left(\frac{\pi}{L}z\right), \quad (1)$$

$$H_\xi=\frac{iB\pi}{q_1L}S_1(c,\cos\eta)J_1{}^1(c,\cosh\xi)\cos\left(\frac{\pi}{L}z\right), \quad (2)$$

$$H_\eta=\frac{iB\pi}{q_1L}S_1{}^1(c,\cos\eta)J_1(c,\cosh\xi)\cos\left(\frac{\pi}{L}z\right), \quad (3)$$

$$E_\eta=\frac{-B2\pi}{q_1\lambda}S_1(c,\cos\eta)J_1{}^1(c,\cosh\xi)\sin\left(\frac{\pi}{L}z\right), \quad (4)$$

$$E=\frac{B2\pi}{q_1\lambda}S_1{}^1(c,\cosh\eta)J_1(c,\cosh\xi)\sin\left(\frac{\pi}{L}z\right), \quad (5)$$

$$E_z=0, \quad (6)$$

where $q_1=q(\cosh^2\xi-\cos^2\eta)^{\frac{1}{2}}$.

In a cylindrical cavity, the TE_{111} mode can always be regarded as a single-wave component if a proper choice of orientation is made. If the cylinder is deformed into an ellipse, two components of the TE_{111} mode must be considered, one with the electric field primarily in the direction of the major axis and known as the even mode and one component with the electric field primarily in the direction of the minor axis and known as odd mode. Equations (1) through (6) represent either of these modes according as the even or the odd Mathieu functions are used.

By setting the tangential component of the electric field in Eq. (4) equal to zero at the surfaces of the cavity,

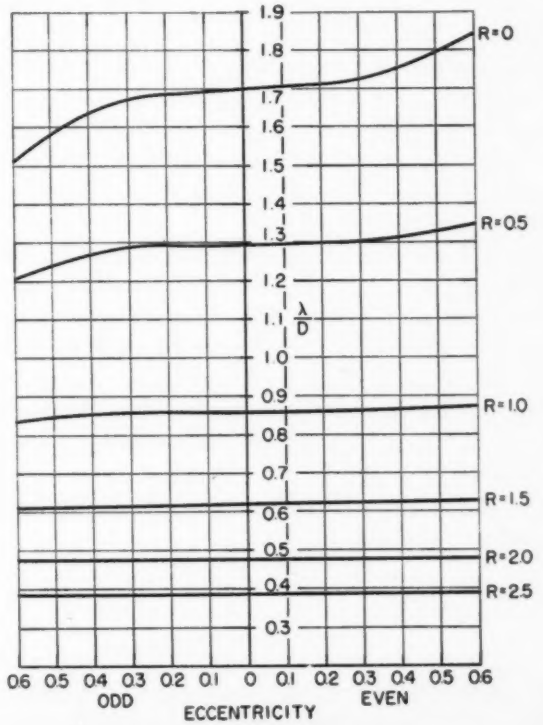

FIG. 1. Resonant wavelength.

[1] N. W. McLachlan, *Theory and Application of Mathieu Functions* (Oxford University Press, London, 1947).
[2] L. J. Chu, J. Appl. Phys. **9**, 583–591 (1938).
[3] J. P. Kinzer and I. G. Wilson, Bell System Tech. J. **26**, 410 (1947).
[4] J. A. Stratton, *Electromagnetic Theory* (McGraw-Hill Book Company, Inc., New York, 1947), p. 375.

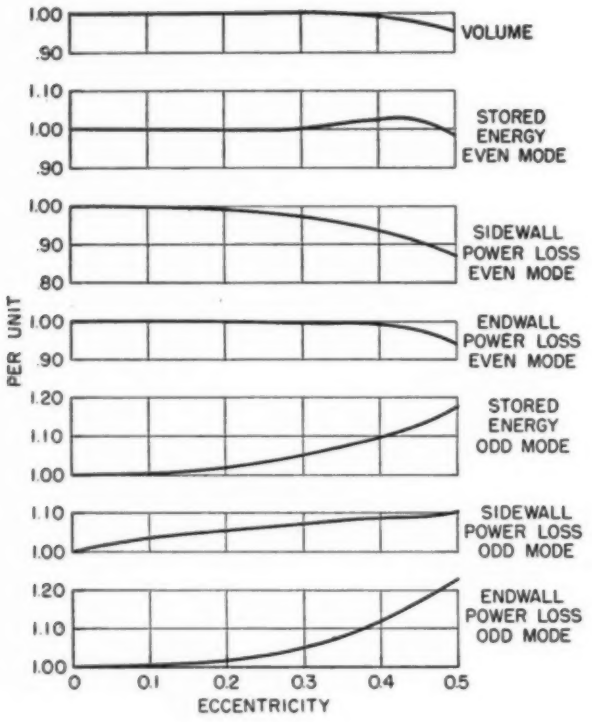

FIG. 2. Components of quality factor.

an expression for the wavelength of the resonant frequency is obtained as follows:

$$\lambda=\frac{1}{[(1/2L)^2+(r/2\pi q)^2]^{\frac{1}{2}}}. \tag{7}$$

A generalized curve for the wavelength is given in Fig. 1. This wavelength is the velocity of a plane wave in the dielectric material divided by the resonant frequency. In Fig. 1, the ratio of the wavelengths are shown for a number of values of the ratio, R, of the diameter to the length of the cylinder.

The odd mode evidences a decrease in resonant wavelength and the even mode shows an increase in resonant wavelength with an increase in eccentricity. These changes are greater for a cylinder which is long compared to the mean diameter than for one that is short.

The quality factor, Q, for each of the components may be obtained from the maximum energy stored in the electric or magnetic field during a cycle and the power loss in the wall and ends of the cavity by the following relationship:

$$Q=\frac{\text{angular frequency times average energy stored}}{\text{average power loss}}. \tag{8}$$

This assumes, of course, that the losses in the dielectric in the cavity are negligible compared to the loss in the metal enclosing the cavity.

The average stored electric energy, U, is given by

$$U=\int_{\text{vol}}\frac{\epsilon}{2}[|E_\eta^2|+|E_\xi^2|]dv \tag{9}$$

The average power loss, PL, is given by

$$PL=\frac{R_s}{2}\int_{\text{sidewall}}[|H_z^2|+|H_\eta^2|]ds + \frac{R_s}{2}\int_{\text{end walls}}\cdot[|H_\eta^2|+|H_\xi^2|]ds. \tag{10}$$

The angular Mathieu functions are expanded in trigonometric series with coefficients given in references 5 and 6. The square of these series are then integrated term by term. The radial functions are expanded in series of Bessel functions with coefficients given by references 5 and 6. The squares of these series are then integrated numerically using Simpson's one-third rule.

Using the error analysis method and the estimated error limits by the method of reference7, the error in the numerical evaluation of the quality factor, Q, is estimated to be less than 0.004 at eccentricities less than 0.3. The error is somewhat greater at larger values of eccentricity.

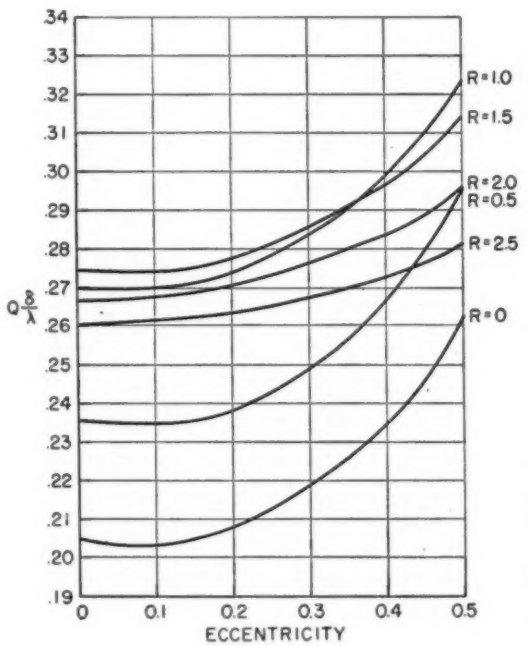

FIG. 3. Quality factor for odd mode.

[5] Stratton, Morse, Chu, and Hutner, *Elliptical Cylinder and Spheroidal Wave Functions* (John Wiley and Sons, Inc., New York, 1941).

[6] *Tables Relating to Mathieu Functions* (The Computation Laboratory, U. S. National Bureau of Standards, 1951).

[7] J. B. Scarborough, *Numerical Mathematical Analysis* (The Johns Hopkins University Press, Baltimore, 1938).

The relative effect of the losses in the side wall and ends is a function of the ratio of diameter to length of the cavity and of the eccentricity. The manner in which each of the factors changes with eccentricity is shown in Fig. 2. For plotting these curves, the same electric field intensity at the center of the cavity is chosen for each case.

The resultant quality factors for cavities of various shapes are shown in Fig. 3 for the odd component mode and in Fig. 4 for the even component mode. The quality factor is plotted in terms of the ratio of the depth of penetration of the wall metal to the resonant wavelength The quality factor shows little change for the even modes with eccentricities of less than 0.4 but a sharp decrease at betweeen 0.4 and 0.5. The quality factor of the odd component mode shows a sharp increase with eccentricity over the range of eccentricities considered.

Although it would be desirable for the sake of completeness to extend the calculations to larger eccentricities, the main interest in elliptical cavities lies in the small eccentricity region since the eccentricities associated with unavoidable deformations of cylindrical cavities fall in this region.

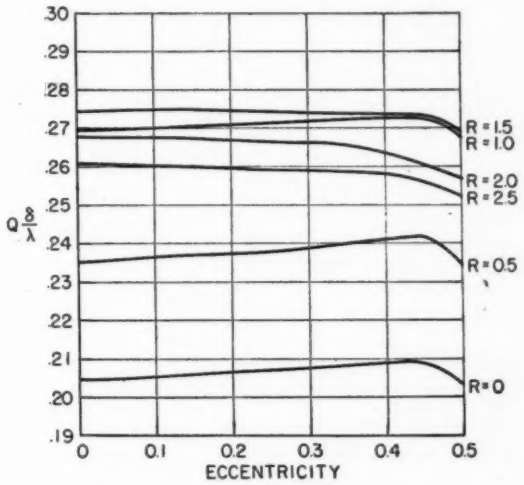

FIG. 4. Quality factor for even mode.

DEFINITION OF TERMS

(ξ, η, z)—elliptical coordinate system.

$S_1(c, \cos\eta)$ and $J_1(c, \cosh\xi)$—first-order angular and radial Mathieu functions where c is Stratton parameter.[4]

$S_1^1(c, \cos\eta)$ and $J_1^1(c, \cosh\xi)$—partial derivatives with respect to argument ξ or η.

r—value of $(c\cosh\xi)$ which is the smallest root of $J_1^1(c, \cosh\xi)=0$.

λ—wavelength of plane wave associated with resonant frequency.

D—mean diameter = perimeter/π.

L—length of cavity.

q—semifocal distance.

e—eccentricity.

δ—depth of penetration.

R_s—surface resistivity.

ϵ—permittivity.

B—amplitude constant.

R—ratio of the diameter to the length of the cylinder.

Electron Microscope Society Meeting

The eleventh annual meeting of the Electron Microscope Society of America will be held at the Pocono Manor Inn, Pocono Manor, Pennsylvania, Thursday through Saturday, November 5, 6, and 7, 1953. Programs with abstracts of papers to be presented will be available October 15 from A. R. T. Denues, Program Chairman, Sloan-Kettering Institute for Cancer Research, 444 East 68th Street, New York 21, New York. Local arrangements are being handled by Kenneth S. McCarty, Veterans Administration Hospital, 130 West Kingsbridge Road, Bronx, New York.

The Ferry Reduction and the Activation Energy for Viscous Flow

I. L. HOPKINS
Bell Telephone Laboratories, Inc., Murray Hill, New Jersey
(Received March 26, 1953)

The relationship proposed by Ferry and his co-workers for the effects of frequency and temperature on the dynamic properties of certain polymers is shown to lead to a method for calculating the activation energy of viscous flow from relaxation, creep, and dynamic test data, the results agreeing with those obtained in steady-state flow. The Ferry reduction explains, and is supported by, observed increases in dynamic modulus and viscosity with increasing temperature.

FERRY and his co-workers[1] have suggested a function for the reduction of dynamic data (and by implication any data dependent upon a distribution function of relaxation times) from any given temperature to any other temperature. This function has been shown by Ferry to agree quite well with observed behavior of polyisobutylene and polyvinyl acetate solutions, as well as of solid polyisobutylene.

The Ferry reduction postulates that as the temperature is changed, the stiffness of each relaxation mechanism is changed by T/T_0, where T is the new and T_0 the original temperature, and the whole spectrum is translated along the τ axis by a factor a, where a is some function of T_0 and T. A further slight refinement by Ferry, not treated here, takes into account the number of chain segments per unit volume by further multiplying $G(\tau)T/T_0$ by ρ/ρ_0, where ρ and ρ_0 are the final and initial densities.

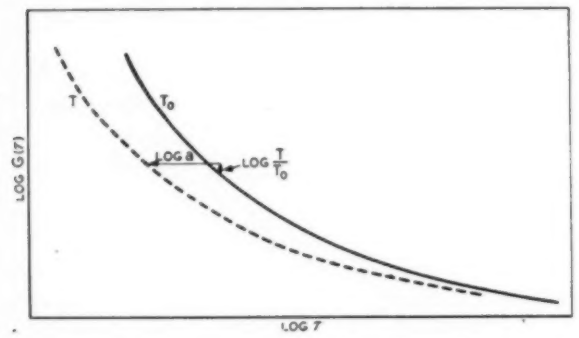

FIG. 1. Shift of relaxation spectrum with temperature. $T>T_0$.

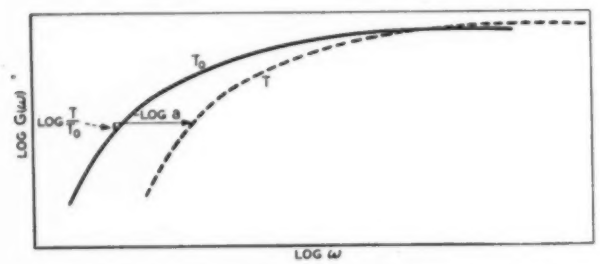

FIG. 2. Shift of dynamic modulus-frequency curve with temperature. $T>T_0$.

[1] Marvin, Fitzgerald, and Ferry, J. Appl. Phys. **21**, 197 (1950), and Ferry, Fitzgerald, Johnson, and Grandine, J. Appl. Phys. **22**, 717 (1951).

Let us consider the effect of such a change in the relaxation spectrum upon six functions, namely,

(1) $G(\omega)$, the dynamic stiffness,
(2) $\omega\eta(\omega)$, the dynamic viscosity-frequency product,
(3) $\eta(\omega)$, the dynamic viscosity,
(4) η, the steady-state viscosity,
(5) $\psi(t)$, the relaxation function, and
(6) $\varphi(t)$, the creep function.

Figures 1–6 show the effect of a change in temperature on the relaxation spectrum and the above functions, with the exception of the steady-state viscosity. It is obvious that if we have curves of any of these functions at various temperatures, the magnitude of a may be determined graphically.

An expression for a as a function of T and the activation energy of viscous flow may be obtained as follows. We have the expression

$$\log\eta=\log A+\frac{E}{2.3RT}=\log A+\frac{E}{4.57T}, \tag{1}$$

in the usual units. A is a proportionality factor and E is activation energy. Hence,

$$\log(\eta/\eta_0)=\frac{E}{4.57}\left(\frac{1}{T}-\frac{1}{T_0}\right)$$

$$=\log\left(a\frac{T}{T_0}\right) \text{ (from Ferry)}, \tag{2}$$

whence

$$\log a=-\frac{E}{4.57T_0}\left(\frac{T-T_0}{T}\right)-\log\frac{T}{T_0}, \tag{3}$$

or if a is known,

$$E=-4.57\frac{T_0T}{T-T_0}\log\left(a\frac{T}{T_0}\right). \tag{4}$$

Since a can be determined graphically from curves as in Figs. 2–6, we have a way for finding the activation energy of viscous flow from dynamic, relaxation, creep, and steady-state viscosity measurements, in which the energy should not appear to be a function of frequency or time.

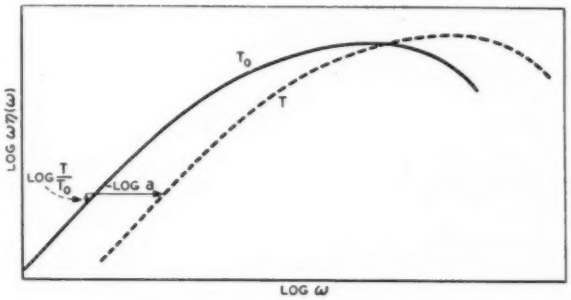

FIG. 3. Shift of the curve of dynamic viscosity-frequency product against frequency with temperature. $T>T_0$.

Referring to Figs. 2 and 4, it may be seen that it is possible to find the dynamic shear modulus and viscosity to *increase* as the temperature is raised, provided only that the slopes of the curves of these functions against frequency be less than certain values. That this may occur in nature is demonstrated in Fig. 7, which shows results of dynamic tests on silicone gum. Figure 8

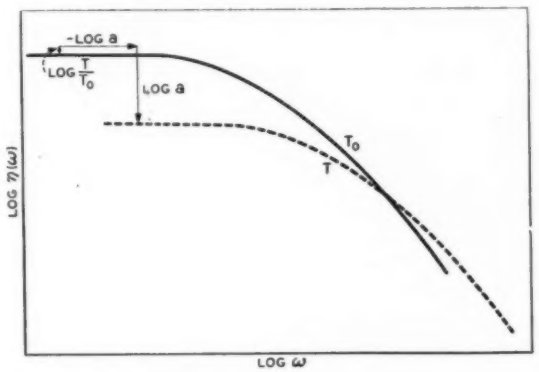

FIG. 4. Shift of dynamic viscosity-frequency curve with temperature. $T>T_0$.

shows that, in the frequency range covered by the experiments, a filled polysiloxane does not manifest this effect, but it seems that if the frequency could have been increased somewhat, the effect would have appeared.

Leaderman and Smith[2] suggested that for polyisobutylene, $\log\eta$ varies linearly with $1/T^2$. Then

$$\log(\eta/\eta_0)=K\left(\frac{1}{T^2}-\frac{1}{T_0^2}\right), \tag{5}$$

where K has the dimensions of (temperature)^2. Comparing this equation with Eq. (2) and eliminating $\log(\eta/\eta_0)$,

$$E=4.57K\left(\frac{1}{T}+\frac{1}{T_0}\right). \tag{6}$$

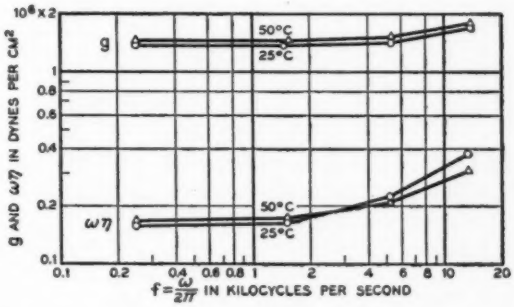

FIG. 7. Dynamic shear modulus and viscosity-frequency product of polysiloxane gum as functions of frequency at 25°C and 50°C.

If the difference between T_0 and T is small, the equation reduces to

$$E\approx 4.57K\left(\frac{1}{T_0}+\frac{1}{T}\right)\approx 9.14\frac{K}{T_0}. \tag{7}$$

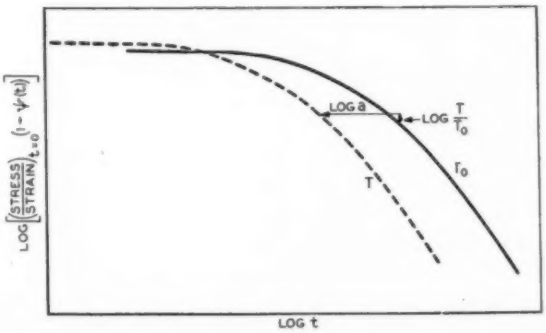

FIG. 5. Shift of relaxation-time curve with temperature. $T>T_0$.

[2] H. Leaderman and R. G. Smith, Phys. Rev. 81, 303 (1951).

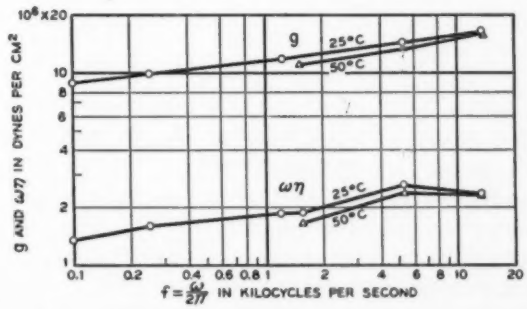

FIG. 8. Dynamic shear modulus and viscosity-frequency product of filled solid polysiloxane as functions of frequency at 25°C and 50°C.

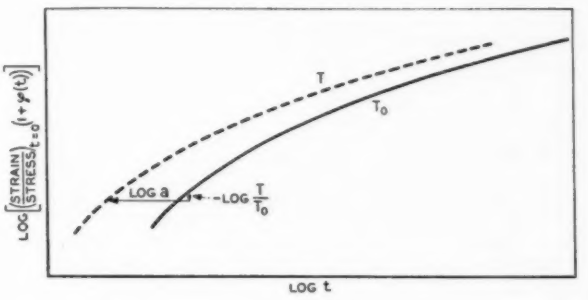

FIG. 6. Shift of creep-time curve with temperature. $T>T_0$.

TABLE I. Activation energy for viscous flow of polyisobutylene.

Molecular wt $M\eta$	Method of testing	Source of data	Time range, seconds	Temp. range C°	E (kcal/mole) Calculated from test data	E (kcal/mole) Calculated from Leaderman and Smith equation
1660	Steady state	Heiss	—	15 to 50	15.3	16
3350	Dynamic stiffness	McSkimin	10^{-5}	15 to 25	16	17
				25 to 35	17	16
				35 to 45	19	16
				45 to 55	16	15
3350	Dynamic viscosity	McSkimin	10^{-5}	15 to 25	16	17
				25 to 35	18	16
				35 to 45	18	16
				45 to 55	17	15
3350	Dynamic stiffness	Hopkins	10^{-3}	25 to 50	12.2	16
3350	Dynamic viscosity	Hopkins	10^{-3}	25 to 50	13.4	16
11 200 to >1 000 000	Steady state	Fox and Flory	—	0	19.3	18
				50	13.7	15
				100	13.2	13
				150	12.0	12
				200	10.6	10
				217	10.3	10
6 600 000	Relaxation	Andrews and Tobolsky	10^{2}–10^{4}	−50 to −30	24	21
				−10 to 30	22	18
				30 to 50	21	16
				50 to 70	17	15
				70 to 100	18	14
				100 to 130	15	13

This form of the equation was used with the Fox and Flory[3] steady-state data of their Table VI; from these data the mean value of K was found to be 0.541×10^{6} (°C)[2]. Then,

$$E=2470\left(\frac{1}{T}+\frac{1}{T_0}\right)\text{ kcal/mole.} \qquad (8)$$

Table I presents the activation energies for viscous flow of polyisobutylenes of various molecular weights, tested in various ways at various temperatures by different experimenters. The steady-state viscosity values obtained by Mr. J. H. Heiss of these Laboratories were as follows:

Temp. °C	Viscosity, poises
25.0	39.64
39.9	11.38

from which, by Eq. (1), $E=15.3$ kcal/mole.

The dynamic measurements by McSkimin were partly given, in a different form, in reference 4, in which the polyisobutylene was referred to as Polymer C of molecular weight $M\eta=4550$. We have here chosen the $M\eta$ value of 3350 as more applicable, although the difference is trivial in view of the insensitivity of activation energy to molecular weight. Differences between melt and dilute solution viscosities of this and some other polymers are discussed by Baker and Heiss.[5]

Measurements of the dynamic shear properties of this polymer at 25°C and 50°C at 266 and 1600 cycles per second were made by the author, using the tuning fork technique described in reference 6 with the tuning

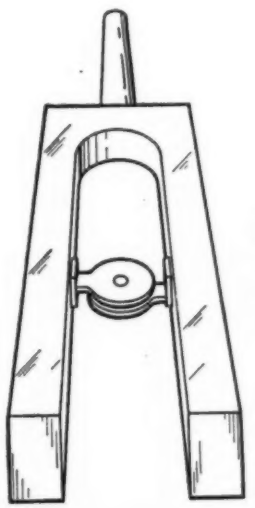

FIG. 9. Tuning fork for measurement of dynamic shear properties of viscous liquids. Area of disks, 1 sq cm. Separation of disks, 0.05 cm.

[3] T. G. Fox, Jr., and P. J. Flory, J. Am. Chem. Soc. **70**, 2384 (1948).
[4] H. J. McSkimin, J. Acoust. Soc. Am. **24**, 355 (1952).
[5] W. O. Baker and J. H. Heiss, Bell System Tech. J. **31**, 306 (1952).
[6] I. L. Hopkins, Trans. Am. Soc. Mech. Engrs. **73**, 195 (1951).

fork equipped as in Fig. 9. The data are given in Fig. 10.

The data from Fox and Flory[3] are taken directly from their Table VI.

The Andrews and Tobolsky[7] relaxation plot in their Fig. 2 has a linear ordinate, differing in this from our Fig. 5. The ordinate of each curve has, however, already been multiplied by $298/T$, rendering the vertical step in our Fig. 5 unnecessary. The values of log$a$ were then

TABLE II. Summary of data.

Polymer	Method and temp. range	E (kcal/mole) Calculated from test data	E (kcal/mole) Calculated from Leaderman and Smith equation
	Butyl rubber and polyisobutylene		
Butyl rubber M169A Polyisobutylene Polyisobutylene	Dynamic, 25°C to 50°C Dynamic, 15°C to 55°C Steady-state flow, 15°C to 50°C	12–19	15–17
Polyisobutylene	Relaxation (Andrews and Tobolsky), −50°C to 130°C	15–24	12–22
Butyl rubber M169A	Relaxation (Hopkins), 25°C to 50°C	24	16
Butyl rubber	Relaxation (Tobolsky *et al.*), 100°C to 130°C	30	13
	Raw and vulcanized Hevea		
Raw Hevea	Steady-state shear (Smallwood), 80°C–140°C	10.2	13
Vulcanized Hevea	Dynamic (Hopkins), 25°C–50°C	12	16
Vulcanized Hevea	Relaxation (Mooney *et al.*, "transient"), 35°C–70°C	≈15	15
Vulcanized Hevea	Relaxation (Mooney *et al.*, "steady"), 35°C–70°C	27	15
Vulcanized Hevea	Relaxation (Tobolsky *et al.*), 100°C–130°C	30	13
Vulcanized Hevea	Relaxation (Hopkins), 25°C–50°C	19–24	16

obtained by simple horizontal measurements between curves, regardless of the ordinate function.

In the last two columns, the activation energies calculated from the data mentioned above are compared with those calculated for the temperatures or temperature ranges involved by means of the Leaderman and Smith relation, Eqs. (7) and (8).

TABLE III. Butyl Rubber M169A.

	Parts by weight
GR-I	100
Tuads	1.5
Captax	1.0
Agerite	0.5
Zinc oxide	5
Stearic acid	1
Sulfur	2.5
Total	111.5

In Table II are given first a summary of the findings of Table I, as well as some additional data for Butyl rubber. The compounding of Butyl rubber M169A is given in Table III and the dynamic tests on it are described in reference 6. The relaxation data for M169A

[7] R. D. Andrews and A. V. Tobolsky, J. Polymer Sci. 7, 221 (1951).

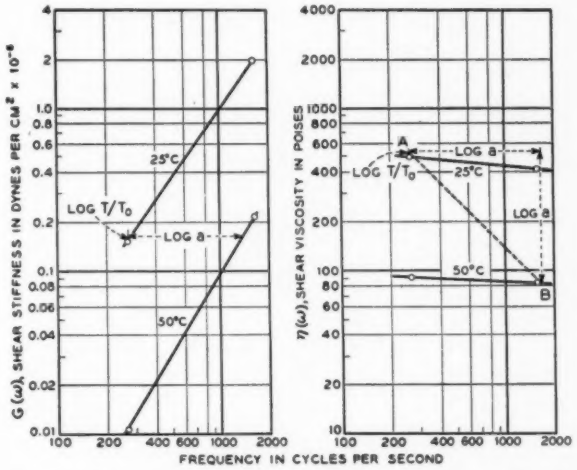

FIG. 10. Dynamic shear stiffness and viscosity of polyisobutylene liquid $M\eta=3550$, as functions of frequency at 25°C and 50°C. Line AB is a 45° construction line starting at A and intersecting the 50°C line at B. The plots of $G(\omega)$ and $\eta(\omega)$ give $a=0.192$ and 0.154, respectively.

are given in Fig. 11, and here, as with the Andrews and Tobolsky data, the T/T_0 step is not necessary, in this case because the ordinate is the ratio of load to original load. These tests were in compression, and each curve is the average of two tests, one at 25 percent and the other at 50 percent strain. The value for E of Tobolsky *et al.*,[8] ≈30 kcal/mole, is as given in the reference.

The second part of this table contains data on raw and vulcanized Hevea rubbers. Smallwood's[9] value is taken directly from his article. The dynamic data on vulcanized Hevea are given in Fig. 12. These were obtained according to reference 6, the rubber compound being that described by Flory, Rabjohn, and Shaffer,[10] with the recipe given in Table IV. The Mooney, Wolstenholme, and Villars[11] values are given in their Tables II and III. The relaxation data on vulcanized Hevea obtained by the author are presented in Fig. 13, with the

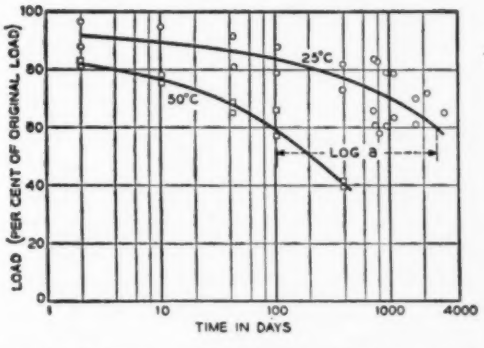

FIG. 11. Relaxation of M169A Butyl Rubber at 25°C and 50°C. $a=0.038$.

[8] Tobolsky, Prettyman, and Dillon, J. Appl. Phys. 15, 380 (1944).

[9] H. M. Smallwood, J. Appl. Phys. 8, 505 (1937).

[10] Flory, Rabjohn, and Shaffer, J. Polymer Sci. 4, 225 (1949).

[11] Mooney, Wolstenholme, and Villars, J. Appl. Phys. 15, 324 (1944).

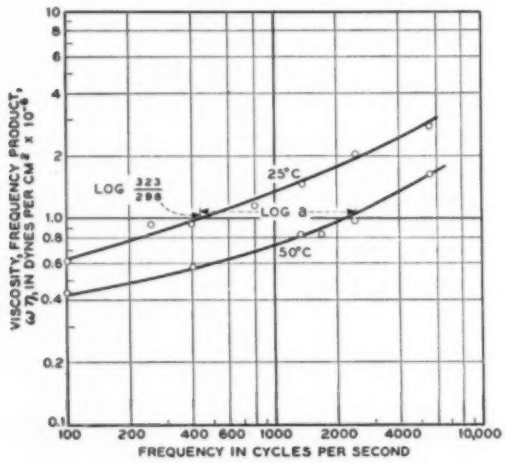

FIG. 12. Dynamic shear viscosity—frequency product of vulcanized Hevea (reference 10) as function of frequency at 25°C and 50°C. $a=0.179$.

construction by which a is obtained. The rubber compound is given in Table V.

DISCUSSION

The variation of dynamic shear modulus and viscosity with temperature appear fully as satisfactory as the steady-state viscosity variation, as the basis for calculation of activation energy for viscous flow. Over a wide range of temperatures and molecular weights, polyisobutylene appears to behave in accordance with Ferry's assumptions, and serious discrepancies begin to appear only where rupture rather than mere dislocation comes into play, or at frequencies or temperatures where all important mechanisms are not similarly affected by temperature changes. The dynamic tests on polymers of all molecular weights, including cross-linked Butyl rubber, and the relaxation data on polyisobutylene of 6 600 000 molecular weight, give activation energies varying from 12 to 24 kcal/mole depending on the temperature, in approximate accordance with Leaderman and Smith's equation for steady-state viscosity. The values of E for relaxation of Butyl rubbers, 24 to 30 kcal/mole, are higher than this equation would indicate.

TABLE IV. Hevea compound.
(Flory, Rabjohn, and Shaffer)

	Parts by weight
Pale crepe	100
Sulfur	2.5
Mercaptobenzothiazole	0.75
Stearic acid	1.0
Zinc oxide	0.5
	104.75

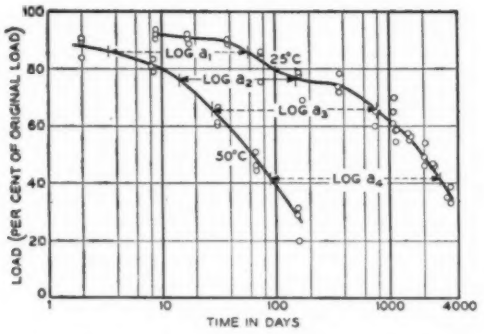

FIG. 13. Relaxation of vulcanized natural rubber at 25°C and 50°C. $a_1=0.062$; $a_2=0.100$; $a_3=0.033$; $a_4=0.032$.

With Hevea the activation energies are more definitely spread into groups. First, raw Hevea in shear, cross-linked Hevea in dynamic tests, and Mooney's[11] "transient" relaxation of cross-linked Hevea result in activation energies of 10 to 15 kcal. These values are in accordance with Leaderman and Smith's equation for polyisobutylene. Second, Mooney's "steady" relaxation, relaxation as measured by Hopkins and by Tobolsky, Prettyman, and Dillon,[8] all working with cross-linked Hevea, resulted in energies of about 25 to 30 kcal/mole. In the first case, the significant motions all are such as to involve movements only of greater or lesser parts of molecular chains past each other; in the second, the rupture of primary valence bonds is involved.

TABLE V. Hevea compound used in relaxation study (Fig. 13).

	Parts by weight
Smoked sheet	75.00
Sulfur	1.50
Zinc oxide	3.00
FT black	3.00
Whiting	13.25
Stearic acid	0.25
Neozone A	0.50
Mineral rubber	3.00
808 Accelerator	0.50
	100.00

SUMMARY

It appears that in cases where the Ferry assumptions are valid, the activation energy for viscous flow may be found equally well from measurements of dynamic stiffness and viscosity, creep, relaxation, or steady-state flow. Polyisobutylene shows remarkable conformity to this concept, and the behavior of raw Hevea, with the relatively scant data at hand, agrees also. The limits of validity of the concept appear to be at the point where either kinetic-theory elasticity or chain slippage without rupture, or both, give way to quasi-crystalline structure and bond rupture, respectively.

A "Double" Camera for Electron Diffraction

SHIGETO YAMAGUCHI
Scientific Research Institute, Ltd., Hongo, Tokyo, Japan
(Received March 30, 1953)

The method of a double camera for electron diffraction here described consists in taking two diffraction patterns simultaneously so that the wavelength of electrons applied to an "unknown" is exactly to that for the reference.

INTRODUCTION

IN usual practice with a conventional electron diffraction set, the reference material is observed immediately after a sample to be examined has been observed. This procedure does not only give rise to prolongation of observation, but also it does not preclude the possibility that the wavelength of electrons applied in the observation of the sample may have differed from that for the reference. It is possible by a "double" camera to deal with a larger number of specimen in a shorter space of time than in the usual case of one camera.

EXPERIMENTAL PROCEDURE AND RESULTS

Two diffraction apparatuses were connected to a common terminal of a high-tension source supplying the two (see Fig. 1). In this way electrons in the two apparatuses were always accelerated by one and the same potential

TABLE I. D, diameters of diffraction rings from a gold foil observed in apparatus (a); D', diameters of diffraction rings observed in apparatus (b); D'/D, ratio between these diameters. The table confirms that the wavelength of electrons in apparatus (a) is the same as that in apparatus (b).

D(mm)	hkl	D'(mm)	D'/D
7.27	(111)	11.03	1.52
8.39	(200)	12.74	1.52
11.86	(220)	18.01	1.518$_5$
13.91	(311)	21.12	1.518
18.28	(331)	27.75	1.518
			Mean 1.518

TABLE II. D_1, diameters of diffraction rings from a gold foil observed in apparatus (a); d_1, spacings of gold crystal determined by x-ray;[a] D_2, diameters of diffraction rings from magnesium oxide observed in apparatus (b); d_2, spacings determined with D_1, d_1, D_2, and Eq. (2); d_x, spacings of magnesium oxide crystal determined by x-ray. The table shows that the spacings of magnesium oxide determined in the present study are checked with those by x-ray.

D_1(mm)	d_1(A)	hkl	D_2(mm)	d_2(A)	d_x[a]	d_x[b]
6.73	2.35	(111)	9.92	2.42	2.42	2.427
7.79	2.03	(200)	11.42	2.102	2.10	2.102
10.99	1.439	(220)	16.17	1.485	1.485	1.486
12.89	1.227	(311)	18.97	1.266	1.266	1.267
16.92	0.935	(331)	24.93	0.963	0.963	0.964

[a] Hanawalt, Rinn, and Frevel, Ind. Eng. Chem., Anal. Ed. 10, 457 (1938).
[b] R. W. G. Wyckoff, *Crystal Structures* (Interscience Publishers, Inc., New York, 1948), Sec. I.

The diffraction pattern of a thin gold foil was observed in apparatus (a) with camera length L_1(150 mm) and that of a gold foil was observed in apparatus (b) with camera length L_2(227 mm). These two observations were carried out simultaneously by means of a hook-up shown in Fig. 1. Table I shows the diameters of diffraction rings taken by apparatus (a) and (b) and the ratio between them. The mean value of these ratios coincides with the ratio existing between the camera lengths of apparatus (b) and (a) i.e.,

$$L_2/L_1=1.51,\ D'/D=1.518=C, \qquad (1)$$

where D' indicates the diameters of diffraction rings observed by apparatus (b) and D indicates those observed by (a). This is a constant independent of wave-

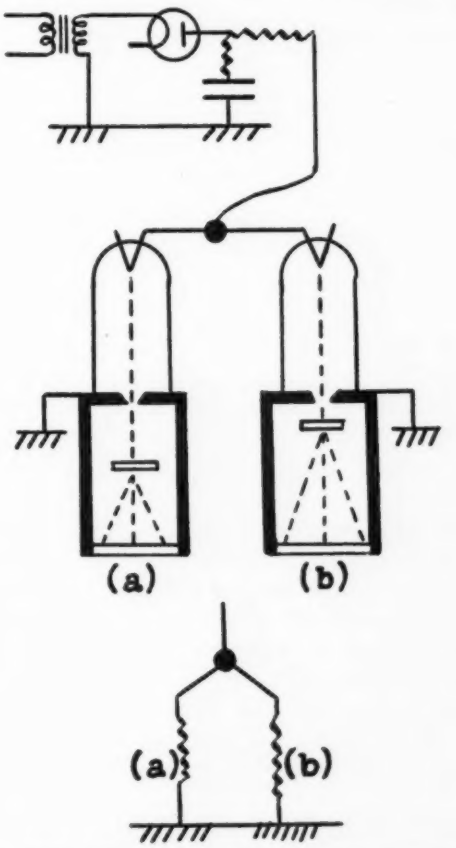

FIG. 1. Here two diffraction apparatus are connected to a common terminal of a high-tension supply. Electrons in the two apparatus are accelerated by one and the same potential. Electron current, about 0.01 ma. Driving potential, about 50 kv.

length applied during observation. The value given by Eq. (1) is defined as the camera constant (C) in the present study. The fact recognized in Eq. (1), that the ratio existing between the diameters of diffraction rings is equal to that existing between the camera lengths, confirms that the wavelength of electrons in apparatus (a) is the same as that in apparatus (b).

The diffraction pattern of a gold foil was observed with apparatus (a), and simultaneously that of magnesium oxide smoke was observed with apparatus (b). The results of observation are shown in Table II, where D_1 indicates the diameters of diffraction rings of gold foil and D_2 indicates those of magnesium oxide. According to the equation

$$d_2 \times D_2/d_1 \times D_1 = C, \quad (2)$$

the spacings d_2 of magnesium oxide crystal can be calculated from d_1 of gold crystal determined by x-ray diffraction, where C is the camera constant defined in Eq. (1). The spacings of magnesium oxide crystal derived in this way are shown in Table II. They are in agreement with those of magnesium oxide crystal determined by x-ray.

DISCUSSION

The method of "double" camera described here is a useful one in case a drastic change of driving potential of electrons takes place accidentally so that it is impossible to stabilize it by a usual method.

There are several factors influencing the precision of measurement of spacings in electron diffraction: (1) measurement of diffraction ring radii, (2) variation in specimen-plate distance, (3) effect of ring width (crystal size), (4) variation in wavelength, and (5) refraction. Under a given condition, factor (4) can have a larger influence on precise measurement of spacings than factor (1) in an ordinary transmission pattern of crystallites in which factors (2) and (5) are negligible. This is the case where electrons are accelerated by a comparatively unstable voltage, i.e., where the variation of accelerating voltage is larger than 670 volts in 5×10^4 volts.* The "double" camera is useful in this case.

I wish to express my thanks to Dr. T. Hori (Shimadzu Seisakusho Ltd., Kyoto, Japan) and to the referee of this journal for their aid in carrying out the present study.

* Using the relations $\lambda=(150/V)^{\frac{1}{2}}$ and $d=L\lambda/R$, where R indicates radius of diffraction ring and V indicates accelerating voltage, estimate of $\delta d/d$ (relative error in spacing determination) can be obtained. For factor (1) $\delta d/d=-\delta R/R$. For factor (4) $\delta d/d=-\delta V/2V$. If $V=5\times10^4$ volts, $R=15$ mm, $d=1.5$A, the uncertainty δR in R is 0.1 mm and the variation δV in V is 670 volts, then $\delta d=-0.01$A for (1) and $\delta d=-0.01$A for (4). This means that the "double" camera might not be useful when high-voltage source is stabilized satisfactorily, i.e., voltage variation is lower than 670 volts in 5×10^4 volts.

JOURNAL OF APPLIED PHYSICS VOLUME 24, NUMBER 10 OCTOBER, 1953

A Note on the Analysis of First-Order Glow Curves

LEONARD I. GROSSWEINER
Chemistry Division, Argonne National Laboratory, Lemont, Illinois
(Received May 11, 1953)

Simple equations are developed which permit the calculation of the trap depth and frequency factor of first-order glow curves from the temperatures of the peak and the half-height. The equation for the trap depth does not depend explicitly on the frequency factor or the heating rate and is accurate to 5 percent over a wide range. Application is made to theoretical glow curves and to an experimental glow curve obtained from the thermoluminescence of ice.

THE analysis of some experimental data on thermoluminescence in ice[1] required the estimation of the trap depth and frequency factor of the individual glow peaks to sufficient accuracy that the data could be checked against the theoretical equation of the glow curve. Equations for these parameters in terms of the temperatures of the glow peak maximum and half-height were derived, and it is believed that their convenience and accuracy is such that they are of general utility.

It was shown by Randall and Wilkins[2] that the equation of the first-order glow curve is

$$I=-C(dn/dt)=Cn_0 s \times\exp\left[-\int_0^T (s/\beta)e^{-E/kT}dT\right]e^{-E/kT}. \quad (1)$$

This expression is based on the decay process,

$$I=-C(dn/dt)=Cnse^{-E/kT}, \quad (2)$$

where n is the number of electrons in traps of depth E at time t, s is a frequency factor, β is the rate of warming, and C is a geometry constant.

Let T^* be the temperature at a glow peak maximum and T' be the temperature at which the low-temperature

[1] E. C. Avery and L. I. Grossweiner, J. Chem. Phys. **21**, 372 (1953).
[2] J. T. Randall and M. H. F. Wilkins, Proc. Roy. Soc. (London) **A184**, 366 (1945).

side of the glow peak attains one-half of its maximum intensity. We have from Eq. (1)

$$\tfrac{1}{2}=\exp[-(E/k)(1/T'-1/T^*)]$$
$$\times\exp\left[-\int_{T'}^{T^*}(s/\beta)e^{-E/kT}dT\right]. \quad (3)$$

By a substitution and integration by parts it may be shown that

$$\int_{T'}^{T^*}e^{-E/kT}dT=T^*e^{-E/kT^*}-T'e^{-E/kT'}$$
$$+(E/k)[Ei(-E/kT^*)-Ei(-E/kT')], \quad (4)$$

where the exponential integral, $Ei(-x)$, is defined as

$$-Ei(-x)=\int_x^\infty(e^{-u}/u)du. \quad (5)$$

For values of E/kT greater than 20, less than 10 percent error is made by dropping terms after the second in the asymptotic expansion,

$$-Ei(-x)=e^{-x}(1/x-1/x^2+2!/x^3-3!/x^4+\cdots). \quad (6)$$

TABLE I. Calculation of trap depths of theoretical glow curves from the temperatures at the maximum and half-height.

E (ev)	s/β ($^\circ K^{-1}$)	T^* ($^\circ K$)	T' ($^\circ K$)	E(calc) (ev)
0.20	10^7	128.8	119.0	0.20
0.40	10^7	249.5	230.2	0.39
0.80	10^7	482	446	0.78
0.40	10^{11}	171.2	162.5	0.42
0.80	10^{11}	334.5	317.0	0.79
0.40	10^{16}	122.2	117.7	0.42
0.80	10^{16}	240.5	231.2	0.78

Therefore, from Eqs. (4) and (6) one has

$$\int_{T'}^{T^*}e^{-E/kT}dT$$
$$\cong[T^*e^{-E/kT^*}/(E/kT^*)]-[T'e^{-E/kT'}/(E/kT')]. \quad (7)$$

Substitution of Eq. (7) into Eq. (3) gives:

$$(E/k)(1/T'-1/T^*)-0.693=[skT^{*2}e^{-E/kT^*}/E\beta]$$
$$\times[1-(T'/T^*)^2\exp\{-(E/k)(1/T'-1/T)^*\}]. \quad (8)$$

If Eq. (2) is differentiated with respect to T, at the glow peak maximum we have

$$E/k=(s/\beta)e^{-E/kT^*}T^{*2}. \quad (9)$$

Thus the coefficient of the right side of Eq. (8) is unity. Further, the exponential term in the right side of (8) is approximately $e^{-1.693}$, and the factor $(T'/T^*)^2$ may be neglected as it affects the value for E by less than two percent where $s/\beta>10^7$. With these approximations we have as the solution to (8)

$$E=1.51kT^*T'/(T^*-T'). \quad (10)$$

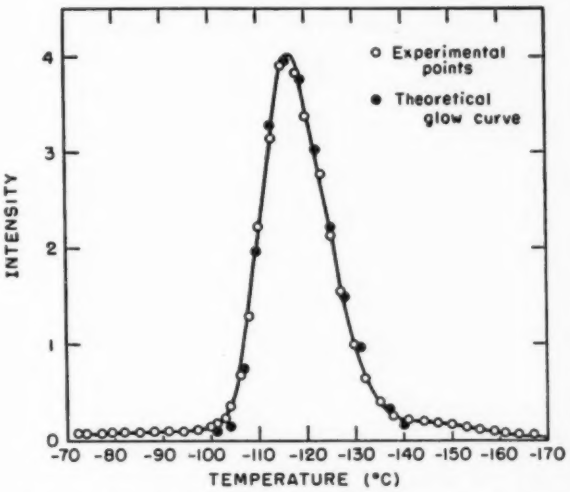

FIG. 1. Comparison of theoretical glow curve using values of E and s from derived equations and experimental data.

This equation for the trap depth does not depend explicitly on s and β. When complex glow curves which cover a wide temperature range are being analyzed, it is sufficient that values of s and β be constant over each glow peak. Equation (10) was checked against theoretical glow curves plotted using Eq. (1) for various values of E and s/β and was found to be accurate to better than ±5 percent (Table I). The mean lifetime for decay at the glow peak may be estimated from Eqs. (9) and (10) giving

$$-n^*/(dn/dt)^*=\frac{2}{3}\frac{T^*(T^*-T')}{T'\beta}. \quad (11)$$

The frequency factor, s, may be calculated from Eqs. (2) and (11).

The usefulness of these equations was exemplified by application to a glow curve obtained from x-ray excited ice which was prepared from triply-distilled water of low oxygen and organic matter content[3] by slow freezing. The sample, a one-inch cylinder, was irradiated with 50 kilovolt tungsten x-rays filtered by 100 mg/cm^2 of aluminum and received a dosage of 35 kiloroentgens at -183°C. The ice was subsequently warmed at a rate of 2.5°C/min and the luminescence detected by a 1P28 photomultiplier using scintillation techniques. Values for T^* and T' of 157.2°K and 147.6° K, respectively, were obtained from the experimental curve, and using Eqs. (2), (10), and (11), values for E and s of 0.31 ev and 5.5×10^7 sec^{-1}, respectively, were calculated. The theoretical glow curve plotted from these values shows good agreement with the experimental data (Fig. 1).

[3] E. J. Hart, J. Am. Chem. Soc. 73, 69 (1951).

Measurement of the Heat of Activation for Sodium Ion Diffusion in Glass

R. KAMEL
Cairo University, Giza, Egypt
(Received April 2, 1953)*

Internal friction peaks resulting from sodium ion diffusion in three kinds of soda glasses have been observed in the temperature range 100° to 200°C for transverse and torsional frequencies between 20 to 400 cps. The heat of activation for sodium ion diffusion was found to range between 17 000–21 000 cal/mole and might probably be slightly dependent on the sodium content. The results obtained were confirmed by electrical resistivity measurements. For quartz glass and for soda glass having Na_2O content less than 4 percent, the internal friction peak of the type discussed here could not be noticed, thus indicating that below a minimum Na_2O content of about 4 percent, ionic sodium diffusion does not contribute to the anelastic behavior.

INTRODUCTION

IN a previous work[1] by the author on transverse internal friction of several solids, the relaxation curve for glass showed two peaks in the frequency range 10–100 cps. One of these peaks could be identified as resulting from thermoelastic currents, but no comment was made at that time on the second peak. An extention of the range of frequencies up to 1500 cps confirmed[2] more definitely the existence of this and other absorption regions in the relaxation spectrum. Ionic diffusion was suspected as a possible origin, but further investigations were necessary to elucidate that point. It is worth while to mention that an internal friction band in the low subsonic spectrum of glass was first reported as early as 1914 by Guye and Vasileff,[3] though they were unaware of its true cause. But it was not before 1941 that Rötger[4] interpreted this band as an ionic relaxation phenomenon. He based his argument on the fact that the activation energy for the temperature shift of internal friction peak with the vibration frequency had approximately the same activation energy as the flow of electric charge through glass. The high mobility of sodium ions relative to other ions present in the glass network as estimated by Lengyel[5] provides a reasonable cause for relaxation by sodium ion diffusion.

Experimenting on slow torsional vibrations Fitzgerald[6] has recently reported an internal friction peak in the relaxation curve for glass resulting from sodium ion diffusion. The temperature of maximum internal friction was shown to vary with the frequency of vibration with an activation energy of about 16 000 cal/mole for chilled glass and 20 000 cal/mole for annealed glass.

It is the aim of the present work to investigate in particular the effect of sodium content on the heat of activation for the diffusion process.

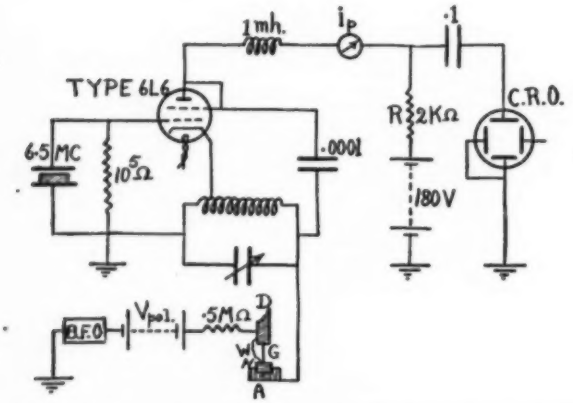

FIG. 1. The experimental arrangement, including the electrostatic exciter and the vibration detector.

EXPERIMENTAL PROCEDURE

1. Excitation and Detection of Vibrations

Glass fibers G (Fig. 1) a few cm in length and having diameters between 0.02 and 0.06 cm were fixed at one end and excited electrostatically to torsional or to lateral vibrations of invisably small amplitudes at frequencies between 20 to 400 cps. The fixed end of the fiber was embedded by lead in a hole bored at the extremity of a heavy brass support D. Torsional vibrations were provoked by applying a periodic electrostatic torque to the free end of the fiber. A light metallic vane N was connected to the extremity of the fiber and was put into electrical connection with the supporting rod by a thin loose copper wire W (British S.W.G. 48). The effect of this wire on the damping was found to be negligible as judged from preliminary experiments with different lengths of W. The vane is raised to a polarized harmonic voltage and is suitably disposed with respect to an electrode A connected to a capacity-operated vibration detector. Lateral vibrations might likewise be excited and could be readily discriminated from torsional vibrations which generally

* The original unrevised manuscript was submitted May 28, 1952.

[1] R. Kamel, Phys. Rev. **75**, 1606 (1949).
[2] Y. L. Yousef and R. Kamel, Nature **167**, 945 (1951); Proc. Math. Phys. Soc. Egypt, **4.4**, 83 (1952).
[3] C. E. Guye and S. Vasileff, Arch. sci. Phys. et nat. **37**, 214, 302 (1914).
[4] H. Rötger, Glastech. Ber. **19**, 192 (1941).
[5] B. V. Lengyel, Z. physik. Chem. **A167**, 295 (1933).
[6] J. V. Fitzgerald, J. Am. Ceram. Soc. **34**, 314, 339, 388 (1951).

have much higher frequencies. Change of the vibration frequency was effected either by changing the length or the weight of the vane N, the maximum load being always less than 1 g.

The vibration detector is essentially a slightly off-tune quartz-crystal oscillator having a frequency of about 6.5 Mc/sec. If the working capacity is chosen on the steep portion of the response crevasse, small capacity changes as would arise from the vibration of N will cause pronounced variations in the anode current i_p. An isolated load resistance R in the plate circuit interprets these variations as voltage variations which could be displayed on a cathode-ray oscillograph C.R.O. or a tube voltmeter. The sensitivity is of the order of $2\cdot10^{-3}$ volt/10^{-6} $\mu\mu$f. The principle of this circuit has been earlier described by Yousef and Sultan.[7]

2. Anelastic Measurements

The internal friction was measured by the resonance method and was calculated from $Q^{-1}=\Delta\nu/\sqrt{3}\nu$, where $\Delta\nu$ is the width of the resonance curve at half-maximum amplitude, and ν is the resonant frequency. The fiber under test together with the electrode A were enclosed

TABLE I. The composition in weight percentages of glasses 1 to 5.

Glass No.	1	2	3	4	5
SiO_2	68	72	70	80.6	100
Na_2O	18	13.6	11	4.4	...
K_2O	2.4	...	6	...	...
Al_2O_3	4.3	0.3	10	2	...
CaO	5.5	11.6	...	...	...
MgO	...	2.5	...	...	...
B_2O_3	...	...	...	11.9	...
Other constituents	1.8	2	3	1.1	...

in a glass tube which could be placed in a cylindrical furnace to allow measurements at different temperatures. The region of uniform temperature along the axis of the furnace is sufficiently long to include the longest specimens used. The glass tube was evacuated from air to reduce external losses. In lateral vibrations experiments, the frequencies were chosen to lie well beyond the thermoelastic relaxation band.

RESULTS

The internal friction at different temperatures was measured for five kinds of silica glasses having Na_2O content ranging from 0–18 percent. Table I gives the composition of each glass. In glasses 1, 2, 3, an internal friction peak for both transverse and torsional vibrations was observed in the corresponding relaxation curve. That this peak is due to sodium ion diffusion was supported by the fact that the sodium ions are almost the only ions freely mobile in the glass network, particularly below 600°C.[8] Relaxation curves at

[7] Y. L. Yousef and F. Sultan, Rev. Sci. Instr. **20**, 533 (1949).
[8] R. Schwarz and J. Halberstadt, Z. anorg. u. allg. Chem. **203**, 365 (1932); **210**, 286 (1933).

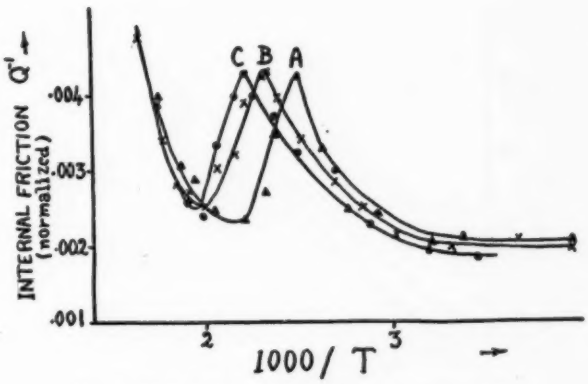

FIG. 2. Relaxation curves for glass 2. $\nu_A=32.2$; $\nu_B=148$; $\nu_C=396$ cps.

different transverse frequencies of vibration are shown in Fig. 2 in a typical example with glass 2. The curves are normalized to the 0.0043 peak observed for the fiber of the lowest frequency. A shift in the position of the peak towards the higher temperature occurs as the working frequency is increased. The relation between the logarithm of the frequency of vibration and the reciprocal of the absolute temperature T at which maximum internal friction was observed is represented by a straight line (Fig. 3) whose slope is proportional to the heat of activation, which is calculated from the relation

$$H=R(\ln\nu_2/\nu_1)/\Delta(1/T),$$

R being the gas constant and $\Delta(1/T)$ the shift in the position of the peak effected by changing the frequency of vibration from ν_1 to ν_2. The values of H obtained for the three soda glasses under test ranged between 17 and 21 kcal/mole and were deduced independently from relaxation curves using torsional and transverse vibrations. The values obtained from the two types of vibration accord satisfactorily with one another as shown in Table II.

Since the relaxation process involved here is the ionic diffusion, it seemed advisable to confirm the results by resistivity measurements. A glass resistance was constructed by forming a small glass bead between two platinum wires acting as electrodes. Resistance measurements at different temperatures up to 300°C

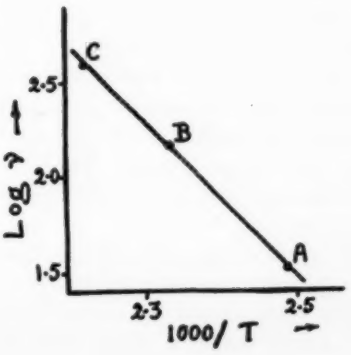

FIG. 3. Temperature dependence of internal friction maxima in glass 2.

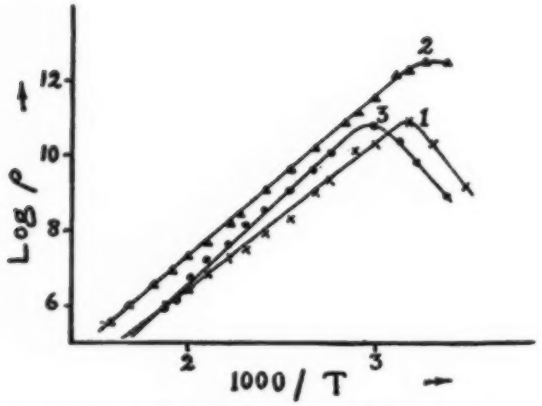

FIG. 4. Temperature dependence of the electrical resistance ρ of glasses 1, 2, 3.

were performed by the leakage method, using an electrometer whose capacity could be changed between 10 $\mu\mu$f and 1 μf by the incorporation of high-grade condensers. Polarization effects were always tested by reversing the direction of flow of charge and were found to be negligible at temperatures below 250°C. The electrometer employed is a new design, details of which are awaiting publication. Briefly, it employs a reed connected to an ac potential and is situated near a charged electrode. The polarized PD sets the reed into resonant vibrations which are detected by the circuit described above. As the charge leaks, the vibration amplitude, as seen on an oscillograph, decays in the same proportion. The small size of the glass bead allows a good temperature control over the specimen, and the method of formation insures small liability to surface impurities. Moreover, since the platinum leads are fused to the bead, the contact area always remains the same.

The temperature dependence of the electrical resistance for glasses 1, 2, 3, is shown in Fig. 4. A bend in these curves was observed near room temperature and is probably due to some unavoidable surface impurity. For ionic conductors, the resistance ρ at an absolute temperature T is given by

$$\rho=\rho_\infty \exp(H/RT),$$

where ρ_∞ is a constant for a given specimen. The slopes of the straight portions in the curves shown in Fig. 4 give values of the activation energy agreeing with those obtained from internal friction measurements for the corresponding glasses. In Table II the results are summarized, and a comparison is made for all the values of the heat of activation obtained by the different methods employed in this investigation. There is reasonable agreement between the present results and those of Rötger and of Fitzgerald.

A consideration of the values of the heat of activation H given in Table II for different soda glasses seems to show some sign of slight dependence on sodium ion concentration. Figure 5 shows the plot of the heat of activation, as observed by different methods, against the Na_2O content C. The coefficient dH/dC in the neighborhood of $C=14$ percent is about -0.45 kcal/mole.

Figure 6 shows the temperature dependence of internal friction for five different glasses. In general, it will be noticed that increasing the number of the effective sodium ions causes an increase in the anelasticity of the specimen. This explains the remarkably small values of internal friction for the quartz glass 5, being 0.00034 at room temperature (20°C) with a temperature coefficient 0.015 between 20° and 100°C. The dependence of the height of the peak on the effective sodium content provides a further justification of the assumption that the present type of relaxation is due to sodium ions.

DISCUSSION

In order to explain the ionic relaxation mechanism in glass the present knowledge concerning its atomic arrangement will be briefly reviewed. Zachariasen[9] seems to be the first to state that the atomic or molecular arrangement in the vitreous glassy state is characterized by an extended network which lacks symmetry

TABLE II. Dependence of the heat of activation as obtained by different methods on the Na_2O content for glasses 1, 2, 3.

Glass No.	Na_2O content percent	H from internal friction transverse	torsional	H from resistivity
1	18	20 000	20 700	20 600 cal/mole
2	13.6	19 000	18 800	19 200 cal/mole
3	11	17 000	16 900	17 400 cal/mole

and periodicity. The randomness of the glassy silica makes possible the existence of large and small interstices. By melting metallic oxides such as Na_2O, K_2O, . . . with glass forming oxides, the vitreous structure of glass is not affected, but only the metallic ions will occupy the inevitable interstices present in the network. The migration of these ions, preferring the wider interstices, during cyclic stressing of such a glass specimen will cause a relaxation process with a relaxation time for each of the relaxing ions. Because of its high mobility relative to other ions, the sodium ion alone seems to be responsible for this relaxation. The curves for glasses 1, 2, 3, show an absorption region which is due to this cause. When such curves are plotted for glass 4 (Pyrex) and the quartz glass 5, the absorption band disappeared (see Fig. 6), denoting the nonexistence of any relaxation in the temperature range investigated. This result is expected in the quartz glass 5 because of the complete vacancy of the interstices from any foreign ions which may cause a relaxation process.

[9] W. H. Zachariasen, J. Am. Chem. Soc. **54**, 3841 (1932); J. Chem. Phys. **3**, 162 (1935).

In glass 4, with 4.4 percent Na_2O content, the disappearance of the absorption band implies that the first few sodium ions present in the glass network are enclosed in the deepest potential holes and thus do not act as free sodium ions. A similar conclusion was reached through electrical conductivity measurements of borate glasses. Thus, Schtschukarew and Müller[10] found that the conductivity generally increases with

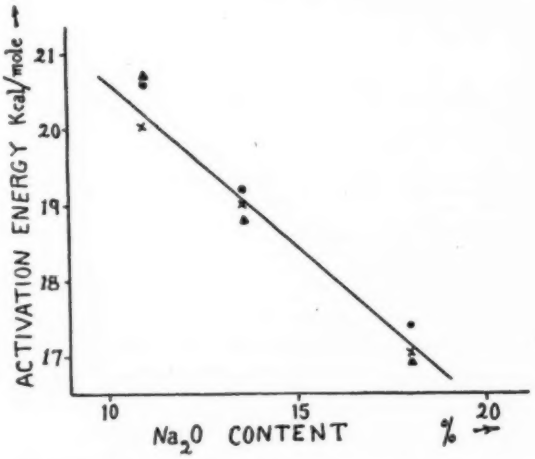

FIG. 5. Variation of the heat of activation with the sodium ion concentration. × Transverse vibration measurements, ▲ Torsional vibration measurements, ⊙ Electrical conductivity measurements.

an increasing content of sodium ions, but above 4 percent Na_2O the increase is much faster than below that composition. For 4 percent Na_2O content a bend was found[11] in the conductivity *vs* concentration curves

[10] S. A. Schtschukarew and R. L. Müller, Z. physik. Chem. A150, 438 (1930).

[11] G. Gehlhoff and M. Thomas, Z. tech. Phys. 6, 544 (1925).

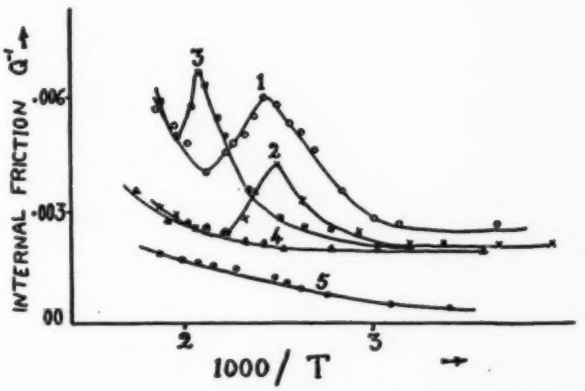

FIG. 6. Temperature dependence of internal friction of different glasses. The frequencies of vibration for the different samples range between 40–210 cps. The Na_2O percentage is respectively 18, 13.6, 11, 4.4, 0 for glass Nos. 1, 2, 3, 4, 5.

for various isotherms. This bend was explained by the assumption that below this concentration the sodium ions acquire the lowest energy levels and thus will contribute nothing to the flow of electric charge through glass. The striking parallelism between conclusions obtained by conductivity measurements and internal friction measurements provides evidence that both phenomena originate from the same mechanism, namely, the sodium ion diffusion.

The conclusion reached by Fitzgerald (see reference 6) that annealing raises the activation energy from 16 to 20 kcal/mole may be accounted for qualitatively by the plausible assumption that annealing gives the sodium ions the opportunity for attaining the lowest energy levels, thus becoming enclosed ions.

The author wishes to acknowledge his indebtedness to Professor Y. L. Yousef for his valuable help during the development of this investigation.

Heat Transfer at High-Power Densities

JOHN S. HICKEY, JR.*
General Electric Research Laboratory, Schenectady, New York
(Received April 29, 1953)

The power densities that liquid metal cooling is capable of are explored. The advantages of liquid metals over conventional water cooling are shown. The presentation is such that one can choose between the available coolants for any particular application with a minimum of background. The work done at the General Electric Research Laboratory in developing a vacuum tube anode capable of handling 5 kw/cm² is covered.

GENERAL

DESIGN of microwave tubes of all kinds has shown a steady trend towards higher voltages and current densities at the anode as our skill increases at present operating frequencies, and as the power level and frequency range is increased. At the present state of the art, the kilowatt per square centimeter is a very convenient unit for measuring anode power density. This unit represents approximately 3×10^6 Btu/hr ft². At this thermal density the temperature gradient in the conducting metal is so great that it greatly influences any cooling system design. A list of gradients for some of the metals normally used in vacuum tubes is given in Table I.

Obviously we cannot exceed the melting point of the metal on one side of the wall and we cannot go much below zero degrees centigrade on the outside. Based on these limitations, Table II gives the maximum length of heat flow path for a density of 1 kw/cm². In practice, temperatures as high as the metal melting point are never allowed. A more realistic figure for total temperature drop through the wall is 500°C. For this condition, the maximum path length, again at 1 kw/cm², is given in Table III.

Tubes having thermal fluxes as high as 10 kw/cm² at the anode surface have been designed. Under this flux, the theoretical maximum length of path is just over $\frac{3}{16}$ inch, if copper is used as the collector.

It is clear that any great length of path between the region of heat generation at the anode face and the coolant interface cannot be tolerated. Therefore, greatly reducing the heat flux density by allowing spherical diffusion through the conductor is impossible. The only practical way to avoid large temperature differences is to bring the cooling liquid as close as possible to the incident electrons. With this sort of design, the maximum permissible wall thickness is given by Table III for 1 kw/cm².

TABLE I. Temperature gradients for heat flux of 1 kw/cm².

Metal	Temp. gradients °C/cm	°F/inch
Stainless steel	5450	24 900
Nickel	2050	9360
Molybdenum	750	3420
Wolfram	725	3310
Copper	254	1160

DESIGN PROBLEMS

The design discussed in this paper is for 10 kw/cm², where the maximum wall thickness is one-tenth that listed in Table III. The first two metals—stainless steel and nickel—are obviously weak in such thin sections. Tungsten would be suitable structurally, but the manufacturing problems involved in all but extremely simple shapes would be serious. Copper and molybdenum are suitable structurally and mechanically.

Molybdenum is now available in a comparatively ductile form so that simple drawn shapes are possible. There has been no trouble drawing the shallow anode cup required in a simple one-stage die at room temperature. More complicated shapes may possibly be processed hot.

Copper is ideal for water-cooled systems with densities up to 1 kw/cm², because of the ease of fabrication by processes such as hobbing and brazing. At higher heat fluxes, mechanical erosion in water systems due to the high velocities required becomes an important factor. Chemically, copper is not good for alkali metal or mercury systems since it amalgamates readily with these metals. A protective film to prevent this amalgamation is a possibility. A small amount of nickel-clad copper was made up, using a very thin skin of nickel to protect the copper. This was welded to stainless steel. Photomicrographs of the weld encouraged the belief that this type of joint would be vacuum tight as well as mercury proof. No further work was done on this design due to the success of our molybdenum-faced anodes.

The major problem in using molybdenum is that of joining it to the vacuum envelope. This must be done inside the tube, since molybdenum has poor oxidation characteristics exposed to air. Very good results have been obtained in brazing molybdenum to stainless steel in dry hydrogen. A commercial brazing alloy, Colmonoy No. 6, is used in a powder form. This alloy is designed to have a very high hot strength. A photomicrograph of one of the joints is shown in Fig. 1, which shows the solder with a region of alloyed molybdenum on one side and a steel alloy on the other. No success

was met in reprocessing poor brazes, as the molybdenum cup buckled badly.

A secondary problem encountered with molybdenum is the wetting of the surface with a coolant when mercury is used. With sodium, NaK, or water, there is no problem since these liquids wet most anything. Ordinarily, mercury in air does not wet pure iron, stainless steel, molybdenum, or anything with which it does not amalgamate. When mercury is circulated in a nonwet system, a dust may be circulated with the mercury and forced against the walls of the passage,

TABLE II. Maximum wall thickness, based on melting point.

Stainless steel	0.25 cm	0.0975 inch
Nickel	0.70	0.276
Molybdenum	3.6	1.42
Wolfram	4.35	1.71
Copper	4.25	1.67

thus lowering the heat-transfer coefficient. It is believed that the heat-transfer coefficient for wet walls is higher than that for clean dry walls. Also, the possibility of contamination of the wall must be guarded against, either by clean systems or by designing for reduced values of heat-transfer coefficient.

Several ways of making mercury wet the walls of its container have been found. All seem to be based on the removal of any surface layer of oxide or dirt that may be present. The method of heating molybdenum to incandescence and then dipping into mercury in vacuum is cumbersome for practical cooling passages. Firing on a thin layer of gold in a hydrogen atmosphere coats the molybdenum or stainless steel with gold in place of oxide and protects the surface until the mercury dissolves off the gold. The mercury then wets the surface very nicely. An adherent copper film which may be

TABLE III. Maximum wall thickness, based on 500°C differential.

	Path	
	Cm	Inches
Stainless steel	0.09	0.03
Nickel	0.24	0.096
Molybdenum	0.67	0.26
Wolfram	0.66	0.26
Copper	1.96	0.77

plated on will do the same job. In both cases, the time needed to dissolve the cover coating is negligibly small, and the amount of adulterant introduced into the mercury system is also small. This contamination could be eliminated by flushing the system with more mercury, but such expense is not warranted. Molybdenum surfaces wet with mercury by either coating technique stand exposure to air quite well. It is impossible to rub off the coating of mercury. Evaporation of the mercury by heat will, of course, remove the coating. The mercury boiler practice of adding magnesium requires that all

FIG. 1. Photomicrograph of molybdenum to stainless steel braze.

oxygen be excluded. It was felt that this requirement would make changing tubes too difficult.

CHOICE OF COOLANT

This study was initiated when difficulties were encountered in a water-cooled tube supposed to run at 5 kw/cm². Consistent trouble with the necessarily small water passages led us to consider liquid-metal cooling.

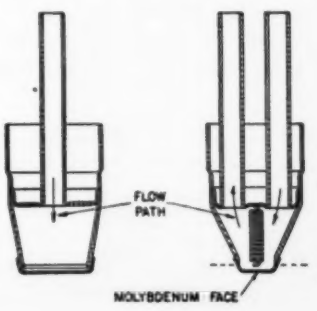

FIG. 2. Liquid metal cooled anode.

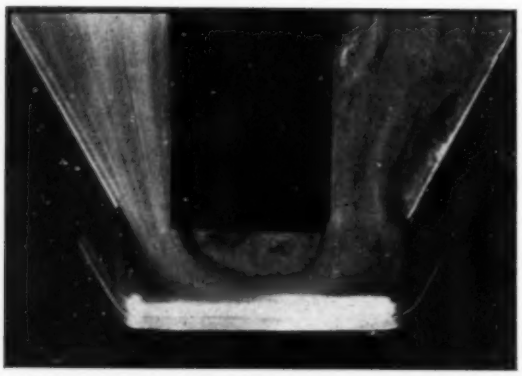

(a)

(b)

FIG. 3. Flow patterns in the cooling passages.

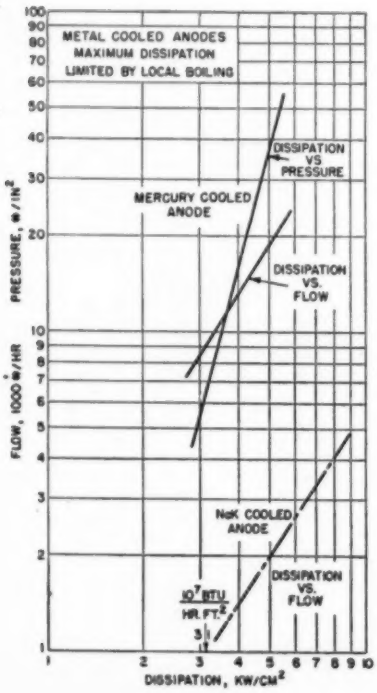

FIG. 4. Maximum dissipation in mercury-cooled diode.

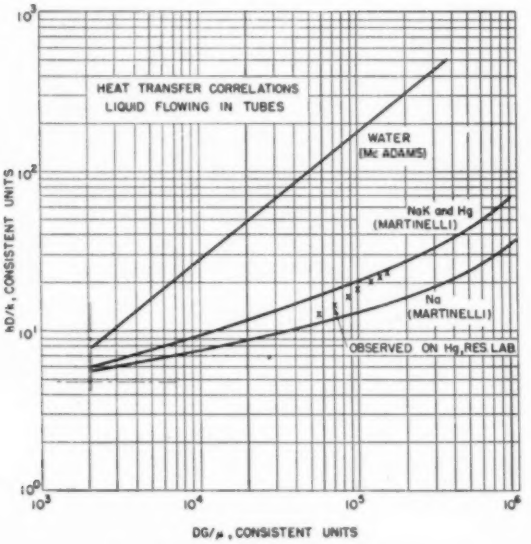

FIG. 5. Heat-transfer correlations.

The first liquid-metal-cooled anodes tested contained NaK under vacuum. They had an active area of one sq cm. A cross section of the final anode is shown in Fig. 2. It may also be seen in Figs. 10 and 11. This

TABLE IV. Physical properties.[a]

T (°F)	ρ (No./hr ft^3)	u (No./hr ft)	k (Btu/hr ft^2, °F/ft)	C (Btu/No. °F)
Na				
300	57.2	1.32	47.8	0.325
400	56.3	1.07	46.9	0.319
500	55.5	0.91	46.0	0.315
NaK—Eutectic, 20 percent Na, 80 percent K				
300	53.9	1.13	15.7	0.266
400	53.1	0.94	16.0	0.264
500	52.3	0.81	16.3	0.262
Hg				
200	833	3.02	8.40	0.033
300	825	2.65	9.31	0.033
400	816	2.42		0.032
H_2O				
100	62.0	1.7	0.358	1.00
200	60.0	0.7	0.406	1.00
300	57.3	0.45	0.454	1.00

T (°C)	ρ (gm/cc)	u (poises) ($\times 10^3$)	k (cal/sec cm^3) (°C/cm)	C cal/gm°C
Na				
150	0.916	5.45	0.197	0.325
200	0.903	4.41	0.194	0.319
250	0.888	3.75	0.190	0.315
NaK—Eutectic, 20 percent Na, 80 percent K				
150	0.863	3.50	0.0648	0.226
200	0.852	3.19	0.0662	0.224
250	0.838	2.79	0.0673	0.222
Hg				
100	13.35	12.1	0.0349	0.033
150	13.23	1.09	0.0385	0.033
200	13.11	1.01		0.032

[a] Taken from *Liquid Metals Handbook*.

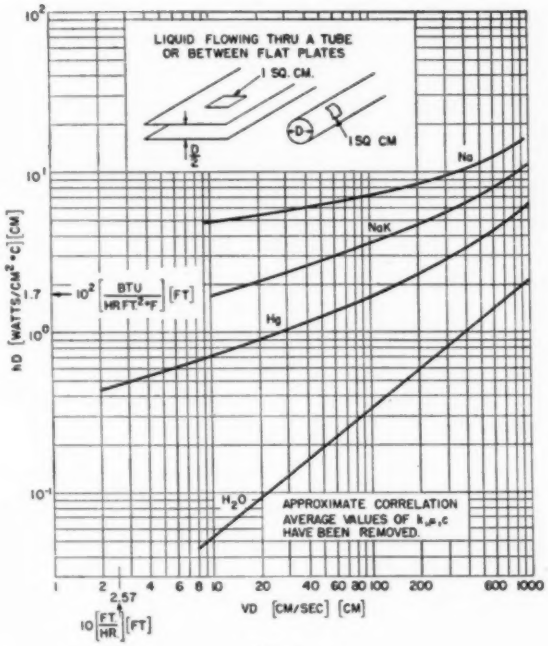

FIG. 6.

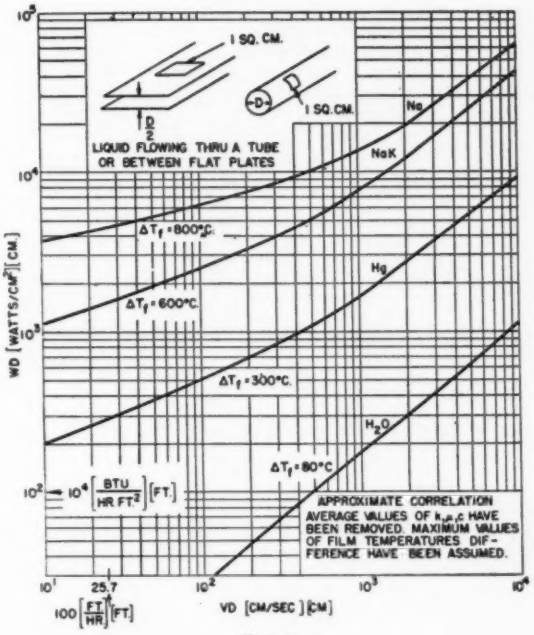

FIG. 7.

FIGS. 6 and 7. Approximate heat-transfer correlations.

anode is interchangeable with the water-cooled anode on a tube under development. They exhibited local boiling at low power densities, as should have been expected. Admitting dry nitrogen to bring the pressure up to atmospheric raised the power density at which local boiling occurred to 4½ kw/cm². The pumping power used was so small (10 watts) that it was felt that mercury might be feasible. An anode designed for NaK was run with mercury in it at about 20 watts pumping power. Failure because of incipient local boiling occurred at 1.5 kw/cm², and increasing the dissipation showed hot spots in the corners of the anode. Investigation on a flow table proved this effect was caused by eddies introduced by a discontinuity at the molybdenum-to-stainless solder joint. Smoothing the joint eliminated the eddy and allowed us to achieve higher dissipations.

This experience points out one important fact about the use of the general heat-transfer correlations. These correlations are for ducts so long that the end effects are negligible. End effects are not always deleterious,[1] but care must be taken to avoid those that are. The flow table is a powerful tool for just this purpose. It consists of an inclined sheet of plate glass over which water is caused to flow in a laminary layer. Large-scale models of any flow system may be blocked out on the glass and the resulting flow pattern will be analogous to that in the original. The greatest limitation of the flow table is that it is restricted to two-dimensional flow. Its value as an illustrative device is so great that many shapes having circular symmetry have been examined on it, neglecting this discrepancy. Flow patterns in a proposed system can be quickly and easily visualized and changes to improve the flow can be tried very easily. The accompanying pair of photographs, Fig. 3, show pictures of the flow in our anode with and without the aforementioned discontinuity at the joint. The eddy in the lower right corner of Fig. 3(a) is clearly visible.

This anode was operated using NaK as a coolant up to 4½ kw/cm² dissipation. The calculated flow at this dissipation gave a Reynolds number of 1500 based on the thickness of the flow path at the anode surface, indicating laminar flow. The same anode with a slightly smaller liquid passage was operated using mercury as a coolant. The mercury pump outlet pressure was set and the dissipation increased until local boiling started. The heat-transfer coefficient was computed, using the

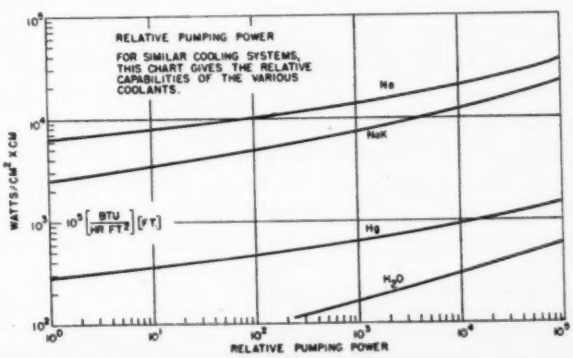

FIG. 8. Relative pumping power for similar cooling systems.

[1] V. D. Sanders, "A mathematical analysis of the turbulent heat transfer in a pipe with a surface temperature discontinuity at the entrance," M. S. thesis, University of California, November, 1946.

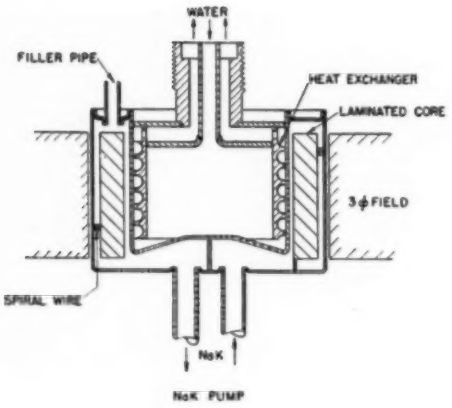

FIG. 9. Cross section of NaK pump.

boiling point of mercury as the wall temperature. The data from one run with mercury and one run with NaK are shown in Fig. 4.

HEAT-TRANSFER CORRELATIONS[2]

The best published data on liquid metals are in Martinelli's[3] paper. The accepted standards on water are given in McAdams.[4] These data, in their original form, are given in Fig. 5. The measured data taken from our mercury cooling run are also shown on this sheet. The bulb temperature of the mercury was used. No points for our NaK cooling runs are shown since our NaK tubes were never operated in the turbulent region. It seems inadvisable to use NaK in laminar flow when mercury in turbulent flow will give the same values of heat-transfer coefficient because of the difficulties involved in handling NaK. The dimensions of the area actually illuminated by electrons were used to compute the heat transfer coefficients. Table IV is a condensed set of the physical properties of the various coolants considered.

The correlation of Fig. 5 is a very neat one and is the only way to present much of the data where the various physical properties vary widely. In any small heat exchanger, such as in a vacuum tube, where the liquids do not depart appreciably from room pressure and temperature, the viscosity, conductivity, and density do not vary greatly over the operating range. For example, variations in the physical properties of mercury are less than 15 percent from 100°C to 250°C, which is well within the accuracy of heat-transfer correlations, generally accepted as ±25 percent. If we eliminate these characteristics of the materials from Fig. 5 we get Fig. 6, which is more useful to an engineer who has to choose between the various coolants. Figure 7 is similar, except that here the variation in boiling point of the coolants at atmospheric pressure is taken into account and reasonable values of film temperature drop are assigned.

The accuracy of these curves decreases as the various parameters are removed and, in the case of water, the final curve may be off as much as two to one.

The last correlation, Fig. 8, is one that plots cooling capability *versus* pumping power. There can be no absolute scale for the power on a generalized curve, but, if a system is operating under certain conditions with one coolant, this chart will tell approximately how the required power will change to vary the heat-transfer coefficient, or will show how the heat-transfer coefficient will vary as the coolant is changed at constant power.

DESCRIPTION OF PUMPS USED

Although an anode that will operate with NaK will also operate using mercury, the same cannot be said for the pumps. The simplest way to pump NaK is electromagnetically, while a centrifugal pump is best for mercury.

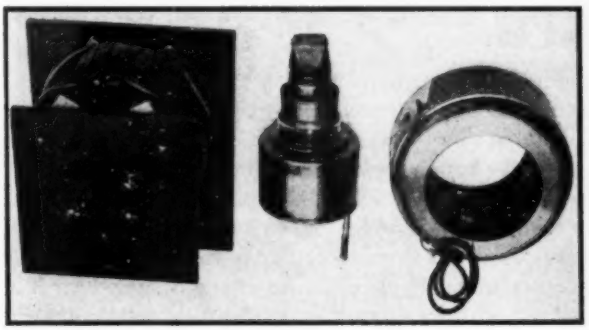

FIG. 10. NaK cooling equipment.

NaK offers many problems in handling. It is extremely active chemically. An oxide film forms on the surface of a pool at room temperatures about as fast as the oxide forms on a pool of lead at 400 or 500°C. The liquid reacts explosively with water forming hydrogen, sodium hydroxide, potassium hydroxide, and heat. Its reaction with human skin is similar to that of concentrated sulfuric acid, so it should be handled accordingly. There is some belief that a NaK-to-water heat exchanger is potentially a very dangerous device.

Because of the physical characteristics of NaK, any pump must be hermetically sealed. Fortunately, its electrical conductivity is so much greater than that of stainless steel that the electromagnetic pump can be made with walls of stainless steel and still have almost all the induced currents flow in the NaK. A cross section of such a pump is shown in Fig. 9. The ac flux is derived from a standard General Electric FHP three-phase stator taken from a ½-hp motor. A laminated core inside the pump supplies the rest of the magnetic path. It was found that our Pittsfield Works uses a dolomite

[2] *Liquid Metals Handbook*, NAVEXOS P 733 (U. S. Government Printing Office) June 1950.
[3] Martinelli, Trans. Am. Soc. Mech. Engrs. **69**, 947 (1947).
[4] W. H. McAdams, *Heat Transmission* (McGraw-Hill Book Company, Inc., New York, 1942).

coating on its transformer laminations that resists NaK attack at moderate temperatures. Use of this material allows the immersion of the core in the NaK and considerably simplifies the pump design. Since our system was so compact and NaK is physically difficult to handle, we did not attempt to measure any pressure drops. Using calculated pressure drops, the pump efficiency comes out about 10 percent.

The NaK-to-water heat exchanger is built coaxially with the pump to reduce the volume of NaK required to fill the system. The shell between the two liquids is a carefully spun, seamless, stainless steel cup. No difficulties were encountered here in the three pumps operated, although the temperature drop through the steel might have been excessive for 10-kw operation.

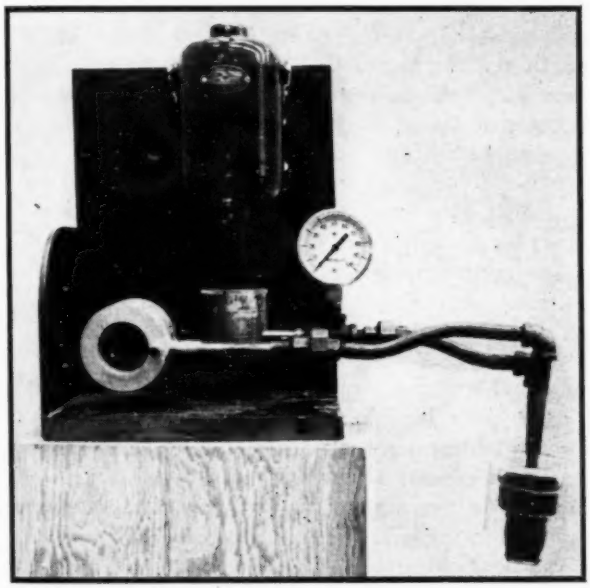

FIG. 11. Mercury-cooling equipment.

The NaK cooler, embodying both the pump and heat exchanger, is shown in the photograph, Fig. 10. The required dc isolating transformer and three-phase field are also shown. The cooler requires a very exacting job of welding, since there are five welds to be vacuum tight in its envelope. The complete cooling system, including the anode volume, contains approximately 125 cc of NaK.

In contrast to the NaK pump, the mercury pump is simplicity itself. A small impeller pump operating at moderate speed easily supplies the required head. With clearances in the pump of the order of $\frac{1}{32}$ inch and a greatly over-rated motor, the efficiency of the pump and motor was 12 percent. Figure 11 is a picture of

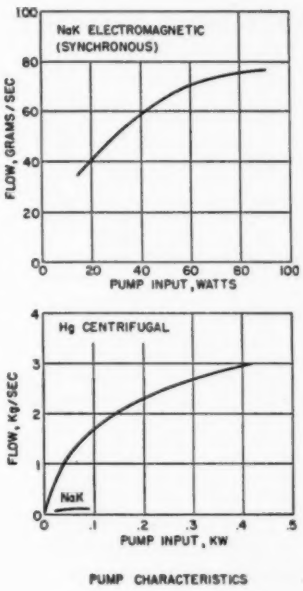

FIG. 12. Liquid metal pump characteristics.

the entire mercury cooling system. The pump impeller is hung on the motor shaft. The upper level of the mercury is just above the impeller so that neither mercury-proof bearings nor seal were required. Compare this with the components in Fig. 10 for NaK. When pumping mercury, great care must be taken to avoid cavitation. This particular system is designed so that the velocity head of the mercury is conserved throughout the entire passage. The bottom of the pump casing is shaped so as to aid in converting this head into angular momentum. It is interesting to note that this pump will not pump one-tenth of this volume if it is required to draw from a reservoir at zero velocity head. Performance characteristics of both pumps are given in Fig. 12.

CONCLUSION

When a device has to be operated in such a manner that dissipations of the order of kilowatts per square centimeter are encountered, it is advisable to consider liquid metals as coolants.

Their advantages are larger passage sizes, lower linear velocities, and much lower pumping powers. Their disadvantages are increased cost of coolant and the difficulty of handling the alkali metals. These factors must be carefully considered in the choice of a coolant for any specific application.

Reference 2, *The Liquid Metals Handbook*, should be required reading for anyone interested in using liquid metals.

Preliminary Results on Photoelectric Yields of Pt and Ta and on Photoionization in O_2 and N_2 in the Vacuum Ultraviolet

N. WAINFAN, W. C. WALKER, AND G. L. WEISSLER
Department of Physics, The University of Southern California, Los Angeles, California

(Received May 11, 1953)

Absolute photoelectric yields of Pt and Ta and photoionization yields in O_2 and N_2 are reported for the spectral region from 436 to 1004 angstroms. The experimental methods as well as the monochromator, light source and associated apparatus are described. The results for Pt and Ta give photoelectric yields between 10^{-1} and 10^{-2} electron per photon for wavelengths shorter than 1000A. These values are 10 to 100 times larger than those obtained for the same metals between 2000A and 3000A. Photoionization results for O_2 indicate that below 700A almost all absorbed photons produce ion pairs, while in the region between 700A and the first ionization limit at 1000A the yield varies rapidly. In the case of N_2 at wavelengths shorter than 796A, its first ionization limit, the yield rises steeply. Below 725A almost all absorbed photons produce ion pairs. The over-all error is estimated to be within ±20 percent.

INTRODUCTION

IN order to understand the initiation and maintainance of various types of gas discharges such as glow discharges, sparks, Geiger counter pulses and others, it is important to analyze the various contributing processes. In general, two groups of such mechanisms may be distinguished; those active in the gas and those active at the electrodes.

One of the important mechanisms active at the negative electrode is the photoelectric emission of electrons produced by ultraviolet light from the discharge. The corresponding parameter which enters into any discussion of the effect of this process on the discharge is the efficiency of electron emission or the photoelectric yield of the cathode. This quantity, usually designated as γ_r, can be expressed either in terms of the number of ejected electrons per incident photon or the photoelectric current per unit light intensity. It can be measured for certain wavelength regions by ordinary photoelectric techniques. For the wavelength region above 2000A the photoelectric yields of many metals have been measured.[1] For the spectral region of the vacuum ultraviolet, however, i.e. from 2000–100A, few data have been obtained. Since this spectral region may be extremely significant for gaseous discharge analysis it seemed important that it be investigated more completely. In 1933 Kenty presented data for Ni, W, Mg, and Constantan[2] at three wavelengths below 1000A. The photoelectric yield of Cadmium from 3130A to 1000A was investigated in 1938 by Baker[3] using a grazing incidence grating monochromator with LiF optics. Between 1938 and the present time very little photoelectric work was done in the vacuum ultraviolet region. Recently, however, Hinteregger and Watanabe[4] obtained data on the photoelectric yields of Ni, Pt, and W for the wavelength region from 2500A to 850A with one further point at 584A. At nearly the same time the authors[5] reported on their first data on Ta and Pt with radiation between 1100A and 450A. In addition to the papers mentioned previously, there have been several papers by S. R. Rao treating the subject of photoelectric yields for the soft x-ray region.[6]

Another mechanism active in the propagation of discharges is that of photoionization in gases. Quantitative data on this subject would also greatly facilitate the interpretation of the formation of ionospheric layers of the earth's atmosphere. Such photoionization cross sections may be inferred from measurements of the absolute absorption coefficients of gases,[7] however they are not in general as unambiguous as the direct determination of the number of ions produced per photon absorbed in the gas.

The first measurements on photoionization were done by Mohler[8] and others on the alkali metal vapors using light in the near ultraviolet region. In 1938 Raether[9] demonstrated with a cloud chamber that photoionization does initiate prespark avalanche formation in atmospheric gases. More recently multiple Geiger counter techniques have been employed to investigate photoionization in gases by, among others, Jaffe and Craggs.[10] The results of these experiments as well as those of Raether's were to extract only an effective absorption coefficient averaged over a very wide wavelength range. It has also been possible to obtain indirect evidence for the existence of photoionization

[1] Hughes and Dubridge, *Photoelectric Phenomena* (McGraw-Hill Book Company, Inc., New York, 1932), p. 135.
[2] C. Kenty, Phys. Rev. **44**, 891 (1933).
[3] R. Baker, J. Opt. Soc. Am. **28**, 55 (1938).
[4] H. Hinteregger and K. Watanabe (private communication, Cambridge Air Force Research Center), June, 1952.
[5] W. C. Walker and N. Wainfan, Bull. Am. Phys. Soc. **26**, No. 6, p. 11, abstract H3 (December, 1952).
[6] S. R. Rao and K. S. S. Iyer, Proc. Indian Acad. Sci. **A13**, (1941). Rao and Ramamurti, Current Sci. (India) **11**, (1942).
[7] Weissler, Lee, and Mohr, J. Opt. Soc. Am. **42**, 84 (1952), (N_2); **42**, 200 (1952), (O_2); **42**, 214 (1952), (Ne); Astrophys. J. **115**, 570 (1952), (H_2).
[8] Mohler and Boeckner, J. Research Natl. Bur. Standards **3**, 303 (1929); Phys. Rev. **28**, 46 (1926).
[9] H. Raether, Z. Physik **110**, 611 (1938).
[10] Jaffe, Craggs, and Balakrushman, Proc. Phys. Soc. (London) **62B**, 39 (1949).

through the study of streamer formation in spark discharges.[11]

APPARATUS AND EXPERIMENTAL PROCEDURE

In order to make an absolute determination of (A) the photoelectric efficiency of a metal sample and (B) the number of ions produced per photon absorbed in a gas, it was necessary to obtain a beam of radiation of the desired wavelength, measure absolutely its intensity and determine (A) the total number of electrons per second that this beam released from a cathode or (B) the number of ion pairs which the same beam generated when passing through a gas-filled ionization chamber.

I. The Monochromator and the Determination of the Photon Flux

For the present experiments a one meter normal incidence grating vacuum spectrograph was converted into a monochromator by fitting the grating holder with a lever arm and precision screw, driven by a constant speed motor, which served to swing the grating through several degrees about a vertical axis, thus enabling light of any wavelength within 2000A of the central image to be focused on a fixed exit slit positioned along the Rowland circle. Because of the relatively wide exit slit employed, approximately 0.6 mm wide, no complications were introduced by the slight defocusing of the light beam caused by rotating the grating away from its position of optimum focus. With this arrangement the resolution of the instrument was limited to 10A.

The light source used with the above mentioned monochromator was a high-voltage, low-pressure spark discharge through a water jacketed ceramic capillary tube. Voltage was supplied to the discharge tube from a Kenotron rectifier circuit charging three banks of condensers, of 0.4 microfarad each, which were in turn discharged periodically through the spark gap by means of a rotary switch. Normally, charging voltages from 10 to 15 kv were supplied to the condensers. During the experiment the discharge was operated in an atmosphere of argon and nitrogen at a pressure of about 100 microns. The intensities of the majority of the spectral lines from this light source in the region from 1100 to 430A were reproducible over periods of several hours to within 5–7 percent.

In order to measure the intensities of the spectral lines in the ultraviolet region, a sensitive calibrated thermocouple was used to calibrate a fluorescent sensitized photomultiplier as a photon counter. The thermocouple and photomultiplier, together with the experimental chamber which held either the photocathode to be tested or a double ionization chamber for the determination of photoionization, were mounted behind three identical slits on a brass block machined to match the Rowland circle of the monochromator. The entire unit composed of the radiation detectors and the experiment chamber, as shown in Fig. 1, was fastened to the film holder of the monochromator.

The thermocouple was first calibrated at atmospheric pressure against a 50-watt carbon filament radiation standard obtained from the Bureau of Standards. The sensitivity of the thermocouple in air was found to be 6.74 μw/μv. After the calibration in air the radiation detector unit was mounted in the spectrograph and light from a 75-watt incandescent lamp, mounted behind a window in the light source, was focused in the central image on the thermocouple slit. The amplified output of the thermocouple was then measured for several different currents through the test lamp. Then the spectrograph was evacuated to a pressure of 10^{-5} mm of Hg and the previous measurements repeated for the same lamp currents. From the resulting data the ratio of the sensitivity of the thermocouple in vacuum to that in air was found to be 7.13. The combined results of both intermediate calibrations gave an average thermocouple sensitivity in vacuum of 0.95 μw/μv.

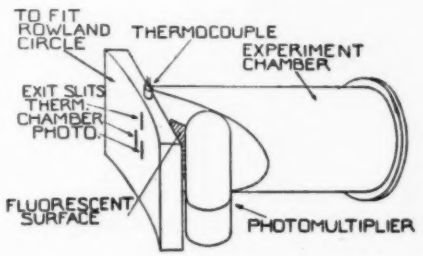

FIG. 1. Radiation detector assembly.

A 1P28 photomultiplier, sensitized to ultraviolet radiation by using the fluorescent light emitted from a sodium salicylate coated screen placed behind one of the slits in the detector assemblage, was calibrated against the thermocouple by measuring simultaneously the response of both for a series of spectral lines in the region from 436A to 1004A. The over-all accuracy in the photon flux measured by the calibrated photomultiplier was estimated to be 15 percent.

II. Procedure to Obtain Photoelectric Yields of Metals

The metal sample whose photoelectric yield was to be measured was mounted, in the form of a 0.002-inch thick sheet, as the cathode in an experimental photocell. By supporting it on two copper rods insulated from the brass base plate, the metal sample could be heated by an electrical current. A ring of 10-mil wire of the same material was mounted 6 mm in front of the metal sample and maintained at 10 volts positive with respect to it to collect electrons. The photocell was mounted behind the 0.6 mm by 2 mm slit of the experimental chamber (Fig. 1).

[11] L. B. Loeb, *Fundamental Processes of Electrical Discharge in Gases* (John Wiley and Sons, Inc., New York, 1939), Chap. X.

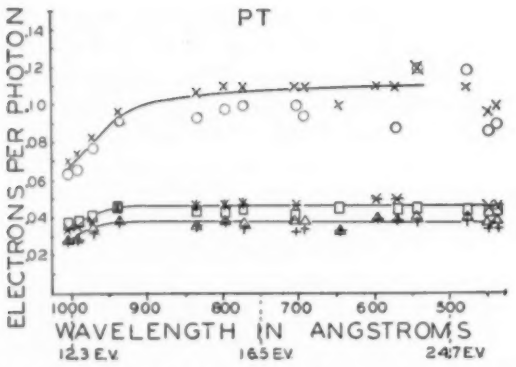

FIG. 2. Photoelectric yield of Pt. ○, ×: untreated cathode, two runs. □, ∗: first heating of cathode to above 1000°C, two runs. +: second heating. △: third heating.

During the experiment the emission current from the photocathode was measured with a Beckman micro-microammeter. The emission current rather than the saturated collection current was measured in order to avoid such disturbing effects as incomplete saturation of the current and the possible picking up of stray electrons from the slit jaws. With the geometry used for this photocell, the dark current was found to be negligible. A pressure of about 10^{-5} mm of Hg was maintained in the photocell during the measurements.

The photoyields of Pt and Ta were measured for both untreated and heat treated surfaces. For both metals the sample was cleaned with acetone, mounted in the experimental photocell, and evacuated. Measurements were then taken of the emission current from the sample and the photon flux incident on it. The sample was then heated in vacuum to a temperature of above 1000°C for two minutes, and after cooling the above measurements were twice repeated.

To test the degree of cleaning accomplished by heating the metal, it was heated and retested several times. The sample was then exposed to air at atmospheric pressure for a measured length of time, and the measurements were repeated. In this manner photoyields in terms of the number of ejected electrons per incident quantum were obtained for 16 spectral lines between 436 to 1004A.

III. Procedure to Obtain Yields of Photoionization in Gases

To make the measurements on photoionization in gases the calibrated light beam was admitted into the experiment chamber which contained two parallel plate ionization chambers in tandem along the axis of the light beam. The ionization chamber nearest the exit slit was designated by the notation C_1 and the other by C_2. Both of these chambers were equipped with guard plates to insure uniform field conditions. The spacing of the plates in the ionization chambers was 10 mm, the length L of the collector plates was 15 mm and the effective path length d between the two ionization chambers was 109 mm. A potential of 10 volts, sufficient to saturate the ion current, was maintained across the ionization chambers. Gas was admitted into the experiment chamber and the pressure measured with a calibrated thermocouple gauge. By the use of a Beckman micro-microammeter the positive ion currents were determined at the collector cathodes of both ionization chambers. Measurements in a high vacuum indicated that the contribution from the photoelectric effect on the chamber walls and the electrodes was negligible.

The total absorption coefficient k was determined from the equation $k=-(\ln i_2/i_1)/d$, using the ion currents obtained as described above, where i_1 is the current collected at ionization chamber C_1 and i_2 that collected at ionization chamber C_2. Knowing k, the photon flux I_0 entering the slit of the experiment chamber, and the distance X_0 from the front edge of ionization chamber C_1 to the slit of the experiment chamber, the number of photons absorbed in the gas under the collector plate of ionization chamber C_1 was determined from the expression $I_0(e^{-kX_0}-e^{-k(X_0+L)})$. By converting the current measured at ionization chamber C_1 to charges per second and comparing this quantity to the number of photons per second absorbed in the effective volume of the same ionization chamber, the number of ions produced in the gas per 100 photons absorbed by the gas could be determined.

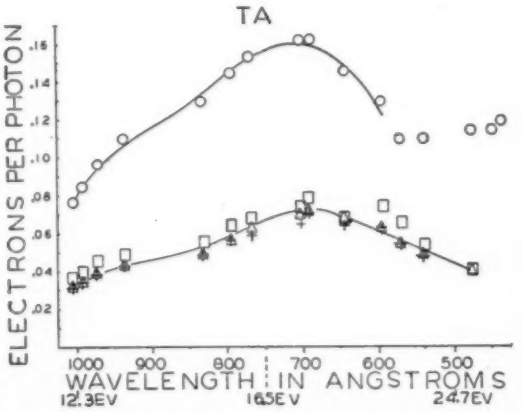

FIG. 3. Photoelectric yield of Ta. ○: untreated cathode. □: first heating of cathode to above 1000°C. +: second heating. △: third heating.

RESULTS

I. Photoelectric Yields of Pt and Ta

The photoyields obtained for a Pt sample are shown in Fig. 2 and were found to increase with decreasing wavelength from 1004A to 833A after which the yield became more or less constant to 436A. Both the untreated and heat treated samples demonstrated this same general behavior. The photoyield was found to decrease somewhat after the sample was degassed by heating, but after the second two minute heating cycle at a temperature above 1000°C no further decrease was noted. A previously heated sample which was exposed to air at atmospheric pressure for seventeen hours showed no tendency to increase its photoyield

to a value characteristic of an untreated surface. Instead it exhibited values almost identical with those of a sample heated through one heating cycle.

Results obtained for a Ta sample are shown in Fig. 3. In this case the yield was observed to pass through a maximum at about 700A. A heated specimen gave smaller yields than an untreated one. This decrease in photoyields with heating continued until after the second two minute heating cycle; additional heating resulted in no further decrease. An estimated accuracy for the absolute value of the yields for both Ta and Pt was ± 20 percent.

A comparison of the photoyields obtained in this investigation for both Ta and Pt at wavelengths shorter than 1000A with those obtained by others for wavelengths longer than 2000A shows that while the yields are of the order of 10^{-3} electron per photon at 2000A and 10^{-6} at 3000A,[12] those at 1000A are of the order of 10^{-1} to 10^{-2}. This comparison is of importance for gas discharge analysis since it indicates that many of the estimates of the effect of the photoelectric process

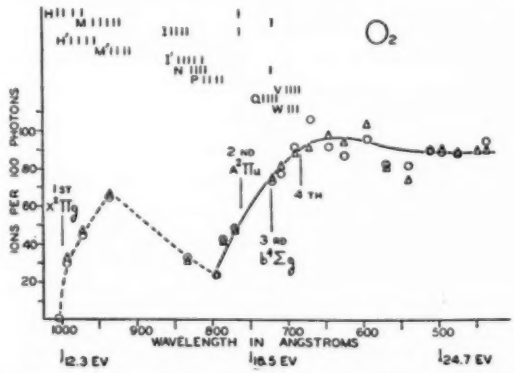

FIG. 4. Photoionization in O_2. ○: data taken at a pressure of 100 microns. △: data taken at a pressure of 50 microns. H, M, I, H′, M′, I′, N, P, V, Q, W indicate the positions of absorption bands as listed by Price and Collins (reference 14). The positions of several ionization limits are also identified by spectroscopic notation.

on the maintainance of an electrical discharge have been based on a yield value of the cathode which was as much as 100 times too small.

The large values of the photoyields at wavelengths below 1000A together with the relative insensitivity of the yields to surface contamination indicate that photoelectric emission for this spectral region may be due to a "volume" effect, from the bound electrons in the metal, instead of the "surface" effect which predominates at longer wavelengths. A more extensive investigation including other metals is now in progress in an attempt to settle this and other problems associated with photoemission in the vacuum ultraviolet.

II. Photoionization Yields in O_2 and N_2

The research on photoionization in gases by the methods described above is an extension of the exploratory work reported previously.[13] The total absorption coefficients found in the present measurements on O_2 and N_2 agreed well with earlier and more accurate data.[7]

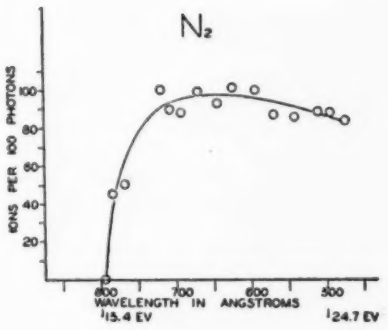

FIG. 5. Photoionization in N_2. Data taken at a pressure of 100 microns.

In Fig. 4 are shown the results on O_2 taken at two pressures. At wavelengths shorter than 650A it can be seen that the absorption may be accounted for by a photoionization process since almost every absorbed photon gives rise to an ion pair. Between the first ionization limit of O_2 at 1000A and 650A the fraction of those absorbed photons which produce ion pairs varies considerably. This latter wavelength range corresponds to a region of many strong absorption bands while below 650A the absorption was found to be continuous.[14] An insufficient number of points was available in the region above 800A (dashed curve in Fig. 4) to justify drawing a smooth curve. It was noted that the variations of the absorption coefficients with wavelength appeared to have no simple relationship to the variations with wavelength of the number of ions produced per 100 photons absorbed. A detailed analysis of the O_2 results will be attempted later.

In Fig. 5 may be seen the photoionization results obtained for N_2. It is indicated here that the number of ions appearing per 100 photons absorbed rises rapidly from zero at 796A, the first ionization limit of N_2, to about 95 at 725A. At wavelengths shorter than 725A the entire absorption mechanism, as in O_2, appears to be due to photoionization.

The total error limits in this part of the experiment were estimated to be within ± 20 percent.

This work is now being refined and will be extended to other gases.

Our thanks are due to Mr. S. W. Bale and his staff for their fine mechanical work on the vacuum monochromator and to Mr. Robert Greiner for his excellent glass blowing. It is also acknowledged with pleasure that the research reported here has been sponsored in part by the U. S. Office of Naval Research and by the Office of Ordnance Research, U. S. Army. Finally, we wish to indicate our appreciation for many helpful discussions with and suggestions from Dr. R. Tousey and Dr. K. Watanabe.

[12] A. v. Engel, *Electrische Gasentladungen* (Julius Springer, Berlin, 1932), p. 124.

[13] N. Wainfan and W. C. Walker, Bull. Am. Phys. Soc. **27**, No. 6, p. 11, abstract H2 (December, 1952).

[14] W. C. Price and G. Collins, Phys. Rev. **48**, 714 (1935).

Electron Compounds of Transition Elements

H. J. Beattie, Jr.
Thomson Laboratory, General Electric Company, West Lynn, Massachusetts
(Received May 16, 1953)

The work of many investigators has strongly indicated that sigma phase is characterized by a certain averaged electronic structure. The characteristic was first thought to be the "electron vacancy" concentration in the *d* band, but it is now appreciated that the density of electrons outside the argon shells may also be a valid criterion. The latter characteristic is used here with the application of H. Jones' theory. The result shows a definite correlation between the homogeneity ranges and the x-ray diffraction patterns for sigma phase and several other complicated structures which occur in alloys of transition metals.

SIGMA phase was first classed as an electron compound by A. H. Sully.[1] Following L. Pauling's ideas and G. V. Raynor's interpretations of aluminum alloys,[2] he suggested that its formation is related to the number of "electron vacancies" in the 3*d* band.[3] Beck and his associates investigated sigma phase in several alloy systems[4] and apparently confirmed Sully by showing that the homogeneity range for sigma phase corresponds with a narrow range of "electron vacancies" in the *d* band. The "electron vacancies" of the elements are numbers due to Pauling; they decrease regularly from chromium to nickel by approximately one per atomic number. Pauling and Ewing[5] pointed out that if an arithmetic series of numbers which are assigned to elements in order of atomic number result in a narrow range of values, so will any other arithmetic series. Bloom and Grant[6] showed that the range of homogeneity for sigma phase corresponds to about $7(3d-4s)$ electrons per atom, and suggested that this result may relate to the complicated structure of manganese, which has 7 electrons outside the argon shell.

The electron compound concept began when Hume-Rothery noted that the various phases of the brass systems are characterized by electron/atom ratios. H. Jones[7] presented a convincing explanation of the complicated gamma-brass structure forming from atoms of nearly equal size at the characteristic electron/atom ratio of 21:13. Jones's theory is based on a Fermi distribution of free electron wave functions modified by the periodic field of the crystal lattice. The results of this theory seem applicable in order to explain the formation of sigma phase and other complicated structures in alloys of transition elements of nearly equal atomic size.

First, let us briefly review certain aspects of the electron-band theory.

The distribution of free electrons in a metal is plotted in momentum space. In the absence of electrical force fields, this distribution is a uniform sphere concentric with the origin. The boundary of this momentum sphere is well defined at 0°K and becomes progressively blurred as the temperature rises. As a result of the Pauli exclusion principle, an increase in electron concentration will cause the momentum sphere to grow larger but not denser.

The effect of the periodic electrostatic field in a crystal lattice is to produce, in momentum space, polyhedra concentric with the origin. The faces of the polyhedra are perpendicular bisectors of the reciprocal radius vectors to the crystallographic reciprocal lattice points. Any electron whose momentum vector terminates on a polyhedron plane will have the proper wavelength and orientation in the crystal to be diffracted by those lattice planes which are associated with the polyhedron face. In order to pass from a state just inside a polyhedron to a state just outside, an electron must acquire a discontinuous increase in energy. The magnitude of this energy discontinuity is related to the intensity of the x-ray Bragg reflection from the diffracting planes.[7]

One imagines an homogenous alloy of a given crystal structure to change its composition so as to produce an increase in free electron density. After the growing momentum sphere reaches the first polyhedron, it flattens out on the inner surfaces of the faces. There is a sharp drop in the rate of electron density increase as the highest occupied energy state as the corners of the polyhedron are filled up. If the energy discontinuity across the polyhedron is considerable and the polyhedron is nearly spherical, the zone will fill up before overlap occurs through the polyhedron faces. The atoms may be shifted to a new crystal structure (which produces a larger polyhedron) with less energy increase than would be required to bring the extra electrons into the high energy states outside the polyhedron. The phase change may even occur while the polyhedron is being filled up, because in this region there is a large increase of maximum energy for a small increase in electron density.

The above, briefly, is the mechanism which operates in electron compounds.

[1] A. H. Sully and T. J. Heal, Research (London) **1**, 288 (1948).
[2] G. V. Raynor and P. C. L. Pfeil, J. Inst. Metals **73**, 387 (1947).
[3] A. H. Sully, Nature **167**, 365 (1951).
[4] S. Rideout and P. A. Beck, "Survey of Portions of the Chromium-Cobalt-Nickel-Molybdenum Quaternary System at 1200°C," NACA TN 2683, April, 1952.
[5] L. Pauling and F. J. Ewing, Revs. Modern Physics **20**, 112 (1948).
[6] D. S. Bloom and N. J. Grant, J. Metals **5**, 88 (1953).
[7] H. Jones, Proc. Roy. Soc. (London) **144**, 225 (1934).

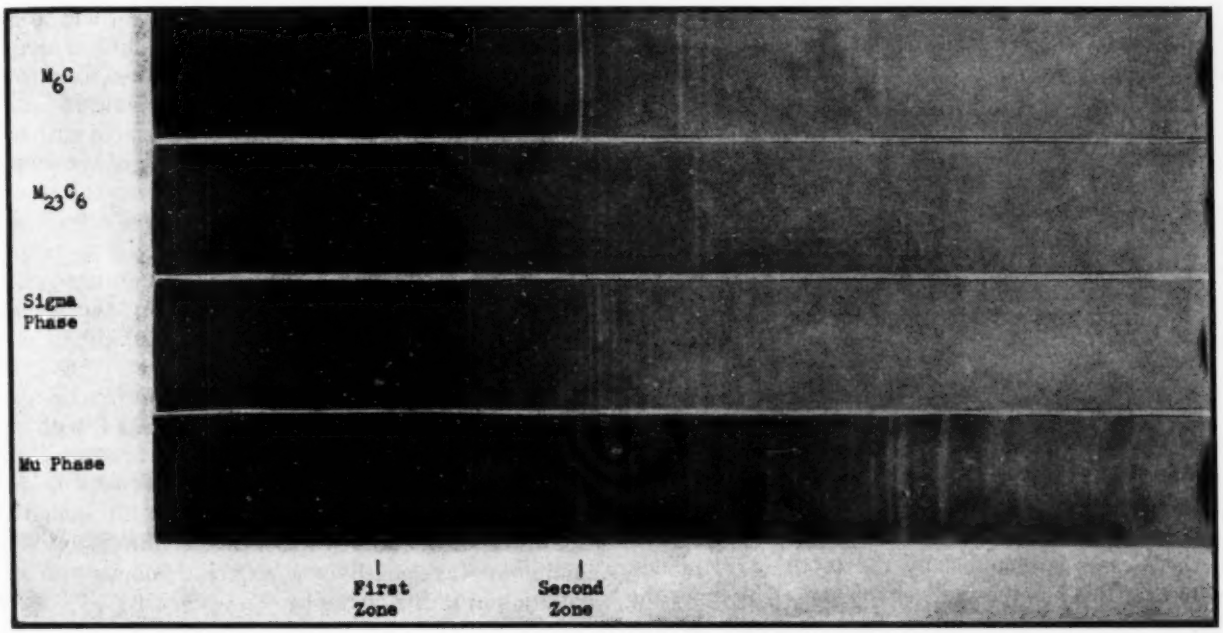

FIG. 1. X-ray diffraction patterns of complicated structures in transition alloys.

The first polyhedron of appreciable energy discontinuity (corresponding to the planes which give strong x-ray Bragg reflections) for metallic lattices usually has a capacity for between 1 and 2 electrons per atom. The lattice spacings associated with this polyhedron are usually in the range 2.0–2.1A. In the present treatment, the transition metals are assumed to have free electron concentrations greater than 2 per atom; therefore, the surface of the momentum "sphere" (which by now is probably not spherical) lies well outside the first polyhedron and will be influenced by the next outer polyhedron.

Berry, Waldron, and Raynor[8] calculated the capacities of the outer polyhedra of the simple metallic lattices. Their calculations show that the outer polyhedron for the body-centered cubic structure has a capacity for exactly seven electrons per atom. This is a totally convex polyhedron (bounded by the (200) and (211) planes) which completely encloses the inner polyhedron (110) and lies totally within the next outer one (220). This means that the surfaces of the momentum "spheres" of vanadium, with 5 free electrons, and of chromium, with 6 free electrons, will lie between the first and second polyhedra of energy discontinuity.

Manganese, whose 7 electrons would just fill up the second polyhedron of the body-centered cubic structure, is past the point where it is more economical energetically to shift to another crystal structure. The second polyhedra for the face-centered cubic and hexagonal close-packed structures will not hold even seven electrons per atom.[8] Manganese requires a structure which is a fairly small distortion of the body-centered cubic lattice, but which has a larger second polyhedron. The alpha manganese structure meets these requirements. It can be pictured as a large cubic unit cell, composed of 27 body-centered cubic unit cells, with 4 extra atoms crowded into it, resulting in a shift in all the atomic positions. Its x-ray diffraction pattern has relatively weak reflections between the very strong (330)–(411) and (552)–(721)–(633) interference lines; hence, these two sets of indices correspond to the first and second polyhedra respectively. Furthermore, the second polyhedron has a sufficient capacity for the 7 electrons of manganese, since its inscribed sphere will hold 7.17 electrons per atom and the total capacity of the polyhedron is 7.45 electrons per atom.

The x-ray diffraction pattern of sigma phase is similar to that of α-Mn in that it shows two clusters of strong interference lines in the vicinity of the strong lines of the α-Mn pattern, and these clusters are separated by an interval of weak lines. Beck and his associates have shown that sigma phase occupies a narrow range of homogeneity with respect to electronic structure, and Bloom and Grant[6] point out that this corresponds with a range of electron-atom ratios for the $(3d-4s)$ electrons in the vicinity of 7.

Chi phase, reported by K. W. Andrews,[9] is a solid solution of transition metals having the α-Mn structure. It is usually observed together with sigma phase, and therefore probably is of similar composition.

Beck also showed that mu phase, $(Fe, Co)_7(Mo, W)_6$, occupies a narrow homogeneity range, which can be shown to lie in the neighborhood of 7 electrons/atom.

[8] Berry, Waldron, and Raynor, Research (London) **3**, 195 (1950).

[9] K. W. Andrews, Nature **164**, 1015 (1949).

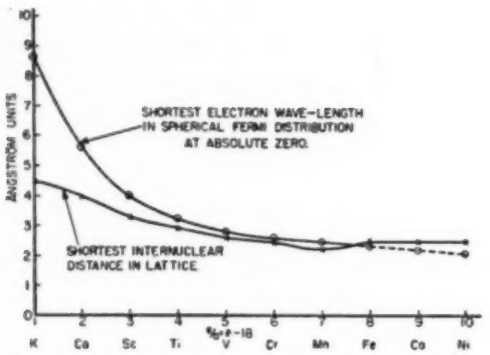

FIG. 2.

Its x-ray diffraction pattern shows a similar "two-cluster" effect.

The complex carbides $M_{23}C_6$ and M_6C give the "two-cluster" diffraction patterns too. The second polyhedron in these cases is bounded by the (660)–(822) planes. Note that this has the same shape and eight times the volume in momentum space (per unit cell) as the (330)–(411) polyhedron for gamma brass. H. Jones[7] calculated that the latter polyhedron has a capacity for 80 electron states per unit cell in the inscribed sphere and 90 in the completely filled polyhedron, of which 84 are occupied. Multiplying these numbers by 8 for the (660)–(822) polyhedron of the carbides gives 640 states in the inscribed sphere, 720 states in the polyhedron and 672 states "probably occupied." Since $M_{23}C_6$ has 92 and M_6C has 96 metal atoms per unit cell, these give a range of 6.95 to 7.83 for $M_{23}C_6$ (6.67 to 7.50 for M_6C) electron states per atom in the region contact of the momentum "sphere" with the second polyhedron. The "probable number of occupied states" is 7.30 for $M_{23}C_6$ and 7.00 for M_6C. The compositions of these carbides correspond well with these $nd-(n+1)s$* electron/atom ranges of ratios.

The homogeneity ranges for all of these phases lie completely between six and eight $nd-(n+1)s$ electrons per atom. Some of their x-ray diffraction patterns are shown in Fig. 1.

The implication of this is that all of the $nd-(n+1)s$ electrons in transition metals and alloys occupy the Fermi momentum "sphere" up to somewhere above 7 electrons per atom. The body-centered cubic structure satisfactorily accommodates up to more than 6 electrons per atom, but at about 7 it is energetically more economical to shift the atoms to a complicated structure having a large unit cell and a high degree of symmetry. At somewhere between 7 and 8 electrons, the second polyhedra of these complicated structures fill up, and some of the $nd-(n+1)s$ electrons begin to occupy atomic orbits, leaving a depleted momentum sphere whose smaller size is accommodated by the simpler crystal structures for elements like iron, cobalt, and nickel.

One may expect that an electron wave function will transform from the plane wave associated with the momentum sphere to an atomic orbit function when its wavelength matches the distance between nearest atomic neighbors in a lattice, for then the boundary conditions are nearly correct in all directions. The minimum wavelength in a spherical momentum distribution at 0°K is given by

$$\lambda_{\min}=\left[\frac{8}{3}\frac{\pi V}{N_c(e/a)}\right]^{\frac{1}{3}}$$

where V is the volume of the unit cell, N_c is the number of atoms per unit cell, and (e/a) is the electron/atom ratio. In Fig. 2 the nearest-neighbor distance and $\lambda_{\min}$ are plotted for all of the elements of the first long period as a function of (e/a). It shows that $\lambda_{\min}$ matches the nearest-neighbor distances between 7 and 8 electrons per atom, the region in which the beginning of transfer to atomic orbits is implied by the pattern of metallic phase transformations.

This treatment is simply an application of H. Jones's theory to the case of high free electron density, wherein the Fermi surface encloses the first Brillouin zone and becomes influenced by the next outer polyhedron. It is felt that this is the proper approach to the problem of alloys composed of transition elements, some of which are not in Periodic Group VIII. When nontransition metals, such as aluminum, are alloyed with transition elements of Periodic Group VIII, whose d shell diameters are appreciably smaller than internuclear distances, the "electron vacancies" in the d shells may consume electrons from the conduction band.

* This notation refers to the states occupied by these electrons in the isolated atom.

JOURNAL OF APPLIED PHYSICS VOLUME 24, NUMBER 10 OCTOBER, 1953

On the Propagation Constant in Gentle Circular Bends in Rectangular Wave Guides—Matrix Theory

A. T. DE HOOP
Technological University, Delft, Netherlands

(Received May 18, 1953)

The propagation constant γ_{mn} of the m,nth mode in a gentle circular bend in a rectangular wave guide is derived with the use of matrix theory.

INTRODUCTION

IN his publication "Reflections from circular bends in rectangular wave guides—Matrix theory"[1] Rice has obtained a general expression for the reflection coefficients due to a gentle bend in a rectangular wave guide. Special attention has been paid to the dominant mode reflection coefficients g_{10}^- and d_{01}^- corresponding to H-bends (magnetic intensity in plane of the bend) and E-bends (electric intensity in plane of the bend), respectively.

However, to obtain the reflection coefficients of the m,nth mode the propagation constant γ_{mn} of this mode must be known. For the latter Rice uses the results obtained by Buchholz[2] and Marshak[3] while using the matrix theory for the aforementioned special cases.

In the present paper it will be shown that extending the work of Rice in both cases (H-bends and E-bends) the propagation constant of the m,nth mode γ_{mn} can be derived with the aid of matrix theory. The results are in accordance with those in reference 1.

1. PROPAGATION OF THE m,nTH MODE IN A GENTLE BEND. H IN PLANE OF THE BEND

In the case of H in plane of the bend we deal with the following form of the vector potential A (see Eq. (1.3-1), reference 1) being $B=0$[4]

$$A=\cos(\pi ny/b)\sum_{l=1}^{\infty}\alpha_{ln}(z)\sin(\pi lx/a), \qquad (1.1)$$

where n has a fixed value and l runs through the values 1, 2, 3, $\cdots$ (Fig. 1). The notations of reference 1 will be followed closely.

In order to determine the propagation constant γ_{mn} we have to find the mth characteristic root of the matrix Γ_a^2 defined by Eq. (1.3-5) of reference 1,

$$\Gamma_a^2=P^{-1}(\Gamma_0^2+S), \qquad (1.2)$$

where

$$P_{rs}=(2/a)\int_0^a(\rho_1^2/\rho^2)\sin(\pi rx/a)\sin(\pi sx/a)dx, \qquad (1.3)$$

$$S_{rs}=-2\pi sa^{-2}\int_0^a\sin(\pi rx/a)\cos(\pi sx/a)dx/\rho, \qquad (1.4)$$

and the elements of the diagonal matrix Γ_0^2 are

$$\delta_l^2=\Gamma_{ln}^2=\sigma^2+(\pi l/a)^2+(\pi n/b)^2, \quad \sigma=i2\pi/\lambda_0, \qquad (1.5)$$

λ_0 = wavelength in free space.

With

$$F=\Gamma_a^2-\Gamma_0^2 \qquad (1.6)$$

Eq. (1.2) becomes

$$F=(P^{-1}-I)\Gamma_0^2+P^{-1}S, \qquad (1.7)$$

where I denotes the unit matrix.

The mth characteristic root of Γ_a^2 is (see Eq. (3.2-2), reference 1)

$$\gamma_m^2=\delta_m^2+F_{mm}+\sum_{s=1}^{\infty}{}'F_{ms}F_{sm}/(\delta_m^2-\delta_s^2), \quad s\neq m. \qquad (1.8)$$

Substituting (1.5) in (1.8) gives

$$\gamma_m^2=\delta_m^2+F_{mm}-\sum_{s=1}^{\infty}{}'F_{ms}F_{sm}a^2/\pi^2(s^2-m^2). \qquad (1.9)$$

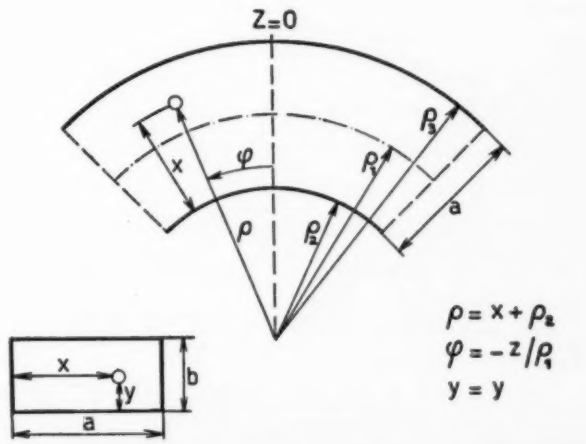

FIG. 1. Coordinate system used in circular bend in a rectangular wave guide.

[1] S. O. Rice, Bell System Tech. J. **27**, 305–349 (1948).
[2] H. Buchholz, Elek. Nachr. Tech. **16**, 73–85 (1939).
[3] R. E. Marshak, "Theory of circular bends in rectangular waveguides," Radiation Laboratory Report (June 24, 1943), pp. 43–45.
[4] S. A. Schelkunoff, *Electromagnetic Waves* (D. Van Nostrand and Company, Inc., New York, 1943), p. 127.

Our first task is to determine the elements of the matrix F by means of the matrix Eq. (1.7). In the case of a gentle bend we have

$$P=I+R, \tag{1.10}$$

where R is a square matrix whose elements are small compared to unity. As the nondiagonal elements must be accurate to within $0(\xi)$, $\xi=a/\rho_1$, and the elements of the principal diagonal to within $0(\xi^2)$, we make use of the asymptotic expansions of R_{ij} and S_{ij} as mentioned in Appendix I, reference 1. When the matrix multiplication is carried out, we find (see Eq. (4.1–4), reference 1)

$$\begin{aligned} F_{ij}&=-R_{ij}\Gamma_{jn}^2+S_{ij},\\ F_{ii}&=\Big(-R_{ii}+\sum_{s=1}^{\infty}R_{is}R_{si}\Big)\Gamma_{in}^2+S_{ii}-\sum_{s=1}^{\infty}R_{is}S_{si}. \end{aligned} \tag{1.11}$$

In our case we need the elements

$$\begin{aligned} F_{ms}&=-R_{ms}\Gamma_{sn}^2+S_{ms},\\ F_{sm}&=-R_{sm}\Gamma_{mn}^2+S_{sm},\\ F_{mm}&=\Big(-R_{mm}+\sum_{s=1}^{\infty}R_{ms}R_{sm}\Big)\Gamma_{mn}^2+S_{mm}-\sum_{s=1}^{\infty}R_{ms}S_{sm}. \end{aligned} \tag{1.12}$$

Because the nondiagonal elements must be accurate to within $0(\xi)$ we have to take the odd values of $s-m$. The value of m is fixed, hence, when m is odd s has one of the values 2, 4, 6, $\cdots$ when m is even s has one of the values 1, 3, 5, $\cdots$. The result is

$$R_{ms}\sim 16\xi ms/\pi^2(s^2-m^2)^2, \tag{1.13}$$

$$S_{ms}\sim 4\xi ms/a^2(s^2-m^2), \tag{1.14}$$

$$R_{sm}\sim 16\xi ms/\pi^2(s^2-m^2)^2, \tag{1.15}$$

$$S_{sm}\sim -4\xi ms/a^2(s^2-m^2). \tag{1.16}$$

The elements of the principal diagonal must be accurate to within $0(\xi^2)$. Hence

$$R_{mm}\sim(\xi^2/4)(1-6/\pi^2m^2), \tag{1.17}$$

$$S_{mm}\sim-\xi^2/2a^2. \tag{1.18}$$

With the values of (1.13)–(1.18) the elements of the matrix F turn out to be

$$\begin{aligned} F_{ms}&=-4\xi ms[4\Gamma_{mn}^2\pi^{-2}(s^2-m^2)^{-2}+3a^{-2}(s^2-m^2)^{-1}],\\ F_{sm}&=-4\xi ms[4\Gamma_{mn}^2\pi^{-2}(s^2-m^2)^{-2}+a^{-2}(s^2-m^2)^{-1}],\\ F_{mm}&=(\xi^2/12)[\Gamma_{mn}^2(1-6\pi^{-2}m^{-2})+6a^{-2}], \end{aligned} \tag{1.19}$$

where in the expressions for F_{ms} and F_{sm} the value of $s-m$ is supposed to be odd.

The summations which arise in the evaluation of F_{mm} are of the type

$$\sum_s s^2(s^2-m^2)^{-p}, \tag{1.20}$$

where the value of $s-m$ must be odd. These summations will be discussed in the appendix. Substitution of the values of (1.19) in (1.9) and use of the sums (1.20) gives the propagation constant γ_{mn} in the bend

$$\gamma_m^2=\gamma_{mn}^2=\Gamma_{mn}^2-(\xi^2/4a^2)[1+\Gamma_{mn}^2a^2(1-6\pi^{-2}m^{-2})+(\Gamma_{mn}a/\pi m)^4(5-\pi^2m^2/3)], \tag{1.21}$$

which is in accordance with Eq. (4.1–10), reference 1.

2. PROPAGATION OF THE m,nTH MODE IN A GENTLE BEND. E IN PLANE OF THE BEND

In the case of E in plane of the bend we deal with the following form of the vector potential B (see Eq. (1.3–11), reference 1), being $A=0$

$$B=\sin(\pi ny/b)\sum_{l=0}^{\infty}\beta_{ln}(z)\cos(\pi lx/a), \tag{2.1}$$

where n has a fixed value and l runs through the values 0, 1, 2, $\cdots$.

In order to determine the propagation constant γ_{mn} we have to find the mth characteristic root of the matrix Γ_β^2 defined by Eq. (1.3–13), reference 1,

$$\Gamma_\beta^2=Q^{-1}(\Gamma_0^2+U), \tag{2.2}$$

where

$$Q_{rs}=(\epsilon_r/a)\int_0^a(\rho_1^2/\rho^2)\cos(\pi rx/a)\cos(\pi sx/a)dx, \tag{2.3}$$

$$U_{rs}=\pi s\epsilon_r a^{-2}\int_0^a\cos(\pi rx/a)\sin(\pi sx/a)dx/\rho, \tag{2.4}$$

where $\epsilon_0=1$ and $\epsilon_r=2$ for $r>0$. The elements of the diagonal matrix Γ_0^2 are

$$\delta_l^2=\Gamma_{ln}^2=\sigma^2+(\pi l/a)^2+(\pi n/b)^2. \tag{2.5}$$

With

$$F=\Gamma_\beta^2-\Gamma_0^2, \tag{2.6}$$

Eq. (2.2) becomes

$$F=(Q^{-1}-I)\Gamma_0^2+Q^{-1}U. \tag{2.7}$$

The mth characteristic root of Γ_β^2 is (see Eq. (3.2–2), reference 1)

$$\gamma_m^2=\delta_m^2+F_{mm}+\sum_{s=0}^{\infty}{}'F_{ms}F_{sm}/(\delta_m^2-\delta_s^2),\quad s\neq m. \tag{2.8}$$

Substituting (2.5) in (2.8) gives

$$\gamma_m^2=\delta_m^2+F_{mm}-\sum_{s=0}^{\infty}{}'F_{ms}F_{sm}a^2/\pi^2(s^2-m^2). \tag{2.9}$$

With the restrictions under consideration and substituting $Q=I+T$ where T is a square matrix whose elements are small compared to unity the elements of the matrix F turn out to be

$$\begin{aligned} F_{ms}&=-T_{ms}\Gamma_{sn}^2+U_{ms},\\ F_{sm}&=-T_{sm}\Gamma_{mn}^2+U_{sm},\\ F_{mm}&=\Big(-T_{mm}+\sum_{s=0}^{\infty}T_{ms}T_{sm}\Big)\Gamma_{mn}^2+U_{mm}-\sum_{s=0}^{\infty}T_{ms}U_{sm}. \end{aligned} \tag{2.10}$$

Using the asymptotic expansions of Appendix I, reference 1, one obtains

$$T_{ms}\sim(\epsilon_m/2)8\xi(m^2+s^2)/\pi^2(s^2-m^2)^2, \quad (2.11)$$

$$U_{ms}\sim(\epsilon_m/2)4\xi s^2/a^2(s^2-m^2), \quad (2.12)$$

$$T_{sm}\sim(\epsilon_s/2)8\xi(m^2+s^2)/\pi^2(s^2-m^2)^2, \quad (2.13)$$

$$U_{sm}\sim-(\epsilon_s/2)4\xi m^2/a^2(s^2-m^2), \quad (2.14)$$

with $m>0$.

The elements of the principal diagonal must be accurate to within $0(\xi^2)$, they turn out to be

$$T_{mm}\sim(\epsilon_m/2)(\xi^2/4)(1+6\pi^{-2}m^{-2}), \quad m>0 \quad (2.15)$$

$$U_{mm}\sim(\epsilon_m/2)(\xi^2/2a^2). \quad (2.16)$$

With the values of (2.11)–(2.16) we obtain the elements of the matrix F

$$\begin{aligned}F_{ms}&=-4\xi[2(m^2+s^2)\pi^{-2}(s^2-m^2)^{-2}\Gamma_{mn}^2\\&\quad+(2m^2+s^2)a^{-2}(s^2-m^2)^{-1}],\\F_{sm}&=-4\xi[2(m^2+s^2)\pi^{-2}(s^2-m^2)^{-2}\Gamma_{mn}^2\\&\quad+a^{-2}m^2(s^2-m^2)^{-1}],\\F_{mm}&=(\xi^2/12)[\Gamma_{mn}^2(1+6\pi^{-2}m^{-2})-6a^{-2}],\end{aligned} \quad (2.17)$$

with $m>0$.

The two series arising in the evaluation of F_{mm} reduce to

$$\sum_s(\epsilon_s/2)(m^2+s^2)^2(s^2-m^2)^{-4}$$

and

$$\sum_s(\epsilon_s/2)m^2(m^2+s^2)(s^2-m^2)^{-3},$$

where the value of $s-m$ must be odd. These series will be discussed in the appendix. Substituting the values of (2.17) in (2.9) and using the results of the appendix gives the propagation constant γ_{mn} in the bend

$$\begin{aligned}\gamma_m^2=\gamma_{mn}^2=\Gamma_{mn}^2+(\xi^2/4a^2)[3-(\Gamma_{mn}a/\pi m)^2(10+\pi^2m^2)\\+(\Gamma_{mn})^4(7+\pi^2m^2/3)],\ m>0\end{aligned} \quad (2.18)$$

which is in accordance with Eq. (4.3-7), reference 1.

Finally, we have to consider the case that $m=0$ and n is arbitrary. However, the value of n has no influence on the determination of the propagation constant γ_{on}, hence we only have to replace Γ_{01} in Eq. (4.3-6), reference 1, by Γ_{on}. The result is

$$\gamma_{on}^2=\Gamma_{on}^2-(\xi^2\Gamma_{on}^2/60)(5+2a^2\Gamma_{on}^2). \quad (2.19)$$

Equations (1.21), (2.18), and (2.19) give the propagation constants for an arbitrary mode generated in a gentle circular bend (either H-bend or E-bend) in a rectangular wave guide. They are correct to within $0(\xi^2)$, where $\xi=a/\rho_1$ and ρ_1 is the radius of curvature of the bend.

APPENDIX

The summations of Sec. 1 reduce to

$$\sigma_p=\sum_s s^2(s^2-m^2)^{-p}, \quad (A.1)$$

where m has a fixed value and $s-m$ must be odd.

At first we consider the case that m is odd, $s=2, 4, 6, \cdots$. As the typical term of σ_p can be expanded in partial fractions,

$$\sigma_p=\sum_s(s^2-m^2)^{-p+1}+m^2\sum_s(s^2-m^2)^{-p}, \quad (A.2)$$

the determination of the summations

$$\tau_p=\sum_s(s^2-m^2)^{-p} \quad (A.3)$$

will be sufficient. Now τ_p can be expanded in the following way:

$$\tau_p=(2m)^{-p}\sum_s[(s-m)^{-1}-(s+m)^{-1}]^p. \quad (A.4)$$

By use of (A.4) we obtain

$$\begin{aligned}\tau_1=(2m)^{-1}\{&[1/(2-m)+1/(4-m)+\cdots+1/(m-4)\\&+1/(m-2)+1/m+1/(m+2)+\cdots]\\&-[1/(m+2)+1/(m+4)+\cdots]\},\end{aligned}$$

or

$$\tau_1=1/2m^2. \quad (A.5)$$

In the same way we obtain τ_2 up to and including τ_5.

$$\tau_2=\pi^2/16m^2-1/2m^4, \quad (A.6)$$

$$\tau_3=-3\pi^2/64m^4+1/2m^6, \quad (A.7)$$

$$\tau_4=\pi^4/768m^4+5\pi^2/128m^6-1/2m^8, \quad (A.8)$$

$$\tau_5=-5\pi^4/3072m^6-35\pi^2/1024m^8+1/2m^{10}, \quad (A.9)$$

By making use of these results we obtain

$$\begin{aligned}\sigma_3&=\pi^2/64m^2,\\\sigma_4&=\pi^4/768m^2-\pi^2/128m^4,\\\sigma_5&=-\pi^4/3072m^4+5\pi^2/1024m^6.\end{aligned} \quad (A.10)$$

When m is even, we obtain for the summations τ_p

$$\tau_1=0, \quad (A.11)$$

$$\tau_2=\pi^2/16m^2, \quad (A.12)$$

$$\tau_3=-3\pi^2/64m^4, \quad (A.13)$$

$$\tau_4=\pi^4/768m^4+5\pi^2/128m^6, \quad (A.14)$$

$$\tau_5=-35\pi^2/1024m^8-5\pi^4/3072m^6. \quad (A.15)$$

By making use of these results we obtain for σ_3, σ_4, and σ_5 the same values as given by (A.10), where m was odd.

The summations arising from Sec. 2 are somewhat more difficult than those of Sec. 1 because of the factor ϵ_s ($\epsilon_s=2$ when $s>0$ and $\epsilon_0=1$). However, carrying out the procedure outlined here, one is led to the same values of σ_3, σ_4 and σ_5 as given in (A.10).

ACKNOWLEDGMENT

The author is indebted to Professor J. P. Schouten of the Technological University Delft for many helpful discussions.

"Brillouin Flow" with Thermal Velocities

J. R. PIERCE AND L. R. WALKER
Bell Telephone Laboratories, Murray Hill, New Jersey

(Received May 19, 1953)

A type of electron flow in a constant magnetic field is described. The beam of electrons is supposed to be everywhere in thermal equilibrium and the usual Brillouin flow is found when the equilibrium temperature tends to zero. Some considerations are put forward bearing on the choice of a suitable beam temperature in specific problems.

THE purpose of this paper is to describe a type of electron flow in a constant magnetic field which is analogous to Brillouin flow[1,2] but which includes the effect of thermal velocities. This is important because it enables us to deduce for an idealized but physically plausible sort of electron flow what portion of the current lies outside a given radius; that is, how large a fraction of the current must be lost if the beam passes through an aperture of a given diameter.

We assume that the electrons in the beam are acted on by electric forces in the r direction which depend on the radius only, and on magnetic forces due to motion in a constant magnetic field of strength B. The equations of motion in the r and θ directions in polar coordinates are

$$F_r = m(\ddot{r} - r\dot{\theta}^2), \tag{1}$$

$$rF_\theta = \frac{d}{dt}(mr^2\dot{\theta}). \tag{2}$$

We make a transformation of coordinates due to Larmor. We let

$$\dot{\theta} = \dot{\theta}_0 + \dot{\theta}_1. \tag{3}$$

Here $\dot{\theta}_0$ is a constant. We also let

$$F_r = F_{re} - er\dot{\theta}B, \tag{4}$$

$$F_\theta = e\dot{r}B. \tag{5}$$

Here F_{re} is the electric force on the electrons. We obtain

$$F_{re} = m(\ddot{r} - r\dot{\theta}_0^2 - 2r\dot{\theta}_0\dot{\theta}_1 - r\dot{\theta}_1^2) + er\dot{\theta}_0 B + er\dot{\theta}_1 B, \tag{6}$$

$$0 = \frac{d}{dt}(mr^2\dot{\theta}_1) + 2mr\dot{r}\dot{\theta}_0 - e\dot{r}rB. \tag{7}$$

We let

$$\dot{\theta}_0 = \tfrac{1}{2}(e/m)B. \tag{8}$$

Then

$$F_{re} - e\left(\frac{1}{4}\frac{e}{m}B^2r\right) = m(\ddot{r} - r\dot{\theta}_1^2), \tag{9}$$

$$0 = \frac{d}{dt}(mr^2\dot{\theta}_1). \tag{10}$$

In our transformed coordinate system the particles move as if in an axially symmetrical electric field specified by a potential V_t which is a function of r only,

$$V_t = V - \tfrac{1}{8}(e/m)B^2r^2. \tag{11}$$

Here V is the actual electric potential.

We will assume without further justification that the charge density of electrons with all velocities in the direction varies with the effective potential V_t as

$$\rho = \rho_0 \exp(eV_t/kT), \tag{12}$$

where T is a temperature assigned to the beam.* Here ρ_0 and e are positive quantities and the charge is negative. We will also use Poisson's equation, which applies to V, not to V_t. We obtain

$$\frac{1}{r}\frac{d}{dr}\left(r\frac{dV}{dr}\right) = \frac{\rho_0}{\epsilon}\exp\frac{e}{kT}\left(V - \frac{1}{8}\frac{e}{m}B^2r^2\right). \tag{13}$$

It is convenient to use the variable

$$U = V - \tfrac{1}{8}(e/m)B^2r^2. \tag{14}$$

Equation (13) then becomes

$$\frac{1}{r}\frac{d}{dr}\left(r\frac{dU}{dr}\right) = -\frac{1}{2}\frac{e}{m}B^2 + \frac{\rho_0}{\epsilon}\exp\left(\frac{eU}{kT}\right). \tag{15}$$

For convenience we may take $U=0$ at $r=0$. For the solutions sought, $dU/dr=0$ at $r=0$.

For Brillouin flow ($T=0$) we have

$$\rho = -\rho_0 = -\frac{\epsilon_0 eB^2}{2m^2}, \quad 0 < r < r_0,$$

$$= 0, \qquad r_0 < r.$$

The total charge per unit length in Brillouin flow is $-\pi r_0^2(\epsilon_0 eB^2/2m^2)$. If the total charge per unit length in the flow under consideration be $-Q$, we may then

[1] L. Brillouin, Phys. Rev. **67**, 260–266 (1945).
[2] J. R. Pierce, *Theory and Design of Electron Beams* (D. Van Nostrand Company, Inc., New York, 1949), chapter IX.

* This amounts to saying that as far as transverse velocities are concerned the electrons are in thermal equilibrium at a temperature T. It would be rash to regard the cathode temperature as the most suitable value for the parameter T in all cases. This matter is discussed in the Appendix.

define a length r_0 by the equation

$$Q=\frac{\pi\epsilon_0 eB^2}{2m^2}r_0^2, \tag{16}$$

and this length will be the radius of a Brillouin flow having the same total charge as the flow considered. We shall use Q and T to characterize the flow and assume that $Q=I_0/V_0$, where V_0 is the mean longitudinal velocity of the beam and I_0, the total current. This is not strictly correct since we have a thermal velocity distribution about the mean longitudinal velocity and the relation between Q and I_0 is thus not unique. However as long as the mean velocity is large compared to the thermal velocity not much harm is done.

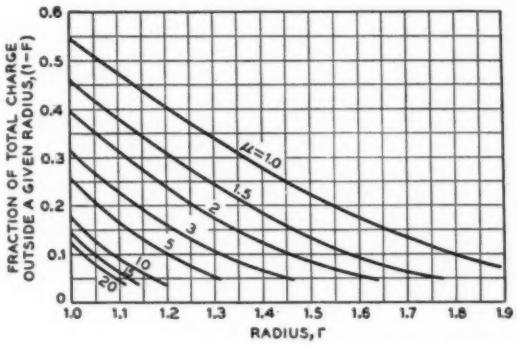

FIG. 1. Fraction of total charge outside a given radius $(1<\mu<20)$.

The charge $-f$, lying between $r=0$ and r, is

$$f=\int_0^r \rho_0 \exp(e/kT)[U]\cdot 2\pi r dr$$

or

$$(\partial f/\partial r)=2\pi\rho_0 r \exp(eU/kT). \tag{17}$$

If $F=f/Q$, the fraction of the total charge lying between 0 and r,

$$1/r(\partial F/\partial r)=(2\pi\rho_0/Q)\exp(eU/kT),$$

or

$$\partial F/\partial S=r_0^2(\pi\rho_0/Q)\exp(eU/kT) \tag{18}$$

if $S=(r^2/r_0^2)$, where r_0 is defined above. Now let us rewrite (15) in terms of S. We have

$$\frac{1}{r}\frac{\partial}{\partial r}\left(r\frac{\partial U}{\partial r}\right)=4\frac{1}{r_0^2}\frac{\partial}{\partial S}\left(S\frac{\partial U}{\partial S}\right)=-\frac{eB^2}{2m}+\frac{\rho_0}{\epsilon}\exp\frac{eU}{kT}$$

or

$$\frac{\partial}{\partial S}\left(S\frac{\partial U}{\partial S}\right)=-\frac{eB^2r_0^2}{8m}+\frac{\rho_0 r_0^2}{4\epsilon}\exp\frac{eU}{kT}$$

$$=-\frac{eB^2r_0^2}{8m}+\frac{\rho_0 r_0^2}{4\epsilon}\cdot\frac{Q}{\pi r_0^2\rho_0}\frac{\partial F}{\partial S}.$$

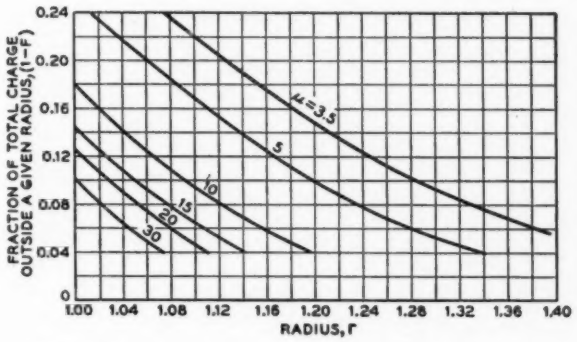

FIG. 2. Fraction of total charge outside a given radius $(3.5<\mu<30)$.

Integrating and recalling that

$$\frac{\partial U}{\partial S}=F=0 \quad \text{at} \quad S=0,$$

we have

$$S\frac{\partial U}{\partial S}=-\frac{eB^2r_0^2}{8m}S+\frac{Q}{4\pi\epsilon}F. \tag{19}$$

But

$$\frac{e}{kT}\frac{\partial U}{\partial S}=\frac{(\partial^2F/\partial S^2)}{(\partial F/\partial S)}$$

and, thus,

$$\frac{\partial^2F}{\partial S^2}=\frac{\partial F}{\partial S}\frac{e}{kT}-\left[\frac{eB^2r_0^2}{8m}+\frac{Q}{4\pi\epsilon}\frac{F}{S}\right]$$

$$=\frac{eQ}{4\pi\epsilon_0 kT}[1-F/S]\frac{\partial F}{\partial S}$$

$$=-\mu[1-F/S]\frac{\partial F}{\partial S}, \tag{20}$$

where

$$\mu=\frac{eQ}{4\pi\epsilon_0 kT}=5.56\frac{I_0}{T_0\sqrt{V_0}}. \tag{21}$$

I_0 is the total current in milliamperes, T_0 is the temperature in thousands of degrees C, and V_0 is the voltage in kv.

Equation (20) now has to be solved subject to $F(0)=0$, $F(\infty)=1$. The solutions depend only upon the parameter μ, which measures the depth of the potential minimum in units of kT. When (20) is solved we have an expression for the fraction F of the total charge lying inside a cylinder of radius $r_0S^{\frac{1}{2}}$ where r_0 is the "cold" Brillouin radius or that calculated for the charge Q assuming $T=0$. The integration of (20) has been carried out for a number of values of μ. Equation (20) is not in a very suitable form for integration since the boundary conditions are given at $S=0$ and $S=\infty$. Putting $F=\mu G$ and $S=\mu t$, we have

$$\frac{d^2G}{dt^2}=-\left[1-\frac{G}{t}\right]\frac{dG}{dt} \tag{22}$$

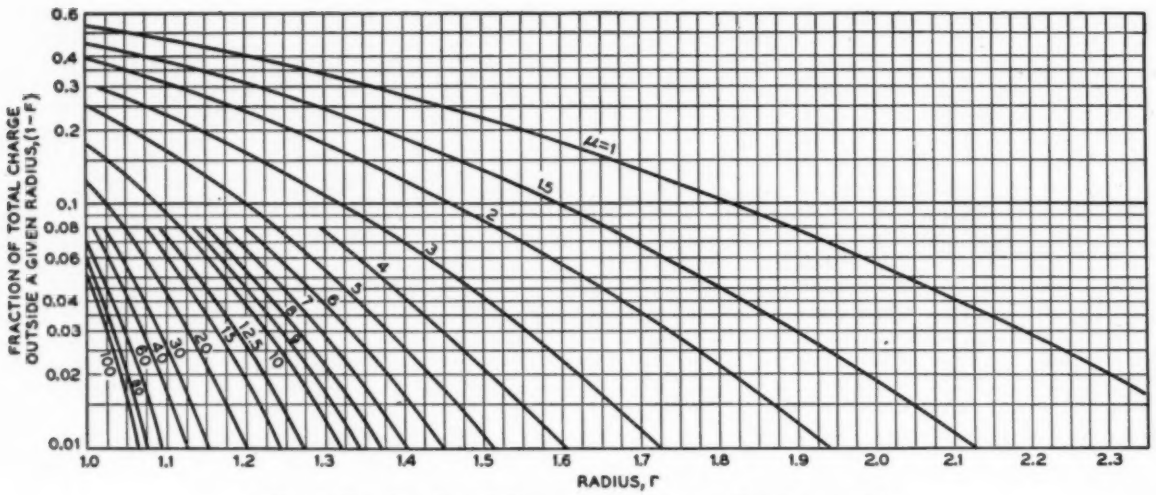

FIG. 3. Fraction of total charge outside a given radius ($1<\mu<100$).

with $G(0)=0$ and $G(\infty)=\mu$. Now any solution of (22) having $G(0)=0$ and $0<(dG/dt)<1$ at $t=0$ will tend to a finite value at $t=\infty$, say μ'. Call this solution $G(t, \mu')$. Then

$$F(S, \mu')=\mu' G\left(\frac{S}{\mu'}, \mu'\right)$$

is a solution of (21) for $\mu=\mu'$. Thus the procedure in integrating is to integrate (22) for suitable initial slopes and find the limiting value μ corresponding to this initial slope. It turns out that the departure of the initial slope from unity decreases extremely rapidly with μ.† It is possible to set up an approximate analytic solution of (22) which can be used to carry one from $t=0$ to a value for which the slope differs from unity by some given amount, say 2 percent. Then the solution may be carried forward numerically by hand calculation.

Figures 1, 2, and 3 show the fraction of the total charge lying outside a given radius as a function of this radius, where the latter is measured in units of the "cold" Brillouin radius.

APPENDIX

If one assumes noninteracting electrons from a cathode at temperature T_c and an electron lens system which produces a perfect image of the cathode with a magnification M, one finds that the transverse velocity distribution of electrons forming the image is very nearly a Maxwellian distribution with a temperature T_c/M^2. We might expect something of the sort; we have changed the beam area by a factor M^2 and we might expect the transverse velocities to be changed by a factor $1/M$, thus giving a distribution corresponding to a temperature of T_c/M^2.

The authors suggest that if the ratio of the nominal or Brillouin beam radius r_0 to the radius of the beam at the cathode is M, it is plausible to use a temperature T_c/M^2.

† It may be shown that for not too small μ, the departure of the initial slope from unity is proportional to $e^{-2\sqrt{\mu}}$.

Erratum: Summation of Slowly Converging Series

[J. Appl. Phys. 24, 1068 (1953)]

IGOR GUMOWSKI
Université Laval, Québec, Canada

A NUMERICAL error, which slipped in during the changing of notation, has been noticed. The constants in the last sentence before the examples should read as follows:

$$b_0=1, \quad b_1=\frac{1}{2}, \quad b_2=\frac{1}{12}, \quad b_3=0, \quad b_4=-\frac{1}{720}, \quad b_5=0, \quad b_6=\frac{1}{30\,240}.$$

Letters to the Editor

Germanium Under Ultrasonic Stress. I: Anelastic Effects

G. S. Baker, L. M. Slifkin, and J. W. Marx
University of Illinois, Urbana, Illinois
(Received June 19, 1953)

PRONOUNCED anomalies have been observed in the temperature dependence of both the Young's modulus and the internal friction of certain germanium single crystals. The original studies were made on five samples, cut in the form of right prisms, with the major axis along the [100] direction. All were obtained from the same large crystal of high purity germanium, kindly supplied by J. Burton of the Bell Telephone Laboratories, which had an initial resistivity of about 30 ohm cm.

Measurements were made by means of the piezoelectric driver-gauge procedure[1] on specimens driven in fundamental longitudinal vibration at 111 kilocycles. The modulus E_{100} for three of the five specimens, measured at vibrational strain maxima of about 10^{-6}, decreased in nearly linear fashion over the temperature range 26°C to 876°C. The temperature coefficient was in excellent agreement with that obtained from previous measurements by Fine[2] over the interval (up to 240°C) in which the two sets of data overlap. This linear temperature dependence has been characterized as *normal*, and is shown by the curve so labeled in the accompanying figure. The logarithmic decrement of the normal

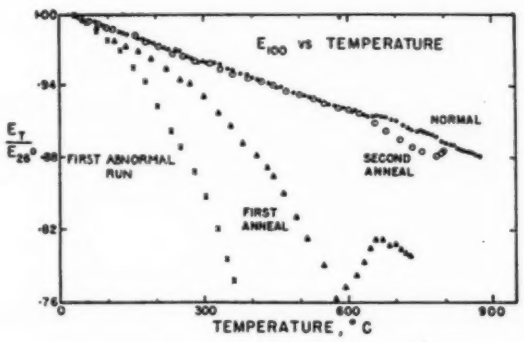

FIG. 1.

specimens, which was of the order of 10^{-5}, showed no marked dependence on temperature as long as the strain maxima were maintained at 10^{-6} or less.

However, two of the five original specimens showed an abnormally large temperature dependence of E_{100}, with the most extreme case illustrated by the curve marked First Abnormal Run in Fig. 1. A very marked temperature dependence of the internal friction was also observed, with the decrement reaching values greater than 10^{-3} above 300°C. After a 12 hour vacuum anneal at 325°C, the same specimen was remeasured, with the results shown by the curve marked First Anneal. An additional anneal of about 12 hours at 500°C served to restore the normal temperature dependence of E_{100} up to 650°C, as indicated by the Second Anneal curve. Abrupt reversals of the kind shown at 570°C on the first anneal curve and at about 770°C on the second anneal data were later observed on other specimens. The greater the departure of E_{100} from normal temperature dependence, the lower the temperature at which the reversal occurs and the more marked the rise.

In all cases the abnormal temperature dependence of the effective Young's modulus is accompained by a large temperature dependent internal friction, an association which suggests that this behavior is caused by the motion of free dislocations. Preliminary measurements indicate a parabolic relationship exists between the abnormal decrement increase $\Delta\delta$ and the abnormal E_{100} decrease ΔE, i.e., $\Delta\delta\alpha(\Delta E)^2$.

It was found that an abnormal effect, qualitatively similar to that described above but of much smaller magnitude, could be produced even at room temperature by severe mechanical shock. When the mechanical shock was administered with the specimen heated to about 125°C the observed abnormality was roughly comparable to, although still less than, that shown by the first anneal curve in the original investigations. It is believed that the original effects may have been produced by handling accidents, or possibly by thermal strain during growth. Quantitative measurements on the effects of loading at higher temperatures are being made. These are complicated by the fact that, unless the specimen is quenched immediately after being stressed, a significant portion of the effect may be lost.

Both normal and abnormal specimens might be expected to contain dislocations, the difference perhaps being that, in the normal material, a saturated Cottrell impurity atmosphere may have accumulated about the dislocations. At high temperatures one might assume the evaporation of impurities from existing dislocations and the freeing of dislocation generators, so that stressing would more readily produce free dislocation lines and result in increased dislocation damping and softer stiffness coefficients.

No statement about the identity of the postulated impurity or impurities can be made at this time. The practice of designating germanium purity on the basis of conductivity may be doubly deceptive. It is obvious that electrically inactive impurities will escape detection, but there is an additional possibility that even the presence of impurities that are normally active electrically may be masked if these lie on dislocation sites.

The writers are indebted to Professor John Bardeen for numerous consultations, and to Professor C. A. Wert and Professor J. S. Koehler for their cooperation during the course of the investigation. The research facilities and funds for this investigation were supplied by the U. S. Office of Naval Research, U. S. Atomic Energy Commission, and Office of Ordnance Research.

[1] J. W. Marx and J. M. Sivertsen, J. Appl. Phys. **24**, 81 (1953).
[2] M. E. Fine, J. Appl. Phys. **24**, 338 (1953).

Germanium Under Ultrasonic Stress. II: Dynamic Yield Point

G. S. Baker, L. M. Slifkin, and J. W. Marx
University of Illinois, Urbana, Illinois
(Received July 3, 1953)

UPON examining the mechanical properties of germanium under static loading at elevated temperatures, Gallagher[1] observed a metallic plasticity, i.e., plastic flow resulting in well defined slip lines, which was characterized by an incubation period that decreased in magnitude as the temperature was raised. In a discussion of this work, Seitz[2] interpreted the data in terms of dislocation-impurity interaction, with the incubation period described in terms of a rate process having an activation energy slightly greater than 1 ev. The term "impurity," as used here, includes actual impurities, vacancies, interstitials of the parent lattice, and broken covalent bonds along the dislocation itself. Seitz pointed out two possibilities:

(1) If the limiting step in the rate process is the actual dissociation of impurity and dislocation, the flow stress should be a unique function of the temperature.
(2) If the rate is determined by the diffusivity of the impurities, the flow stress should exhibit both time and temperature dependence.

The present authors have employed a piezoelectric driver-gauge arrangement[3] to produce vibrational strains ranging up to about 3×10^{-4}, simultaneously measuring the effects of these cyclic

loads upon both the internal friction and the effective elastic moduli of germanium. Both transient and residual effects were observed. In a previous publication, Ge was defined as being normal, in the mechanical sense, if the elastic moduli, measured at strain amplitudes of less than 10^{-6}, exhibited an approximately linear temperature dependence above room temperature. The data reported here were obtained on normal Ge specimens ($\rho \sim 20$ ohm cm), cut with the major axis parallel to a [111] direction and driven in fundamental longitudinal vibration at about 37 kilocycles.

At room temperature E_{111} showed no detectable dependence on strain amplitude ($\Delta E < 0.01$ percent), while the logarithmic decrement first increased slightly, then decreased, remaining within the 10^{-5} region as the vibrational strain maxima was increased from about 10^{-7} to 3×10^{-4}, a change corresponding to a variation in axial stress maxima from about 0.002 kg/mm² to about 5 kg/mm² in the Ge specimen. Although the slip direction in Ge is not yet determined, it follows from the cubic symmetry of the material that the resolved shear stress would be about one-half the axial stress. The decrement behavior is consistent with the

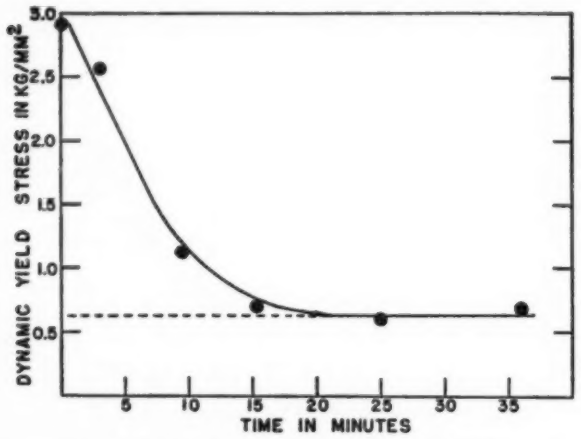

FIG. 1. Decrease in dynamic yield stress as a function of the time at a constant temperature of about 614°C.

"dislocation-in-a-box" model[5] suggested by studies of dislocation damping in metals. No residual change in decrement was produced in the normal material at room temperature by these vibrational stresses.

When the measurements were extended to higher temperatures, it was found that, in the neighborhood of 500°C and above, the specimens exhibited all of the characteristics of a dynamic yield point at the larger strains. The manifestation of the yield phenomena in cyclic loading has been discussed in detail in a separate publication.[5] Although an abrupt increase in the internal friction occurs when the yield stress is reached, this increase is not of itself a sufficient indication of a true yield phenomenon. Such abrupt increases can be associated with vibrational stresses in excess of the elastic limit, even where no yield phenomena occur. The most reliable criterion for the determination of cyclic yield points is the behavior of the effective elastic modulus, as evidenced by the resonant frequency of the specimen, which decreases abruptly when the yield stress is reached *and continues to decrease even though the vibrational stress is reduced*. If the driving frequency of the system is held constant at the resonance frequency at which yielding occurs, a series of periodic pulses, or "gasps," are then observed in the vibrational strain amplitude pattern of the system.[6,7]

The magnitude of the upper cyclic yield stress was observed to decrease with time on standing at constant temperature, as shown in the accompanying figure. In terms of the impurity-dislocation model, these measurements indicate that, at the given loading rate, the initial values of the yield stress are determined by the diffusivity of the impurities, rather than by the dissociation of impurity and dislocation. If sufficient time is allowed, the yield stress reaches a constant value characteristic of a given temperature. The ultimate values at three temperatures were:

Temperature, °C	Ultimate yield stress in kg/mm²
523	1.10
560	0.78
614	0.52

In these experiments, the zero time point was taken as the time at which the yield stress came into the field of view of the apparatus. The present measurements were largely exploratory in nature, with specimen heating rates as low as 1°/minute, so that the time of arrival at a given temperature would not be too significant. In future experiments of this nature it is planned to employ rapid heating rates up to the predetermined temperature, a procedure made possible by these preliminary observations.

In germanium, as in the case of metals subjected to large ultrasonic stresses,[5] there was no evidence of slip lines resulting from this type of cyclic loading. A partial recovery of the large internal friction increase associated with the yield phenomena occurred when the stress was removed. A study of the kinetics of this process is being made and should prove valuable. It is worth noting here that efforts to extend the internal friction and Young's moduli measurements up to the melting point of Ge have been complicated by the fact that the material fails to support its own weight several degrees below melting. The change in dimensions is macroscopic, and it results in a nonsignificant increase of the resonant frequency above 930°C. Below this temperature the nearly linear temperature dependence of the effective elastic moduli, measured at strain maxima less than 10^{-6}, gives no indication of a phase change.

The authors wish to thank Dr. J. Burton, of the Bell Telephone Laboratories, for his assistance in securing germanium crystals.

* This research was supported by the U. S. Atomic Energy Commission, the U. S. Office of Naval Research, and the Office of Ordnance Research.

[1] C. J. Gallagher, Phys. Rev. **88**, 721 (1953).
[2] F. Seitz, Phys. Rev. **88**, 722 (1953).
[3] J. W. Marx and J. M. Sivertsen, J. Appl. Phys. **24**, 81 (1953).
[4] Baker, Slifkin, and Marx (to be published).
[5] J. W. Marx and G. S. Baker (to be published).
[6] S. Takahasni, J. Appl. Phys. **23**, 866 (1952).
[7] J. W. Marx, J. Appl. Phys. **23**, 1406 (1952).

Thermal Effects in Point Contact Rectifiers

H. L. ARMSTRONG*
Radio and Electrical Engineering Division, National Research Council, Ottawa, Canada
(Received March 30, 1953)

A FEATURE of the reverse voltage *vs* current, characteristic for most point contact germanium rectifiers, is the fact that the voltage usually has a maximum, the curve for currents larger than that at which the maximum occurs corresponding to a negative resistance. Figure 1 shows such a characteristic, for a 1N34. It is usually considered that this feature, which is not found in measurements made with sufficiently short pulses, is due to thermal effects.[1-3] This discussion attempts to discuss these effects in terms of a simple model. For this purpose the following assumptions will be made.

(a) In the absence of thermal effects, the reverse current of most ordinary point contact rectifiers, when the applied potential is greater than ten volts or so, is given by

$$i = a \exp[b(v^{\frac{1}{2}} - c)/kT], \qquad (1)$$

i = reverse current; v = reverse voltage; k = Boltzmann's constant; T = absolute temperature (ambient); a, b, and c are constants. Reference 3 gives both theoretical and experimental reasons for believing that this relation is correct.

(b) The contact between the whisker and the germanium is approximately a hemisphere of radius r_0. All the heat developed in the rectifier, which is equal to iv watts, is developed at this

contact. Only a small amount of this heat flows out through the whisker, most of it flowing through the germanium.

(c) The thermal conductivity of germanium varies inversely with temperature, as is true with most nonmetallic crystals.[4] (Certainly it decreases with increasing temperature.[5]) Heat flow in the germanium is radial, and the dimensions are so large compared with r_0 that the piece may be taken as infinite. The temperature at infinity is T, the ambient.

Then the equation of temperature becomes (θ is temperature in the germanium)

$$(2\pi r^2 g/T)(d\theta/dr) = -iv. \tag{2}$$

g/T is the thermal conductivity. Since $\theta \to T$ as $r \to \infty$, the solution is

$$\theta = T \exp(iv/2\pi gr). \tag{3}$$

Now when thermal effects occur in the rectifier, the temperature at $r = r_0$, as given by (3) should be substituted for the ambient temperature in (1). This gives

$$i = a \exp[(bv^{\frac{1}{2}} - c)(e^{-iv/2\pi gr_0})/kT], \tag{4}$$

A new constant, i_s is now defined by

$$i_s = a \exp(-b/kT). \tag{5}$$

The advantage of this is that, when thermal effects are negligible

$$i = i_s \exp(bv^{\frac{1}{2}}/kT) \tag{6}$$

thus plotting $\ln i$ *vs* $v^{\frac{1}{2}}$ gives a straight line,[3] of intercepted i_s and slope b/kt.

For the 1N34 of Fig. 1, such a plot, of results taken at about 300°K, gave $b/kt = 0.58$, $i_s = 18\mu a$. Also, at that temperature, c/kt is expected to be about 28.

When these values are inserted, (4) can be put into the form

$$(28 - 0.58v^{\frac{1}{2}})/(24 - \ln i) = \exp(iv/2\pi gr_0) \tag{7}$$

or

$$\ln\{(1 - 0.0207v^{\frac{1}{2}})/(24 - \ln i)\} = (iv/2\pi gr_0) - \ln 28. \tag{8}$$

Figure 2 is a plot of the quantity on the left of Eq. (8) *vs* iv, the data being those shown in Fig. 1. A reasonable fit is obtained to a straight line, of slope about 0.2. The theoretical slope should be $1/2\pi gr_0$. If one takes from reported measurements[5] $g \sim 180$ watts/cm, and assumes $r_0 \sim 10^{-3}$ cm, the theoretical slope is about 1. This agrees in order of magnitude, which is perhaps all that can be expected from so simple a model. If heat flow through the whisker, etc. were allowed for, this would roughly have the effect of increasing g, which would change the result in the right direction. A further possibility is to determine the point of maximum

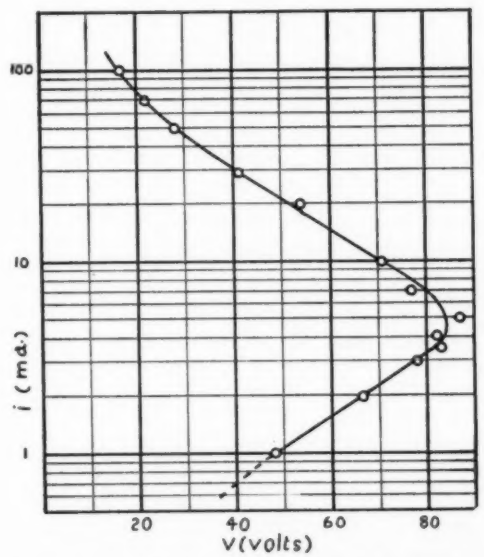

FIG. 1. Reverse characteristics of a 1N34 rectifier.

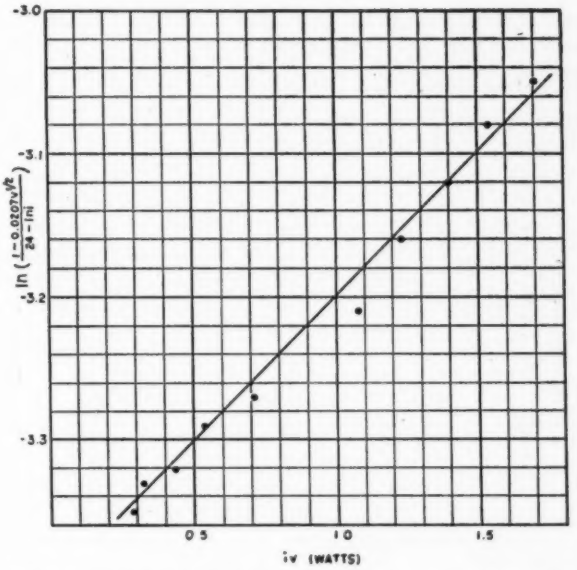

FIG. 2. Characteristic shown in Fig. 1 replotted according to Eq. (8).

voltage. This comes when $dv/di = 0$. If we write (4) in the form

$$f(i, v) = i - a \exp[bv^{\frac{1}{2}} - c][\exp(-iv/2\pi gr_0)/kT] \equiv 0, \tag{9}$$

and by the methods of implicit functions,[6] it is seen that $dv/di = 0$ when $\partial f/\partial i = 0$. This, with some manipulation, gives, at the maximum point

$$\exp iv/2\pi gr_0 = iv(c - bv^{\frac{1}{2}})/2\pi gr_0 kT. \tag{10}$$

Since, at the voltages concerned $bv^{\frac{1}{2}} \ll c$, and $c/kT \gg 1$, this gives approximately

$$iv = 2\pi gr_0 kT \tag{11}$$

at the maximum.

Since i increases rapidly with temperature, this predicts that the maximum voltage will decrease rapidly with increasing temperature. Moreover, units having the smallest reverse currents at low voltages should have the highest maximum voltage. Both of these predictions are known to be qualitatively true.

If results from the 1N34 used here are put in (11), at the maximum point $iv \approx 0.4$ watt, and from the figures already given $2\pi gr_0 kT/c \approx 0.04$. Again, the effect is as if g were too small, and the agreement could be improved by some allowance for heat lost otherwise than through the germanium.

In the development of these ideas, the author obtained much assistance from discussions with Dr. J. H. Simpson of this laboratory.

* Now at Clevite-Brush Development Company, Cleveland, Ohio.

[1] E. Billig, Phys. Rev. **87**, 1060 (1952).
[2] L. P. Hunter, Phys. Rev. **81**, 151 (1951).
[3] J. H. Simpson and H. L. Armstrong, J. Appl. Phys. **24**, 25 (1953).
[4] C. Kittel, *Introduction to Solid State Physics* (John Wiley and Sons, Inc., New York, 1953), p. 82ff.
[5] A. Grieco and H. G. Montgomery, Phys. Rev. **86**, 570 (1952).
[6] F. S. Woods, *Advanced Calculus* (Ginn and Company, New York, 1934), second edition, p. 93.

The Electromotive Force Developed by a Creeping Zinc Crystal

FRANCES DUNKLE COFFIN AND SIDNEY L. SIMON
Lewis Flight Propulsion Laboratory, National Advisory Committee for Aeronautics, Cleveland, Ohio

(Received June 8, 1953)

SINCE the work of Roscoe[1] in 1936, it has been recognized that the nature of the surface affects the creep characteristics of a metal. The electromotive force produced by a given metal electrode is also known to be extremely sensitive to the surface

state of the metal and to the amount of cold work which it has undergone. Experiments carried out in this laboratory as part of a study of surface effects on creep have indicated that the creep rate of a zinc single crystal is increased if the surface is slowly electropolished during creep, and that a reversal of the current will cause the creep rate to decrease (Fig. 1).

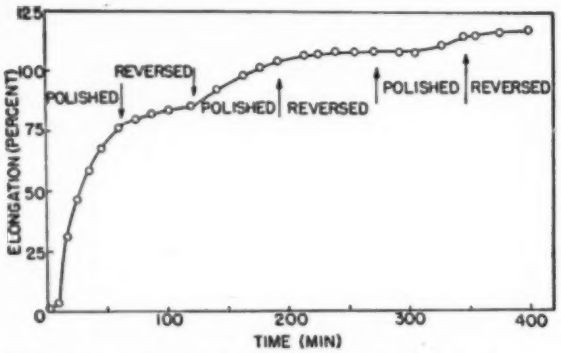

FIG. 1. Effect of alternate electropolishing and plating on the creep rate of a zinc single crystal. Crystal number, 48-F, initial stress = 129 g/mm², 24.5°C.

In view of these facts, additional experiments were undertaken to measure the emf developed by a creeping crystal and to see what correlations might be made between the surface state, the cold work undergone by the crystal, and the emf developed. The crystals were prepared in the manner previously described.[2] All except the active section of the crystal was insulated from the electrolyte with a thin coating of paraffin. A glass hook fused to the bottom of the cell served to support one end of the crystal, and the load was attached to the opposite end. The cell used for the measurements may be represented as follows:

$$\mathrm{Zn(crystal)/0.01}M\ \mathrm{ZnSO_4/Zn(polycrystalline)}.$$

The reference electrode was wire of the same diameter as the crystal. A Brown recording potentiometer was used to measure the emf developed, and the elongation was followed with a cathetometer.

A nominal load of 5 g was used to support the crystal in position until the actual load was applied. The cell was allowed to come to thermal and electrical equilibrium overnight before loading. The emf of the unloaded crystal varied from section to section, and seemed to be slightly orientation dependent. When the load was applied, a sudden increase in emf occurred. This sharp rise was then followed by a gradual decay to a value which was different from that observed before loading. This is illustrated in Fig. 2, where the circles give the emf in millivolts *vs* time, and the triangles the percent elongation *vs* time. This curve, which is typical of many recorded shows that the creeping wire becomes more negative when loaded, i.e., has a greater tendency to go into solution.* The creep curve may be represented by the equation $e=at/(1+bt)$, where e = elongation in cm/cm, t = time in minutes, $a=1.30\times10^{-2}$, and $b=1.35\times10^{-3}$. The applied stress was 94 g/mm².

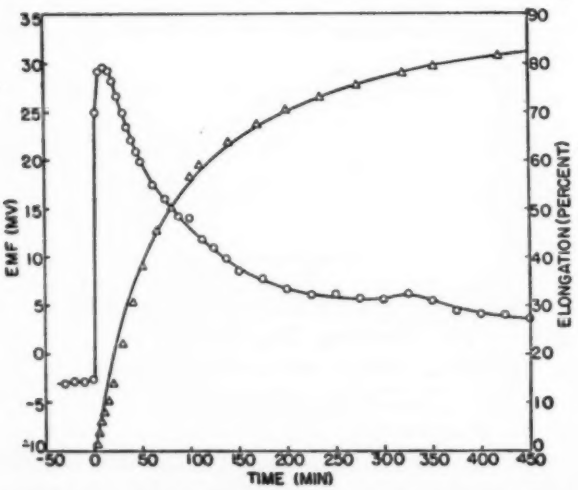

FIG. 2. Electromotive force developed by a creeping zinc crystal (circles). The triangles represent the creep curve of the crystal. Crystal number X-3, initial stress = 94 g/mm², 30°C.

This sudden emf which is generated appears to be the result of the plastic deformation rather than a change in the nature of the crystal surface, since if the crystal is unloaded before the final equilibrium value is approached, a sudden drop in emf is observed. Additional loads applied to the creeping crystal result in new emf peaks of the same order of magnitude, but of much shorter duration.

From emf studies of this type, much interesting thermodynamic data for the creeping crystal may be obtained. By correlation of the amount of work done on the crystal, the free-energy changes, and the influence of temperature and load on the emf, it should be possible to estimate the entropy changes within the crystal.

[1] R. Roscoe, Phil. Mag. **21**, 399 (1936).
[2] F. D. Coffin and A. L. Weiman, J. Appl. Phys. **24**, 282 (1953).
* Because of the small scale employed in Fig. 2, it is impossible to reproduce all of the detail visible in the chart from the recorder. Fluctuations of less than 1 mv have not been plotted; the significance of these is uncertain at present.

Erratum: The Potential of Two Current Point Sources in a Homogeneous Conducting Prolate Spheroid

[J. Appl. Phys. **24**, 496–497 (1953)]

JAMES R. WAIT
Radio Physics Laboratory, Defense Research Board, Ottawa, Canada

The factor

$$\frac{(n-m)!}{(n+m)!}$$

in Eqs. (7) and (9) should be replaced by

$$\left[\frac{(n-m)!}{(n+m)!}\right]^2.$$

Time Effects in the Hysteresis Loop of Polycrystalline Barium Titanate

MALCOLM MCQUARRIE
Sprague Electric Company, North Adams, Massachusetts
(Received June 8, 1953)

IT is known that polycrystalline barium titanate exhibits a decrease of capacitance with time.[1–3] In studying this effect we have noted changes in the hysteresis loops at 60 cycles similar to those found by Kambe[4] and Young[5] in their study of the effect of voltage on the hysteresis loops.

We find that a "new" specimen (very recently cooled from a temperature above the Curie temperature) has the usual hysteresis loop as shown in Fig. 1(A), but that as the material ages, the maximum polarization and the remnant polarization decrease by about the same absolute amount (with consequently a relatively larger decrease in the area of the hysteresis loop), until the loop shows a distinct propellor shape, as shown in Fig. 1(B).

This effect can be partially reversed by application of a strong alternating field for several minutes or by heating to a temperature below the Curie temperature. Heating to a temperature above the Curie temperature completely restores the original loop form.

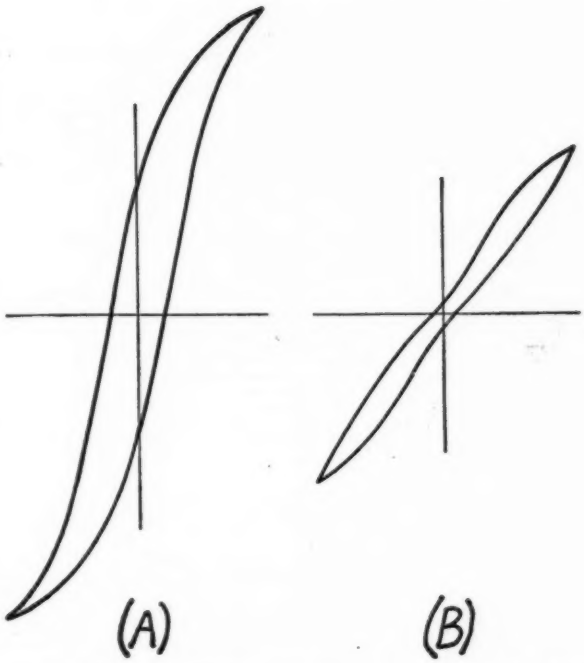

FIG. 1. Hysteresis loops of polycrystalline barium titanate (A) immediately after cooling from above the Curie temperature and (B) after remaining for several weeks at 25°C. Both loops taken on the same piece (a disk about 0.5 mm thick and 1.2 cm in diameter) under the same voltage (about 560 volts peak, 60 cycles).

These effects are consistent with measurements of the dielectric constant and dissipation factor at low field strengths. It is found that the percentage decrease in power factor is about ten times the percentage decrease in capacitance for the same length of time.

Apparently the process is a "settling" of the domain configuration into a more stable one through a time-consuming process. This "settled" state can be upset by the input of mechanical, electrical, or thermal energy to the system. However, in the case of mechanical or electrical energy the specimen is destroyed before complete reversal of the process (which can be achieved by heating above the Curie temperature) is attained.

[1] R. R. Roup, Am. Ceram. Soc. Bull. 29, 160 (1950).
[2] Novosil'tsev, Khodakov, and Schulman, Doklady Akad. Nauk, S.S.S.R. 83, 829 (1952).
[3] B. H. Marks, Electronics 21, (8) 116 (1948).
[4] K. J. Kambe, J. Phys. Soc. Japan 8, 15 (1953).
[5] D. R. Young, J. Appl. Phys. 22, 523 (1951).

Erratum: Instabilities in the Smooth-Anode Cylindrical Magnetron

[J. Appl. Phys. 23, 562–567 (1952)]

LAWRENCE A. HARRIS
University of Florida, Gainesville, Florida

Equation (38) should read

$$E\theta = (1/r)(\partial\varphi/\partial\theta) = +(n/r)(m/e)\omega\eta F_1 e^{j\psi}.$$

This correction changes the sign of Y_2 in Eqs. (39), (48), and (49). Finally, Eq. (53) becomes

$$\omega = -n\omega_H \pm [2\omega_H^2/(1+g_1)]^{\frac{1}{2}}.$$

These changes invalidate the previous conclusions and show that the smooth-anode magnetron is a stable system with a set of real characteristic frequencies.

The author is grateful to Dr. J. R. Pierce for inquiries leading to the discovery of this error and to Mr. S. P. Yu for checking all the calculations.

A Note on Shock Propagation in Brass

JACOB SAVITT
U. S. Naval Ordnance Laboratory, White Oak, Maryland
(Received May 6, 1953)

IN a recent paper, Shreffler and Deal[1] describe a photographic technique for the study of the free surfaces of metals under the accelerations produced by the detonation of high explosives. The high precision measurements of the initial free surface velocities of naval brass plates, in contact with Composition B explosive as a function of plate thickness which they present, show a very special and interesting discontinuity when plotted as shown in Fig. 1. The reciprocal of the initial free surface velocity of the

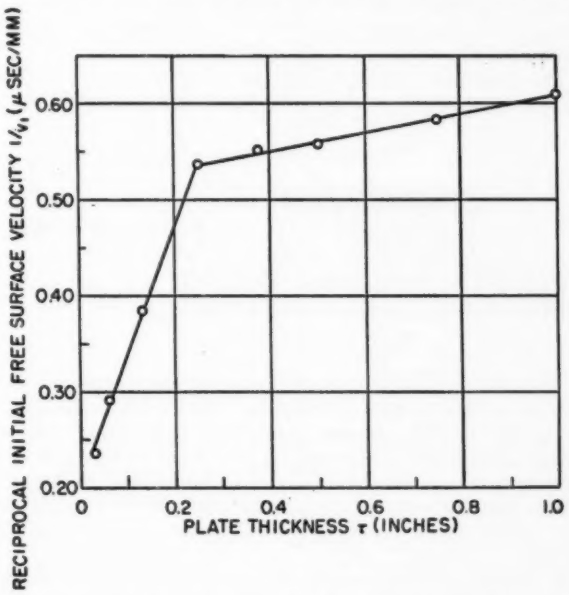

FIG. 1. Special plot of the Shreffler-Deal initial free surface velocity of explosive accelerated naval brass plates showing the discontinuity in the slope of $1/v_1$.

brass plate $1/v_1$ is apparently a linear function of the plate thickness τ. For τ greater than $\frac{1}{4}$ inch the rate of change of $1/v_1$ with respect to τ is less than ten percent of that observed for τ less than $\frac{1}{4}$ inch. The mechanism responsible for this very real abrupt change in slope is not clear.

[1] R. G. Shreffler and W. E. Deal, J. Appl. Phys. 24, 44 (1953).

Molded Thermionic Cathodes

D. MACNAIR, R. T. LYNCH, AND N. B. HANNAY
Bell Telephone Laboratories, Inc., Murray Hill, New Jersey
(Received June 29, 1953)

MOLDED thermionic cathodes have been developed which consist of sintered mixtures of nickel powder and alkaline earth oxides. Coomes and Forsbergh[1] made studies of a similar system; no information concerning their findings has been published, however.

With only a small loss in emission levels as compared with sprayed oxide cathodes, the molded cathodes offer many advantages in ruggedness. They show great resistance to deactivation effects such as gas attack, ion bombardment, and the drawing of high dc currents. The emitting material, which presents a metallic-like surface, may be machined directly, and a variety of forms are readily fabricated. As practical thermionic emitters, particularly in applications demanding ruggedness of the cathode, molded cathodes are believed to be very promising. The cathodes are made by compressing mixtures of nickel powder and alkaline

earth carbonates, in suitably shaped steel dies, by means of a laboratory hydraulic press. The pressed form is sintered after ejection from the die. After sintering, the cathode may be machined to any desired shape. Special geometries, such as are used in certain gun-type cathodes, can be machined, but for structures of this type this machining operation may be eliminated by the use of a properly shaped plunger in the pressing operation. Becker, Biondi, and Robinson of these Laboratories have devised a method for making molded cathodes in the form of sleeves, such as are used in magnetrons; the preparation of molded cathodes for this purpose involves many fewer steps than does the commonly used matrix cathode.

In Fig. 1 is shown a typical cathode structure. The emitting mixture comprises only the top 0.003—0.005 in. of the molded cathode, the remainder being pure nickel. This is done to keep breakdown times to the order of a few minutes.

The pulsed saturation emission as a function of temperature, for the molded and five other types of cathodes, is shown in Fig. 2.

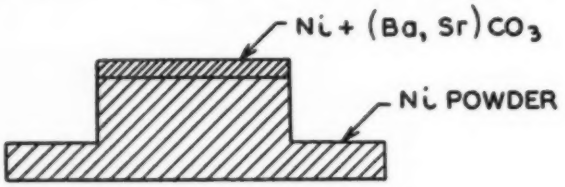

FIG. 1. Typical molded cathode.

In addition, a curve showing dc emissions for a typical molded cathode is shown. Because of their resistance to deactivating effects, the molded cathodes permit the drawing of higher dc current densities than are practicable with sprayed cathodes, by operating the molded cathode at, e.g., 900–950°C. dc currents greater than 10 amp/cm² have been drawn at 950–1000°C for brief periods; no life studies have been conducted at these current densities.

As molded cathodes appear particularly interesting for high anode voltage applications, the majority of the life tests have been carried out under such conditions. Lives up to 5000 hours are obtained with cathodes operating at 851°C, drawing 500 ma/cm² at an anode voltage of 500v. Life tests at 1200v have given similar results.

Molded cathodes have been exposed to 1 atmos of air at room temperature and at operating temperatures, with no effect on their activity. In some cases, this has been done several times on a single cathode with complete recovery of the emission after each exposure. Cathodes that have been operated for some time have been removed from tubes, exposed to laboratory air for a week or more, remounted in a tube, and have shown full activity immediately, with little degassing. Under dry conditions the breakdown of the cathode before mounting in the tube is feasible, for example by carrying out the sintering process in vacuum.

Comparative data on the resistance of sprayed and molded cathodes to deactivation by O_2 and CO have been obtained. The two types of cathodes were studied in a pump station arranged so that a parallel flow of gas through the two tubes could be obtained under conditions of continuous pumping. By using adjustable leaks, any steady-state pressure could be obtained in the tubes. For these tests, in order to have similar dc emission densities, the molded cathodes were operated at 850°C, and the sprayed cathodes, which used an active nickel base, at 800°C. The gas exposure was carried out with the cathodes at these temperatures, as were the emission tests which were made immediately after the gas was pumped out. Typical results obtained were as follows: One minute of O_2, at a pressure of 2×10^{-5} mm, deactivated a sprayed cathode from 35 ma to 10 ma, although it could be reactivated rather readily; 10 min exposure to O_2 at 4×10^{-5} mm then reduced the current from this cathode from 35 ma to <0.1 ma. Reactivation was now more difficult, but could still be accomplished. Finally, 30 minutes exposure to O_2, at a pressure of

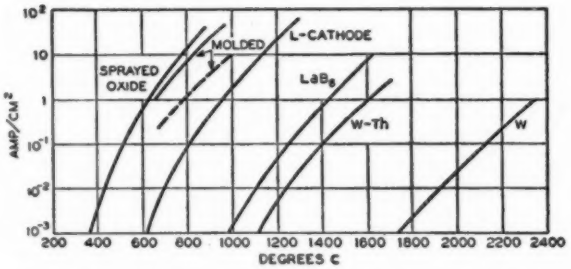

FIG. 2. Pulsed saturation emission as a function of temperature for several types of cathodes. Temperatures given are true temperatures. Two curves are given for the molded cathode, (70 percent nickel—30 percent double carbonate). The full curve represents pulsed saturation emission, and the dotted curve shows dc levels. The curves for the sprayed cathode, thoriated tungsten, and tungsten have been taken from Hermann and Wagener, *The Oxide-Coated Cathode* (Chapman and Hall, Ltd., London 1951), p. 96. The LaB_6 data are from Lafferty, J. Appl. Phys. **22**, 229 (1951). The L-cathode data are from Lemmens, Jansen, and Loosjes, Philips Tech. Rev. **11**, 341 (1950). The latter authors present a figure similar to this for several of these cathodes.

4×10^{-5} mm deactivated the sprayed cathode to a few microamperes, and reactivation attempts failed to produce appreciable currents. Under these same conditions, the molded cathodes were completely unaffected or showed only minor, transitory effects in their thermionic activity (within 10 percent of their initial activity in either direction).

Likewise, with exposure to CO at pressures up to 1×10^{-4} mm and times up to 30 minutes, the sprayed cathodes showed large deactivation effects, similar to the data quoted for O_2, with only slight variations appearing for the molded cathodes.

Using the procedure just described, comparative tests of sprayed and molded cathodes were made under ion bombardment conditions. The tests were similar to those described above, with the exception that high anode voltages were applied during the gas exposure. With argon at 1×10^{-4} mm pressure, and anode voltages of 1100 volts, a fivefold decrease in the sprayed cathode emission was observed in 1–2 hours, with no significant change in the molded cathode emission. Examination of the cathode surfaces showed that most of the coating had been knocked off the sprayed cathode by the ion bombardment, with relatively minor mechanical deterioration of the molded cathode surface, as might be expected in view of its essentially metallic character.

[1] E. A. Coomes and P. W. Forsbergh, Jr., U. S. Patent No. 2,543,439.

On the Synthesis of Reactance 4-Poles

HERBERT J. CARLIN AND R. LA ROSA
Microwave Research Institute, Polytechnic Institute of Brooklyn, Brooklyn, New York

(Received June 15, 1953)

BY utilizing a recent theorem of Belevitch[1] on the realizability of an n-terminal pair network (n port) in terms of scattering coefficients, it is possible to derive in a direct fashion general formulas for the elements of the impedance or admittance matrix of a lossless 2-port which, when terminated in a resistor, realizes a prescribed physical driving point impedance. Also these formulas may be used to specify a reactive transducer which, when operated between resistive terminations, realizes a physical insertion gain function. Solutions of this problem have also been given by Darlington[2] and Cauer,[3] but the derivation given here is especially simple and straightforward.

Suppose a gain function of a real angular frequency variable is specified $G(\omega)=P/N$, where P and N are even polynomials in ω, and $0\leqslant G(\omega)\leqslant 1$, $-\infty\leqslant\omega\leqslant\infty$. G is the ratio of powers delivered to a unit resistive load from a generator with one ohm internal resistance with and without the required reactive 2-port inserted between load and generator terminals. In references 2 and 3, P and N were multiplied by common factors to make P a perfect

square. The derivation which follows does not require this, though the final formulas lead to the same networks.

The function G defined above is precisely equal to the squared amplitude of the voltage scattering coefficient S_{12} of the desired reactive 2-port, $G(\omega)=|S_{12}(j\omega)|^2$. Since this function is even and positive, it may be written

$$|S_{12}(j\omega)|^2=\frac{P}{N}=\frac{q_0-pr_0}{u_2-pv_2}\frac{q_0+pr_0}{u_2+pv_2}, \tag{1}$$

where q_0, r_0, u_2, v_2 are even polynomials in $p=j\omega$ with real coefficients. The pairs oj factors of Eq. (1) are respectively conjugate along $j\omega$. Factors indicated with the plus sign contain no right half p plane roots, and those with the minus sign contain no left half p plane roots. Since the voltage scattering matrix must be symmetric, unitary, and its elements analytic in the right half p plane,[1] the following equations hold for the voltage scattering functions:

$$S_{12}=S_{21}=\pm\frac{q_0-pr_0}{u_2+pv_2}, \tag{2}$$

$$S_{11}=\frac{u_1+pv_1}{u_2+pv_2}, \tag{3}$$

$$S_{22}=-S_{11}^*\frac{S_{12}}{S_{12}^*}=-\frac{u_1-pv_1}{u_2+pv_2}\frac{q_0-pr_0}{q_0+pr_0}. \tag{4}$$

u_1 and v_1 are even polynomials in p with real coefficients. u_1+pv_1 may have left and right half p plane zeros and are found by factoring the numerator of

$$|S_{11}(j\omega)|^2=1-|S_{12}(j\omega)|^2=\frac{(u_1-pv_1)}{(u_2-pv_2)}\frac{(u_1+pv_1)}{(u_2+pv_2)} \tag{5}$$

into a pair of polynomials which are conjugates along $p=j\omega$, as indicated in Eq. (5).

It will be noted that S_{12} in Eq. (2) is given with no left half p plane root factors. From Eq. (4) this assures the analyticity of S_{22} in the right half p plane as well as the satisfaction of the unitary requirements. However, it is also permissible (not necessary) for S_{12} to have left half p plane roots if it also has additional zeros in the right half p plane symmetrically located with respect to the imaginary p axis. The additional factors occur when the polynominal P is a perfect square. In this case, the resulting networks will generally be simpler if S_{12} is chosen with symmetric root factors (Eq. (4) shows that the pairs of factors then cancel out of S_{22}) rather than all in the right half plane, though either option leads to a physical network. It is clear, therefore, that a reactive 2-port cannot be a minimum phase shift network unless all its zeros of transmission occur at real frequencies.

If a physical input impedance is specified,

$$Z=\frac{m_1+pn_1}{m_2+pn_2}, \tag{6}$$

where m_1, m_2, n_1, n_2 are even polynomials in p, the voltage scattering coefficients of a reactive 2 port, which when terminated in unit resistance has an input impedance equal to Z, may be derived. These are the same as given in Eqs. (2)–(4) with

$$S_{11}=\frac{Z-1}{Z+1}=\frac{u_1+pv_1}{u_2+pv_2} \tag{7}$$

and

$$m_1m_2-p^2n_1n_2=P=(q_0-pr_0)\ (q_0+pr_0). \tag{8}$$

The voltage scattering matrix (S) may now be transformed into an impedance or admittance matrix by

$$[Z]=[I-[S]]^{-1}[I+[S]], \tag{9}$$

$$[Y]=[I+[S]]^{-1}[I-[S]]. \tag{10}$$

I is the identity matrix.

If both $[I-[S]]$ and $[I+[S]]$ are singular the reactive two-port network is realized by an ideal transformer. In the nondegenerate case substituting the elements of $[S]$ as given by Eqs. (2)–(4) into Eqs. (9) and (10) yield:

$$z_{11}=\frac{EvS_{12}^*(1+S_{11})}{OdS_{12}^*(1-S_{11})}=\frac{A}{pB}, \tag{11}$$

$$z_{22}=\frac{EvS_{12}^*(1-S_{11})}{OdS_{12}^*(1-S_{11})}=\frac{C}{pB}, \tag{12}$$

$$z_{12}=\frac{|S_{12}|^2}{OdS_{12}^*(1-S_{11})}=\frac{\pm P}{pB}, \tag{13}$$

and

$$y_{11}=\frac{EvS_{12}^*(1-S_{11})}{OdS_{12}^*(1+S_{11})}=\frac{C}{pD}, \tag{14}$$

$$y_{22}=\frac{EvS_{12}^*(1+S_{11})}{OdS_{12}^*(1+S_{11})}=\frac{A}{pD}, \tag{15}$$

$$y_{12}=\frac{|S_{12}|^2}{OdS_{12}^*(1+S_{11})}=\frac{\pm P}{pD}, \tag{16}$$

where Ev="Even part of," Od="Odd part of."

$$A=q_0(u_2+u_1)+p^2r_0(v_2+v_1)=q_0m_1+p^2r_0n_1, \tag{17}$$

$$B=q_0(v_2-v_1)+r_0(u_2-u_1)=q_0n_2+r_0m_2, \tag{18}$$

$$C=q_0(u_2-u_1)+p^2r_0(v_2-v_1)=q_0m_2+p^2r_0n_2, \tag{19}$$

and

$$D=q_0(v_2+v_1)+r_0(u_2+u_1)=q_0n_1+r_0m_1. \tag{20}$$

Since Eqs. (11) through (16) were derived directly from a scattering matrix satisfying all the Belevitch criteria, they must be physically realizable by a reactive 2-port with lumped passive elements.

* Indicates complex conjugate along $j\omega$.

[1] V. Belevitch, Ann. Tele. **6**, 302–312 (1951).
[2] S. Darlington, J. Math. and Phys., **28**, 257–353 (1939).
[3] W. Cauer, E.N.T., vol. 16, p. 161–163 (1939) (in German).

Shot Noise in Junction Transistors

H. C. Montgomery and M. A. Clark
Bell Telephone Laboratories, Murray Hill, New Jersey
(Received July 20, 1953)

MEASUREMENTS of the noise figure of a recent p-n-p alloy transistor (Fig. 1) showed the familiar $1/f$ spectrum at low frequencies, leveling off to about 3 db at higher frequencies. The level portion of the noise-figure spectrum agrees with a simple calculation based on thermal noise in the body resistance and shot noise in the junctions. This is believed to be the first time that transistor noise figure measurements have been in agreement with calculations from basic physical principles, thus fulfilling the hope expressed by Shockley in 1950 that "noise will be reduced toward the minima set by Johnson and shot noise."[1] The calculation does not cover the low frequency $1/f$ portion,

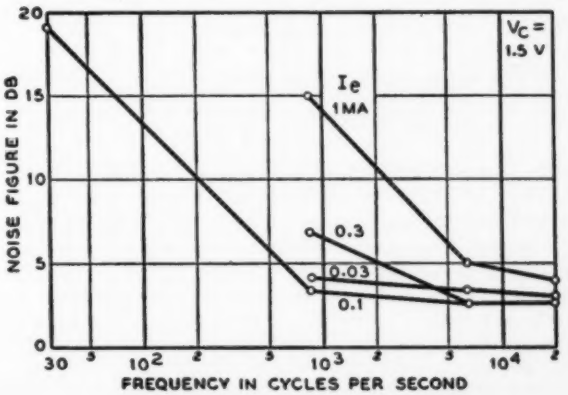

FIG. 1.

which is still unexplained, but does define a minimum limit on noise performance.

Thermal noise is associated with the spreading resistance R_b of the base region, given by the Nyquist relation

$$v^2=4kTR_b \tag{1}$$

(unit band width, k=Boltzmann's constant; T=absolute temperature). Similar noise voltages associated with emitter and collector body resistance are usually negligible.

Shot noise arises in the emitter and collector junctions because of the discrete and random nature of conduction of charge across the junction.[3] The shot noise current in the emitter junction is given by the Schottky formula

$$i^2=2qI_e$$

(q=electronic charge, I_e=emitter current). An additional component due to the saturation current is negligible under the usual bias conditions. The dynamic resistance r_e of the emitter junction is approximately kT/qI_e (again neglecting saturation current), which gives

$$v^2=i^2r_e^2=2kTr_e. \tag{2}$$

In the case of the collector junction, only the saturation current I_{co} contributes to the shot noise, since the balance of the current is a facsimile of the emitter current (at least up to frequencies where transit effects in the base region are important):

$$v^2=i^2r_c^2=2qI_{co}r_c^2 \tag{3}$$

(r_c=collector junction resistance).

Expressions (1), (2), and (3) represent equivalent noise voltages in series with the base, emitter, and collector terminals, respectively. From these, one can calculate the noise figure of the transistor[3] for grounded base operation from a generator impedance R_g:

$$F=1+\frac{R_b}{R_g}+\frac{1}{2}\frac{r_e}{R_g}\left[1+\frac{I_{co}}{I_e}\left(\frac{R_g+r_e+R_b}{\alpha r_e}\right)^2\right]. \tag{4}$$

Noise figures calculated from (4) are compared in the table with the measured volumes at 20 kc for the transistor of Fig. 1.

$I_{co}=3.4\times10^{-6}$ amp, $\alpha=0.9375$, $R_b=302$ ohms, $r_e=0.026/I_e$ ohms

I_e	0.03	0.1	0.3	1	milliamp
F (calculated)	3.1	2.0	1.6	1.5	db
F (measured)	3.0	2.7	2.8	3.7	db

Petritz[4] has calculated noise behavior from a rather different viewpoint. His results are of the same order of magnitude but differ in some detail from those calculated here. The limited experimental data presented here are inadequate to differentiate between the two methods.

[1] W. Shockley, *Electrons and Holes in Semiconductors* (D. Van Nostrand Company, Inc., New York, 1950), Sec. 12.1.
[2] V. F. Weisskopf, "On the Theory of Noise in Semiconductors, etc." NDRC Division 14, Rept. 133 (May 12, 1943).
[3] H. C. Montgomery, Proc. Inst. Radio Engrs. **40**, 1461–1471 (1952).
[4] R. L. Petritz, Proc. Inst. Radio Engrs. **40**, 1440–1456 (1952).

A Note on the Cylindrical Antenna of Noncircular Cross Section

Y. T. Lo*
Channel Master Corporation, Ellenville, New York
(Received May 13, 1953)

COMMONLY used antenna towers are of noncircular cross section. In order to apply the theory of circular cylindrical antenna on these practical cases, according to Hallén,[1] it is necessary only to take their so-called equivalent radii. In this paper simple and exact formulas have been obtained for cylindrical antennas of polygonal cross section of n sides and also of elliptical cross section.

Case 1. Cylindrical antenna of polygonal cross section. Following Hallén,[1] the equivalent radius ρ of a uniform cylindrical antenna

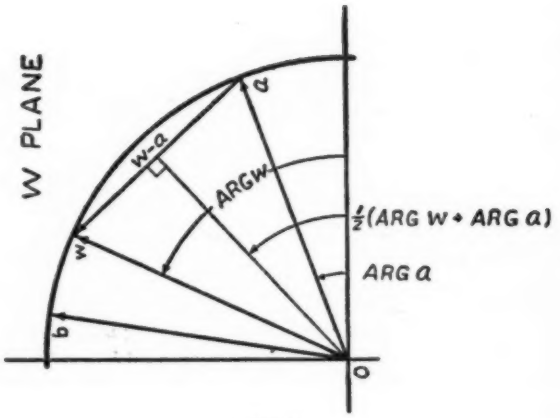

FIG. 1.

is defined by the expression:

$$\int\sigma\log 1/r dS=\log 1/\rho\int_S\sigma dS=-Q\log\rho, \tag{1}$$

where σ is the surface density of charge; r is the distance from a typical point of charge density σ to an arbitrary point in the same cross section; dS is an element of length around the periphery; Q is the total charge per unit length. Clearly, the equivalent radius is defined by the invariance of the capacity per unit length.

The following function will transform the region outside a polygon in the Z plane into a region exterior to a unit circle in the W plane, with infinity invariant[3]

$$Z=\int(W-a)^{\alpha-1}(W-b)^{\beta-1}\cdots W^{-2}dW, \tag{2}$$

$$|a|=|b|=\cdots=1, \tag{3}$$

$$(\alpha-1)+(\beta-1)+\cdots=2, \tag{4}$$

where $\alpha\pi$, $\beta\pi$, $\cdots$ are the exterior angles at the vertices A, B, $\cdots$ of the polygon in the Z plane that correspond to the points a, b, $\cdots$ on the unit circle in the W plane. The circle has unit radius because of Eq. (3). Equation (4) expresses the geometric fact that the sum of the exterior angles of a closed polygon with n sides is $(n+2)\pi$. Equation (2) may be verified by writing out the differential and taking its argument, remembering that the argument of a product of complex numbers equals the sum of their arguments.[3] Thus

$$dZ=(W-a)^{\alpha-1}(W-b)^{\beta-1}\cdots W^{-2}dW, \tag{5}$$

$$\arg dZ=(\alpha-1)\arg(W-a)+(\beta-1)\arg(W-b)+\cdots-2\arg W+\arg dW. \tag{6}$$

From Fig. 1 we see that

$$\arg(W-a)=1/2\arg W+\arg a)+1/2(\pi) \tag{7}$$

and also that

$$W=e^{i\theta},\ dW=Wjd\theta,\ \arg dW=\arg W+1/2(\pi). \tag{8}$$

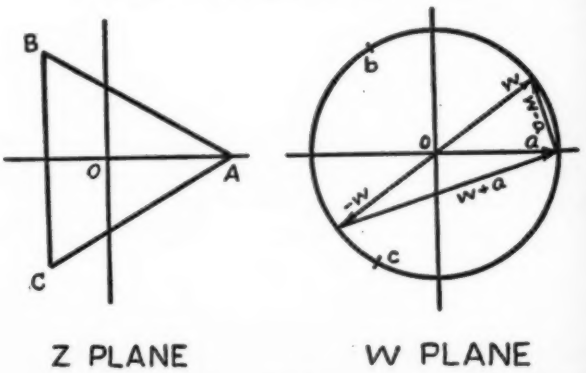

FIG. 2.

TABLE I.

n	ρ/d
2	$\frac{1}{4}$
3	0.4214
4	0.5903
5	0.7563
6	0.920

When these values are inserted in Eq. (6) arg$W$ cancels out so that as W moves along the circle from a to b, argdZ is constant which means that Z moves along a straight line. When W crosses b, $(W-b)$ changes sign so arg$(W-b)$ changes by π and dZ changes direction by $(\beta-1)\pi$. A similar statement applies to each vertex so that Eq. (2) does transform the unit circle in the W plane into a polygon in the Z plane.

For a regular polygon of n sides the change of direction at each vertex is $2\pi/n$ so that each term in Eq. (4) is $2/n$ and to agree with Eq. (3) we write

$$a=1,\ b=e^{2j\pi/n},\ c=e^{4j\pi/n},\cdots. \tag{9}$$

Equation (5) may now be written

$$dZ=(W-1)^{2/n}[W-\exp(j2\pi/n)]^{2/n}\cdots \times[W-\exp(j2\pi\langle n-1\rangle_{hn}/n)]^{2/n}W^{-2}dW \tag{10}$$

Since the product $(W-1)[W-\exp(j2\pi/2)]\cdots[W-\exp(j2\pi\times\langle n-1\rangle_{hn}/n]$ represents a polynomial of nth order with roots at 1, $\exp(j2\pi/n),\cdots,\exp(j2\pi\langle n-1\rangle_{hn}/n)$, evidently it is equal to (W^n-1). Thus if $W=e^{j\theta}$ Eq. (10) may be written

$$dZ=(W^{n/2}-W^{-n/2})^{2/n}W^{-1}dW=2^{2/n}\sin^{2/n}\tfrac{1}{2}n\theta\exp[j(1+2/n)\pi/2]d\theta.$$

We have already seen that as θ moves along the cylinder from a to b in Fig. 2, dZ moves along the side of the polygon from A to B. Thus d, the length of the side of the polygon is, since the absolute value of the exponential is unit,

$$d=2^{2/n}\int_0^{2\pi/n}\sin^{2/n}\tfrac{1}{2}n\theta d\theta=2^{1+4/n}\left[\Gamma\left(\frac{1}{n}+\frac{1}{2}\right)\right]^2\left[n\Gamma\left(1+\frac{2}{n}\right)\right]^{-1}, \tag{11}$$

where the integration is carried out by Dwight 855.3 with $u=\frac{1}{2}n\theta$. The radius of a circle equivalent to an n-sided regular polygon is, therefore, given by

$$\rho=n\Gamma\left(1+\frac{2}{n}\right)d/2^{1+4/n}\left[\Gamma\left(\frac{1}{2}+\frac{1}{n}\right)\right]^2. \tag{12}$$

Based upon this formula, the value of ρ for simple cases has been tabulated in Table I. For $n=2$, the polygon is degenerated into a strip. Incidentally, the values for $n=2$, 4, have been given by Hallén.

Although the formula (12) is applicable only to regular polygons, the transformation of (2)–(4) can be employed for irregular polygon as well. However, the possibility of the evaluation of the integral will depend upon the irregularity of the polygon.

Case 2. Cylindrical antenna of elliptical cross section. For this case, let[4]

$$W=Z+a/Z,$$

where a is an arbitrary real quantity.

Let

$$W=U+jV$$

and

$$Z=\rho e^{j\theta}.$$

Then

$$U=(\rho^2+a^2)\cos\theta/\rho,\quad V=(\rho^2-a^2)\sin\theta/\rho,$$

and

$$U^2/(\rho^2+a^2)^2+V^2/(\rho^2-a^2)^2=1/\rho^2. \tag{13}$$

For a circle in Z plane, or $\rho=$const, the above Eq. (13) will result in an ellipse in the W plane with major and minor axes

$$A=(\rho^2+a^2)/\rho,\quad B=(\rho^2-a^2)/\rho.$$

Hence, solving for ρ,

$$\rho=(A+B)/2. \tag{14}$$

When $B=0$, the ellipse degenerates again into a strip with a width equal to $d=2\times$ the length of focus

$$=2(A^2-B^2)^{\frac{1}{2}}=4\rho,$$

which checks with the value obtained in the previous case.

* This work has been done in the Electrical Engineering Department, University of Illinois, in 1950.

[1] E. Hallén, Nova Acta Regiae Soc. Sci. Upsaliensis, Ser. IV, 11, No. 4, 1–44, (1938).

[2] H. Bateman, *Partial Differential Equations of Mathematical Physics* (Dover Publications, New York), pp. 305–306.

[3] W. R. Smythe, *Static and Dynamic Electricity* (McGraw-Hill Book Company, Inc., New York, 1939), first edition, pp. 71, 80–81.

[4] See reference 3, pp. 90–91.

Force on a Shorted Ring in a uhf Field in a Coaxial Cavity

SURINDRA N. KALRA
Division of Physics, National Research Council, Ottawa, Ontario, Canada
(Received July 2, 1953)

THE change in potential energy of a short-circuited metallic ring in an alternating magnetic field, owing to the interaction of the induced current in the ring and the magnetic field, can be made the basis of a measurement of high-frequency power. If the circumference of the ring is small compared to a wavelength, then to a first approximation it may be assumed that the presence of the ring does not affect the magnetic field in its vicinity. The potential energy $U_{(R,\theta)}$ for a coaxial system with the ring at a current maximum is then given by the expression (in rationalized mks system of units)

$$U_{(R,\theta)}=\frac{\mu\pi r^4QP\sin^2\theta}{R^2\omega L_r\lambda\ln b/a}, \tag{1}$$

where μ=permittivity of the medium, r=radius of the ring, Q=Q factor of the cavity, P=power input to the cavity, R=radial distance of the center of the ring, from the cylindrical axis of the cavity, ω=angular frequency, L_r=total rf inductance of the shorted ring, λ=wavelength, b=inside radius of the outer cylinder, a=outside radius of the inner cylinder, and θ=angle between the plane of the ring and the direction of the magnetic field.

It has been assumed in Eq. (1) that the magnetic field is constant over the area of the ring. This introduces an error of less than 0.5 percent for the constants used in this experiment. The torque on the ring is given by $-(\partial U/\partial\theta)$ and has been considered by Solow[1] and others. The radial force F_r acting on the ring is

$$F_R=-\left.\frac{\partial u}{\partial R}\right|_{\theta=\text{constant}}=\frac{2\mu\pi r^4QP\sin^2\theta}{R^2\omega L_r\lambda\ln b/a}. \tag{2}$$

A preliminary check of Eq. (2) was made with $\theta=90°$, frequency $f=787$ mc/s, $r=0.4$ cm, $R=4.1$ cm, $Q=5000$, and $P=0.38$ watt. The radial force was measured by observing the difference in the weight of the ring with power on and power off. The difference in weight Δm is given by

$$\Delta m=F_r/g=0.20\times10^{-9}\ kg=0.20\ \text{microgram}, \tag{3}$$

where g is the gravitational acceleration in meters/sec^2. Δm was measured with a quartz torsion balance[2] made by the Atomic Energy Division of the National Research Council of Canada, which has a sensitivity of 0.01 microgram. The observed $\Delta m=0.26$ microgram agrees with the calculated value within the experimental error. Efforts are being made to improve the accuracy of this experiment.

It is seen from Eqs. (2) and (3) that except for power P and the Q factor of the cavity (a dimensionless quantity) all other quantities are expressed in fundamental units of mass, length, acceleration and time, permittivity and inductance. The constants

involved are directly measured or calculated; when the power input P is greater than 5 or 10 watts all the quantities can be measured to an accuracy greater than 0.1 percent (with the possible exception of Q). If this method is used for the measurement of power, the ultimate accuracy will be largely dependent on the accuracy to which Q can be determined. This method suggests a means of determining the power on an absolute basis at ultra-high and microwave frequencies. An estimate of over-all accuracy readily obtainable is about 1 percent for powers of a few watts.

The author wishes to thank the National Research Council of Canada for the award of a Fellowship and Dr. J. T. Henderson and Mr. R. Bailey for their help and encouragement.

[1] M. Solow, "Theoretical Study of an Electrodynamic Ammeter for Very High Frequencies," CRPL Preprint 50-15 (National Bureau of Standards; January 12, 1950). Other references will be found in this paper.
[2] H. Carmichael, Can. J. Phys. **30**, 524-555 (1952).

Bounds for Entropy

NELSON M. BLACHMAN
U. S. Office of Naval Research, Washington, D. C.
(Received June 8, 1953)

SINCE it is often not easy to evaluate the entropy integral of communication theory,[1]

$$H=-\int p(x)\log p(x)dx, \tag{1}$$

it is desirable to have easily calculated bounds for this quantity. Five inequalities which H must satisfy are presented here. First, we have

$$H\geqslant -\log p_{\max}, \tag{2}$$

since the rectangular distribution has the least entropy for a given maximum height. Second, if X is the mean absolute deviation of x from its mean value x_0, we have

$$H\leqslant \log 2eX, \tag{3}$$

since, for a given X, the distribution

$$p(x)=(2X)^{-1}\exp(-|x-x_0|/X)$$

has the greatest entropy. Third, if s is the standard deviation of x (the rms deviation from x_0), we have

$$H\leqslant \tfrac{1}{2}\log 2\pi e s^2, \tag{4}$$

since, of all the distributions with a given s the Gaussian has the greatest entropy.

Fourth, by expanding the $\log p$ in (1) about x_0 in a two-term Taylor series with remainder, we find that

$$-\log p(x_0)-\tfrac{1}{2}s^2\log''_{\max}p\leqslant H\leqslant -\log p(x_0)-\tfrac{1}{2}s^2\log''_{\min}p, \tag{5}$$

where $\log''_{\min}p$ and $\log''_{\max}p$ are the extrema of the second derivative of $\log p$. These lower and upper bounds are equal for and exponential distribution (e.g., $p(x)=a\exp(-ax)$ for $x>0$) and for a rectangular distribution as well as for a Gaussian distribution.

Last, by introducing the transformation in (1), $p=ep_{\max}q$, we are led to an integral $\int q\log q dx$ with $q\leqslant 1/e$. In this range the integrand is a monotonic function of q. Now $\log q$ may be expanded about the x for which p is maximum in a two-term Taylor series with remainder, the linear term dropping out because $\log' p=0$ at the maximum. If this expression is used for $\log q$ and its exponential is used for q in evaluating the integral, the following inequality is obtained for the entropy:

$$\tfrac{1}{2}(-2\pi/\log''_{\min}p)^{\frac{1}{2}}p_{\max}-\log ep_{\max}\leqslant H\leqslant \tfrac{1}{2}(-2\pi/\log''_{\max}p)^{\frac{1}{2}}p_{\max}-\log ep_{\max}. \tag{6}$$

These lower and upper bounds are equal for a Gaussian distribution. If $\log''_{\max}p$ is positive, Eq. (6) provides no upper bound for H. Unless natural logarithms are used throughout and entropy is measured in nits, the first term of each of the bounds in Eq. (6) should be multiplied by the factor $(\log e)^{\frac{1}{2}}$.

This inequality can be written in a weaker but interesting form by making use of an inequality existing among its arguments. Using the two-term-plus-remainder series expansion of $\log p$, we obtain from the normalization of p the inequality

$$(-\log''_{\max}p/2\pi)^{\frac{1}{2}}\leqslant p_{\max}\leqslant(-\log''_{\min}p/2\pi)^{\frac{1}{2}},$$

which permits us to write Eq. (6) in the form

$$\tfrac{1}{2}(\log''_{\max}p/\log''_{\min}p)^{\frac{1}{2}}-\log ep_{\max}\leqslant H\leqslant \tfrac{1}{2}(\log''_{\min}p/\log''_{\max}p)^{\frac{1}{2}}-\log ep_{\max} \tag{7}$$

provided that $\log''_{\max}p$ is negative. For distributions whose tails fall off faster than those of a Gaussian distribution, Eq. (5) provides only a lower bound and Eq. (6) only an upper bound, since $\log''_{\min}p=-\infty$. For distributions whose tails fall off more slowly than those of a Gaussian distribution, $\log''_{\max}p\geqslant 0$, and the situation is reversed. Inequality (7) is useful only in the intermediate case.

C. E. Shannon, Bell System Tech. J. **27**, 379, 623 (1948).

Forming Silicon Point Contact Transistors

HAROLD JACOBS, FRANK A. BRAND, AND WESLEY MATTHEI
Signal Corps Engineering Laboratories, Fort Monmouth, New Jersey
(Received July 10, 1953)

A NEW technique has been developed whereby p- and n-type silicon crystals can be formed to exhibit noticeable transistor action.

This method consists of pressing minute chips or particles of a suitable impurity material between a pointed 80-mil tungsten electrode and the silicon sample. Upon the passage of currents of high density through this junction in an atmosphere of nitrogen, considerable local heating and arcing was observed. After this treatment, the samples exhibited the properties of n-p-n and p-n-p point contact transistors (depending on the impurity used) to a much greater extent than the unprocessed silicon specimens.

Best results were obtained when antimony was used to form the p-type samples and aluminum to form the n-type crystals. Typical values based on over fifty tests for each type crystal are indicated in Table I. These data show the results of tests run before and after processing.

In addition, dynamic voltage gains of forty to one and power gains of eighteen to one were often observed, after forming the n-type silicon. Under these conditions r_{11} was approximately

TABLE I. Operating characteristics of p- and n-type silicon before and after processing.

Sample (Crystal type)	Emitter voltage Volts	Collector voltage Volts	Emitter current ma	Collector current ma	Static current multiplication α	Dynamic voltage gain
Control (p type)	1.30	28.4	6.0	9.0	0.03	1.0
Formed (p type)	0.20	40.5	3.0	10.3	1.07	23.0
Control (n type)	7.50	36.2	1.5	4.5	0.15	1.0
Formed (n type)	0.70	59.0	1.5	4.5	1.30	25.0

800 ohms; r_{22} was 13 000 ohms, and the current multiplication (α) was 2.0. The maximum current multiplication factors ranged from 5.2 to 2.0.

The p-type samples were supplied by the Naval Research Laboratories. The resistivity of this material was in the range of 0.1 ohm-cm to 1.0 ohm-cm. Two different sources of n-type materials were used, the resistivities of which were from 1.0 to 5.0 ohm-cm. Several specimens were supplied by Dr. P. H. Keck of the Signal Corps Engineering Laboratories. Further experiments in forming higher purity silicon are now in process and will be reported at a future date.

Acknowledgment should be made to Mr. Alexander Ramsa for his assistance in carrying out these experiments.